

# Measurements of Combustion Dynamics with Laser-Based Diagnostic Techniques

Thesis by

Dal Mo Kang

In Partial Fulfillment of the Requirements

for the Degree of

Doctor of Philosophy



California Institute of Technology

Pasadena, California

2006

(Defended December 2, 2005)



## ACKNOWLEDGEMENTS

First, I would like to show my gratitude to my advisor, Prof. Fred E. C. Culick, for his guidance and patience to encourage me during my study in Caltech. I also would like to thank the committee members, Prof. Melany Hunt, Dave Goodwin, and Hans Hornung for their efforts to support me through my graduate study in Caltech.

Al Ratner, professor of Mechanical and Industrial engineering, in University of Iowa, has been a good teacher and, at the same time, a best friend to me. I will never forget what he has done for me to support and guide me, even serving my thesis committee going through all the troubles to cross the continent.

I thank Dr. Robert K. Cheng, in Lawrence Berkeley Livermore National Laboratory for providing me with the ‘precious’ swirl burner system, and even a newer one after I ruined the first one during an experiment. I feel indebted to Jeff and Laurent for helping me with the calibrations and providing me valuable advises regarding LIF experiments. And I appreciate the JPC members – Kevin Parkin, Robert Moeller for amusing me with discussions on a variety of social, political and scientific issues, and Francesco Ciucci, Winston Pun, and Steve Palm for their help in my initiation with the graduate studies. I thank Melinda Kirk for facilitating everything I did in Caltech.

I want to thank Carlos Pinedo (MURF), Vivek Singhal for experimental set-ups and, also, Huang Yun, Hui Gao, and Brett Bathel in University of Iowa for their help and friendship in Iowa.

I want to acknowledge my friends in Caltech, Lance Cai, Min Tao, Fuling Yang, and Yongqiang Liang, and members of CKGSA, too many to mention, for their love and respect for me. And I also appreciate former Caltech members, especially Dr. Dong Eui Chang and Dr. Ki Baek Kim for their support and care.

I thank my friends in Korea (too many to mention, but you know who you are!) who always have been encouraging and inspiring me through hard times, I really appreciate your love and support. I would like to show my special thanks to Wounjoo Lee, and Youngmin Hong who always stayed beside me in times of difficulties.

I show my love and respect to my sisters, Jin Sook, In Sook, Hye Sook, Eun Sook, and Miyoung, and their families. Finally, I would like to show my deepest love and respect to my parents, Bum Goo Kang and Jung Soon Lee for their dedication and sacrifice for their only son. All the achievements I've made belong to you!

Again, I would like to thank everybody, including those who may not have been mentioned above for the limited space (yes, you are one of them!), for everything they did to help this thesis make its way out to the world.

Thank you very much!

## ABSTRACT

Since the early days of gas turbine engines, combustion/flow instability inside the combustor has been an issue in many engines, but little has been understood as to how the dynamics of the system involved contribute to the instability. The primary objective of this work is to provide general experimental procedures and to validate methods for examining the dynamic behaviors of combustion systems, and to provide accurate measurements of the combustion dynamics for use as a foundation for further theoretical and numerical research. Knowledge of the fundamental dynamics of combustion systems is crucial in understanding and modeling the flame behavior and enabling the use of insights in design process and for creating robust active control of combustors.

Since mixing plays significant roles in combustion processes, the dynamics of fuel/air mixing were studied. A non-premixed burner was examined with acoustic excitations at 22~55 Hz to assess the mixing and its relation to the thermo-acoustic coupling. Phase-resolved acetone-PLIF was used to image the mixing, and from this the unmixedness was calculated, which quantifies the degree of mixing. The results show that (1) the acoustic waves induce periodicity in the degree of mixing; (2) the way the unmixedness behaves coincides well with the behavior of the Rayleigh index, implying the degree of mixing is a major factor in determining the stability of the combustion system; (3) the two-dimensional measurements of temporal unmixedness effectively visualize the shear mixing zone.

A second low-swirl premixed burner was studied to examine the impact of acoustic waves on the combustion dynamics. Measurements were performed with OH-PLIF, with acoustic forcing up to 400 Hz. Swirl burners at higher pressure are industry standard, and this study examined the dynamics at elevated combustor pressure. The results show that (1) the thermo-acoustic coupling seems to be closely coupled to the vortices generated at the flame boundary; (2) high magnitude of flame response coincides with the high absolute value of Rayleigh index; (3) the way the thermo-acoustic coupling is distributed over the space is highly dependent on the excitation frequencies; (4) high pressure suppresses the sensitivity of combustions system to outside disturbances.

**TABLE OF CONTENTS**

<b>Acknowledgements</b>	<b>iii</b>
<b>Abstract</b>	<b>v</b>
<b>Table of Contents</b>	<b>vii</b>
<b>List of Figures</b>	<b>xii</b>
<b>List of Tables</b>	<b>xxi</b>
<b>CHAPTER 1 INTRODUCTION</b>	<b>1</b>
<b>1.1 Motivation</b>	<b>1</b>
<b>1.2 Objectives</b>	<b>8</b>
<b>1.3 Literature Survey</b>	<b>10</b>
1.3.1 Behavior of Mixing	10
1.3.2 Measurements of Combustion Dynamics	13
<b>1.4 A Précis of the Thesis</b>	<b>17</b>
<b>CHAPTER 2 STUDY OF LASER INDUCED FLUORESCENCE</b>	
<b>WITH NO LIF</b>	<b>20</b>
<b>2.1 Introduction</b>	<b>21</b>
2.1.1 Motivation	21
2.1.2 Objectives	23
<b>2.2 Experimental Configurations</b>	<b>24</b>

2.2.1 Test Section	24
2.2.2 Laser System	27
2.2.3 Optical Configurations	29
2.2.4 Detection System	32
<b>2.3 Procedure</b>	<b>32</b>
<b>2.4 Results</b>	<b>35</b>
2.4.1 Preliminary Data	35
2.4.2 Saturated LIF Spectral Scan	38
2.4.3 The LIF Results	40
<b>2.5 Summary</b>	<b>51</b>

## **CHAPTER 3 MEASUREMENTS OF THE DYNAMIC**

<b>RESPONSE OF MIXING</b>	<b>55</b>
<b>3.1 Introduction</b>	<b>56</b>
3.1.1 Background	56
3.1.2 Objectives	60
<b>3.2 Experimental Configurations</b>	<b>60</b>
3.2.1 Acoustic Driving System	60
3.2.2 Laser and Optical Configurations	62
3.2.3 Test Section	65
3.2.4 Data Acquisition	68
3.2.5 The Controller	68
<b>3.3 Experimental Procedure</b>	<b>69</b>

<b>3.4</b>	<b>Results</b>	<b>71</b>
3.4.1	Temporal Behavior of Mixing	73
3.4.2	Phase-Resolved Behavior of Mixing	82
<b>3.5</b>	<b>Summary</b>	<b>99</b>

## **CHAPTER 4 MEASUREMENTS OF THE COMBUSTION**

	<b>DYNAMICS OF A SWIRL-STABILIZED BURNER</b>	<b>102</b>
<b>4.1</b>	<b>Purpose</b>	<b>103</b>
<b>4.2</b>	<b>The Thermo-Acoustic Coupling</b>	<b>104</b>
<b>4.3</b>	<b>OH PLIF</b>	<b>106</b>
<b>4.4</b>	<b>Experimental Configurations</b>	<b>109</b>
4.4.1	Laser System for OH PLIF	109
4.4.2	Filtering the PLIF Signal	110
4.4.3	Fuel/Air Feed System	110
4.4.4	The Swirl Burner	113
<b>4.5</b>	<b>Experimental Procedure</b>	<b>115</b>
4.5.1	General Procedure	115
4.5.2	Post-processing	117
<b>4.6</b>	<b>Results</b>	<b>118</b>
4.6.1	Combustor Pressure and Heat Release Rate	119
4.6.2	Local Distribution of the Rayleigh Index	123
4.6.3	Global Rayleigh Index	137
4.6.4	Global Flame Response	138

4.6.5 Local Distribution of Flame Response	141
<b>4.7 Summary</b>	<b>147</b>
<b>CHAPTER 5 FURTHER STUDY OF SWIRL BURNER</b>	
<b>COMBUSTION DYNAMICS</b>	<b>150</b>
<b>5.1 Introduction</b>	<b>151</b>
<b>5.2 Experimental Configuration</b>	<b>153</b>
5.2.1 The Swirler	153
5.2.2 Premixer and Burner	154
5.2.3 High Pressure Chamber	157
5.2.4 Data Acquisition	161
<b>5.3 Experimental Procedure</b>	<b>161</b>
<b>5.4 Results and Discussion</b>	<b>164</b>
5.4.1 Distribution of Local Rayleigh Index	165
5.4.2 Global Rayleigh Index and Flame Response	174
5.4.3 Distribution of Local Flame Response	179
<b>5.5 Summary</b>	<b>190</b>
<b>CHAPTER 6 CONCLUDING REMARKS</b>	<b>193</b>
<b>Appendix A Laser-induced Fluorescence: An Introduction</b>	<b>201</b>
<b>A.1 Background</b>	<b>202</b>

A.1.1	Theoretical Background	202
A.1.2	PLIF	205
<b>A.2</b>	<b>Characteristics of Acetone PLIF</b>	<b>206</b>
<b>Appendix B</b>	<b>INTRODUCTION TO THE RAYLEIGH INDEX</b>	<b>211</b>
<b>B.1</b>	<b>Introduction</b>	<b>212</b>
<b>B.2</b>	<b>Mathematical Formulations</b>	<b>213</b>
B.2.1	Governing Equations	202
B.2.2	Linear analysis of Rayleigh's criterion for small amplitude motion	217
B.2.3	Nonlinear Analysis of Rayleigh's Criterion	218
<b>Appendix C</b>	<b>FLOWMETER CALIBRATION</b>	<b>221</b>
<b>Appendix D</b>	<b>COMBUSTION DYNAMICS DATA</b>	<b>225</b>
<b>REFERENCES</b>		<b>267</b>

## LIST OF FIGURES

Figure 1.1. Pressure wave amplification.	2
Figure 1.2. Effect of equivalence ratio on NO <sub>x</sub> production (from Rosfjord 1995).	4
Figure 1.3. Diagram of active control and combustor response.	6
Figure 1.4. Experimental Works as a Basis for Theoretical and Numerical Research.	7
Figure 1.5. Idealized Flow of Information (from AGARDograph, Culick, 2005).	8
Figure 1.6. Visualization of mixing with and without imposed acoustic oscillation (350 Hz) (Hardalupas et al. 2002)	11
Figure 1.7. Basic schematics of chemiluminescence and laser induced fluorescence (Adapted from Wolfrum, 1998)	14
Figure 2.1. Burner assembly.	24
Figure 2.2. The flow control board for regulating fuel/air/seeded gas flows (a); and the flow diagram (b).	25
Figure 2.3. Energy level diagram of NO (adapted from Daily et al. 2005).	28
Figure 2.4. Mixer/Doubler system.	29
Figure 2.5. Schematic drawing of the optical setup used for the measurements (top), and the ICCD camera (bottom).	31
Figure 2.6. Normalized Fluorescence of NO measured in a 1 bar NO-cell.	35
Figure 2.7. LIF-Base calculations of NO-LIF spectrum.	36
Figure 2.8. Excitation scans in a 4.27 atm spray flame doped with NO using narrowband linear-LIF detection and broadband linear-PLIF detection.	37
Figure 2.9. Relative Fluorescence signal obtained from a stoichiometric and a rich flame ( $\phi=1.35$ ).	39

Figure 2.10. Fluorescence Signal normalized over the maximum at a mixture ratio of 1.35 with CO <sub>2</sub> dilution.	39
Figure 2.11. Spectral Scan of a $\phi=1.25$ flame seeded with N <sub>2</sub> as in Table 2.1.	41
Figure 2.12. Spectral Scan of a $\phi=1.35$ flame seeded with N <sub>2</sub> as in Table 2.1.	41
Figure 2.13. Spectral Scan of a $\phi=1.25$ flame seeded with CO <sub>2</sub> as in Table 2.1.	42
Figure 2.14. Spectral Scan of a $\phi=1.35$ flame seeded with CO <sub>2</sub> as in Table 2.1.	42
Figure 2.15. Saturation curve for NO-LIF ( $\phi=1.25$ ).	44
Figure 2.16. Saturation curve for NO-LIF ( $\phi=1.35$ ).	44
Figure 2.17. Spectral scan close to the peak for $\phi=1.25$ with N <sub>2</sub> and CO <sub>2</sub> dilution and a laser energy per unit area of 3.00 mJ/mm <sup>2</sup> .	46
Figure 2.18. Spectral scan close to the peak for $\phi=1.35$ with N <sub>2</sub> and CO <sub>2</sub> dilution and a laser energy per unit area of 3.00 mJ/mm <sup>2</sup> .	46
Figure 2.19. Spectral scan close to the peak for $\phi=1.25$ with N <sub>2</sub> and CO <sub>2</sub> dilution and a laser energy per unit area of 3.65 mJ/mm <sup>2</sup> .	47
Figure 2.20. Spectral scan close to the peak for $\phi=1.35$ with N <sub>2</sub> and CO <sub>2</sub> dilution and a laser energy per unit area of 3.65 mJ/mm <sup>2</sup> .	47
Figure 2.21. Spectral scan close to the peak for $\phi=1.25$ with N <sub>2</sub> and CO <sub>2</sub> dilution and a laser energy per unit area of 4.12 mJ/mm <sup>2</sup> .	48
Figure 2.22. Spectral scan close to the peak for $\phi=1.35$ with N <sub>2</sub> and CO <sub>2</sub> dilution and a laser energy per unit area of 4.12 mJ/mm <sup>2</sup> .	48
Figure 2.23. Spectral scan close to the peak for $\phi=1.25$ with N <sub>2</sub> and CO <sub>2</sub> dilution and a laser energy per unit area of 4.78 mJ/mm <sup>2</sup> .	49
Figure 2.24. Spectral scan close to the peak for $\phi=1.35$ with N <sub>2</sub> and CO <sub>2</sub> dilution and a laser energy per unit area of 4.78 mJ/mm <sup>2</sup> .	49
Figure 2.25. Spectral scan close to the peak for $\phi=1.25$ with N <sub>2</sub> and CO <sub>2</sub> dilution	

and a laser energy per unit area of 5.19 mJ/mm <sup>2</sup> .	50
Figure 2.26. Spectral scan close to the peak for $\phi=1.35$ with N <sub>2</sub> and CO <sub>2</sub> dilution and a laser energy per unit area of 5.19 mJ/mm <sup>2</sup> .	50
Figure 2.27. Spectral scan close to the peak for $\phi=1.25$ with N <sub>2</sub> and CO <sub>2</sub> dilution and a laser energy per unit area of 5.57 mJ/mm <sup>2</sup> .	51
Figure 3.1. The combustion chamber.	61
Figure 3.2. Schematic of the Acetone PLIF.	63
Figure 3.3. A random single shot image (left hand side) and a cropped, phase-averaged image (right hand side, phase angle of 15 degrees) at 32 Hz.	64
Figure 3.4. Region of Interest (top) and the Sectional View of Burner (bottom).	65
Figure 3.5. The Gas Feed System (top) and the Acetone Seeder (bottom).	67
Figure 3.6. Fast Fourier Transformed pressure signal at 22, 27, and 32 Hz.	71
Figure 3.7. Fast Fourier Transformed pressure signal at 37 and 55 Hz.	72
Figure 3.8. Temporal Unmixedness measured at the neck of the eductor block (the region marked with red arrow in Figure 3.4 (top), Fernandez et al. 2003).	73
Figure 3.9. Distribution of temporal unmixedness, at 22 Hz (a), 27 Hz (b), and 32 Hz (c).	74
Figure 3.10. Distribution of temporal unmixedness at 37Hz (a) and 55Hz (b). Reacting (LHS) and non-reacting (RHS) cases.	75
Figure 3.11. Temporal Unmixedness factors with excitation at 1 (top), 2 (middle), 3 (bottom) above the eductor block.	76
Figure 3.12. The locations where the measurements are made (top), and (b) the fuel concentration distribution at 1, 2, 3 cm above the eductor block at 22 Hz.	79
Figure 3.13. The fuel concentration distribution at 1, 2, 3 cm above the eductor block at 27 Hz (top) and 32 Hz (bottom).	80
Figure 3.14. The fuel concentration distribution at 1, 2, 3 cm above the eductor block at 37Hz (top) and 55Hz (bottom).	81
Figure 3.15. Fuel concentration distribution by phase at 22 Hz.	83
Figure 3.16. Fuel concentration distribution by phase at 27 Hz.	84
Figure 3.17. Fuel concentration distribution by phase at 32 Hz.	85

Figure 3.18. Fuel concentration distribution by phase at 37 Hz.	86
Figure 3.19. Fuel concentration distribution by phase at 55 Hz.	87
Figure 3.20. Power density spectrum of fuel mixture fraction for 32Hz, reacting flow (from Fernandez et al. 2003).	88
Figure 3.21. Response of fuel/air mixing to the imposed acoustic oscillations.	90
Figure 3.22. Oscillatory behaviors of global mixing presented with reference acoustic wave.	92
Figure 3.23. Comparison of phase shifts of mixing and flame behaviors.	93
Figure 3.24. Time lags (top) and measurements (bottom).	95
Figure 3.25. Relationship between changes in mixing behaviors and flame response.	96
Figure 3.26. Relationship between changes in mixing behaviors and flame response.	97
Figure 3.27. 3-D representation of global unmixedness vs. excitation frequency and phase.	98
Figure 4.1. Energy levels of Hydroxyl radical (Eckbreth, 1996).	107
Figure 4.2. The pumping laser scanning for (1,0) band of OH excitation.	108
Figure 4.3. Saturation of LIF signal to avoid the signal quenching.	109
Figure 4.4. Diagram of the fuel/air feed system.	112
Figure 4.5. The swirl premixed burner installed on top of a premixer (left); and the shape of the flame (averaged at 110Hz, $\phi = 0.6$ , right).	113
Figure 4.6. The swirl burner assembly.	113
Figure 4.7. The swirler.	114
Figure 4.8. FFT of the pressure signal (left) and heat release fluctuation (right) at $\phi = 0.60$ and excitation frequencies 27, 125, and 240 Hz.	120
Figure 4.9. Heat release fluctuation at $\phi = 0.5$ as a function of excitation frequency and phase during one cycle of the imposed acoustic wave.	121
Figure 4.10. Heat release fluctuation at $\phi = 0.6$ as a function of excitation frequency and phase during one cycle.	122
Figure 4.11. Heat release fluctuation at $\phi = 0.75$ as a function of excitation frequency and phase during one cycle.	122
Figure 4.12. Sketch of the swirl flame.	128
Figure 4.13. Local distribution of Rayleigh index at $\phi = 0.50$	

(at selected frequencies, refer to Appendix D the rest of the data).	129
Figure 4.14. Local Distribution of Rayleigh index at $\phi = 0.60$	
(at selected frequencies, refer to Appendix D for the rest of the data).	130
Figure 4.15. Local distribution of Rayleigh index at $\phi = 0.75$	
(at selected frequencies, refer to Appendix D the rest of the data).	131
Figure 4.16. Local Rayleigh index distribution at different frequencies, $\phi = 0.50$ .	132
Figure 4.17. Local Rayleigh index distribution at different frequencies, $\phi = 0.60$ .	132
Figure 4.18. Local Rayleigh index distribution at different frequencies, $\phi = 0.75$ .	133
Figure 4.19. Local Rayleigh index distribution along the flame boundary at each frequency, $\phi = 0.50$ .	134
Figure 4.20. Local Rayleigh index distribution along the flame boundary at each frequency, $\phi = 0.60$ .	135
Figure 4.21. Local Rayleigh index distribution along the flame boundary at each frequency, $\phi = 0.75$ .	136
Figure 4.22. Wave numbers of Rayleigh index fluctuation along the flame boundary.	137
Figure 4.23. Global Rayleigh index (vs. excitation frequency).	137
Figure 4.24. Magnitude (top), and phase shift (bottom) of flame response.	139
Figure 4.25. An example of relevance between the phase shift and Rayleigh index.	143
Figure 4.26. Magnitude (left), and phase shift (right) of flame response, $\phi = 0.50$ .	144
Figure 4.27. Magnitude (left), and phase shift (right) of flame response, $\phi = 0.60$ .	145
Figure 4.28. Magnitude (left), and phase shift (right) of flame response, $\phi = 0.75$ .	146
Figure 5.1. The new swirler (swirler B).	153
Figure 5.2. Premixer, burner, and swirler assembly.	154
Figure 5.3. High Pressure Chamber (Diagram).	159
Figure 5.4. High Pressure Chamber.	160
Figure 5.5. Rayleigh index distribution, 1 atm, $\phi = 0.50$ , swirler A.	167
Figure 5.6. Rayleigh index distribution, 1 atm, $\phi = 0.63$ , swirler A.	168
Figure 5.7. Rayleigh index distribution, 1.5 atm, $\phi = 0.63$ , swirler A.	169
Figure 5.8. Rayleigh index distribution, 1.0 atm, $\phi = 0.55$ , swirler B.	170
Figure 5.9. Rayleigh index distribution, 1.5 atm, $\phi = 0.55$ , swirler B.	171

Figure 5.10. Wave number distribution.	173
Figure 5.11. Global Rayleigh Index for swirler A (top), B (middle), and altogether (bottom).	176
Figure 5.12. Global combustion response. Magnitude (a, b) and phase shift (c, d); swirler A (a, c) and swirler B (b, d).	177
Figure 5.13. Global combustion response (data for both swirlers A and B); magnitude (top) and phase shift (bottom).	178
Figure 5.14. Local response at 1.0 atm, $\phi = 0.50$ with swirler A. Magnitude in dB (right hand side); phase in degrees (left hand side).	180
Figure 5.15. Local response at 1.0 atm, $\phi = 0.50$ with swirler A. Magnitude in dB (right hand side); phase in degrees (left hand side).	181
Figure 5.16. Local response at 1.0 atm, $\phi = 0.63$ with swirler A. Magnitude in dB (right hand side); phase in degrees (left hand side).	182
Figure 5.17. Local response at 1.0 atm, $\phi = 0.63$ with swirler A. Magnitude in dB (right hand side); phase in degrees (left hand side).	183
Figure 5.18. Local response at 1.5 atm, $\phi = 0.63$ with swirler A. Magnitude in dB (right hand side); phase in degrees (left hand side).	184
Figure 5.19. Local response at 1.5 atm, $\phi = 0.63$ with swirler A. Magnitude in dB (right hand side); phase in degrees (left hand side).	185
Figure 5.20. Local response at 1.0 atm, $\phi = 0.55$ with swirler B. Magnitude in dB (right hand side); phase in degrees (left hand side).	186
Figure 5.21. Local response at 1.0 atm, $\phi = 0.55$ with swirler B. Magnitude in dB (right hand side); phase in degrees (left hand side).	187
Figure 5.22. Local response at 1.5 atm, $\phi = 0.55$ with swirler B. Magnitude in dB (right hand side); phase in degrees (left hand side).	188
Figure 5.23. Local response at 1.5 atm, $\phi = 0.55$ with swirler B. Magnitude in dB (right hand side); phase in degrees (left hand side).	189
Figure A.1. Jabłonski Diagram.	202
Figure A.2. A typical experimental set-up for LIF measurements.	204
Figure A.3. Schematic diagram of Planar LIF.	206

Figure A.4. Acetone vapor pressure versus temperature (Lozano et al. 1992).	207
Figure A.5. Acetone absorption spectrum corresponding to excitation from the ground state to the first excited singlet (Lozano et al. 1992).	208
Figure A.6. Relation between fluorescence signal and the intensity of laser excitation (Lozano et al. 1992).	209
Figure A.7. Relation between fluorescence signal and the intensity of laser excitation (Lozano et al. 1992).	210
Figure C.1. Flow rate calibration for the fuel flow controller.	223
Figure C.2. Flow rate calibration for the air flow controller.	224
Figure D.1. FFTed pressure signal (left) and heat release fluctuation (right) at $\phi = 0.50$ .	227
Figure D.2. FFTed pressure signal (left) and heat release fluctuation (right) at $\phi = 0.50$ .	228
Figure D.3. FFTed pressure signal (left) and heat release fluctuation (right) at $\phi = 0.50$ .	229
Figure D.4. FFTed pressure signal (left) and heat release fluctuation (right) at $\phi = 0.50$ .	230
Figure D.5. FFTed pressure signal (left) and heat release fluctuation (right) at $\phi = 0.50$ .	231
Figure D.6. FFTed pressure signal (left) and heat release fluctuation (right) at $\phi = 0.50$ .	232
Figure D.7. FFTed pressure signal (left) and heat release fluctuation (right) at $\phi = 0.60$ .	233
Figure D.8. FFTed pressure signal (left) and heat release fluctuation (right) at $\phi = 0.60$ .	234
Figure D.9. FFTed pressure signal (left) and heat release fluctuation (right) at $\phi = 0.60$ .	235
Figure D.10. FFTed pressure signal (left) and heat release fluctuation (right) at $\phi = 0.60$ .	236
Figure D.11. FFTed pressure signal (left) and heat release fluctuation (right)	

at $\phi = 0.60$ .	237
Figure D.12. FFTed pressure signal (left) and heat release fluctuation (right)	
at $\phi = 0.75$ .	238
Figure D.13. FFTed pressure signal (left) and heat release fluctuation (right)	
at $\phi = 0.75$ .	239
Figure D.14. FFTed pressure signal (left) and heat release fluctuation (right)	
at $\phi = 0.75$ .	240
Figure D.15. FFTed pressure signal (left) and heat release fluctuation (right)	
at $\phi = 0.75$ .	241
Figure D.16. FFTed pressure signal (left) and heat release fluctuation (right)	
at $\phi = 0.75$ .	242
Figure D.17. FFTed pressure signal (left) and heat release fluctuation (right)	
at $\phi = 0.75$ .	243
Figure D.18. Distribution of local Rayleigh index, $\phi = 0.50$ .	244
Figure D.19. Distribution of local Rayleigh index, $\phi = 0.50$ .	245
Figure D.20. Distribution of local Rayleigh index, $\phi = 0.60$ .	246
Figure D.21. Distribution of local Rayleigh index, $\phi = 0.60$ .	247
Figure D.22. Distribution of local Rayleigh index, $\phi = 0.75$ .	248
Figure D.23. Distribution of local Rayleigh index, $\phi = 0.75$ .	249
Figure D.24. Local magnitude (left), and phase shift (right) of flame response, $\phi = 0.50$ .	250
Figure D.25. Local magnitude (left), and phase shift (right) of flame response, $\phi = 0.50$ .	251
Figure D.26. Local magnitude (left), and phase shift (right) of flame response, $\phi = 0.50$ .	252
Figure D.27. Local magnitude (left), and phase shift (right) of flame response, $\phi = 0.50$ .	253
Figure D.28. Local magnitude (left), and phase shift (right) of flame response, $\phi = 0.50$ .	254
Figure D.29. Local magnitude (left), and phase shift (right) of flame response,	

$\phi = 0.50$ .	255
Figure D.30. Local magnitude (left), and phase shift (right) of flame response, $\phi = 0.60$ .	256
Figure D.31. Local magnitude (left), and phase shift (right) of flame response, $\phi = 0.60$ .	257
Figure D.32. Local magnitude (left), and phase shift (right) of flame response, $\phi = 0.60$ .	258
Figure D.33. Local magnitude (left), and phase shift (right) of flame response, $\phi = 0.60$ .	259
Figure D.34. Local magnitude (left), and phase shift (right) of flame response, $\phi = 0.60$ .	260
Figure D.35. Local magnitude (left), and phase shift (right) of flame response, $\phi = 0.75$ .	261
Figure D.36. Local magnitude (left), and phase shift (right) of flame response, $\phi = 0.75$ .	262
Figure D.37. Local magnitude (left), and phase shift (right) of flame response, $\phi = 0.75$ .	263
Figure D.38. Local magnitude (left), and phase shift (right) of flame response, $\phi = 0.75$ .	264
Figure D.39. Local magnitude (left), and phase shift (right) of flame response, $\phi = 0.75$ .	265
Figure D.40. Local magnitude (left), and phase shift (right) of flame response, $\phi = 0.75$ .	266

**LIST OF TABLES**

Table 1.1. Previous work in oscillating flames.	15
Table 2.1. Mass flow rates of gases.	26
Table 3.1. Comparison of various tracer molecules.	59
Table 4.1. Flow rates.	111
Table 5.1. Flow rates.	156

# Chapter 1

## Introduction

---

### 1.1 Motivation

Combustion has been, is, and for the foreseeable future, will be the primary method of generating power and providing energy for transportation. There has been a steady progression from outdoor wood fires to coal burning stoves to modern methane and kerosene-fueled gas turbines. For probably just as long, various forms of disturbances have plagued these systems and have been the focus of efforts to understand and control them. Outdoor wood fires suffer from shifting winds and wood-charcoal arrangements resulting in variable amounts of smoke going in various directions. Coal stoves often suffer from uneven airflow and combustion, often causing hot and cold spots and uneven heating, reducing the life of the stove. Even in modern gas turbines, combustion instability continues to plague many systems, causing everything from elevated pollution levels to (occasionally) catastrophic failure. In turbines, same as in the other systems

previously mentioned, the primary cause is variability in fuel-air mixing.

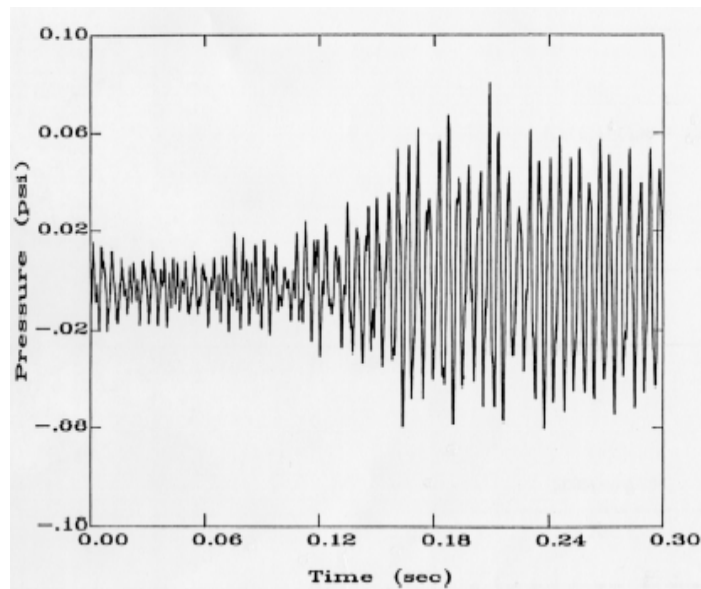


**Figure 1.1. Pressure wave amplification.**

In gas turbine combustors, this variability is induced primarily by acoustic waves. The acoustic waves are the result of coupling of unsteady heat release and the combustor geometry. Finally, the heat release is tied to the variability in fuel-air mixing and to the local velocity field (which is influenced by the acoustic waves). Therefore, understanding combustion instability requires accurate measurement, modeling, and understanding of a range of physical processes. For example, when the fuel-air mixing process interacts with acoustic waves in the presence of combustion, sudden growth in combustion intensity can occur, typically at certain modes or wave frequencies as determined by the local geometry (see Figure 1.1).

The interaction between vortices (mixing), sound (acoustic, or pressure oscillations), and

combustion heat release can lead to self-excited oscillations that prohibit desired operational conditions and can even lead to structural damages. In fact, any unsteadiness in the rate of combustion will be a source of sound, generating pressure and velocity fluctuations (Dowling 2000). In practical terms, this meant that gas turbines (and most other devices) were designed so that they operated at conditions far way from those that induce significant combustion instability.

Stricter government regulations in pollutant emissions forced gas turbine manufacturers to find ways to reduce the level of nitric oxides (NO<sub>x</sub>) production. There are several different pathways through which the various NO<sub>x</sub> compounds are produced, including the thermal mechanism, the prompt (HCN-based) route, the N<sub>2</sub>O coupled mechanism, and the fuel-bound nitrogen pathway (Warnatz et al. 2000, Pun 2001). Of these, based on current gas-turbine research, the thermal route is the primary NO<sub>x</sub> production pathway. Reduction of NO<sub>x</sub> produced by the thermal mechanism is usually achieved by lowering the flame temperature; that effect can be achieved by running the combustion system at decreased equivalence ratio (well below the stoichiometric levels). For this reason, lean premixed combustion processes are presently employed in many industrial applications. However combustion in the lean region is especially susceptible to instabilities, primarily because there exists an unstable combustion regime (Figure 1.2) near the lean blow out limit.

Oscillatory heat release, coupled with a system's natural acoustics, is generally identified as the primary feedback mechanism of self-excited combustion instabilities. Effective

means to measure and evaluate the dynamic behavior of combustion systems will significantly facilitate the design and evaluation of new and existing combustion systems such that the severity of problems arising due to the unintended oscillatory phenomena can be mitigated (at the design phase) and attenuated (in production models).

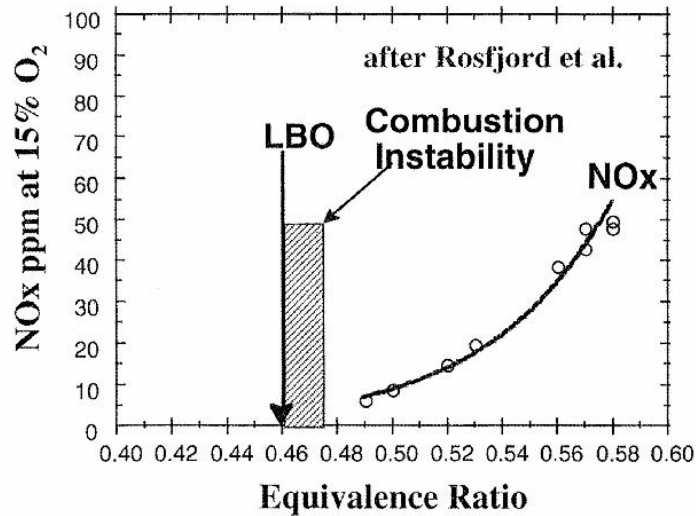


**Figure 1.2. Effect of equivalence ratio on NO<sub>x</sub> production (from Rosfjord 1995).**

Previously, measurement of parameters describing combustion dynamics, particularly the flame's response to outside disturbances, has been performed through chemiluminescence imaging (either of the whole flame, or of a particular species therein, Lieuwen 2002). Since chemiluminescence produces spatially-averaged images of the flame region, they are often too blurry and/or under-resolved for accurate determination of flame zone behavior (Ratner et al 2002 or 2003). This effectively masks the local flame dynamics. OH and CH LIF have also been previously performed, but never in a systematic attempt to produce generalized response functions based on local flame behavior. If local

variables are not measured, then the results tend to be specific to the burner and its geometry. Also, much of the existing research has been carried out by measuring natural oscillations, which are a function of burner geometry, and specific operating conditions. This means that the acoustic wave energy will vary from condition to condition, and it is nearly impossible to discern the true local conditions.

The primary goals of this work are to provide an experimental basis for developing tools to examine the dynamic behavior of practical combustion systems; and, based on these findings, to provide accurate measurements of parameters describing combustion dynamics so as to enable design of minimal-instability combustors. In the pursuit of these goals, the effects of forced acoustic oscillations on the behavior of heat release and fuel/air mixing are investigated. The experimental determination of the dynamic response of a given combustion system to outside disturbances, and the development and demonstration of a methodology for producing these measurements, are the primary tasks to be pursued in this thesis.

The significance of the present work lies in the fact that it employs both a precise measurement technique (Planar Laser Induced Fluorescence or PLIF) and forced acoustic conditions. Since the acoustic field is defined by an externally controlled, local pressure conditions are known through the flame region. This means that spatially resolved, time dependent measurements can be made so as to measure the general flame response parameters. Since the local response is a function of only local parameters, it is possible to apply these values to any combustor configuration. This allows the use of any burner

that can produce the desired range of operating conditions and produces results that are independent of the burner.

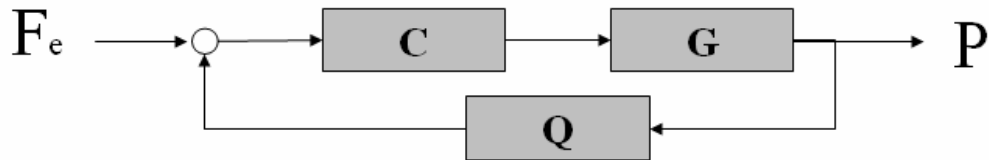


**Figure 1.3. Diagram of active control and combustor response, the control effort (if any), C; the combustor dynamics, G; feedback, Q, due to the combustion dynamics where  $F_e$  is the source of outside disturbances.**

Figure 1.3 shows two fundamental categories: the combustor dynamics (G) - the fluid mechanical and other physical processes; and the combustion dynamics (Q), the feedback path which is the global and local dynamics of combustion processes and their sensitivity to time-dependent changes in the environment such as chemical reaction, and mixing of fuel and air. Here, C refers to the controller, which, when successfully developed, would attenuate unwanted oscillatory behaviors. The approach to be demonstrated here will lay foundations for better understanding of flame dynamics, modeling the combustion dynamics ((Q) in Figure 1.3); and produce a database which can be used in the various phases of designing and actively controlling robust combustion systems (see Figure 1.4 for the relationship).

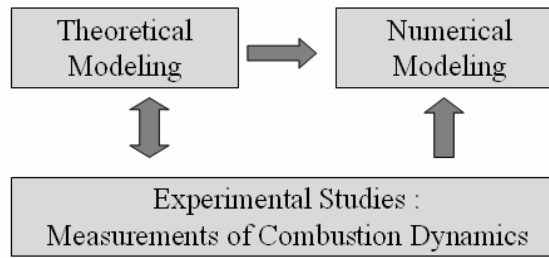


**Figure 1.4. Experimental Works as a Basis for Theoretical and Numerical Research.**

Based on Lord Rayleigh's observation, the following formulas can be derived for the energy added/subtracted per a cycle of oscillation (Culick 1987).

$$(1.1) \quad \Delta E = K \int dV \left[ \frac{1}{T} \int_t^{t+T} \dot{Q}'_r p' dt \right]$$

Here  $\dot{Q}'_r$  stands for the fluctuation of the combustion energy release rate per unit volume that is in phase with the pressure fluctuation;  $K$  is a constant; the inner integral is over one period  $\tau$  of the oscillation; and the outer integral ranges over the volume of the combustor. Then the fluctuation  $\dot{Q}'_r$  appears as the primary source of the unsteady acoustic field, as in the formula (1.1).

A basic premise of this work is that the local values of  $\dot{Q}'_r$  are in fact determined by local values of the variables characterizing the flow field such as the pressure, velocity, and chemical species distributions. Therefore, if the fundamental dependence can be found for a particular system of reactants, a basis exists for understanding the causes of combustion instabilities in any combustor using the same reactants and primarily due to  $\dot{Q}'_r$ .

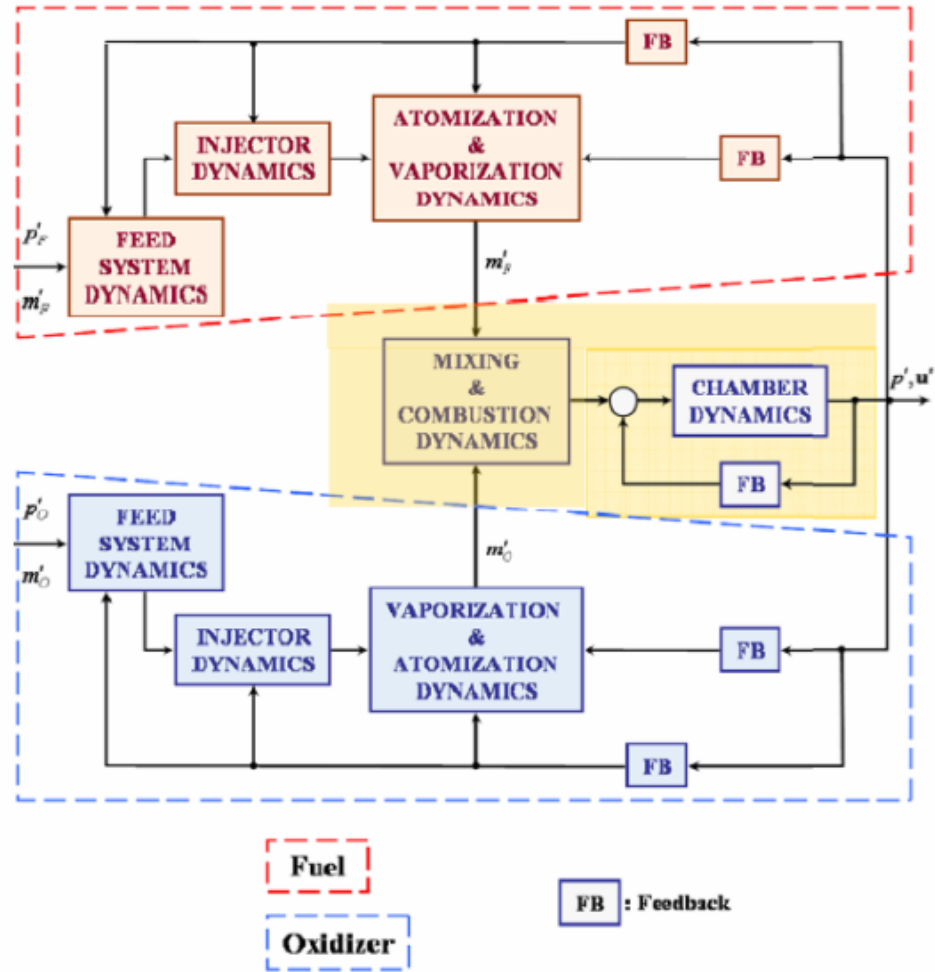


Figure 1.5. Idealized Flow of Information

(adapted from AGARDograph, Culick 2005).

In Figure 1.5, the idealized diagram of information flow for the control of combustion phenomena. The focus of this work is on the shaded region at the middle (Figure 1.5), developing tools and database for experimentally determining the dynamic behavior of mixing and combustion phenomena.

## 1.2 Objectives

Experimental works concerned with active control of combustion instabilities have been largely approaches directed to specific cases, tending to ignore the problem of determining the details of the mechanisms of dynamical behavior and instabilities. The present work is concerned with developing a general experimental methodology for evaluating the combustion dynamics, and laying the foundations for actively controlling combustion dynamics by measuring global and local parameters describing the dynamics of combustion.

The main objectives of this work are

- To make accurate measurements of the fluid mechanical and thermo-acoustic responses of burners for use in designing and actively controlling the combustion system;
- To provide a general procedure for determining combustor responses to sources of instabilities, laying the foundation for methods of treating combustion instabilities as part of the design process for combustors; and
- To build up a database of combustion dynamics for comparison with simulated or theoretically predicted results, such that the collection of data may be used as a reliable reference for verifications.

The most important point is that when all the describing flow field variables such as velocity field (done by many researchers), temperature, and thermo-acoustic coupling (obtained with current measurements) are obtained for the given fluid-dynamic conditions, then the data will be directly applicable for other burners if we can describe the flow field variables and  $q'$  to describe the flame behavior.

## 1. 3 Literature Survey

### 1.3.1 Behavior of Mixing

Many authors have examined various aspects of lean premixed combustion schemes (e.g., Cohen et al. 2001). Heneghan et al. (1990) showed that the level of acoustic oscillations increased as the equivalence ratio ( $\phi$ ) was reduced to the 'lean' side from the stoichiometric conditions. Shih et al. (1996) showed that such instabilities are found in a certain range of equivalence ratio. Reduced heat release rate due to the lean-burn scheme was alleged to be the main cause of such unstable flame behavior in lean-burn combustion, since the low fuel/air ratio (equivalence ratio) decreased the amount of heat release which, in turn, caused a lack of balance between the acoustic amplification and damping in the combustor (Shih et al. 1996).

According to Lieuwen et al. (1998), combustion instabilities could be caused and significantly amplified by the oscillatory behavior of mixing (unmixedness) especially in leaner regions. They numerically simulated the amplification of acoustic waves in the presence of mixture fraction oscillations, while fluctuations in other parameters such as the inlet flow rate and temperature did not take part in amplifying the acoustic waves. Cohen et al. (2001, 2003) studied the control authority of combustion actuating the fuel/air mixing (unmixedness) by modulating the fuel flow using high frequency valves. This work showed that the ability of the fuel actuator to affect the mechanism behind the thermo-acoustic coupling was tied strongly to the mixing of the actuated fuel flow with the remainder of the premixed reactants.

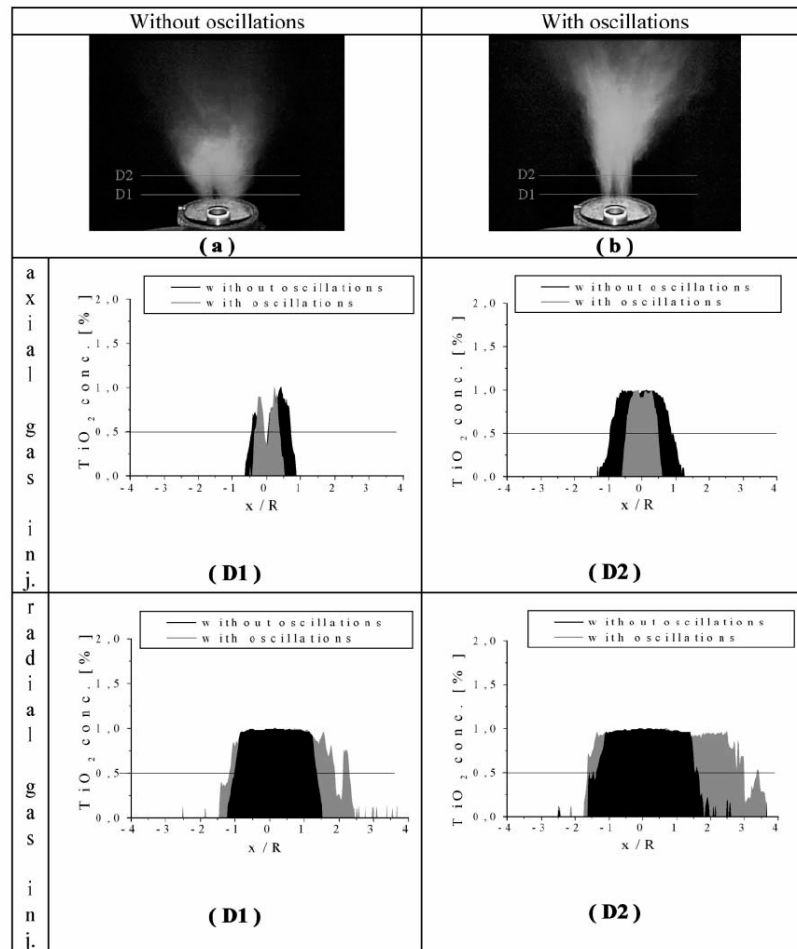


**Figure 1.6. Visualization of mixing with and without imposed acoustic oscillation (350 Hz) (Hardalupas et al. 2002)**

Acoustic forcing was employed in several different works. Works by Demare et al. (2004, PIV, LDV) and Hardalupas et al. (2002, chemiluminescence) used acoustic forcing to control the fuel jet stream as an approach to problems such as flame reattachment, blowout, and poor combustion (Figure 1.6). The acoustic forcing was given at the secondary flow (air) at the inlet stream, not as a combustor pressure at a few selected frequencies. They showed that structures (vortices due to jet deceleration), disorganized by the superposition of the forcing wave, lead to quasi-homogeneous turbulence which

provides efficient mixing and improves the combustion. It was shown, also in the works on fuel jet break-up (Kim et al. 1993), and the behavior of gas phase mixing in a confined geometry without mean flow (Matta et al. 1996), that the mixing is enhanced by resonant acoustic forcing.

In Figure 1.6, the darker region is the concentration of  $\text{TiO}_2$ , the seeded species for the 'fuel' stream. It shows the contribution of acoustic forcing at resonance (350 Hz for their system) in causing better mixing (wider region of fuel spreading).

A study of the acoustic coupling between fuel injectors and an applied acoustic field has been carried out by Anderson et al. (1998), but only includes cold flow experiments. Shih et al. (1996) carried out studies to assess the importance of reactant unmixedness on combustion stability, and found that instabilities occur in certain ranges of equivalence ratio near stoichiometric operating conditions. They suggested that the fluctuating fuel distribution under incompletely mixed conditions could significantly contribute to the heat release fluctuations that drive unstable combustion. For our work, the results reported by Shih et al. (1996) formed the starting point in that the non-premixed flow field with fluctuations in mixing caused by the acoustic field may be highly susceptible to the fluctuating and even unstable combustion. The acoustic oscillations in these works were embedded in the fuel stream to modulate the degree of mixing. In many cases, such as those mentioned above, the combustion phenomena were studied without being confined in closed combustors. In our work, the acoustic field is confined in a large combustor as a bulk motion inside the combustor. The magnitudes of the driving

acoustic waves were maintained at constant values using a feedback controller.

### **1.3.2 Measurements of Combustion Dynamics**

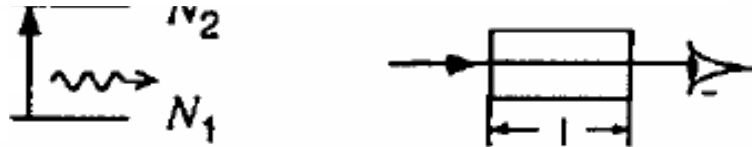
There are a number of technical approaches to the measurements of combustion dynamics. Especially there are three methods that have been used to obtain data for investigating combustion dynamics. The following are the methods in order of increasing spatial resolution. See Figure 1.7 for the simple schematics of how these measurements are done.

- (i) measurement of the transfer function for a combustion region by detecting transmission and reflection of acoustic waves (e.g., Culick 2001);
- (ii) chemiluminescence, measuring radiation from certain species participating in a combustion zone exposed to pressure oscillations (e.g., Kendrick et al. 1999, Venkataraman et al. 1999, Kappei et al. 2000); and
- (iii) planar laser-induced fluorescence, measuring radiation induced by pulses of laser output incident on a combustion zone exposed to pressure oscillations (e.g. Cadou et al. 1998, Pun et al. 2003).

Mainly the third method is used in the present work. Pun (2001) clarified the serious limitations in resolution or precision of chemiluminescence method. Figure 1.7 shows simple schematic diagrams of how chemiluminescence and LIF technique work. As shown, to put the case very simply, the chemiluminescence is the flame as we see it

(Figure 1.7 (a)), while the LIF signal is obtained by excitation and spontaneous emission of species (Figure 1.7 (b)).

(a) Chemiluminescence



(b) Laser Induced Fluorescence (including PLIF)

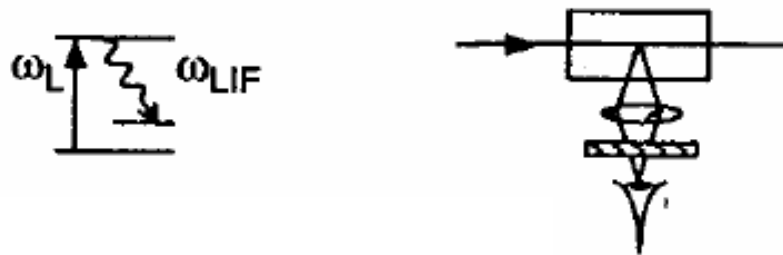


**Figure 1.7. Basic schematics of chemiluminescence and laser induced fluorescence**

**(Adapted from Wolfrum 1998)**

The great disadvantage of chemiluminescence is that the radiation collected is emitted along the entire line of sight in the direction defined by the orientation of the PMT or camera. Since radiation may also be absorbed, the final intensity at the observation point does not in general represent only the activity of species produced in chemical reactions. Consequently, as shown by Pun et al. (2001), seriously misleading results are often obtained. Nevertheless, the method was the first to provide results for combustion dynamics (see Table 1.1) and has given useful contribution to understanding combustion instabilities.

	Chemiluminescence	PLIF
Naturally Unsteady	<ul style="list-style-type: none"> <li>• Sterling and Zukoski (1991) (188 Hz)</li> <li>• Broda et al. (1998) (1750 Hz)</li> <li>• Kendrick et al. (1999) (235 Hz, 355 Hz)</li> <li>• Venkataraman et al. (1999) (490 Hz)</li> <li>• Kappei et al. (2000) (370–460 Hz)</li> <li>• Bernier et al. (2004) (400 Hz)</li> </ul>	<ul style="list-style-type: none"> <li>• Cadou et al. (1991) (43 Hz)</li> <li>• Shih et al. (1996) (400 Hz)</li> <li>• Cadou et al. (1998) (328 Hz)</li> </ul>
Acoustic Forcing	<ul style="list-style-type: none"> <li>• Chen et al. (1993) (300 Hz, 400 Hz)</li> <li>• Durox et al. (2002) (0 - 400 Hz)</li> <li>• Schuller et al. (2003) (0 - 400 Hz)</li> </ul>	<ul style="list-style-type: none"> <li>• Cadou et al. (1998) (360 Hz, 420 Hz)</li> <li>• Pun et al. (2003) (22-55 Hz)</li> </ul>

**Table 1.1. Previous Work in Oscillating Flames.**

Chemiluminescence of the CH radical, an excellent marker for the reaction zone, has been used by a number of researchers to study heat release in an unsteady flame. They can be categorized into two groups; measurements using a PMT with a slit obscuring a portion of the flame to obtain some spatial (typically axial) resolution (Sterling 1991, Chen et al. 1993, and Kappei et al. 2000); and fully two-dimensional imaging using a CCD based camera (Broda et al. 1998, Kendrick et al. 1999, and Venkataraman et al. 1999). Of these works, only Chen et al. (1993) involved an acoustically forced flame, but used a photo-multiplier tube (PMT) with a slit configuration that obtained only integrated one-dimensional information.

The first demonstration of 2D (planar) LIF of the hydroxyl radical in a flame was apparently performed by Dyer and Crosley (1982). This technique has been used to measure a variety of chemical species in unsteady reacting flows, including OH as a measure of the heat release (Cadou et al. 1991; and Shih et al. 1996), and NO seeded fuel

to measure the temperature field (Cadou et al. 1998). A summary of these various works involving both chemiluminescence and PLIF is provided in Table 1.1, including the acoustic frequencies in the studies.

Most experimental work to characterize various combustor configurations has been done on naturally unstable systems (Table 1.1). However, the results are specific to the combustors tested, and provide little insight to how a particular injector or burner design will behave in a different combustor. A study of the acoustic coupling between fuel injectors and an applied acoustic field has been carried out by Torger (1998), but only includes cold flow experiments. Work by Chen et al. (1993) with premixed flames was specifically designed to simulate solid rocket propellants. It contained one-dimensional spatial results and used only two forcing frequencies. The study by Cadou et al. (1998) was based on a specific 2D dump combustor configuration, and showed little response to non-resonant forcing. Durox et al. (2002) and Schuller et al. (2003) measured the flame response to forced acoustic oscillations of up to 400 Hz, but the burner was placed in open air. The response function was based on the pressure and velocity measurements though they measured the CH fluorescence without phase-resolution. A more generalized body of work is required to provide industry with guidelines that will be useful in designing stable combustion systems.

In the works by Dowling et al. (1984), Bloxsidge et al. (1988), and Langhorne (1988), a general theoretical model was constructed based on experimental measurements of 'reheat buzz', a combustion instability observed in a thrust augmentator. The

experimental data and procedure served as the foundation for the next step in the research where the data are used as the fundamental reference for theoretical modeling of the behavior of the combustion system. The experimental approach does not involve a forced acoustic excitation that is crucial in determining the dynamic response of the system, though. Also, the lack of spatially resolved measurements would only provide data useful for one dimensional model which is far too simplified. These works, however, show the direction in which the present thesis work is headed.

Only Cadou (1998) and Pun (2003) previously used PLIF to investigate the dynamics of a forced combustion system. The current series of experiments began essentially where Dr. Pun finished who showed chemiluminescence is smeared too much due to the integral effect of the line of sights, and that PLIF is a great alternative to overcome this shortcoming of the chemiluminescence technique. Otherwise, as Table 1.1 shows, in previous applications of PLIF, to unsteady flames, results were obtained only for naturally oscillating systems. Pun, however, forced the system at only 5 low frequencies (22, 27, 32, 37, 55 Hz). Only by forcing over a range of frequencies can one obtain data for transfer functions and truly informative results for the combustion dynamics. The current work employs a wider range (up to 400 Hz) of excitation frequencies.

#### **1. 4 A Précis of the Thesis**

The present work is concerned with developing a general experimental methodology for evaluating combustion dynamics; and laying the foundation for actively controlling combustion dynamics by measuring global and local parameters describing the dynamics

of combustion. The technique employed here is laser-based, thus non-intrusive in contrast to methods using probing devices which perturb the flows. Local and global parameters that describe the dynamics of combustion such as the Rayleigh index, flame responses, and mixing (unmixedness) are calculated from the measurements. The data, when combined with other flow field variables such as velocity, temperature, etc., will provide a valuable database. The results should serve as a starting point for theoretical and numerical research for the development of combustion systems with more stable performance.

Development of this technique has been achieved by a step-by-step approach; the thesis consists of three main parts. The first portion of the thesis, Chapter 2, deals with the technical issues that arise when laser induced fluorescence (LIF) measurements are made in real environments. Highly turbulent flame environments (such as those found in real combustors) exhibit large variations in local chemical composition. Product gases can be mixed into reactants in various quantities, and in this way can affect both the actual chemistry and the measured chemical concentrations. Since LIF measurements are becoming more common in real environments, it was decided to first examine the impact this might have on measurements of chemical species of interest, particularly NO. It is well established that the LIF signal can decrease in intensity due to collision quenching, that is when the species of interest suffers collision with other species and undergoes a subsequent loss of energy (de-excitation from the excited electronic state). Certain species, such as oxygen and carbon dioxide, are known have stronger quenching characteristics than nitrogen. Hence, the reliability of the signal strength is a matter of

great importance in turbulent environments where the quenching is both variable and unknown. Chapter 2 describes systematic testing and quantification of this effect.

In the second part of the thesis, Chapter 3, the dynamic behavior of mixing is studied with a non-premixed jet burner. The way that they are coupled to the flame behavior and the chamber acoustics is presented. Many practical combustion systems employ partially-premixed or non-premixed schemes, and in these systems mixing plays a very important role to determine the dynamic behavior of the systems. In this part of the thesis, temporal (over time) and global (over the measurement volume) measurements of the behavior of mixing is presented, and discussed in comparison with the measurements of the oscillatory flame behavior made by Pun (2001).

The third part of the thesis, consisting of Chapters 4, and 5, is based on phase-resolved OH-PLIF measurements of combustion dynamics. The theory on which the OH-PLIF and thermo-acoustic coupling measurements are based is briefly addressed for the current experimental setting in Appendix B. In Chapter 4 and 5, measurements of thermo-acoustic coupling under forced acoustic condition are presented. A wider range of excitation frequency was employed (Chapter 4, up to 400 Hz) with varying equivalence ratio ( $\phi = 0.5, 0.6, \text{ and } 0.75$ ), and measurements at higher ambient pressure inside the combustor were also made in an attempt to extend the experimental conditions.

Chapter 6 concludes the current work with a discussion of directions for the future research.

# Chapter 2

## Study of Laser Induced

## Fluorescence with NO LIF

---

This chapter deals with the practical aspect of the use of laser induced fluorescence (LIF) technique. LIF is the main tool used in the studies of measuring the parameters describing the behavior of mixing (Chapter 3) and combustion dynamics (Chapter 4 and 5). However, use of LIF has problems related to the physical properties of the technique such as the signal loss due to quenching effects. As preliminary to the work covered in subsequent chapters, the availability of the LIF technique is tested with NO-LIF, one of the simplest and most widespread schemes to measure the pollutant concentrations. Work on signal reduction (or quenching) is presented along with a practical solution (signal saturation).

## **2.1 Introduction**

High temperatures and heat transfer rates make it difficult to probe combustion systems with the desired spatial and temporal resolution. Combustion processes are delicately stabilized and thus easily affected by the intrusion of probing devices. Due to these inherent difficulties in probing combustion phenomena with an acceptable degree of precision, the knowledge required for empirical and theoretical advances is limited. To overcome the difficulties, a number of laser-based diagnostic techniques, which are non-intrusive, have been developed in the last couple of decades and have become valuable tools for the study of many aspects of combustion processes (Wolfrum 1998).

Laser Induced Fluorescence (LIF) has been demonstrated as a reliable technique for measuring the concentrations of minor species such as OH, CO, CH and NO under various combustion environments. However, LIF is predicted to lose accuracy due to collisional quenching and absorption (Paul et al. 1996), for example under highly pressurized environments.

The problem of signal loss is critical when a quantitative measurement of NO-LIF is to be performed in post-flame regions where the presence of oxides of carbon and water enhances collisional quenching and absorption and therefore lowers the measured LIF signal.

### **2.1.1 Motivation**

Nitric oxide (NO) is an atmospheric pollutant whose output from real combustion systems is strictly regulated due to the environmental concerns, and therefore needs to be monitored. Quantitative measurements of nitric oxide concentrations with laser-induced

fluorescence (LIF) have attracted significant interest in recent years (Tamura et al. 1998, Nooren et al. 2000, Bessler et al. 2002).

LIF is a non-intrusive technique which does not interfere with the fluid dynamics inside the volume of interest; the method is used by many researchers for various purposes. LIF measurements are becoming more common in real experimental environments; measurements of mixing (acetone-PLIF, Chapter 3), and combustion heat release (OH-PLIF, Chapters 4 and 5) in subsequent chapters of this thesis work are examples of the use of the LIF technique.

Collisional quenching is a process that involves collisions excited state molecules with other molecules that result in the loss of excitation energy as heat instead of as emitted light. This process is always present to some extent in solution samples; species that are particularly efficient in inducing the process are referred to as collisional quenchers (e.g. iodide ions, molecular oxygen, nitroxide radical, Johnson, 1998). High pressure, strong turbulence and impurities in fuel/air mixture typically are present in the systems of practical interests, which are susceptible to signal quenching.

Collisional quenching can have a strong impact on the reliability of LIF measurements. So as a beginning of the series of works on measuring combustion dynamics, to clarify and find a way to avoid this problem in works in latter chapters employing LIF techniques, it was decided to first examine the impact this might have on measurements of chemical species of interest, particularly NO.

Many NO-LIF measurements have been made in stable laminar flames (e.g., Reisel 2000, and Nguyen et al. 1996), which are commonly used to study the chemical kinetics of

combustion of gaseous fuels. In this chapter, we discuss a study that was performed on a McKenna burner in a combustion environment where the effects of fluid-dynamics on the flame were minimized, thus allowing the current investigation to be focused on the details of signal quenching and other minor problems, avoiding the difficulties arising with turbulent flow. Laminar flames are also ideal objects to develop ways to apply laser spectroscopy to practical combustion systems.

### **2.1.2 Objectives**

The objective of this chapter is to clarify signal quenching in LIF measurements and show how signal saturation works to reduce the severity of the quenching effect to improve the signal reliability. This is the first part of the thesis work, dealing with the problem of LIF signal quenching and saturations for use in the later parts of the thesis. The acetone PLIF technique (Chapter 3) and OH PLIF technique (Chapters 4 and 5) share the same principles with LIF of NO described in the current chapter.

A steady, premixed, rich ( $\phi=1.25$  or  $\phi=1.35$ ), methane/air flat flame at atmospheric pressure with dilution is used to evaluate the response to collisional quenching. The dilution is either pure nitrogen or pure carbon dioxide. The dilution is chosen so that the NO levels and temperature are approximately the same for each stoichiometric ratio in the probed zone, while the concentrations of quenching species change significantly. Carbon dioxide and nitrogen are respectively a strong and mild quencher, i.e., the effect of carbon dioxide on signal quenching is significant, while that of nitrogen is relatively weak.

The results of laser power variation on NO-LIF spectrum in the vicinity of the  $\gamma(0,0)$   $Q_2(27)$  are to be described for the two different dilutions and the effects of quenching are shown.

## 2.2 Experimental Configurations

### 2.2.1 Test Section

In Figure 2.1, the steady, premixed, methane/air flat flame burner at atmospheric pressure with dilution is shown. The premixed flat flame studied here is obtained using a non-cooled McKenna burner, with an inner diameter of 5 cm.

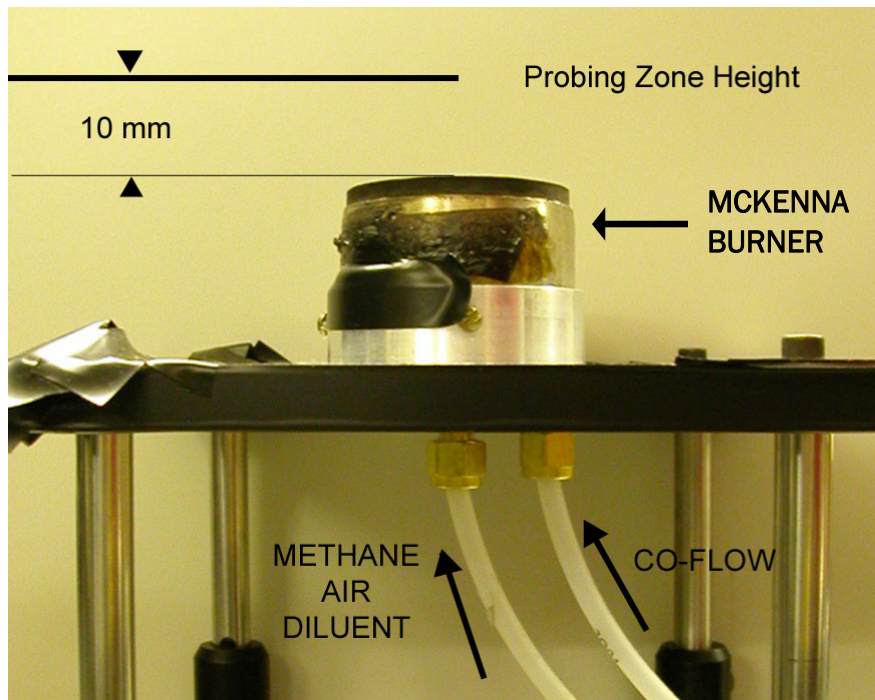


**Figure 2.1. Burner assembly.**

The burner is typically run under rich conditions,  $\phi=1.25$  or  $1.35$ . This choice is based on the following considerations:

1. Under rich conditions such as those quoted above, the NO concentrations are relatively high, around 40-50 ppm
2. The temperature in the probed zone (15 mm above the burner) for the two cases ( $\phi=1.25$  and  $\phi=1.35$ ) are very close ( $\pm 2\%$ ).
3. The flame is stable even with a heavy seeding.

Either pure nitrogen or carbon dioxide (the molar ratio of carbon dioxide or nitrogen dilution and air is set to be  $\sim 0.2$ ) are used for dilution for fuel/air mixture stream.

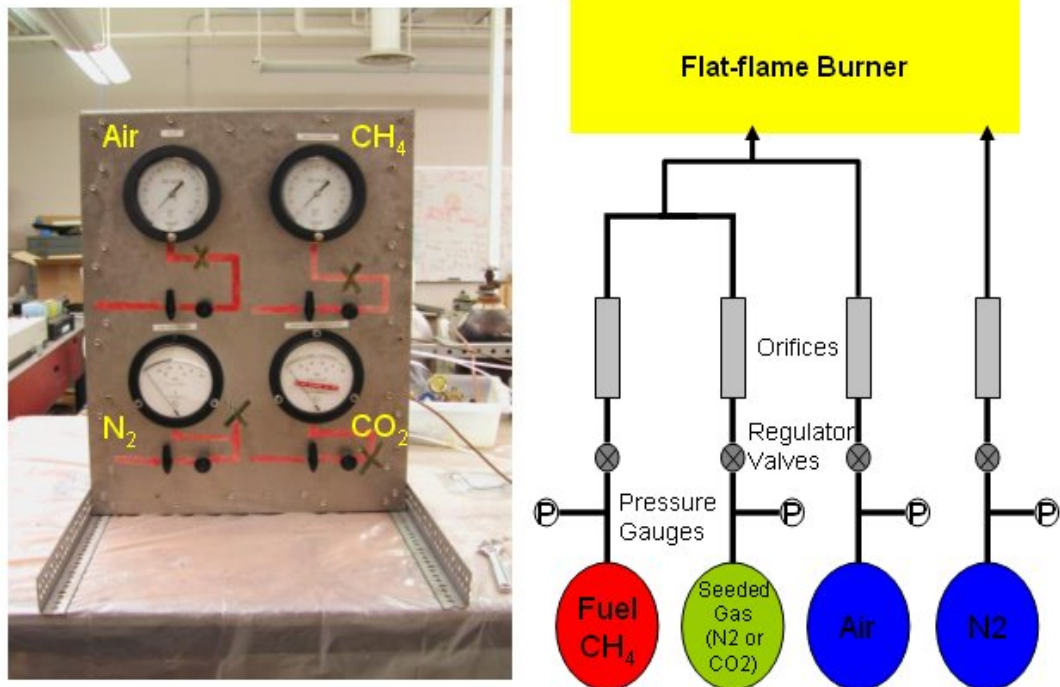


**Figure 2.2. The flow control board for regulating fuel/air/seeded gas flows (a); and the flow diagram (b).**

Flow rates were controlled using a custom made control board (Figure 2.2). The flow control board is composed of four elements, each consisting of a pressure gauge (Ashcroft Q-4907, pressure range 0-100 psi, 0.25% accuracy), an on-off shut off valve, a 2  $\mu\text{m}$  pore size filter (Swagelok SS-4FW-2), a fine control needle valve and an O'Keefe Controls sonic sapphire orifice (J-SS-26, J-SS-30, J-SS-40 and J-B-35). The gaseous inputs of these 4 elements were air, methane, carbon dioxide, nitric monoxide or nitrogen doped with 1% nitric oxide.

The calibration of the sapphire orifices was performed using digital Omega mass flow control modules (Omega FMA 868-V-Ethane, 872A-V-Air and 872A-V-AIR). The calibration curves obtained for the sapphire orifices we used was found to be in accord with the specifications from O'Keefe Controls Inc. (error 5%). The orifices were found to be 3% off, and this error was accounted for.

The mass flow rates (expressed in grams per second) and seeded quantities are presented in Table 2.1.

	$\phi$	$m'_{\text{AIR}}$	$m'_{\text{CH}_4}$	$m'_{\text{CO}_2}$	$m'_{\text{N}_2}$
CASE I	1.25	0.447	0.0326	0	0.0274
CASE II	1.25	0.447	0.0326	0.0286	0
CASE III	1.35	0.447	0.0352	0	0.0274
CASE IV	1.35	0.447	0.0352	0.0286	0

**Table 2.1. Mass flow rates of gases (all numbers in g/s).**

### 2.2.2 Laser System

A laser system is required to produce the probing beam for the measurements. The laser beam is generated by a YAG pumping laser and frequency tunable Dye laser (Figure 2.5), then the mixer/doubler system (Figure 2.4) adjusts the wavelength of the beam to excite the species of interest (here, the NO molecules).

The laser system is based on a pulsed Nd:YAG solid-state laser (Continuum Powerlite 9010) operating at 10 Hz, pumping a tunable dye laser (Continuum ND6000), which in turn drives a mixer/doubler system (U-oplaz) as shown in Figure 2.5. The Nd:YAG laser generates up to 2000 mJ/pulse at 1064 nm (IR), and is equipped with a Second Harmonic Generator (SHG) system to provide frequency doubled beam of 1000 mJ/pulse at 532 nm (green). The 532 nm YAG laser beam pumps the dye laser, while excess energy at 1064 nm (energy not converted to 532 nm) is passed through a delay line. The delay line allows the 1064 nm beam to coincide spatially and temporally with the output of the dye laser for frequency mixing purposes. The mixer/doubler system, shown in more detail in Figure 2.4, was custom designed in cooperation with Dr. Sheng Wu of U-oplaz Technologies, for optimal energy conversion by special tuning of the BBO crystals (Wu et al. 2000).

A mixture of Rhodamine 590 and 610 in methanol is used to optimize power conversion efficiency of the doubled output of the Nd:YAG near 572.55 nm (>200 mJ/pulse). The output of the dye laser is then frequency-doubled to approximately 286 nm and mixed with the 1064 nm fundamental of the Nd:YAG Laser to produce 225.58 nm laser light. This pumps the  $\gamma(0,0)$   $Q_2(27)$  band of NO which minimizes the interference with O<sub>2</sub> LIF and decrease temperature sensitivity (Lee et al. 2002, Paul et al. 1996). Energy in excess

of 18 mJ/pulse is easily produced by this system. This experiment did not require operation at full power, and approximately 4 mJ/pulse in the measurement volume was used. Figure 2.3 shows the energy level diagram of NO, and the excitation wavelength (225.58 nm or approximately  $44,300 \text{ cm}^{-1}$ , Daily et al. 2005).

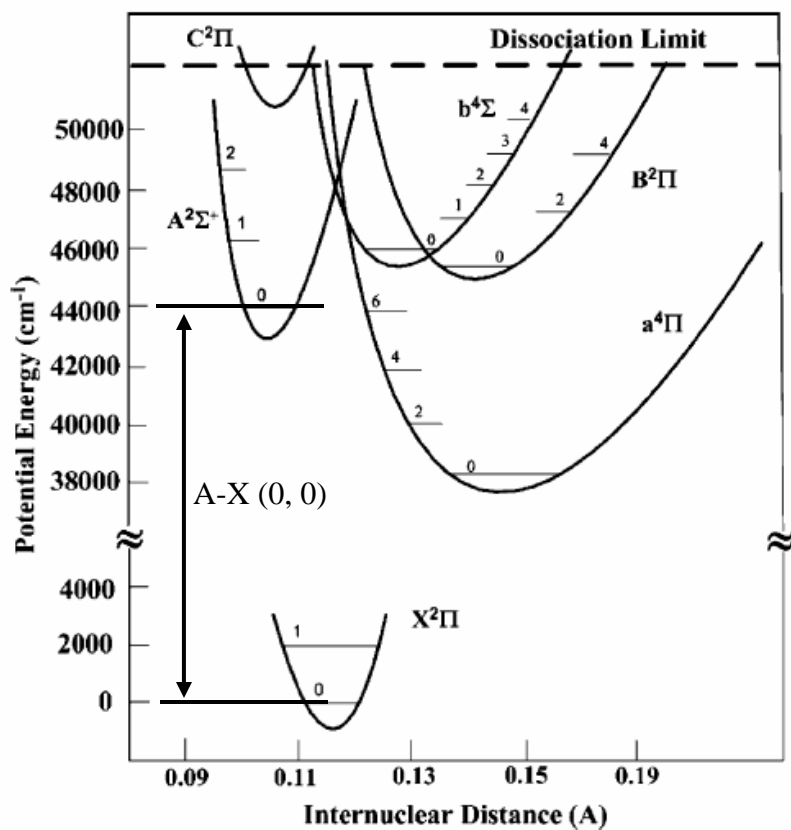
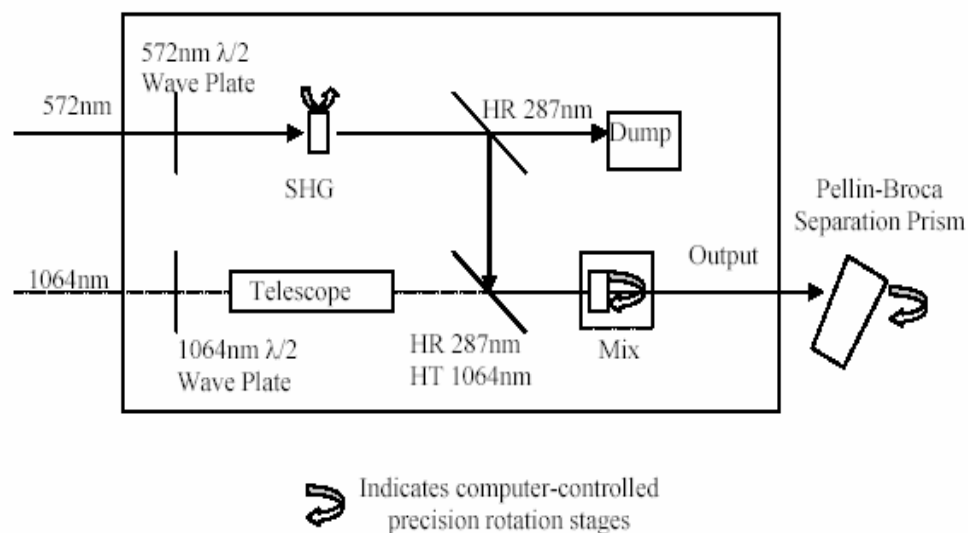


Figure 2.3. Energy level diagram of NO (adapted from Daily et al. 2005).



**Figure 2.4. Mixer/Doubler system.**

Characteristics of the laser beam around the wavelength 225.58 nm are reported:

1. The line width (FWHM) is  $1.0 \text{ cm}^{-1}$ ;
2. The duration of the laser pulse is 8 ns;
3. The polarization of the laser beam is linear and vertical;
4. The frequency stability of the dye laser is  $0.05 \text{ cm}^{-1}/\text{K/hr}$  ( $1 \text{ pm}/\text{K/hr}$ )
5. The absolute accuracy of the Dye Laser output is 0.005 nm.

### 2.2.3 Optical Configurations

The polychromatic laser beam output of the laser system is spectrally separated using the Pellin-Broca prism (PLBC-10.0-79.5-UV, Figure 2.5). The output of the lasing system is then spatially filtered by means of a pinhole (Beam Selector, 6 mm of diameter) and the 225.58 nm laser beam is selected. This beam is then directed to the probing zone using the combination of a mirror (CVI TLM1-225-45P-1025) and a right angle prism (Lambda

Research Optics P90-25U-225-308). The beam is then split in two portions by a 50-50 beam splitter (LEO BS-226-45P-R50-UF-2038) to measure the laser beam intensity and to image the signal at the same time.

The pumping beam is spatially filtered by a pinhole and focused by a spherical lens of focal length of 550 mm (CVI BICX-25.4-572.7-UV) into the probing zone, as indicated in Figure 2.5. After passing through the flame, the probing beam is blocked using a beam dump.

Some important features are as follows.

1. The probing volume is located at the center of the burner and set at 10 mm above the burner.
2. The optics used in this experiment are all high-quality although we should mention a couple of problems:
  - None of the spherical lenses (SL) are coated. And they all slightly fluoresce. This fluorescence is blocked using masks and pin-holes.
  - The right-angle prisms smear the laser beam and produce additional fluorescence, which is appropriately blocked by pin-holes or masks. By using several masks a signal to noise ratio of between 70 and 120 is achieved in LIF measurements.

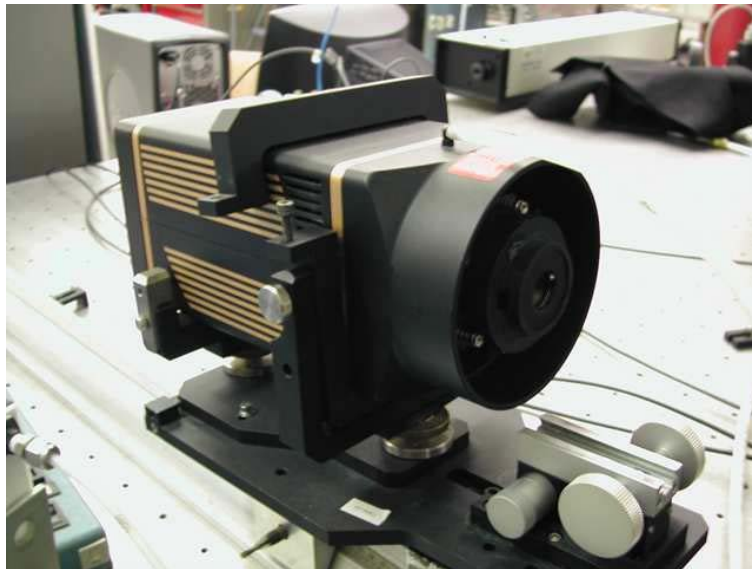
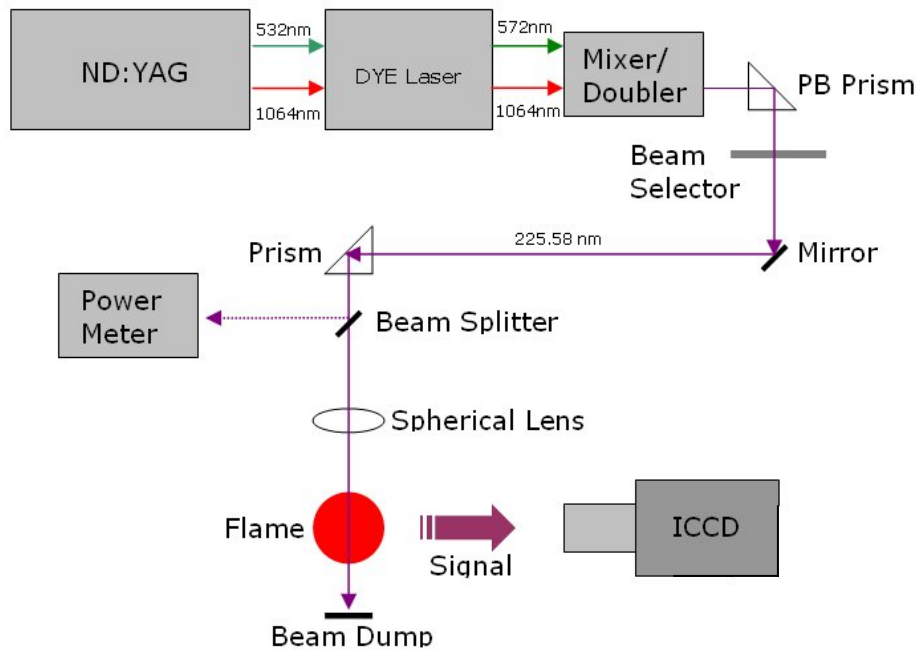


**Figure 2.5. Schematic drawing of the optical setup used for the measurements (top), and the ICCD camera (bottom).**

### 2.2.4 Detection System

The detector for the fluorescence signal is an intensified CCD camera (Roper Scientific/Princeton Instruments ICCD-MAX, Figure 2.5 bottom), which uses a 512 x 512 Thomson CCD array, operated with a gate width of 90 ns. Due to the requirement of high quantum efficiency and fast gating, the micro-channel plate (MCP) of the camera is slowly gated (90 ns, versus the ~8 ns laser pulse and < 20 ns fluorescence), and operates at its maximum quantum efficiency (~30%). Attached to the camera is a catadioptric (similar to Cassegrain telescope), all-reflective f/1.2 UV lens with a focal length of 105 mm. The lens provides exceptionally high light throughput, as well as minimizing spherical and chromatic aberrations. This results in a spatial resolution of 215  $\mu\text{m}$  x 215  $\mu\text{m}$  per pixel at the focal plane with an image size of 11  $\text{cm}^2$ .

A timing generator (ST133A, Roper Scientific) is synchronized to the laser pulse and controls the camera timing. The fluorescence images are generated by binning the horizontal pixels by 10, yielding a 2.15 mm horizontal resolution and by binning the pixels vertically by 3, gives a 750  $\mu\text{m}$  vertical resolution.

## 2.3 Procedure

The procedure introduced here is quite a general one. The planar laser induced fluorescence (PLIF) technique, the main experimental tool to be used in subsequent chapters, follows almost the same configuration and procedure. The difference lies in the fact that the laser induced fluorescence (LIF) presented here is a point wise measurement with the laser beam focused on a single point in space, while the beam is widened

vertically by a cylindrical lens to make the beam a sheet-shaped to give a spatial resolution (two-dimensional) by exciting all the molecules in the path of the beam-sheet in PLIF.

1. Set up necessary gas flows
  - Nitrogen purge through ICCD camera.
2. Check optical alignment
  - Focus the ICCD camera on a card in the test section. Ensure the laser beam is passing through the probed volume cleanly. Align the pumping and the probing beams by inserting a quartz test window (thickness 10 mm) or alternatively a dye-test cell.
3. Set experimental conditions.
  - A. Set methane, air and dilution flow rates.
  - B. Set the correct co-flow rate.
  - C. Allow laser beam to pass through test section.
4. Perform experimental preparation.
  - Set the dye laser fundamental frequency to 572.530 nm.
5. Imaging.
  - Take 30 images; store the sum of the 30 images.
  - Repeat this procedure three times.
6. Laser Scan.
  - Repeat step 6 by performing a Dye-Laser fundamental frequency scan from 572.530 to 572.570 nm for spectral scan (see Figure 2.9 to 2.27). This is

approximately where the NO molecules are excited after the beam is frequency doubled and mixed with 1064nm beam (refer to Figure 2.2).

7. Imaging to Imaging Variations

- Repeat step 6, 50 times for each of the following frequencies 572.540, 572.555 and 572.570.

8. Power input change

- Change the power input of the Nd:YAG laser by reducing the Q-Switch delay of 2  $\mu$ s.
- Repeat steps 5 to 9.

9. Change experimental conditions.

- Changes mass flow rates of the flat-flame gas inputs (see Table 2.1).
- Repeat steps 4-8 until experimental session is complete.

## 2.4 Results

### 2.4.1 Preliminary Data

Some preliminary spectral scans of saturated NO-LIF in a 1 bar NO-test cell were performed (Figure 2.6, taken by Ramirez in our group) and compared to calculated spectra from LIF-base<sup>1</sup> in the vicinity of 225.58 nm (Figure 2.7). The test cell was filled with an N<sub>2</sub> and NO (1.05 %, volumetric) mixture.

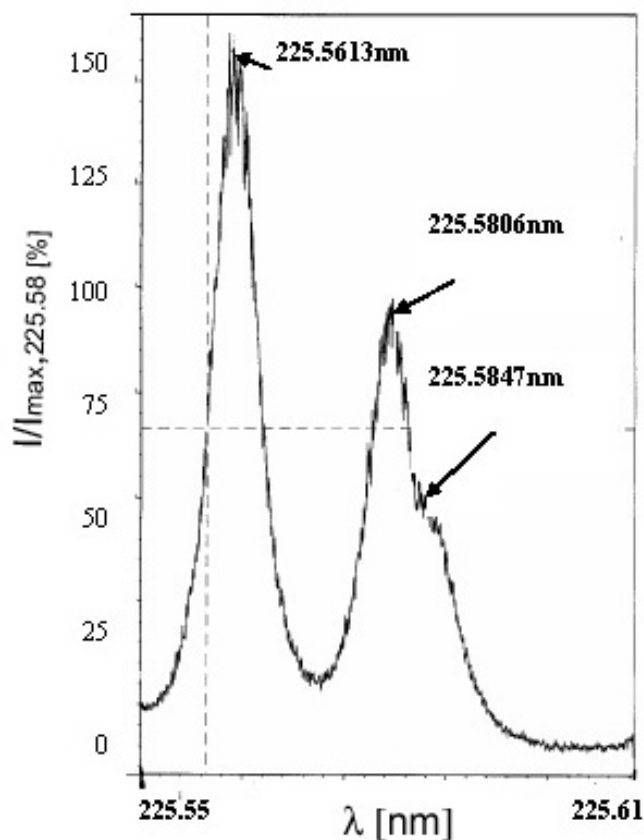


**Figure 2.6. Normalized Fluorescence of NO measured in a 1 bar NO-cell. The cell is filled with an N<sub>2</sub> and NO (1.05 %, volumetric) mixture (data by Ramirez, Jet Propulsion Center, California Institute of Technology, not published).**

<sup>1</sup> A Database and Spectral simulation program for diatomic molecules (Luque, 2002) developed by J. Luque from SRI Inc., Menlo Park, CA.

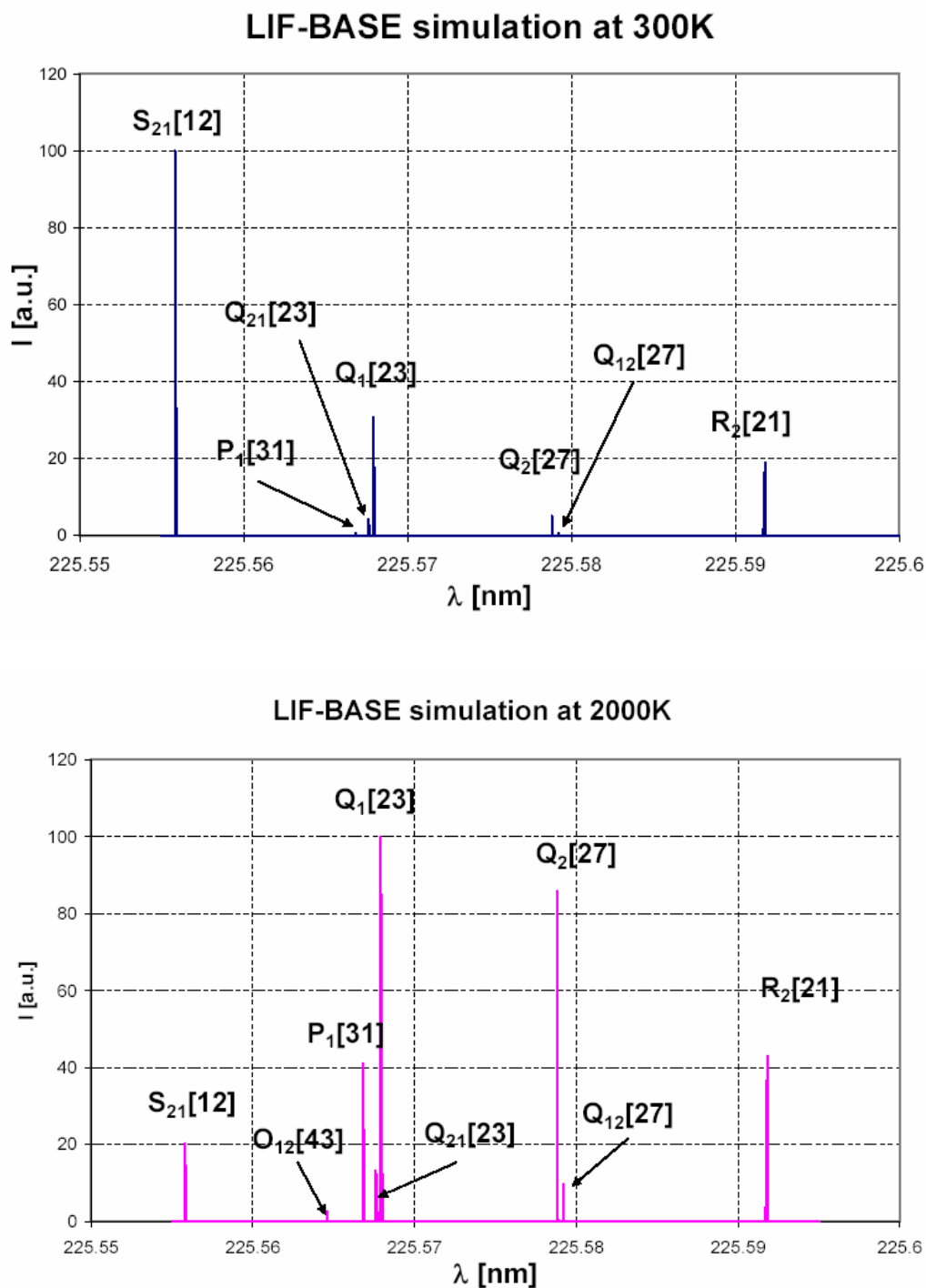


**Figure 2.7. LIF-Base calculations of NO-LIF spectrum; Lorentzian Profile, Temperature set to 300K and 2000 K, pressure set to 1.0 atm with 0.0001 nm resolution (LIF-BASE software used for calculation).**

Because of the  $1.0 \text{ cm}^{-1}$  ( $=0.005 \text{ nm}$ ) spectral line-width of the laser, at  $225.58$  two transitions are effectively excited (see for comparison Figure 2.7 having a much higher resolution). It is important to note that, since the test cell is filled with nitrogen, the effects of laser absorption and collisional quenching can be neglected.

Cooper and Laurendeau (2000) performed a dual<sup>2</sup> linear-LIF and linear-PLIF measurement.

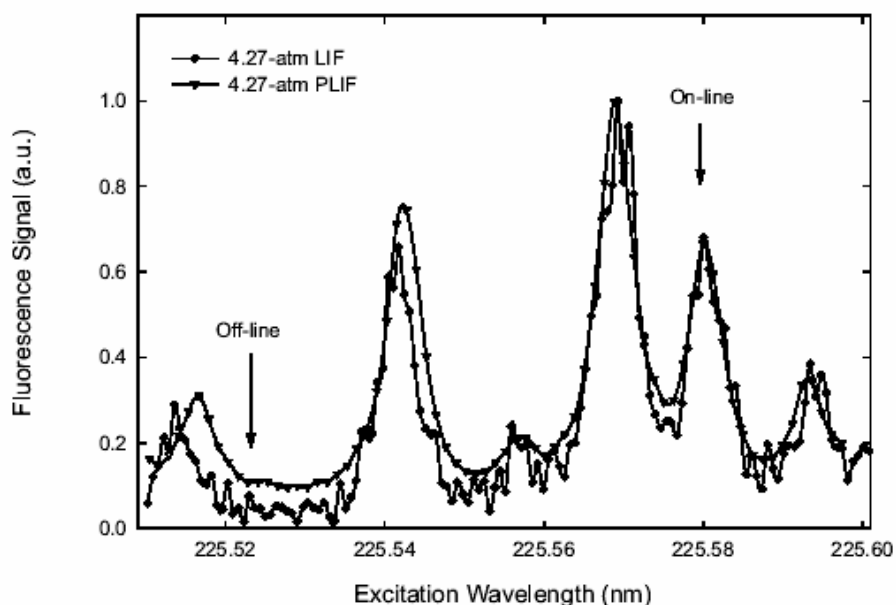


**Figure 2.8. Excitation scans in a 4.27 atm spray flame doped with NO using narrowband linear-LIF detection and broadband linear-PLIF detection. The NO on-line  $Q_2(27)$  and the off-line excitation are labeled. The line-width of the laser beam in this case is  $0.5 \text{ cm}^{-1}$  (Cooper and Laurendeau 2000).**

<sup>2</sup> The two measurements are different in regard to the detection scheme; a narrowband detection scheme was employed for Linear LIF (2nm FWHM window centered at 235.78) a broadband detection scheme was employed for linear PLIF (98nm FWHM window center at 250 nm)

This measurement is evidently different from the one reported in Figure 2.8 but it is important to note the strong interference between the two lines even if LIF is performed in the linear regime and the laser line-width FWHM in this case is half of the one employed in the present work.

#### **2.4.2 Saturated LIF Spectral Scan**

After performing a cold flow spectral scan, saturated LIF and spectral scans in the experimental test section were performed at various stoichiometric ratios to study the behavior of each absorption spectrum of NO molecules. The scanning of the spectral line is important since a good knowledge of the locations of spectral peaks is required to excite the species at the right frequency of the pumping laser beam. The spectral line shapes are Lorentzian in theory when the chemical mixture is pure, but the collisional broadening (inhomogeneous broadening) occurs in flows with high degree of impurities such as combustion processes.

From the following data we read:

1. The  $Q_2(27)$  and  $Q_1(23)$  transition are, relatively to the adjacent transitions, insensitive to temperature.
2. The peak magnitudes, locations and line-shapes of the spectral scans in flames are slightly shifted compared to values obtained in the test-cell. This shift depends on stoichiometry and dilution.
3. The shape of the transition (see Figure 2.9) is dependent on stoichiometry, but same tendency holds for irregardless of the stoichiometry and the presence of quenching particles (Figure 2.10)

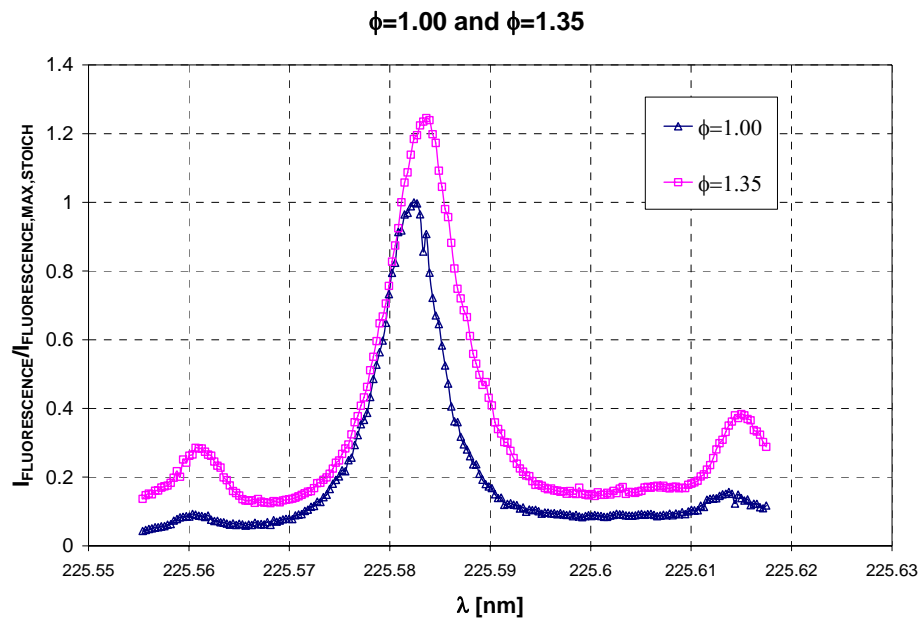


**Figure 2.9. Relative Fluorescence signal obtained from a stoichiometric and a rich flame ( $\phi=1.35$ ); normalized by the maximum fluorescence signal at  $\phi=1.00$ .**

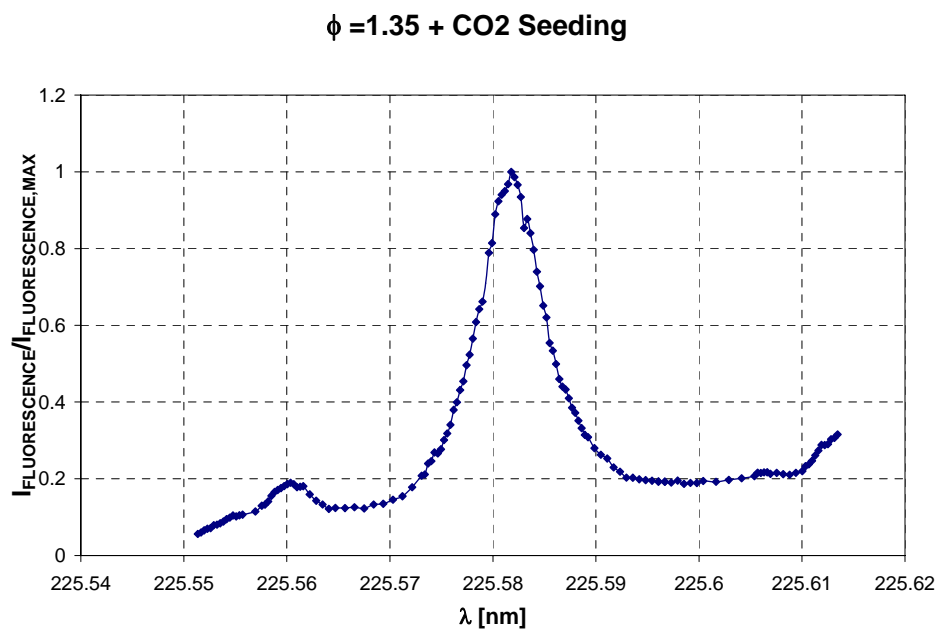


**Figure 2.10. Fluorescence Signal normalized over the maximum at a mixture ratio of 1.35 with  $\text{CO}_2$  dilution.**

The absorption line for  $\phi=1.35$  seeded with  $\text{CO}_2$  shown in Figure 2.10. However, since the peak shifts for different stoichiometry, special care was taken to tune the pumping laser at the appropriate wavelength for each set of conditions.

### **2.4.3 The LIF Results**

Based on the preliminary tests presented in the previous section, the LIF experiments were performed. The comparison of the spectral scans over the short region of absorption peak of NO molecules around 225.58nm (the  $\gamma(0,0)$   $Q_2(27)$  band of NO with least interference by  $\text{O}_2$ ) is presented in Figures 2.11 through 2.14 with varying laser power.

It should be noted that the curves presented are normalized over the peak signal of fluorescence measured at average laser energy per unit area of  $5.19 \text{ mJ/mm}^2$  for  $\text{N}_2$  dilution. It is shown that as the pumping laser strength goes up, the signal strength gets saturated, or the increase in the signal strength converges to zero. These four figures show the fundamental behavior of signal strength versus the pumping beam strength, and thus important points for the application of the LIF signal concisely.

**Spectral scan: laser beam intensity vs. the signal strength (N<sub>2</sub> Seeded)**

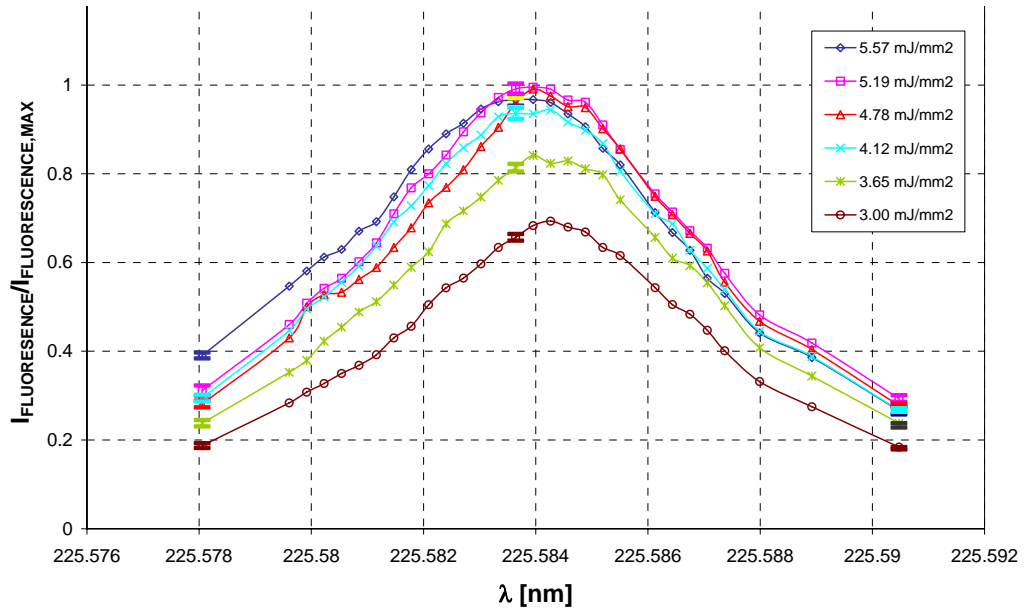


**Figure 2.11. Spectral Scan of a  $\phi=1.25$  flame seeded with N<sub>2</sub> as in Table 2.1.**

**Spectral scan: laser beam intensity vs. the signal strength (N<sub>2</sub> Seeded)**

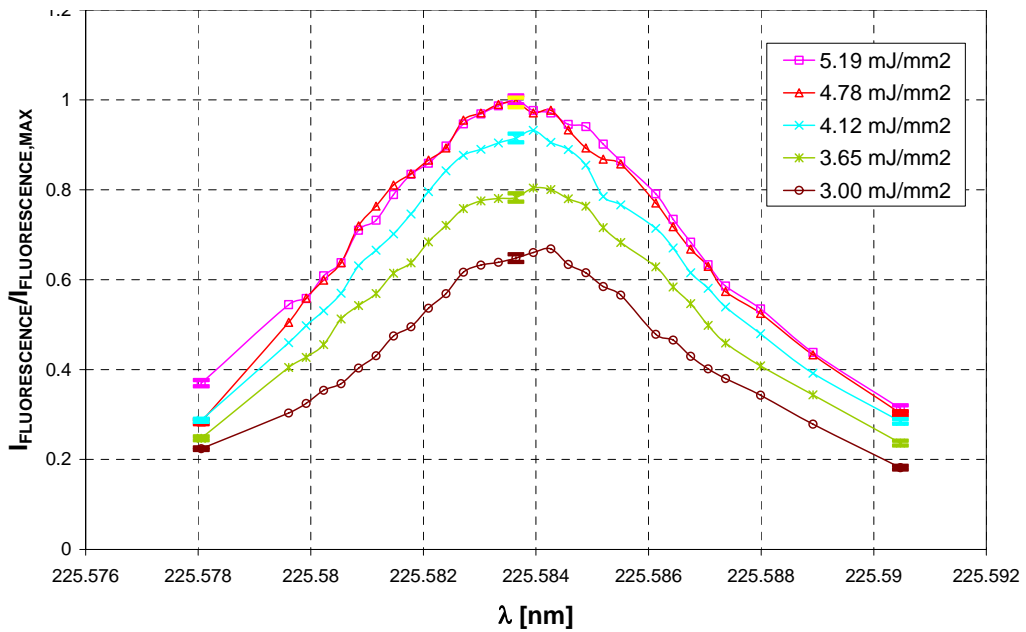


**Figure 2.12. Spectral Scan of a  $\phi=1.35$  flame seeded with N<sub>2</sub> as in Table 2.1.**

### Spectral scan: laser beam intensity vs. the signal strength (CO<sub>2</sub> Seeded)

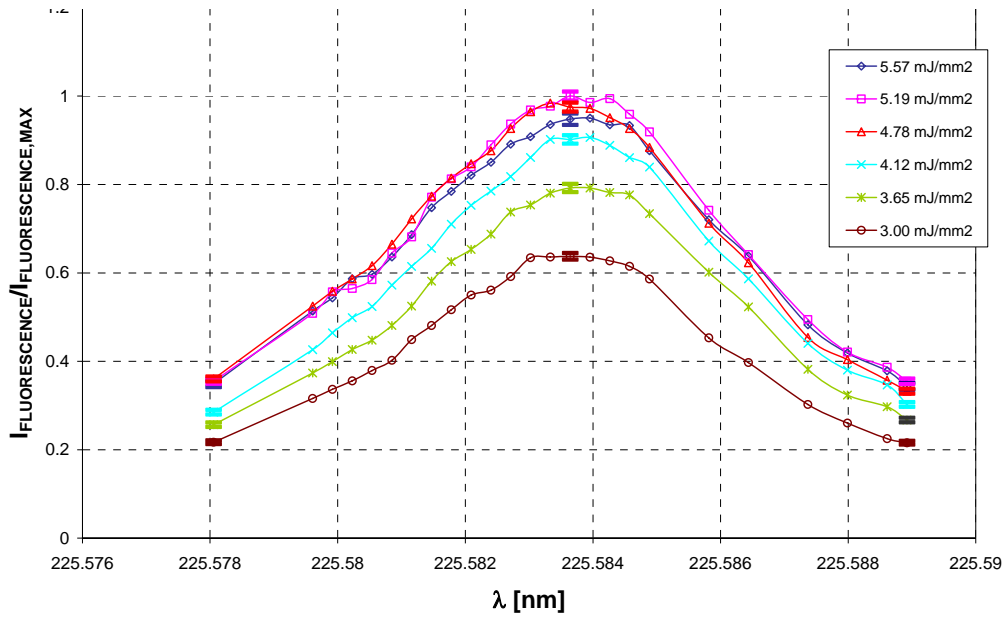


Figure 2.13. Spectral Scan of a  $\phi=1.25$  flame seeded with CO<sub>2</sub> as in Table 2.1.

### Spectral scan: laser beam intensity vs. the signal strength (CO<sub>2</sub> Seeded)

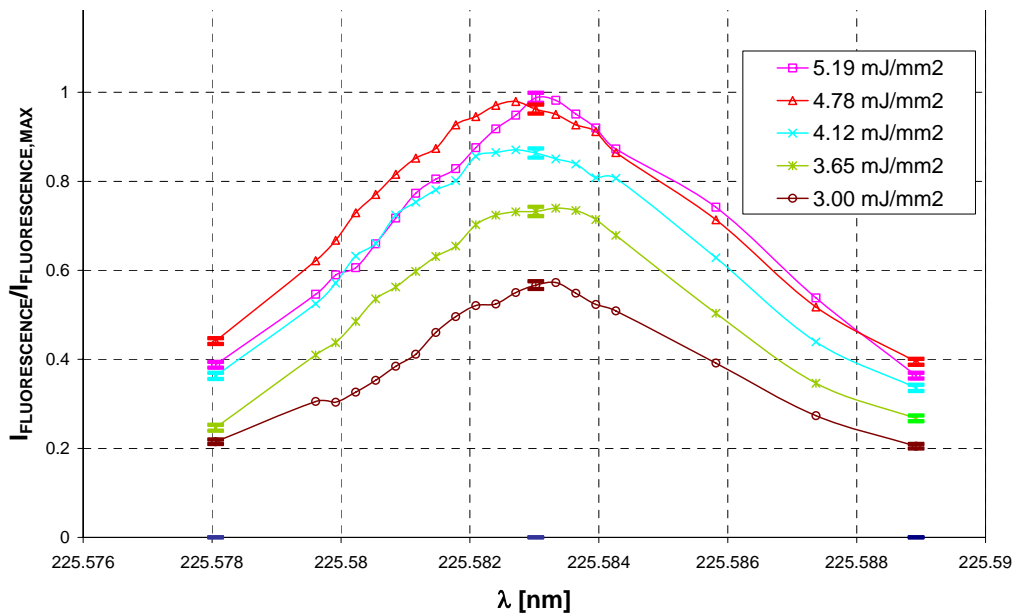


Figure 2.14. Spectral Scan of a  $\phi=1.35$  flame seeded with CO<sub>2</sub> as in Table 2.1.

While Figures 2.11 to 2.14 depicts the effects signal saturation for different seeded species ( $N_2$  and  $CO_2$ ), the effects of quenching species on the degree of signal loss is presented in Figures 2.15 and 2.16.

As shown in figures 2.11 through 2.14, when the pumping laser power increases the fluorescence intensity increases. It is important to note that at low laser power the measured fluorescence in the flame with  $CO_2$  dilution is lower than in the flame with  $N_2$  dilution, this quantifies the effect of collisional quenching by some species such as  $N_2$  and  $CO_2$ . It is clear that  $CO_2$  has greater effect on LIF signal quenching than  $N_2$ .

When the laser spectral saturation irradiance is computed using the relation

$$(2.1) \quad I_{v,sat}^0 = \frac{E_{PULSE} / A}{\tau_{PULSE} \Delta \nu_L}$$

the following equation is obtained:

$$(2.4) \quad I_{v,sat}^0 \approx 5.19E7 \frac{W}{cm^2 cm^{-1}}$$

which is closer to the theoretical results of Eckbreth (1996) than the one measured by Reisel et al. (1993).

One of the important observations here is the effect of over-saturation (Cattolica, 2003): by increasing the laser energy per unit area over  $5.19 \text{ mJ/mm}^2$ , the fluorescence signal begins to drop (See Figures 2.15 & 2.16).

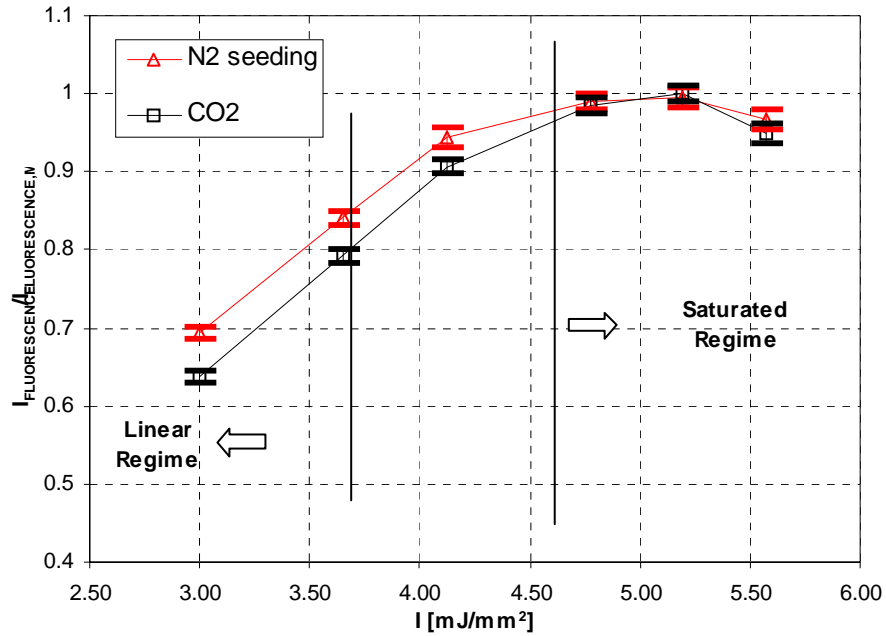


Figure 2.15. Saturation curve for NO-LIF the peak fluorescence signal is plotted against the energy per pulse and unit area for the two different dilutions ( $\phi=1.25$ ).

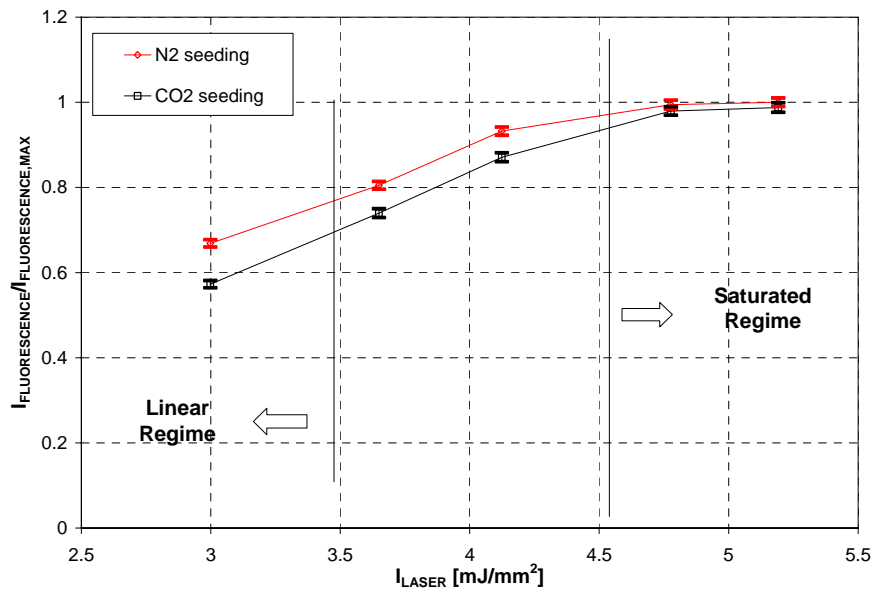
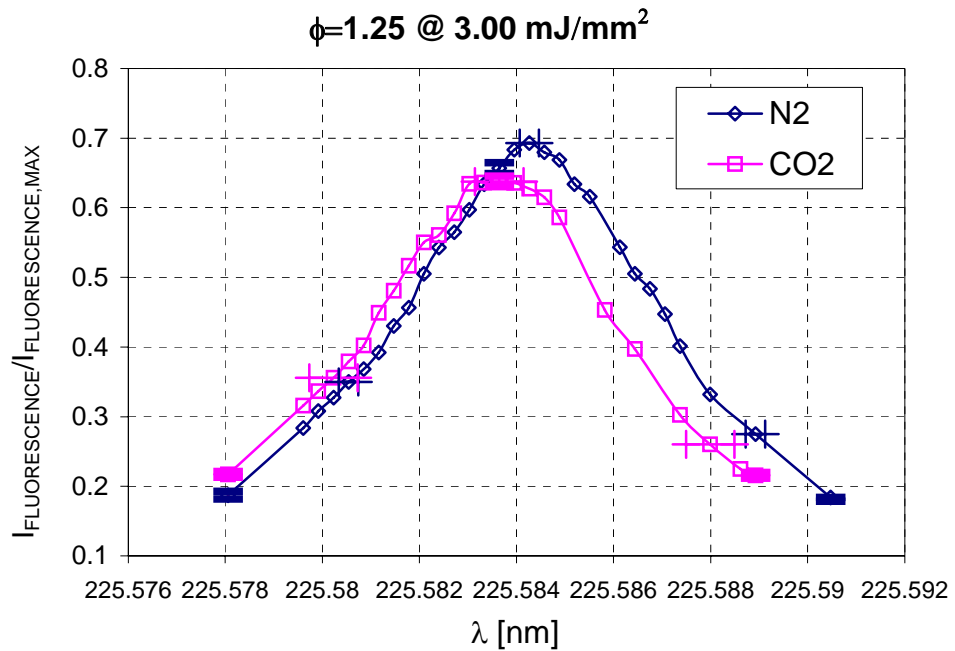


Figure 2.16. Saturation curve for NO-LIF the peak fluorescence signal is plotted against the average laser energy flux for the two different dilutions ( $\phi=1.35$ ).

It is also interesting to compare the scans performed for different dilutions with the same laser power (Figures 2.17 through Figure 2.27). Note that in Figures 2.17 through Figure 2.22 the horizontal bars indicate the estimated uncertainty in the laser output wavelength, while the vertical bars indicate the standard deviation of the measurement.

As the power of the pumping beam is increased, the peak height increases for curves in each graph. It is also to be seen that the peak distance between N<sub>2</sub> and CO<sub>2</sub> dilution curves decreases when the laser power increases. At the higher wavelength excitation (wavelength from 225.584 to 225.590 nm) the distance between the N<sub>2</sub> dilution and CO<sub>2</sub> dilution curves is higher than at lower wavelengths (wavelength from 225.574 to 225.583 nm) where almost no difference is noticed. This means there occurs more signal quenching at lower-energy level excitation. At 3.00 mJ/mm<sup>2</sup> a 2 pm laser wavelength shift from the peak value can lead to an 18% difference in the two cases, by increasing the laser intensities this effect decreases. For example at 4.12 mJ/mm<sup>2</sup> a 2 pm shift will induce an 11% error. At saturation (over 4.78 mJ/mm<sup>2</sup>), no such detuning effect is shown, although the peaks are not at the same location.

In short, the results show that 1) the signal drops more when the excited at lower energy level; 2) this tendency decreases with as the pumping beam strength gets closer to the saturation level; so 3) this shows the importance of beam strength saturation in overcoming the quenching effect and the error that could be caused by the peak-shift.



**Figure 2.17. Spectral scan close to the peak for  $\phi=1.25$  with N<sub>2</sub> and CO<sub>2</sub> dilution and a laser energy per unit area of 3.00 mJ/mm<sup>2</sup>.**

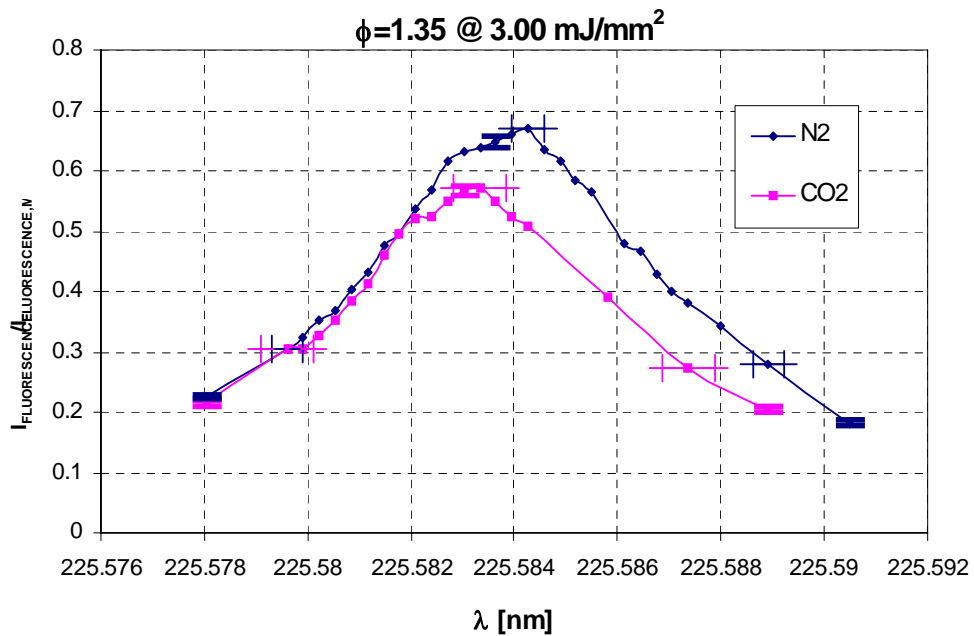


**Figure 2.18. Spectral scan close to the peak for  $\phi=1.35$  with N<sub>2</sub> and CO<sub>2</sub> dilution and a laser energy per unit area of 3.00 mJ/mm<sup>2</sup>.**

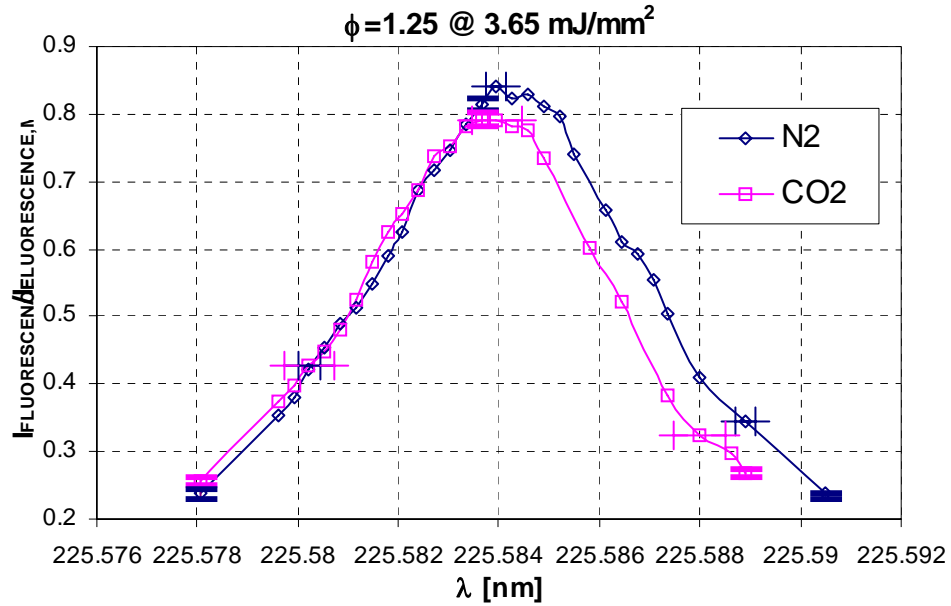


Figure 2.19. Spectral scan close to the peak for  $\phi=1.25$  with  $\text{N}_2$  and  $\text{CO}_2$  dilution and a laser energy per unit area of  $3.65 \text{ mJ/mm}^2$ .

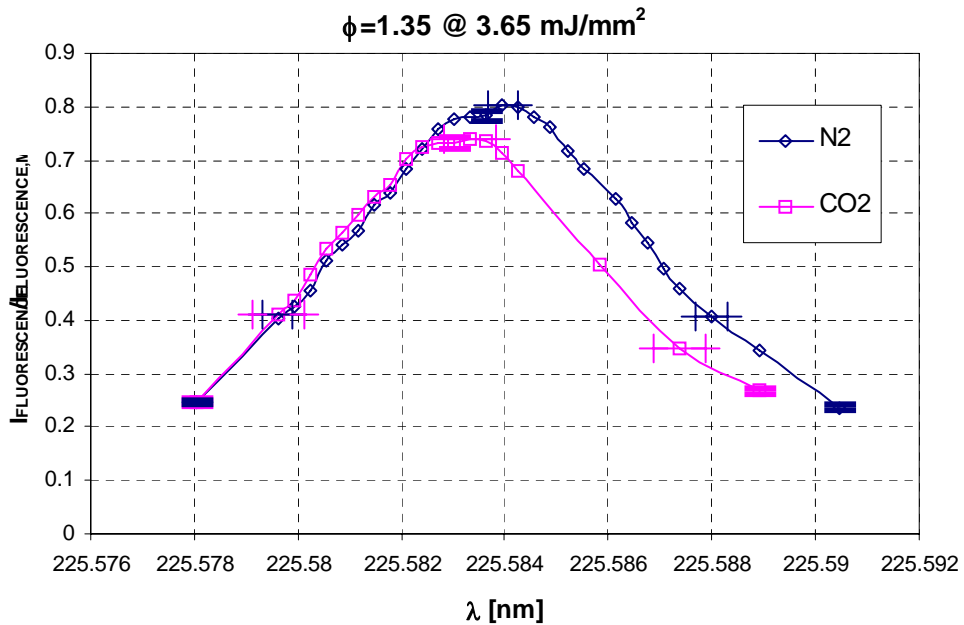
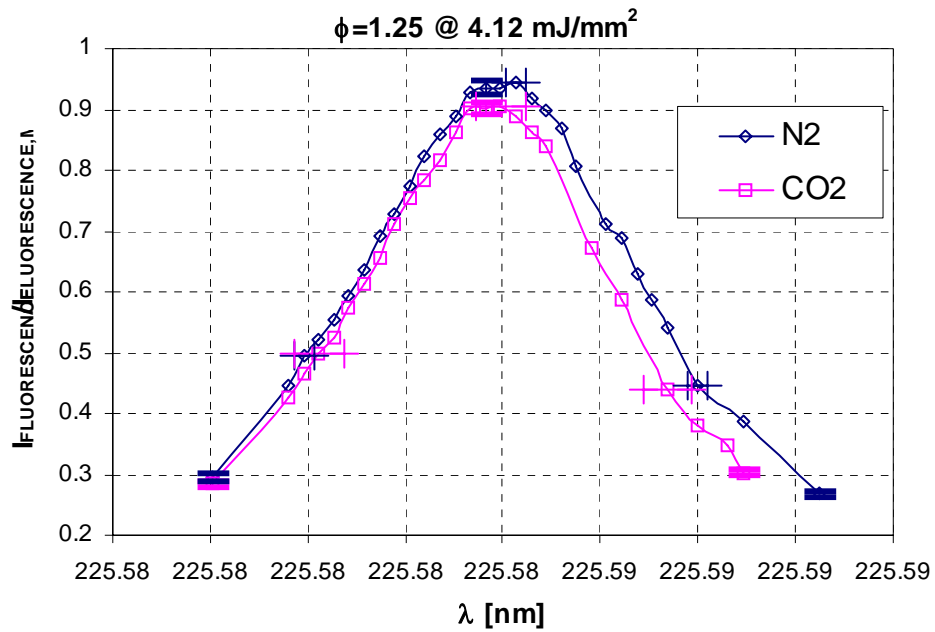
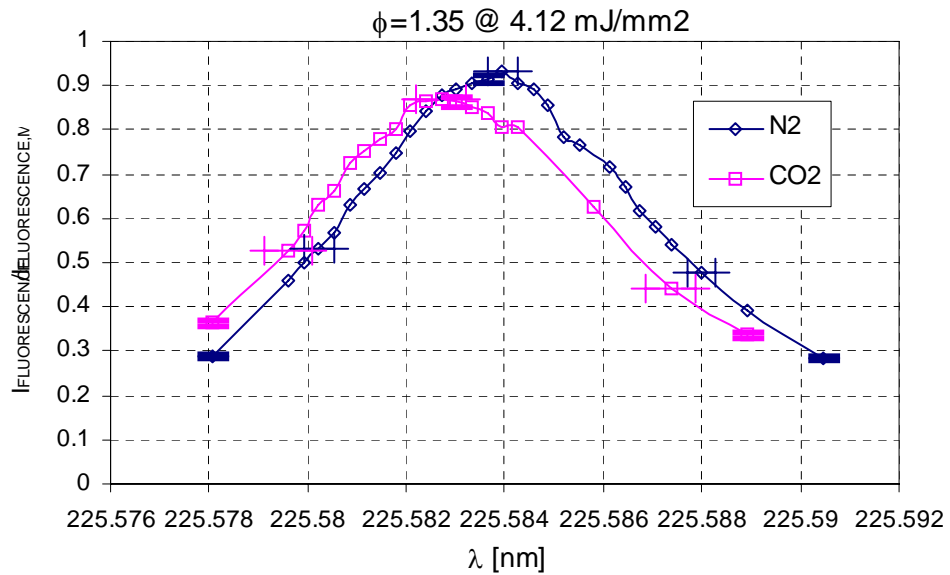


Figure 2.20. Spectral scan close to the peak for  $\phi=1.35$  with  $\text{N}_2$  and  $\text{CO}_2$  dilution and a laser energy per unit area of  $3.65 \text{ mJ/mm}^2$ .



**Figure 2.21. Spectral scan close to the peak for  $\phi=1.25$  with  $\text{N}_2$  and  $\text{CO}_2$  dilution and a laser energy per unit area of  $4.12 \text{ mJ/mm}^2$ .**



**Figure 2.22. Spectral scan close to the peak for  $\phi=1.35$  with  $\text{N}_2$  and  $\text{CO}_2$  dilution and a laser energy per unit area of  $4.12 \text{ mJ/mm}^2$ .**

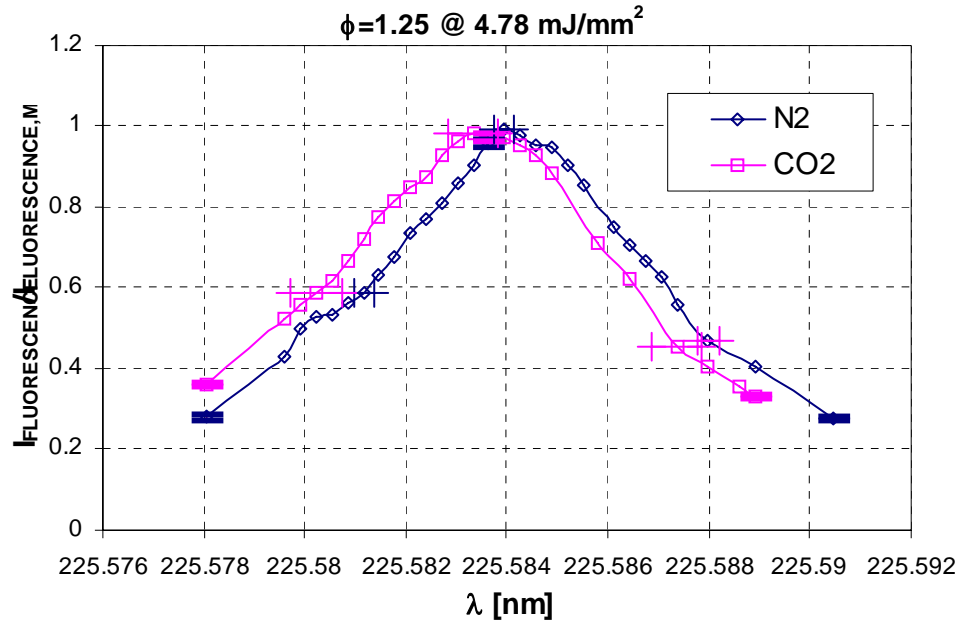


Figure 2.23. Spectral scan close to the peak for  $\phi=1.25$  with N<sub>2</sub> and CO<sub>2</sub> dilution and a laser energy per unit area of 4.78 mJ/mm<sup>2</sup>.

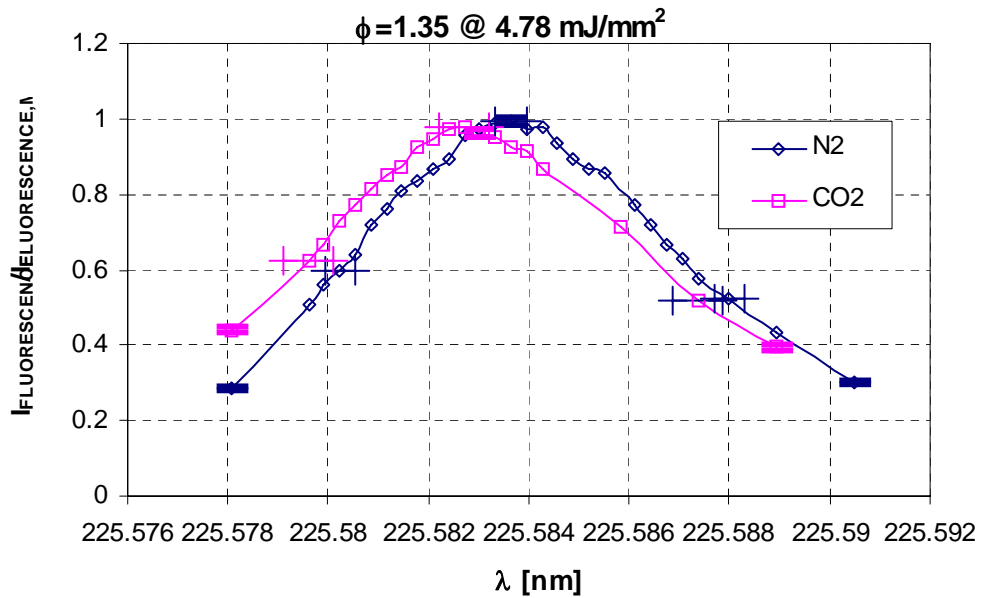
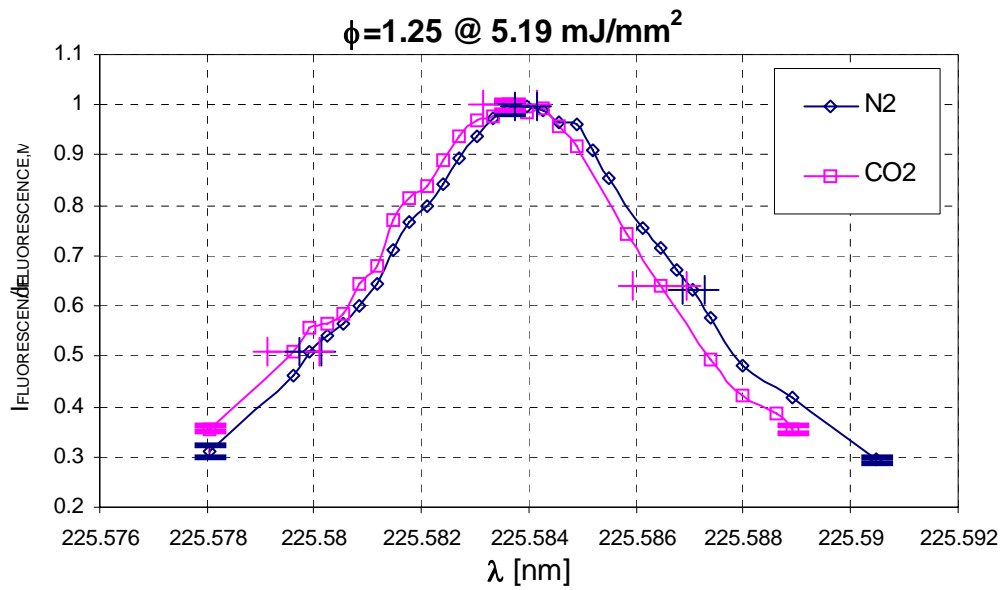
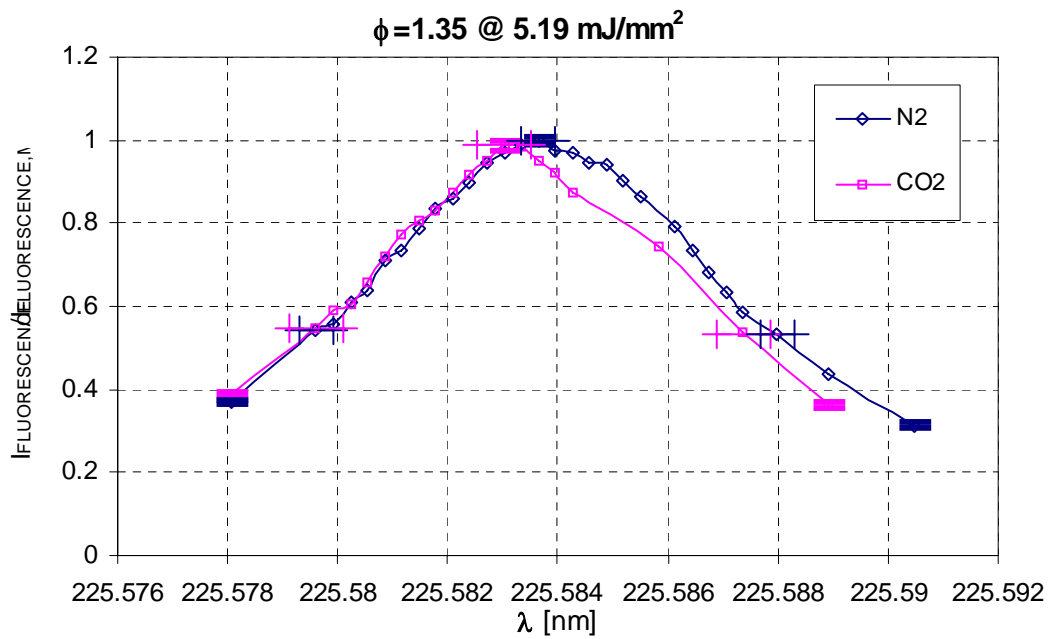


Figure 2.24. Spectral scan close to the peak for  $\phi=1.35$  with N<sub>2</sub> and CO<sub>2</sub> dilution and a laser energy per unit area of 4.78 mJ/mm<sup>2</sup>.



**Figure 2.25.** Spectral scan close to the peak for  $\phi=1.25$  with  $\text{N}_2$  and  $\text{CO}_2$  dilution and a laser energy per unit area of  $5.19 \text{ mJ/mm}^2$ .



**Figure 2.26.** Spectral scan close to the peak for  $\phi=1.35$  with  $\text{N}_2$  and  $\text{CO}_2$  dilution and a laser energy per unit area of  $5.19 \text{ mJ/mm}^2$ .

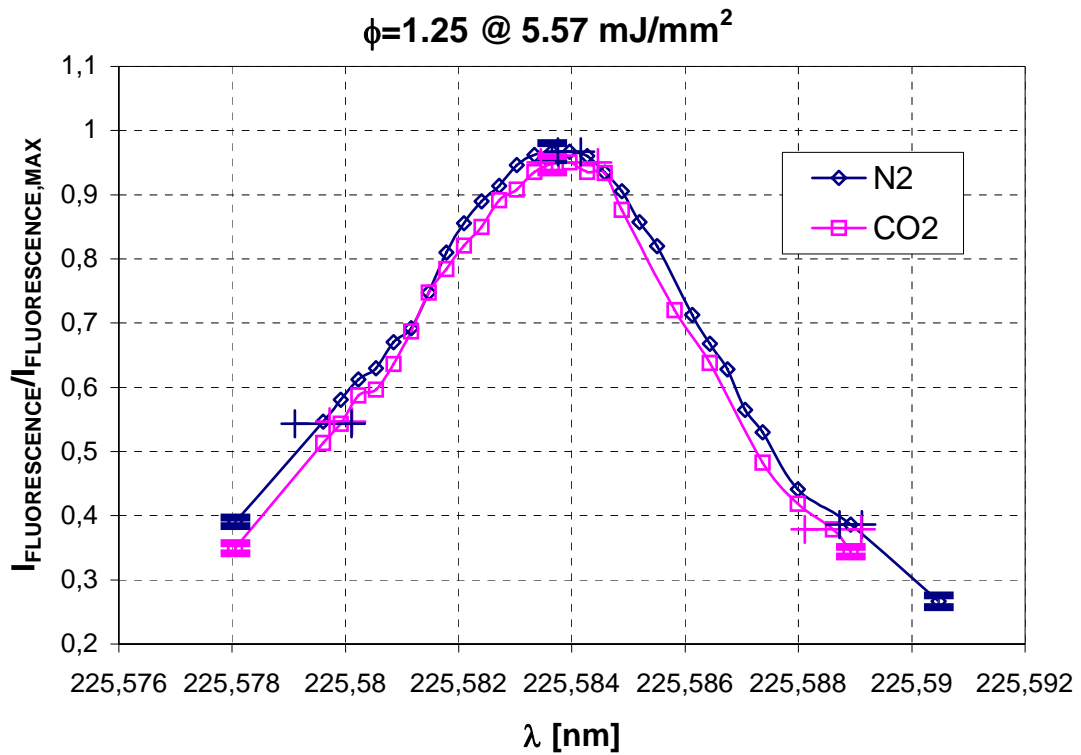


**Figure 2.27. Spectral scan close to the peak for  $\phi=1.25$  with N<sub>2</sub> and CO<sub>2</sub> dilution and a laser energy per unit area of 5.57 mJ/mm<sup>2</sup>.**

The results obtained at the mixture fraction of 1.25 are confirmed for  $\phi=1.35$  (As seen in the previous Figures 2.11 to 2.26).

## 2.5 Summary

The current chapter deals with the practical use of laser induced fluorescence (LIF) technique. This is a technical, preliminary part to the latter part of the series of experiments presented in this thesis. The subsequent part of this thesis work relies on the LIF technique very much as the main tool of investigation. The signal of LIF can lose

strength, or intensity, due to the signal loss caused by the collision and scattering of signal in the presence of certain ‘quenching’ species such as oxygen and carbon dioxide. Hence the reliability of the signal strength has always been of concern when it comes to using the technique in a ‘quenching environment’ where there exists high level of quenching species (e.g. carbon dioxide and water in combustion environment).

An important point from the results of these tests is that when a certain level of excitation intensity is reached, the signal strength level stays steady, giving us an estimate of the minimum amount of energy needed to avoid quenching by certain species. It is also shown that, for species like nitrogen and carbon dioxide, saturation can be reached for reliable measurements.

So far as the author is aware, this work is the first reported description of over-saturation (to the author’s knowledge, at the time of reporting the results at 39<sup>th</sup> Joint Propulsion Conference, Huntsville, AL, 2003). It can be seen in Figures 2.14 and 15 that if the energy per unit area is increased above  $5.19 \text{ mJ/mm}^2$ , the fluorescence signal begins to drop. This effect may be photo-chemically induced and must be accounted for in the later quantitative saturated NO-LIF experiments.

In the test section, the amount of absorption is around 40%. Schultz et al. (2003) suggest that the major species responsible for absorption are  $\text{CO}_2$  and  $\text{H}_2\text{O}$ . Therefore if the probed region is characterized by large amounts of water or carbon dioxide, such as the post-flame regions, adjustment for absorption has to be taken into account. For example,

large diffusion flames, Bunsen or Cheng's Low-Swirl flames (Littlejohn et al. 2003) require calibration for absorption.

The excitation provided by the different lines is also strongly dependent on laser energy per pulse per unit area. Our measurements suggest also that the response to quenching of the lines  $Q_1(23)$  and  $Q_2(27)$  are different; this difference has to be accounted for when doing quenching corrections with a  $\sim 0.5\text{-}1.0\text{ cm}^{-1}$  line-width laser. In fact the spectral scan around the  $Q_2(27)$  transition performed with a line-width of  $0.5\text{ cm}^{-1}$  by Cooper et Lauredeau (2000) suggest strong interference between the rotational lines even if linear fluorescence is performed. If a  $0.25\text{ cm}^{-1}$ , or smaller, wide laser beam is employed, this effect is very much reduced. This type of narrow band excitation was the strategy employed by Paul et al. (1996) for measuring quenching corrections.

Variable two-line excitation also results in effective peak shifting as the relative contribution by each line varies. Peak shifting has to be accounted for unless a very narrow band and frequency drift controlled laser is used. The peak shift appears to depend on stoichiometry,  $\text{CO}_2$  concentrations, as well as Dye laser grating de-calibration. Further experiments and analysis treating the topic of peak shifting are needed to accurately quantify the effect. Current measurements show a peak shift of up to 3 pm but with an uncertainty of 5 pm. Several techniques can be employed for removing frequency drift (see Cooper and Lauredeau, 1997) and diminishing the line-width of the laser.

Some important conclusions can be drawn for NO-LIF or NO-PLIF applied to turbulent combustion. Several corrections must be taken into account in order to be able to produce quantitative data in flames where a post-flame region is probed (for example in a McKenna or Cheng type burner). First, absorption must be taken into account (Schultz et al. 2003). Also, quenching corrections must be estimated (Nguyen et al. 1996). Line-width effects on quenching are also important, because, as seen previously not all the excitation frequencies respond in the same way to quenching. Corrections due to the beam profile must be accounted for as well as corrections for quenching. A small frequency shift in laser beam can induce big errors due to off-peak excitation, especially in the outer portion of the laser sheet where the laser intensity is lower or in regions where mixing entrains higher CO<sub>2</sub> or H<sub>2</sub>O concentrations. These effects depend on the local concentration of quenchers and their impact can be partially reduced by employing narrow line-width lasers.

In conclusion, complementing NO-LIF measurements at 226 nm with measurement of local carbon dioxide and water concentration, especially in combustion environments, would greatly improve the accuracy and fidelity of the measurement.

# Chapter 3

## Measurements of the Dynamic Response of Mixing

---

Mixing is a significant factor in determining the stability of combustion systems and as an actuation method for active control of combustion instabilities, where fuel/air mixture fraction, or the local distribution of equivalence ratio matters. This chapter describes the measurements of the behavior of fuel/air mixing made for a non-premixed jet flame to provide a basic understanding of the dynamics of mixing affected by outside disturbances, the imposed acoustic waves. Unmixedness is calculated as a means to quantify the degree of mixing, and the behavior of this quantity is studied to analyze the dynamics of fuel/air mixing under the effect of forced acoustic oscillations. Comparison with thermo-acoustic coupling is made to show the relevance of the mixing to the flame behavior. Phase-resolved acetone PLIF was used to image the flow field of both reacting and non-reacting flows.

### 3.1 Introduction

Mixing is a significant factor in combustion dynamics. The rate of heat production, fuel-efficiency, and pollutant (NO<sub>x</sub>, unburned hydrocarbons, and etc.) formation are all affected by the mixing of fuel and air. The local distribution of equivalence ratio due to the uneven mixing of fuel and air, and its response to the combustion dynamics is of great concern in any combustion processes that take place without the full mixing of fuel and air prior to injection. According to Lieuwen et al. (1998), combustion instabilities could be caused by the oscillatory behavior of mixing, and especially so in fuel lean regions. Also, modulating the fuel/air mixing using high speed valves or acoustic forcing in the main or secondary fuel feeding line is widely used as a means of actuation in active control of combustion dynamics (Cohen et. al. 2001).

In many cases, such as those mentioned Chapter 1 (1.3.2), combustion phenomena were studied without being confined in combustors. In this work, the combustion is confined to a large volume with imposed bulk acoustic motion. The magnitudes of the driving acoustic waves were set to a constant value (0.1 % of the ambient pressure) using a feedback controller.

#### 3.1.1 Background

As a means to quantify the degree of mixing in the flow field, the unmixedness factor has been defined and widely used (e.g., Dimotakis et. al. 1990, Fric et. al. 1993).

The global unmixedness is defined as

$$(3.1) \quad U_g = \frac{\sigma_g^2}{(1 - \langle x \rangle_g) \cdot \langle x \rangle_g},$$

where  $\sigma_g$  is the standard deviation and  $\langle x \rangle_g$  average of fuel concentration over the entire 2-D image, instead of one point, with many measurements. The unmixedness is a normalization (Dimotakis et al. 1990) of the variance  $\sigma_g^2$  by the maximum possible value for the given  $\langle x \rangle_g$ , evaluated by the variance of Housdorf relation,  $\sigma_g^2 = \langle x \rangle \cdot (1 - \langle x \rangle)$ . When the fuel is completely mixed and homogeneously distributed,  $U$  is zero; when no mixing occurs,  $U$  is unity. A two-dimensional image collapses to a single value by this definition, which gives a quantitative measure of the magnitude of the variation of fuel/air mixing, the degree of fluctuation in fuel concentration over the entire region.

The local temporal unmixedness is defined as in the work by Fric (1993),

$$(3.2) \quad U_t = \frac{\sigma_t^2}{(1 - \langle x \rangle_t) \cdot (\langle x \rangle_t)},$$

where  $\sigma_t$  is the standard deviation of the fuel concentrations drawn from repetitive measurements at the specific location, and  $\langle x \rangle_t$  is the average of fuel concentration at that location. The subscript, 't', is used to denote that the quantity is a 'temporal' value. In respect to temporal unmixedness ( $U_t$ ), higher values of  $U$  mean greater fluctuations in the fuel concentration. Thus, where  $U$  is larger can be interpreted as a region with severe alternations in fuel concentration, thus a region where more shear mixing occurs than in locations with lower values. Since the definition is defined on each location (pixels in images, in this case), two-dimensional distribution can be acquired, and, of course, the 'temporal' unmixedness is different in meaning from the 'global' unmixedness in that the 'temporal' unmixedness indicate the degree of fuel concentration fluctuation at a location over time, while the 'global' unmixedness is a measure of how the fuel is homogeneously distributed over the space, without regard to the time.

An analysis of combustion-driven oscillations will inevitably involve the well-known Rayleigh's criterion discussed by Lord Rayleigh (1945). Following the development by Culick (1987), it can be stated formally as

$$(3.3) \quad \Delta E = \frac{\gamma - 1}{\bar{p}} \int dV \int_t^{t+\tau} p' q' dt,$$

where  $\Delta E$  is the incremental energy added to the acoustic field over a period  $\tau$  due to the coupling between the fluctuating pressure  $p'$  and the fluctuating heat release  $q'$ . A positive value of  $\Delta E$  tends to drive the unstable process, whereas a negative  $\Delta E$  tends to damp out the oscillations (see Appendix B for details).

The above equation can be modified to yield a frequency-driven or forced Rayleigh index that has been non-dimensionalized and normalized as:

$$(3.4) \quad R_f = \int_0^1 \frac{p' q'}{p_{rms} \bar{q}} d\xi,$$

where  $p_{rms}$  is the root-mean-square of the amplitude of the driving pressure wave;  $\bar{q}$  is the mean intensity of the heat release per unit volume;  $p'$  is redefined as the driving pressure amplitude; and  $q'$  is the fluctuation in heat release per unit volume (Pun 2001).

Acetone PLIF was used as the measurement technique in the current work. Many efforts (Lozano et al. 1992, Thurber et al. 1997, 2001, Meyer et al. 2002, Demayo et al. 2003, Yip et al. 1994) focused on measurement of fuel concentration using acetone PLIF where the acetone had been similarly introduced as a fuel marker. Among those cited, the work by Lozano et al. (1992) is by far the most concise and best starting point for constructing the current measurement technique. The work gives introduction to the basic implementation and the physics involved with acetone-LIF related issues such as

temperature, pressure dependences (see Appendix A for more information).

The attractions of acetone PLIF are that it is 1) non-intrusive, 2) instantaneous with life time of 4 ns, 3) very effective in molecular-marking flows of fuel or air with little possibility of affecting the flow significantly, and 4) allowing high spatial and temporal resolution with high signal to noise ratio in general. Acetone has a high vapor pressure, so it is easy to seed into any kind of gaseous stream. Acetone is also cheap and relatively safe to use compared to other fluorescing molecules.

Acetone is a very strong absorber and emitter over a broadband of wavelengths, which allows measurement of low concentration levels. For a given temperature and pressure, acetone fluorescence is linear with acetone concentration (many molecules are not linear with concentration).

There are several other species used as tracer molecules (Table 3.1), and each of them has different characteristics. As shown in table 1, for example, acetone absorbs around 225 ~ 320 nm, and emits at 350 ~550 nm peaking at 435 nm with duration of 4 ns. Here B.P. means boiling point,  $\sigma$ , molecular absorption cross section,  $\phi$ , the fluorescence efficiency (the quantum yield). Of these, ‘Biacetyl’ is vulnerable to O<sub>2</sub> quenching, ‘Acetaldehyde’ is carcinogenic and optically thick thus requiring very strong pumping laser power, and ‘Hexafluoroacetone’ is known to be very toxic (Lozano et al. 1992).

	B.P.	Absorption	$\sigma_{\max} (\times 10^{-20} \text{ cm}^2)$	$\phi_f$	Emission (nm)	$\tau_f$	$N \sigma \phi C$
Acetone	56 °C	225–320 nm	4.7 (275 nm)	0.2%	350–550 (435)	4 ns	$7.2 \times 10^{13}$
Biacetyl	88 °C	340–470 nm	8 (417 nm)	0.25%	420–520 (485)	15 ns	$7.0 \times 10^{12}$
Acetaldehyde	21 °C	250–340 nm	4.6 (290 nm)	0.15%	350–480 (420)	4 ns	$1.0 \times 10^{14}$
Hexafluoroacetone	–26 °C	245–355 nm	3.1 (302 nm)	1.85%	410–580 (430)	84 ns	$1.2 \times 10^{15}$

**Table 3.1. Comparison of various tracer molecules (Lozano et al. 1992).**

In the present work, acetone is introduced in the fuel stream with a three-way valve system. The fuel/acetone mixture is intended to be homogeneously mixed, and the distribution of acetone in the fuel/acetone-air mixture is expected to be ‘marking’ the fuel distribution in the fuel-air mixture stream.

### **3.1.2 Objectives**

The objective of the present work is to examine the effect of acoustic oscillations, as sources of unstable dynamics inside the combustor, on the fuel/air mixing. This also includes study of the link between behaviors of mixing behavior and flame under these same conditions. The current work builds on that previously performed (Pun et al. 2003) by focusing on the fuel-air flow structure upstream of the flame front. It is also of great interest to establish the way the behavior of mixing is quantified and described, as part of the series of works presented in this thesis work, to establish a general experimental procedure to study combustion dynamics.

## **3.2 Experimental Configurations**

The experimental set-up consists of sub-sections as depicted below. The laser system (PLIF configuration) and acoustic system generates the measurable signals, which are acquired by the appropriate data acquisition devices (ICCD Camera and the piezo-electric pressure transducer).

### **3.2.1 Acoustic Driving System**

A schematic view of the acoustic chamber is shown in Figure 3.1. The acoustic chamber is made of an aluminum central section and a stainless steel top that houses the loudspeakers (Cerwin-Vega model Vega 124), and allows direct exhaust of the product gases at the top. The exhaust port is open to the atmosphere which creates an acoustically open exit condition for acoustic wave resonance. The bottom of the chamber creates a closed-end acoustic condition. The speakers are 12 inches in diameter and powered by a 1000 W power amplifier (Mackie M1400i). A function generator (Wavetek 171) provides the input signal.

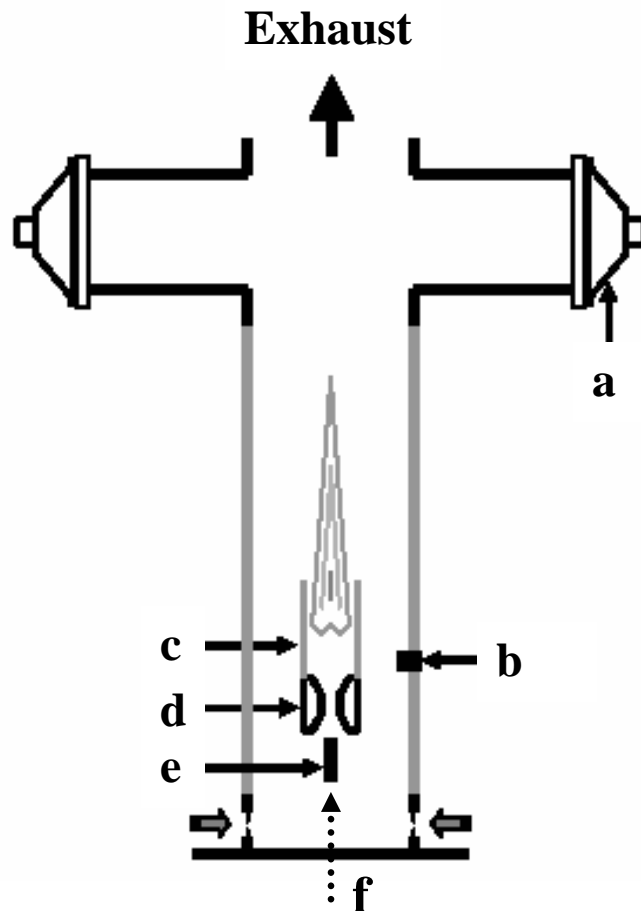


**Figure 3.1. The combustion chamber: (a) loud speakers, (b) pressure transducer, (c) fused-silica burner tube, (d) eductor (burner) block, (e) fuel spud, arrows at the bottom indicate the air inlet, and (f) the fuel supplied.**

The amplitude of the fundamental driving mode (the acoustic waves) is actively controlled by custom-designed electronics (Palm, in progress), which measure the pressure in the acoustic chamber at the burner with a pressure transducer (PCB 106B50), and appropriately scale the power output of the speakers. The signal from the transducer is notch-filtered to ensure that the intended driving mode is correctly amplified or attenuated.

The piezoelectric pressure transducer (106B50) is located at a height of 3 inches above the fuel spud, where the flame sits. This transducer features high sensitivity (493.3 mV/psi) and stable thermal characteristics. A PCB model 482A16 power supply and amplifier, with the gain set at 100, powered the transducer.

### **3.2.2 Laser and Optical Configurations**

The laser system and optical components are practically identical to those described in Sections 2.2.2 and 2.2.3. In the present work, though, the DYE laser tunes the 532 nm pumping beam to 560 nm using the Rhodamine 590 perchlorate dye alone. Then the 560 nm beam is frequency-doubled without being mixed, by the mixer/doubler system (manufactured by U-oplaz) to produce 280 nm probing beam. The probing beam, then, is reflected off mirrors and prisms to form a beam path as shown in Figure 3.2.

A cylindrical lens (the focal length,  $f = -400$  mm) and a spherical lens ( $f = 1000$  mm) are used to form a laser sheet focused at the center of the flame. The fluorescence signals are expected in the range of 350-550 nm.

The beam intensity was chosen to be in the linear regime of signal as discussed in Chapter 2, where each image was scaled by the corresponding beam strength measured off of one of the beam deflecting points in Figure 3.2.

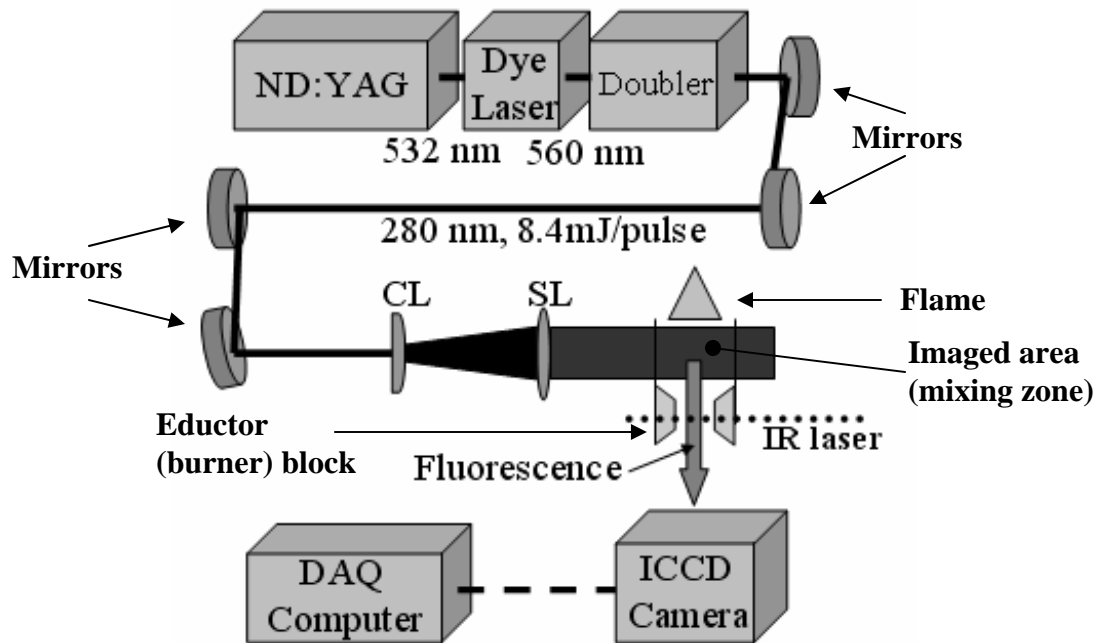


**Figure 3.2. Schematic of the Acetone PLIF.**

The PLIF images were captured on an intensified CCD camera (described in Section 2.2.4) with a size of 300 by 225 pixels to image 5.5 by 4.1 cm mixing area, giving 183  $\mu\text{m}$  by 183  $\mu\text{m}$  spatial resolution. The images are cropped and reduced in size to avoid the uncertainties since the PLIF signal is known to be not reliable under too high temperature (over 1000 K, Lozano et al., 1992). The PLIF signal passes through a UV high-pass filter (SCHOTT NG-5, glass filter) which blocks all wavelengths lower than

300 nm to gather the fluorescence signal expected at around 350 and 550 nm with 100 ns gating width for the camera (refer to Chapter 2 for details about the camera).

Images are taken at random phases of pressure waves, with the camera gating signal being recorded by the data acquisition system along with the pressure signal so as to enable appropriate post-processing. Post-processing involves sorting the images by the phases of imposed acoustic oscillations, creating phase-averaged images, and normalizing based on the shot-to-shot laser intensity and other quantities. The laser power for the experiment is 10 mJ/pulse, which is approximately  $0.412 \text{ mJ/pulse/cm}^2$  of intensity barely enough or less than enough for saturating the signal; this is why the normalization is required. A single shot image and a phase-averaged image are shown in Figure 3.3.

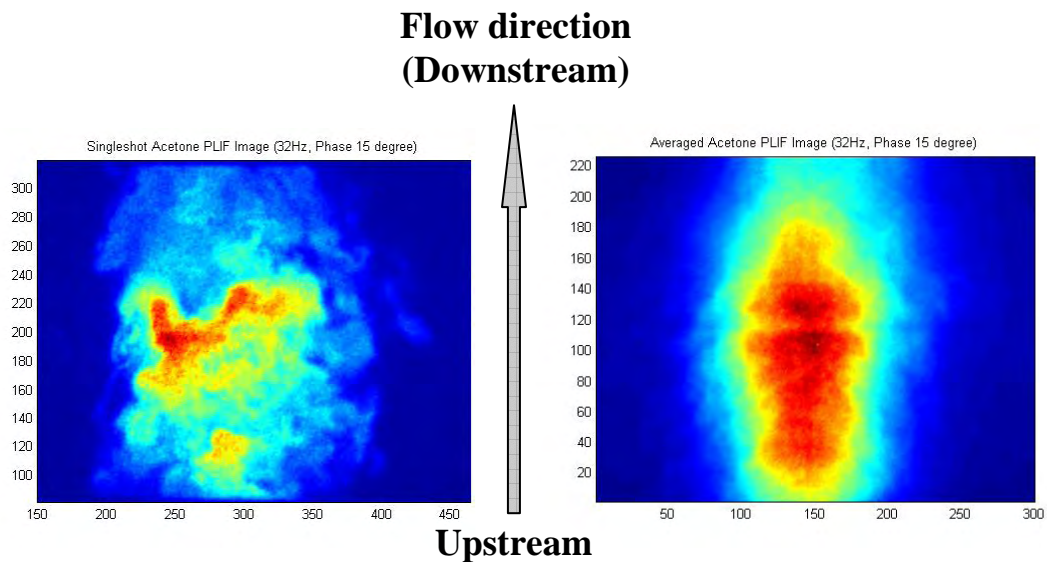


**Figure 3.3. A random single shot image (left hand side) and a cropped, phase-averaged image (right hand side, phase angle of 15 degrees) at 32 Hz. Horizontal and vertical units are in pixels.**

## 3.2.3 Test Section

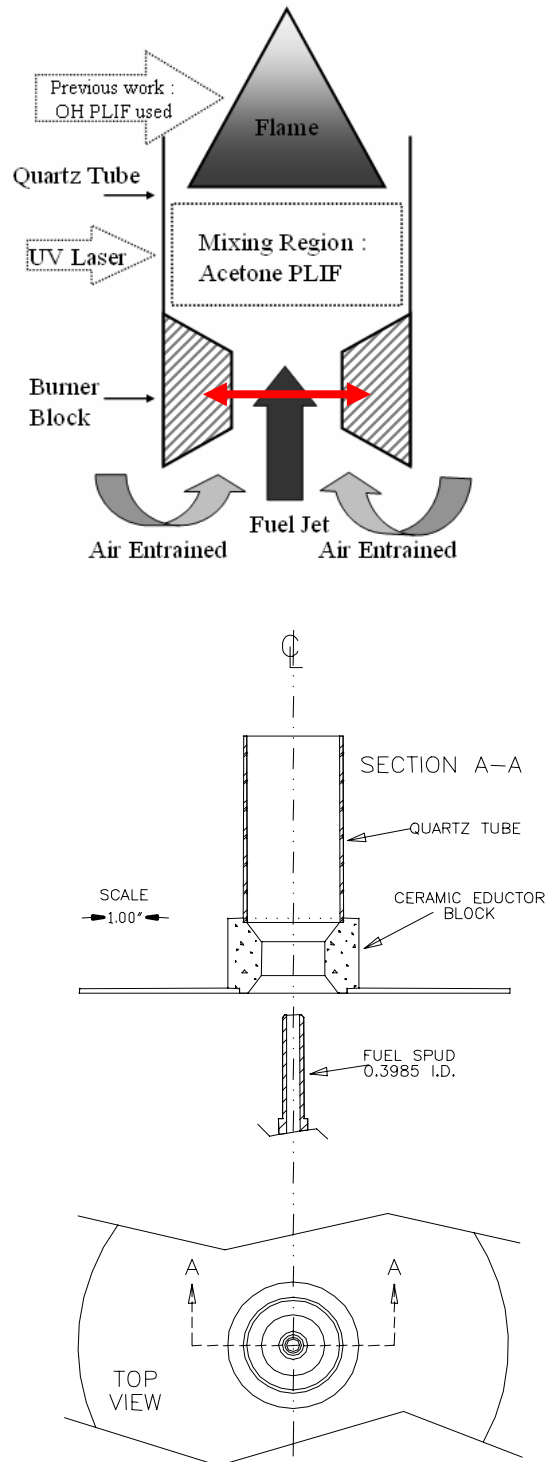


**Figure 3.4. Region of Interest (top) and the Sectional View of Burner (bottom).**

The burner (top, Figure 3.4) is a traditional jet-mixed type burner with flame anchoring approximately in the middle of the quartz tube, with the exact height depending on the specific flow conditions. The fuel jet is 50% methane and 50% nitrogen with acetone seeded, and air is entrained and drawn into the jet as the flow moves through the burner. The fuel jet speed is approximately 20 m/s at the outlet of the 1.0 cm diameter fuel spud, yielding  $Re \sim 10,000-20,000$ . The quartz tube is 5.72cm wide on each side and 11.43cm tall and is made of fused silica/quartz to enable observation and measurement of the flame.

Figure 3.5 provides details of the gas feed system. Fuel for the burner is 50% methane premixed with 50%  $CO_2$  gas to increase the mass flow. The premixer inlets for each gas are choked, in order to prevent disturbances from propagating upstream and affecting flow rates. The mixture is subsequently passed through a laminar flow element (Meriam Model 50MJ10 Type 9), the temperature measured by a type-K thermocouple and a digital thermometer (Analog Devices, Model AD2050-K), the pressure drop measured by a barocel pressure sensor (Datametrix model 590D-10W-3P1-H5X-4D, 1400 electronic manometer) and the flow rate determined. It then exits the fuel spud and entrains atmospheric air into the stream.

Acetone is seeded by a custom made device as illustrated by bottom, Figure 3.5. The fuel stream is channeled into a can full of acetone, then redirected back to the fuel spud. The can containing acetone is submerged in a water basin to be kept at a constant (room) temperature.

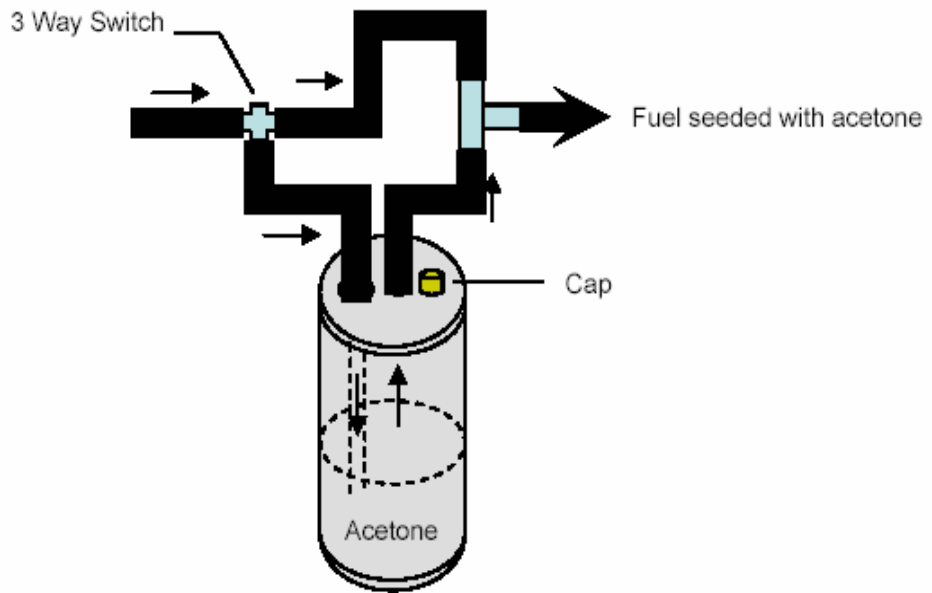
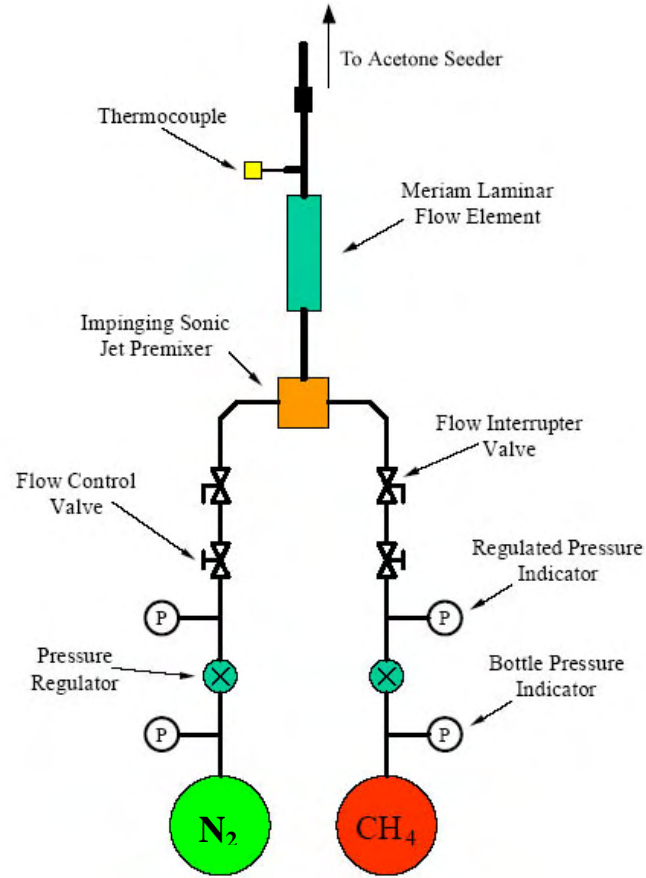


Figure 3.5. The Gas Feed System (top) and the Acetone Seeder (bottom).

### 3.2.4 Data Acquisition

The computer used in the data acquisition system consisted of an Intel Pentium 4 1.8 GHz processor with 512 MB RAM and 200 GB of total hard drive space (actual data took up 30 GB). Installed in the computer is a NI-DAQ 6024 PCI (National Instrument) 16-bit data acquisition boards capable of 4 differential channel measurements capable of up to 100 kHz. The channels are given to: pressure, fed-back signal, laser shot-to-shot intensity, and camera gating signals. Also in the same computer is the PCI controller card for the Princeton Instruments ICCD camera. The software used for the data acquisition is National Instruments LabView 7.0.

### 3.2.5 The Controller

A custom electronics unit (a feedback controller) used in the experiments were designed and built by Mr. Steven L. Palm. This regulates the power amplifier output to the acoustic drivers. Output from the pressure transducer (PCB 106B50) is notch filtered by the controller to determine the amplitude of the fundamental frequency the acoustic drivers are producing in the chamber. This is compared with an adjustable preset value in the controller, which uses PI control to regulate the system to ensure a constant pressure amplitude at the transducer location (a height of 12 inches, approximately level with the flame stabilization zone).

More details on this equipment can be found in the Ph.D. thesis of the designer (Palm, *in progress*).

### 3.3 Experimental Procedure

#### 1. Laser preparation

- Optimize the mixer/doubler tuning crystal angles for maximum energy conversion.
- Check the laser beam profile and power. Leave for 15 minutes to reach the steady state.

#### 2. Set gas streams

- Cooling air for the acoustic drivers.
- Nitrogen purge gas through ICCD camera.
- Open valve for fuel/nitrogen stream, and direct the stream to the acetone seeder.
- Check the stream stability with pressure meter.
- Turn on the ventilation pump.

#### 3. Optical alignment

- Check the laser beam path with cards at each point of beam deflection to ensure that the beam is directed in the right way.
- Focus the ICCD camera on a card in the test section. Ensure the laser sheet is passing through the probed volume cleanly and focused at the center.

#### 4. Beam profile calibration

- Minimize laser energy throughput using the wave plate. Set camera gain to 1, and gate width to 10 ms.

- Allow laser sheet to impinge on fluorescent card and acquire the beam profile with the ICCD camera, placing card in three different positions (left, center, right).
  - Return camera gain to 200, and gate width to 100 ns and wave plate to allow maximum laser energy throughput.
5. Prepare devices.
    - Light the burner and set methane and nitrogen flow rates.
    - Set acoustic driver power on controller, and activate drivers.
  6. Perform pre-runs (duration approximately 3 minutes).
    - Start LabView data acquisition program.
    - Start WinView camera imaging software, typically taking 300 images (limited by system RAM).
  7. End experiments
    - LabView and WinView routines end automatically
    - Turn off fuel flows, extinguishing the flame.
    - Turn off acoustic drivers.
  8. Repeat experiment.
    - Repeat steps 6-8 until more than 1800 images have been acquired at a particular test condition.
  9. Change experimental conditions.
    - Change the acoustic driving frequency.
    - Repeat steps 4 through 8 until experimental session is complete.
  10. Shutdown systems.

- Shut off the laser.
- Turn off the ventilations and other related devices.
- Store data acquired – burn DVDs for post-processing and archival.

### 3.4 Results

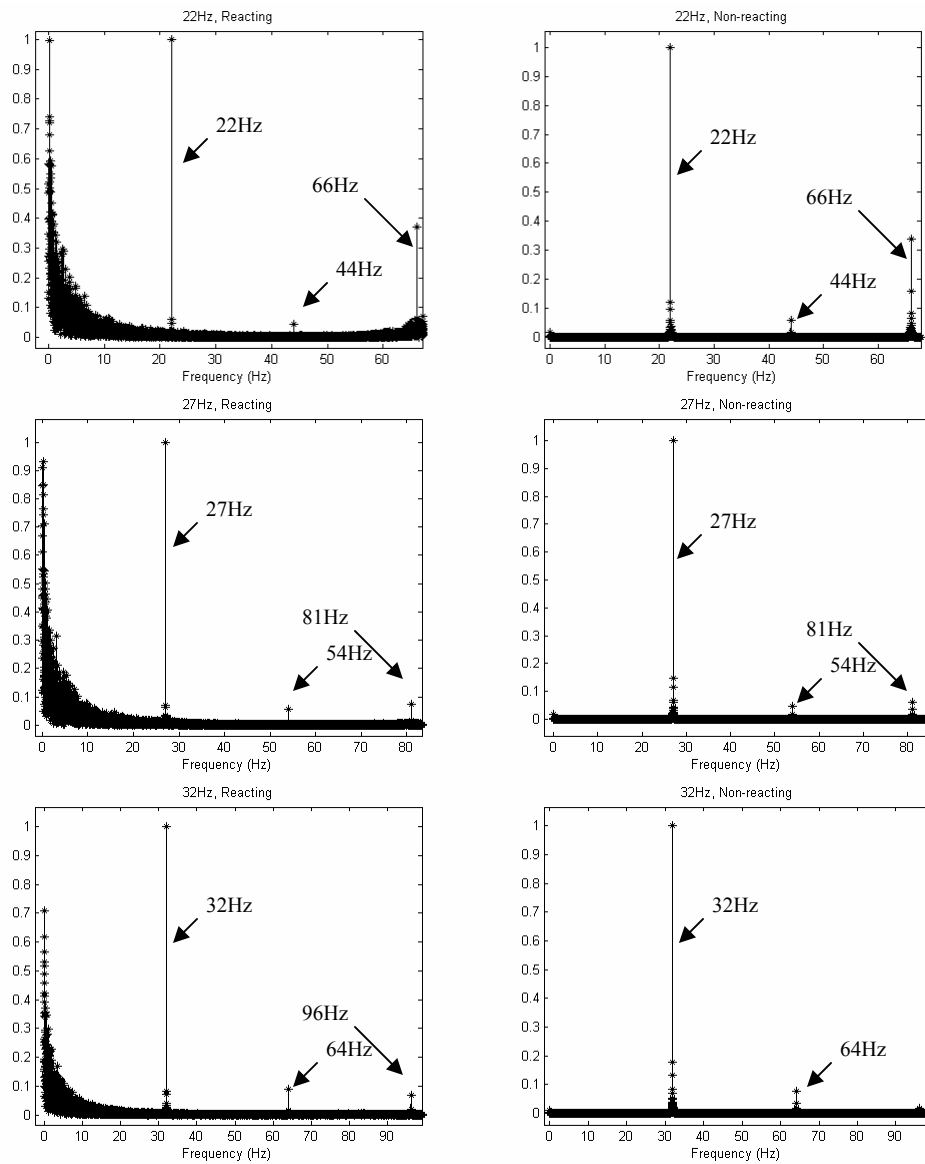


**Figure 3.6. Fast Fourier Transformed pressure signal at 22, 27, and 32 Hz. Reacting (LHS) and non-reacting cases (RHS).**

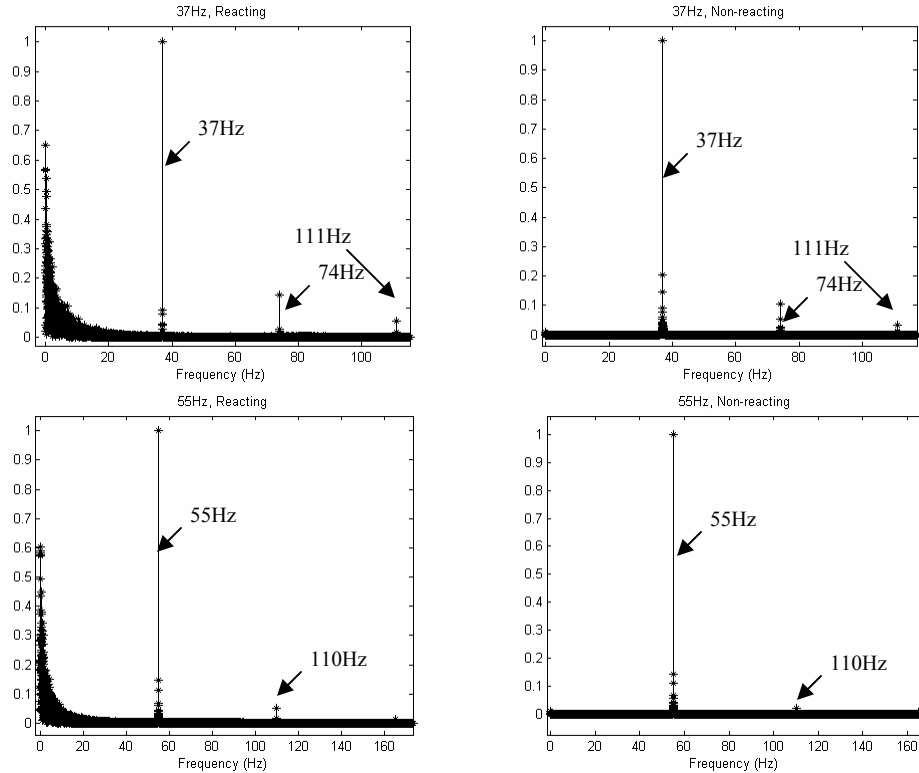


**Figure 3.7. Fast Fourier Transformed pressure signal at 37 and 55 Hz. Reacting (LHS) and non-reacting cases (RHS).**

The role of combustion processes in causing higher uncertainties in fuel/air mixing is obvious from comparison with the non-reacting cases (Figure 3.6 and 3.7), where the fast Fourier transformed pressure signals show clear differences. Given that all other experimental conditions are the same, there exists a region of irregular pressure fluctuations only for the reacting cases due to the generation of sound waves by the irregular burning of the turbulent flame. This phenomenon, whose name, the ‘ $1/f$  error’, derives from the shape of ‘ $f(x) = 1/x$ ’ graph in the frequency range lower than the excitation frequency (the dark shaded regions in the left hand side of

Figure 3.6 and 3.7), is observed in a wide variety of experimental efforts, where random processes, such as the turbulent mixing and burning affected by acoustic perturbations, have significant contributions. The amplitude of waves generated by the turbulent burning of fuel is significant. This is due to fluctuations in the local equivalence ratios in the flame area, caused by irregularities in the fuel/air mixing in the upstream.

### 3.4.1 Temporal Behavior of Mixing

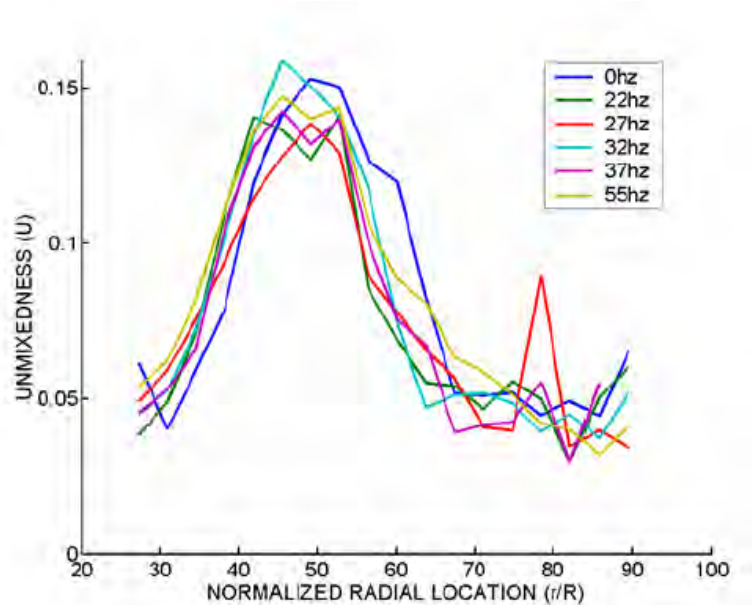
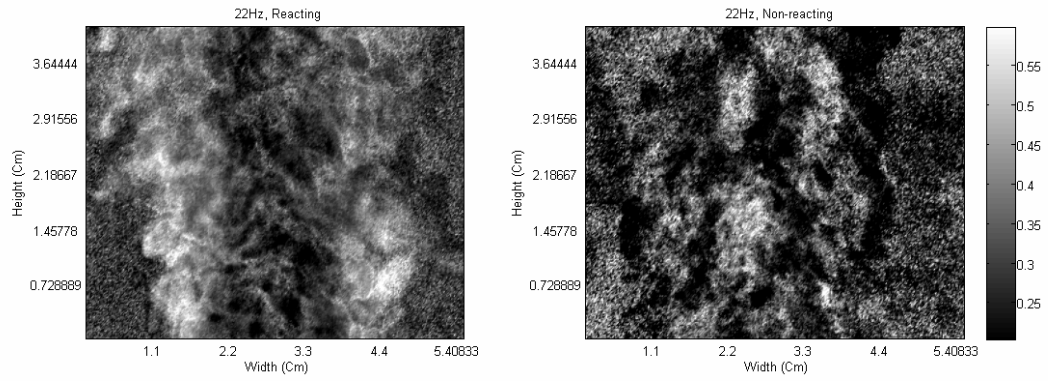
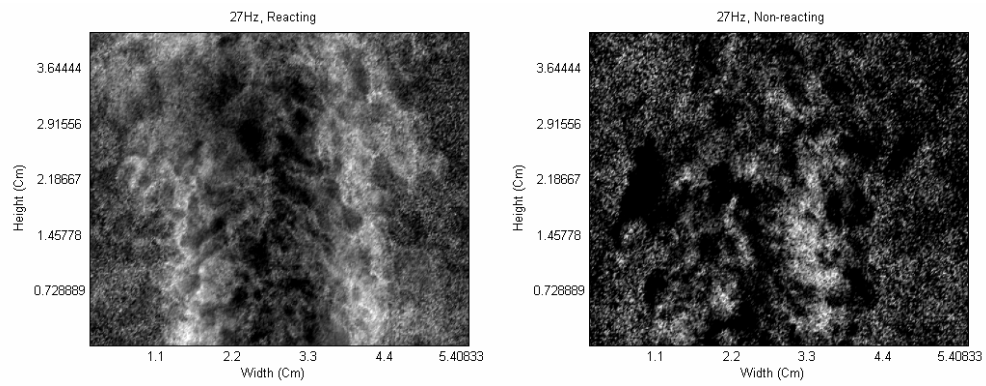


**Figure 3.8. Temporal Unmixedness measured at the neck of the eductor block (the region marked with red arrow in Figure 3.4 (top), Fernandez et al. 2003).**

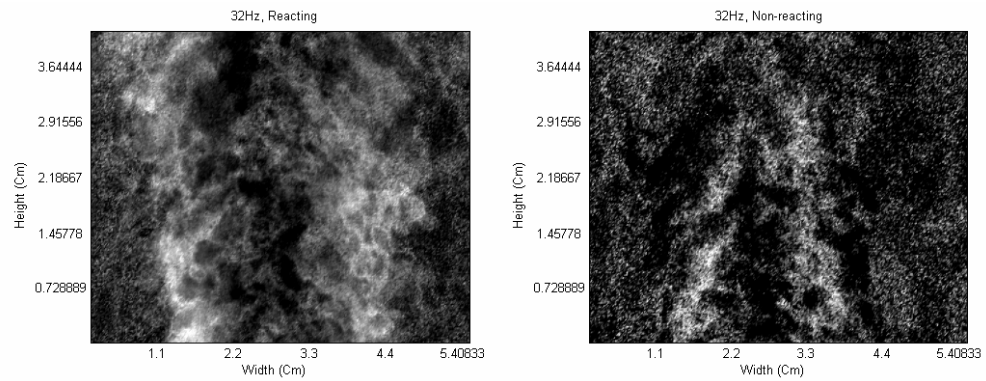
It can be seen in Figure 3.8 that high values of temporal unmixedness occur in the shear mixing layer of the flow, in the range of 30-60% of the normalized radial location from the center. There is little variation in the overall unmixedness structure for excitation at different frequencies, with all plots indicating the same general mixing layer structure.



(a)



(b)



(c)

**Figure 3.9. Distribution of temporal unmixedness at 22Hz (a), 27Hz (b), and 32Hz (c). Reacting (LHS) and non-reacting (RHS) cases (at the center of the cylindrical mixing region).**

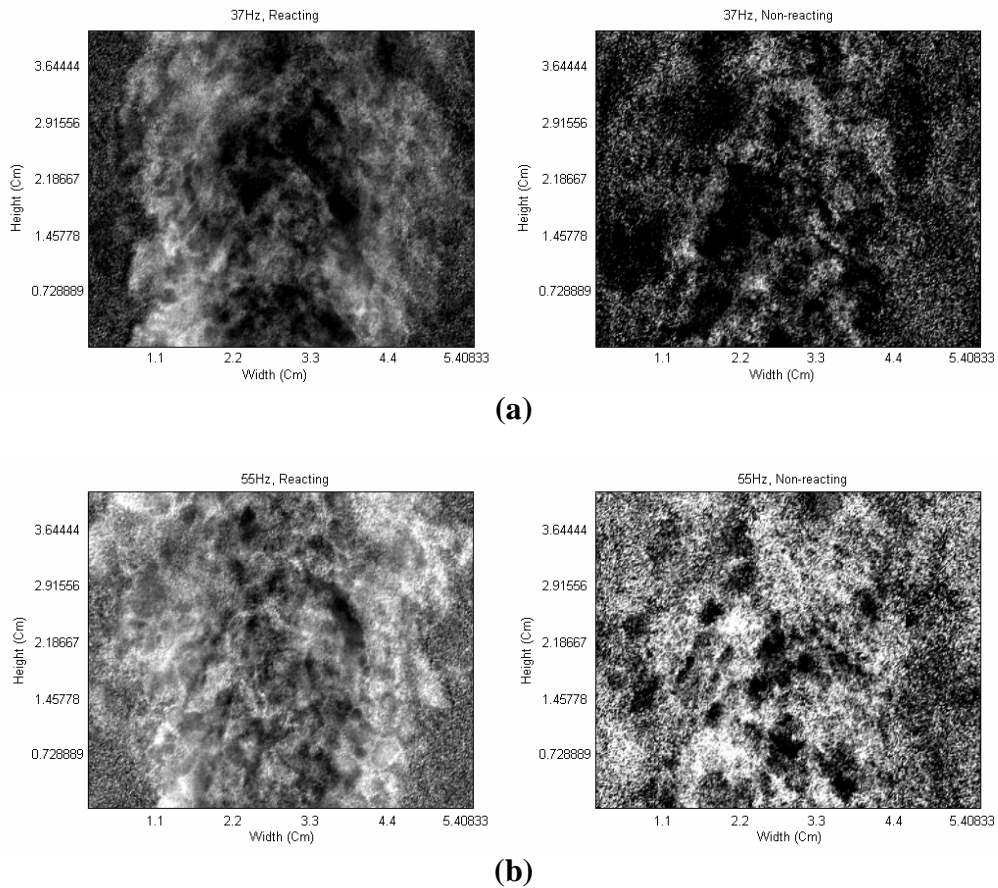


**Figure 3.10. Distribution of temporal unmixedness at 37Hz (a) and 55Hz (b).**

**Reacting (LHS) and non-reacting (RHS) cases. The color scheme is the same as in Figure 3.9, scaled to 0.2-0.6 (at the center of the cylindrical mixing region).**

In Figures 3.9 and 3.10, lighter shading indicates a region with a higher value of unmixedness, thus marking a region of high fuel concentration fluctuation. Further downstream from the eductor block (the ceramic burner block), the shear mixing zone widens to 30 – 80% (3.5 – 4.8 cm in LHS of Figures 3.8 and 3.9). The low temporal unmixedness in the core region, 0 – 30 % distance from the center (or 2.7 to 3.5 cm in the figures), is due to the high, and relatively uniform, fuel concentration. Cross sectional

views cut from Figures 3.9 and 3.10 at longitudinal distances of 1-3 cm from the burner block are shown in Figure 3.11.

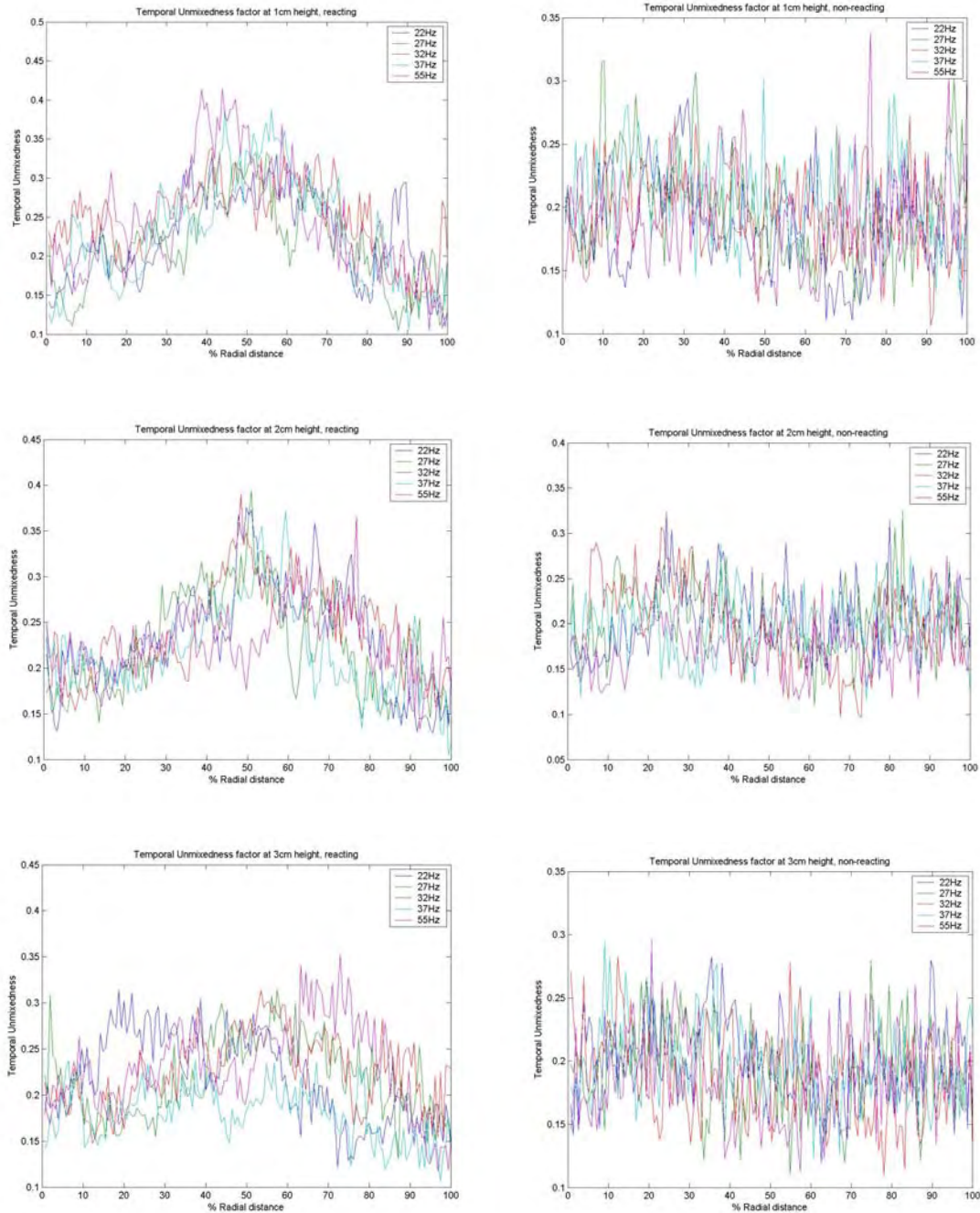


**Figure 3.11. Temporal Unmixedness factors with excitation at 1 (top), 2 (middle), 3 (bottom) above the eductor block. Reacting flow (LHS), and Non-reacting flow cases (RHS).**

Left hand side (LHS) of Figure of 3.11 shows the measured ‘Temporal Unmixedness’ for the reacting cases at three heights above the eductor block while the right hand side (RHS) figures show the distribution for non-reacting cases. There is little temporal variation of mixing in the non-reacting case in both the radial and vertical location. On the other hand, the LHS of Figure 3.11 shows a relatively strong peak at the center (radially) and a slow drop with increasing vertical location. This is, most likely, a direct result of buoyancy.

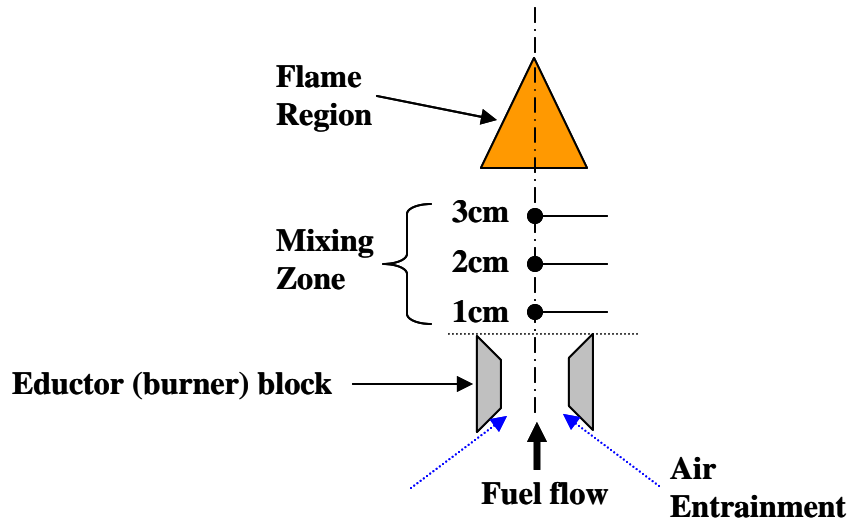
The reacting cases have a flow with significant post-reaction buoyancy, creating an enhanced vertical velocity component. This means that for the same vertical location, the reacting flow cases will resemble lower vertical locations (earlier times) in the non-reacting cases. This is evidenced by the fact that the non-reacting cases are mostly mixed by the time the flow reaches the imaging area while the reacting flows are still undergoing mixing. It also appears that the stabilizing presence of the flame (due to gas expansion) also slows the mixing process.

Qualitatively, while the fuel/air mixing keeps the same structure downstream, the measured gradients are less, that is, the degree of fluctuation in fuel/air mixing is decreasing downstream. In the core region close to the center, the variation is very small as expected from the results shown in Figures 3.8 to 3.10. This is because the fuel core region still consists mostly of fuel and most mixing occurs at the edges. This is most easily seen in Figures 3.12 to 3.14.

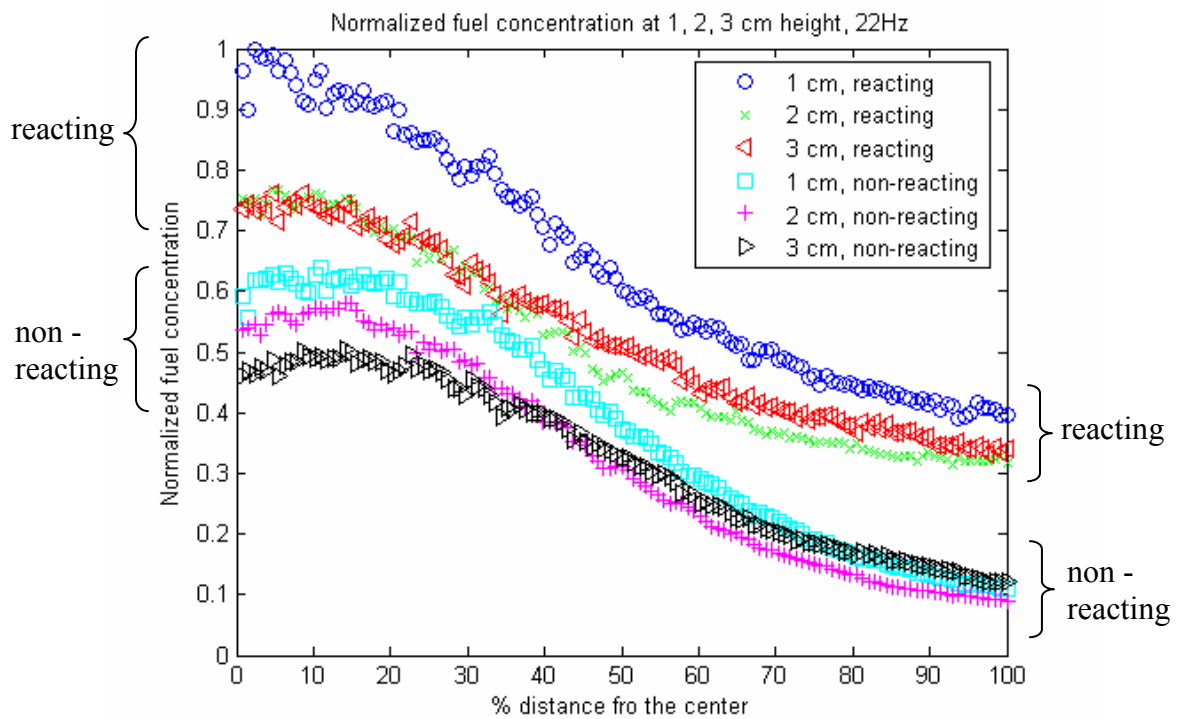
Figures 3.12 through 3.14 show fuel concentration distributions in that region at the same condition normalized by the maximum at each excitation frequency. As the flow goes

down stream, less fluctuation in the fuel/air mixing occur giving smaller unmixedness values in the outer flow region, 60-80% of the radial distance from center. It is evident that acoustic forcing has a weaker smaller impact on the mean methane concentration than does the presence of combustion. Both reacting and non-reacting cases show the flow self-similarity that would be expected of a simple jet.

Comparison between frequencies 22, 27Hz, and 32-55Hz show that the fuel concentrations at the higher frequencies (32-55Hz) are lower than the non-reacting cases. This means the fuel is better spread over the space in the reacting flow cases due, presumably, to the effect of acoustic excitations.



(a) Locations where the concentration is measured (not to scale)



(b) Fuel concentration distribution

Figure 3.12. The locations where the measurements are made (top), and (b) the fuel concentration distribution at 1, 2, 3 cm above the eductor block at 22 Hz.

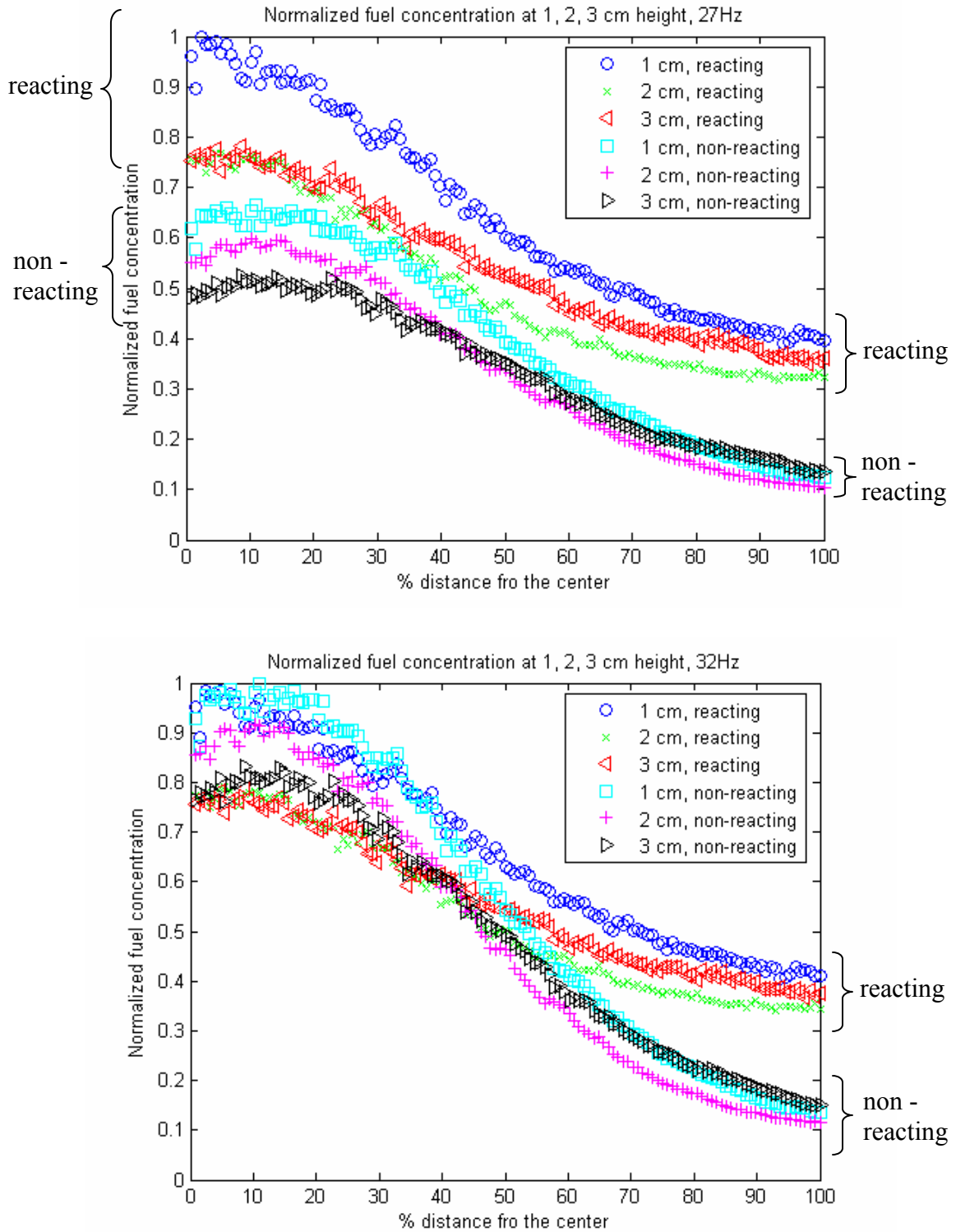


**Figure 3.13. The fuel concentration distribution at 1, 2, 3 cm above the eductor block at 27 Hz (top) and 32 Hz (bottom).**

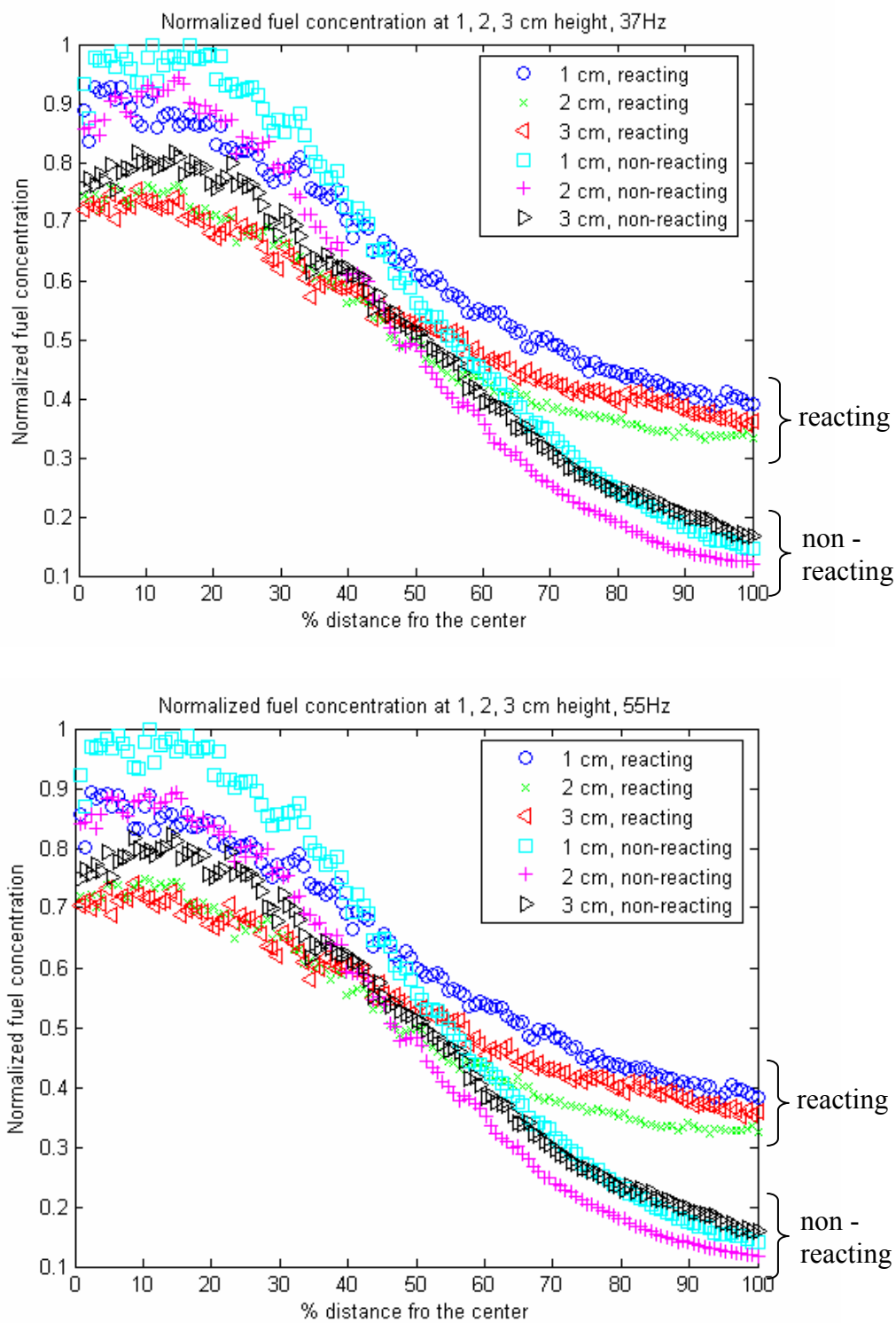


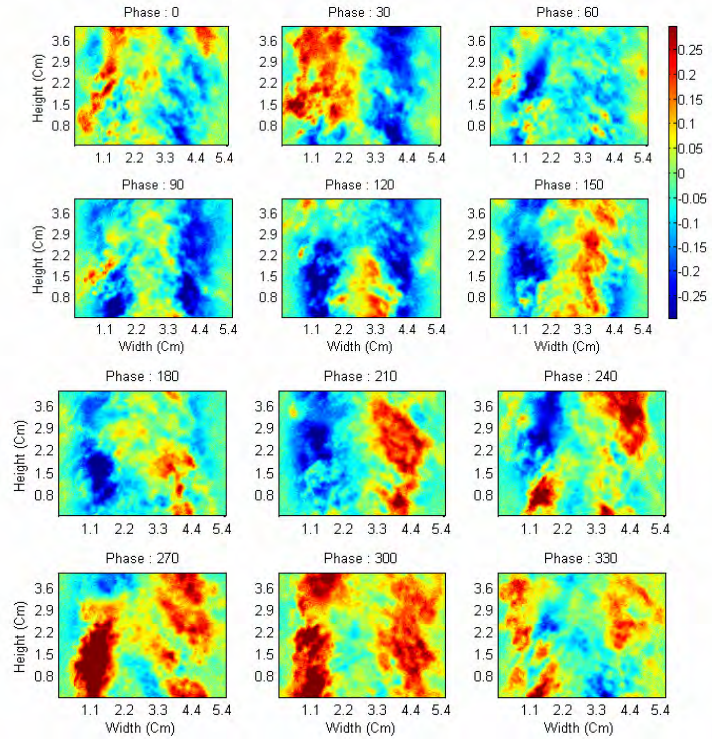
**Figure 3.14.** The fuel concentration distribution at 1, 2, 3 cm above the eductor block at 37Hz (top) and 55Hz (bottom).

### 3.4.2 Phase-Resolved Behavior of Mixing

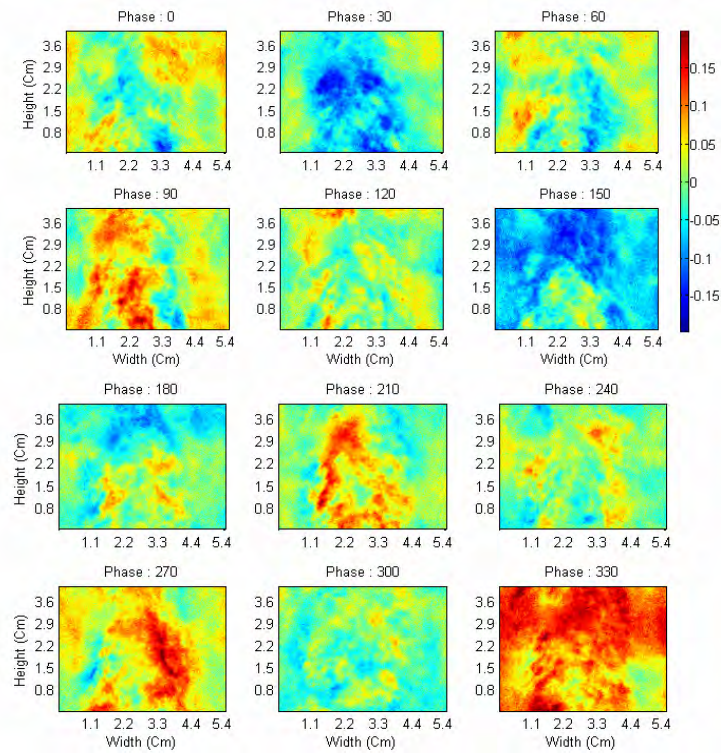
In this section, the phase-resolved behavior of mixing is presented. The term ‘phase-resolved’ means that the data presented have a resolution by phase thus it is possible to tell the differences in quantities behaviors by the phase in one cycle (e.g., 0 to 360 degrees). The resolution of the phase is 10 degrees in this work, and throughout the entire thesis work.

The global unmixedness here is defined by equation 3.1 above. As opposed to the definition for the temporal unmixedness factor that was used for the previous section (3.4.1) where the data are collected many times at one point, this time a 2-D image collapses to a single value by this definition. This measure of unmixedness gives ideas on how much mixing of fuel and air is occurring in the zone.

Figures 3.15 through 3.19 show the behaviors of fuel concentration distribution in the mixing zone. The data presented is one step right before the ‘unmixedness’-the degree of homogeneity in fuel/air mixing. For example, at 37 Hz (Figure 3.17), the reacting case, the highest overall fuel concentration occurs at the pressure node (0, 180 degree), then decreases subsequently through 30(210) and 60(240) degrees until the pressure anti-nodes (90, 270 degree). Here colors tagged with positive values indicate regions with higher than average fuel concentration (red and yellow), while the negative-valued contours indicate regions with lower than the average (dark and light blue). The domain size shown here is 55 mm by 41 mm. The values indicate the relative deviation of fuel concentration at that location from the mean fuel concentration over the entire imaged field. The phases are those of excitation acoustic oscillations.

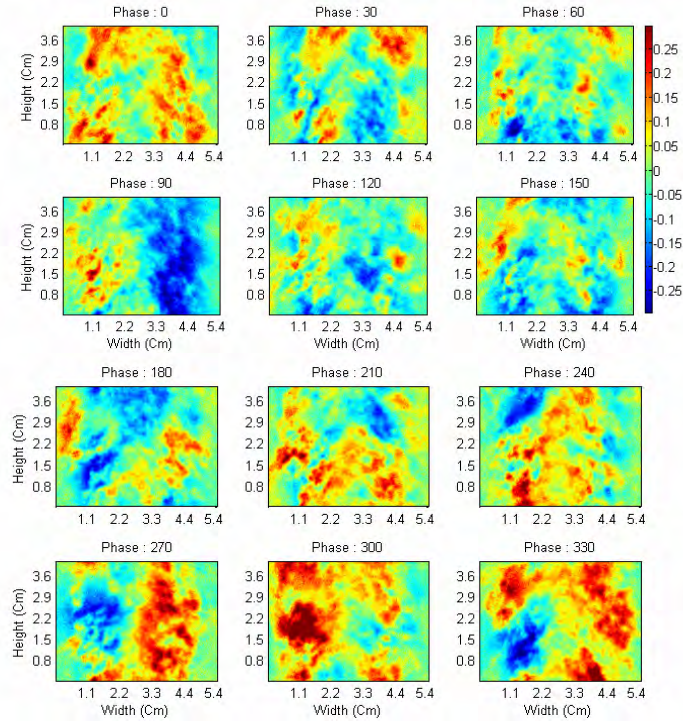


(a) Reacting flow

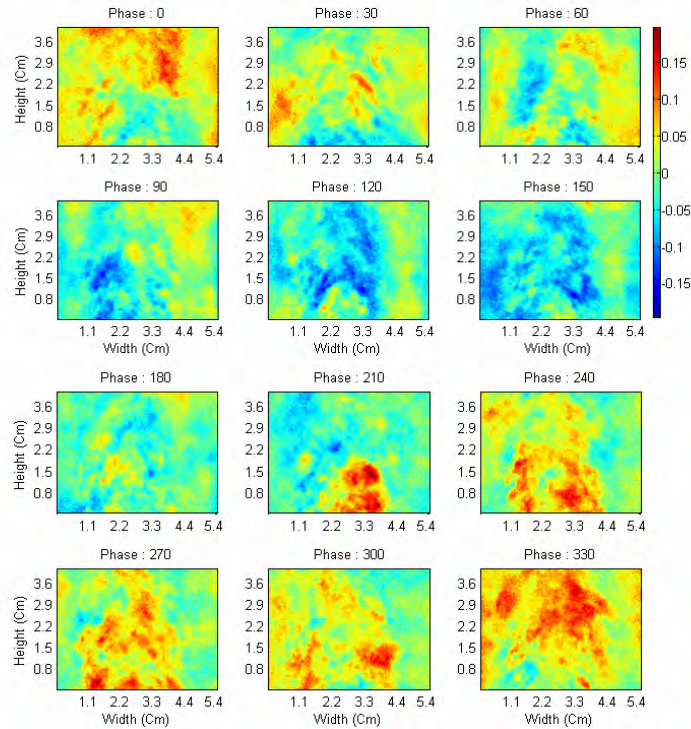


(b) Non-reacting flow

**Figure 3.15. Fuel concentration distribution by phase (0, 30, 60, 90, 120, 150, 180, 210, 240, 270, 300, 330 degrees). (a) Reacting, and (b) non-reacting flow cases at 22 Hz.**

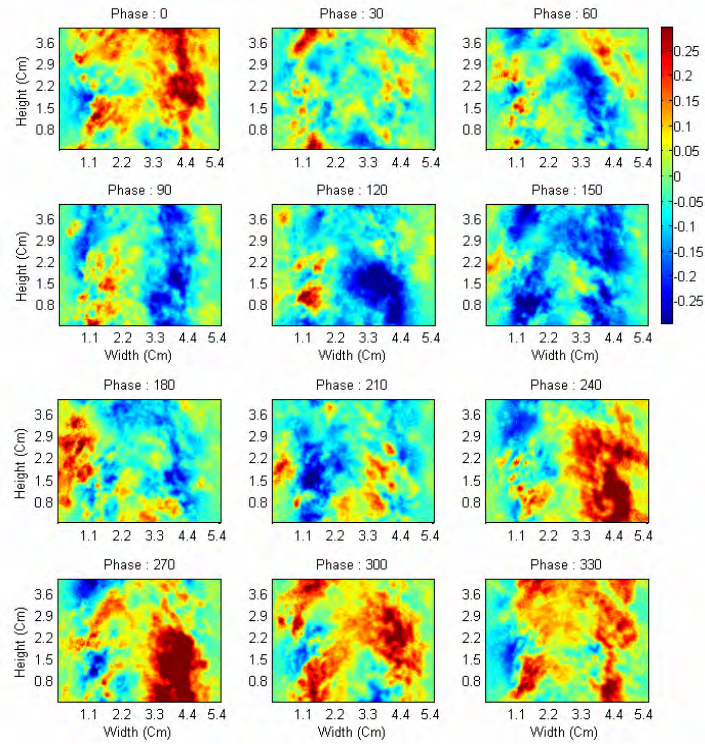


(a) Reacting flow

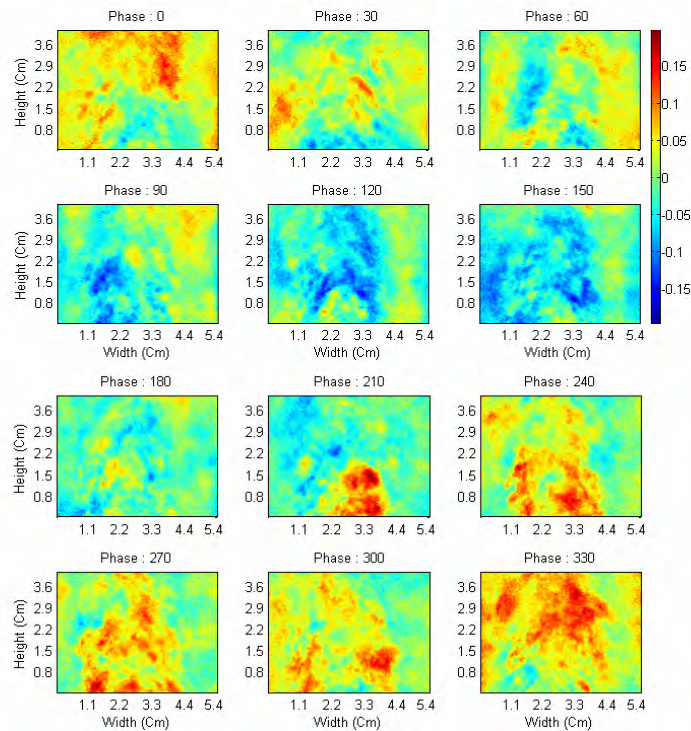


(b) Non-reacting flow

**Figure 3.16. Fuel concentration distribution by phase (0, 30, 60, 90, 120, 150, 180, 210, 240, 270, 300, 330 degrees). (a) Reacting, and (b) non-reacting flow cases at 27Hz.**

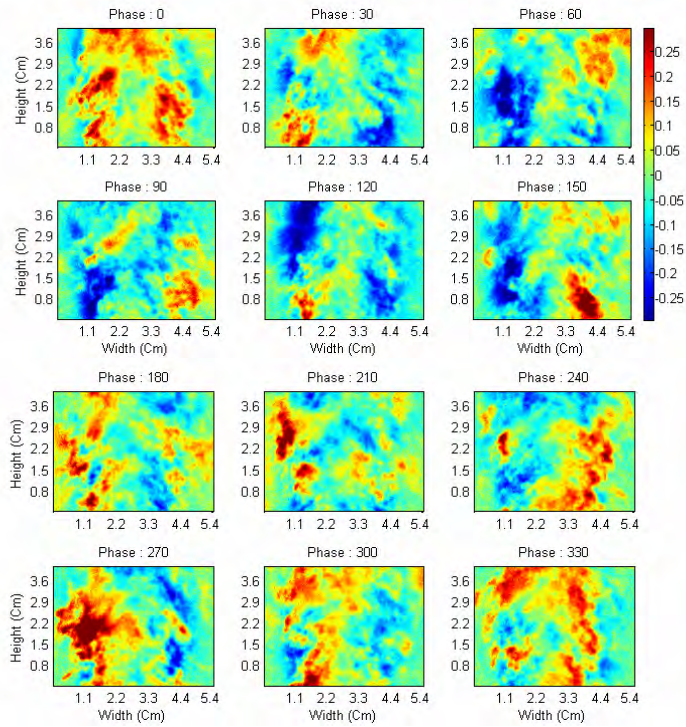


(a) Reacting flow

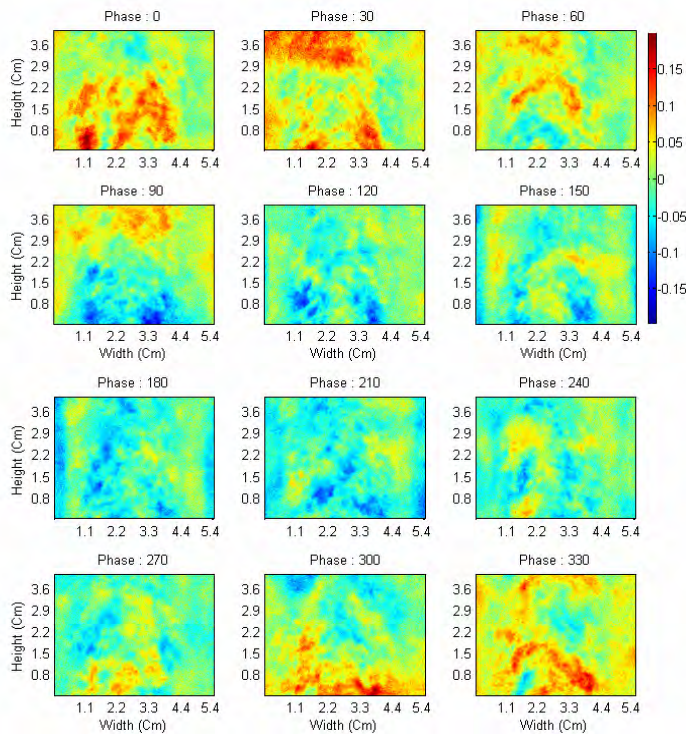


(b) Non-reacting flow

**Figure 3.17. Fuel concentration distribution by phase (0, 30, 60, 90, 120, 150, 180, 210, 240, 270, 300, 330 degrees). (a) Reacting, and (b) non-reacting flow cases at 32Hz.**

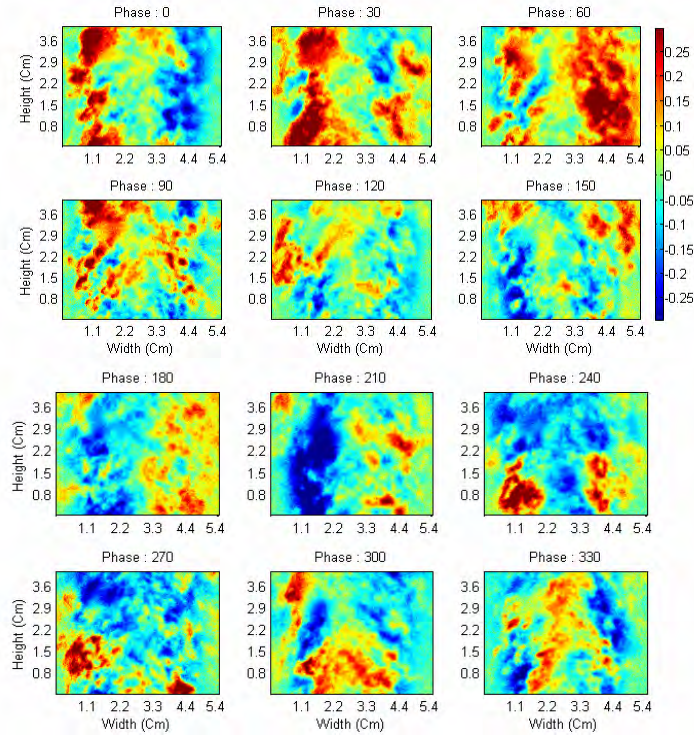


(a) Reacting flow

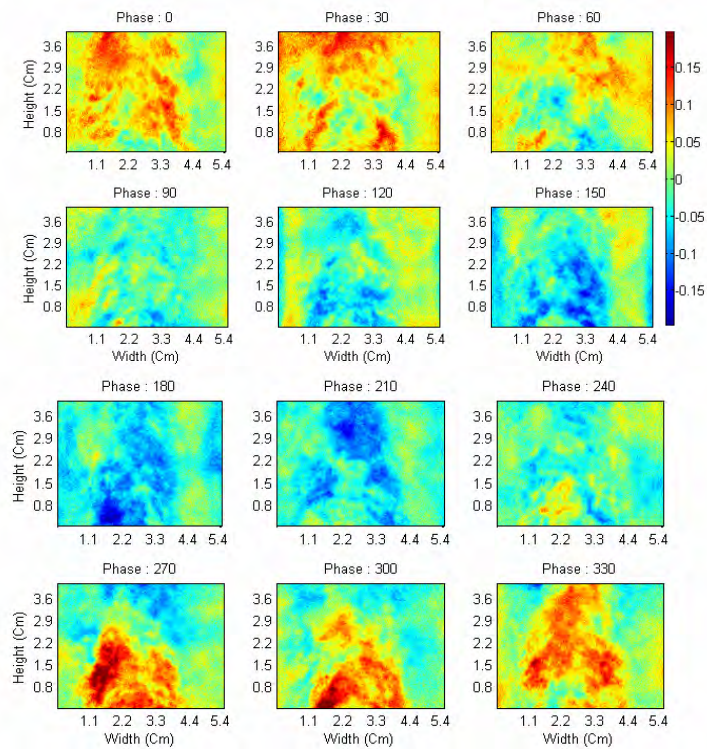


(b) Non-reacting flow

**Figure 3.18. Fuel concentration distribution by phase (0, 30, 60, 90, 120, 150, 180, 210, 240, 270, 300, 330 degrees). (a) Reacting, and (b) non-reacting flow cases at 37Hz**

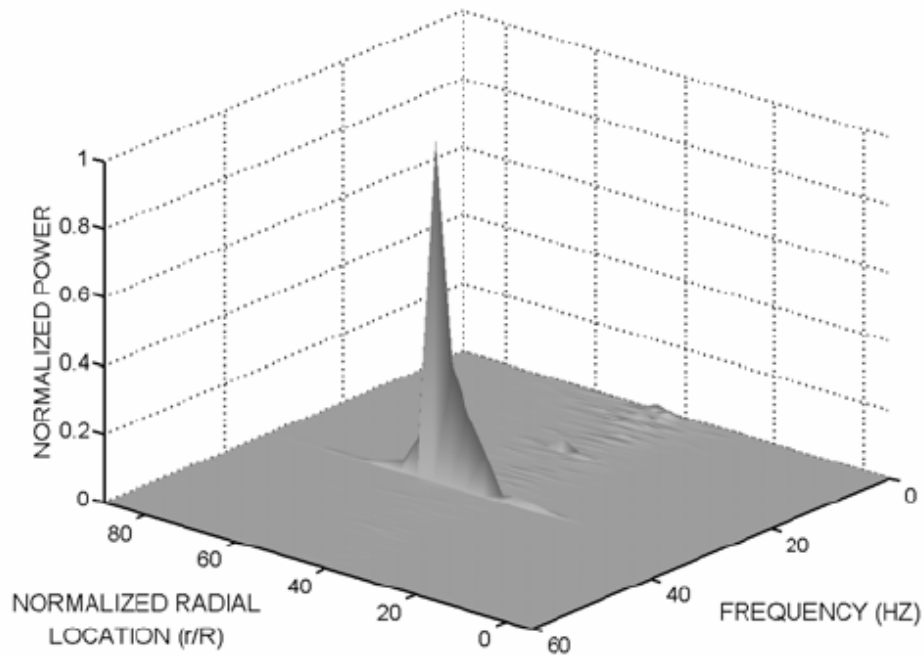


(a) Reacting flow



(b) Non-reacting flow

Figure 3.19. Fuel concentration distribution by phase (0, 30, 60, 90, 120, 150, 180, 210, 240, 270, 300, 330 degrees). (a) Reacting, and (b) non-reacting flow cases at 55Hz.



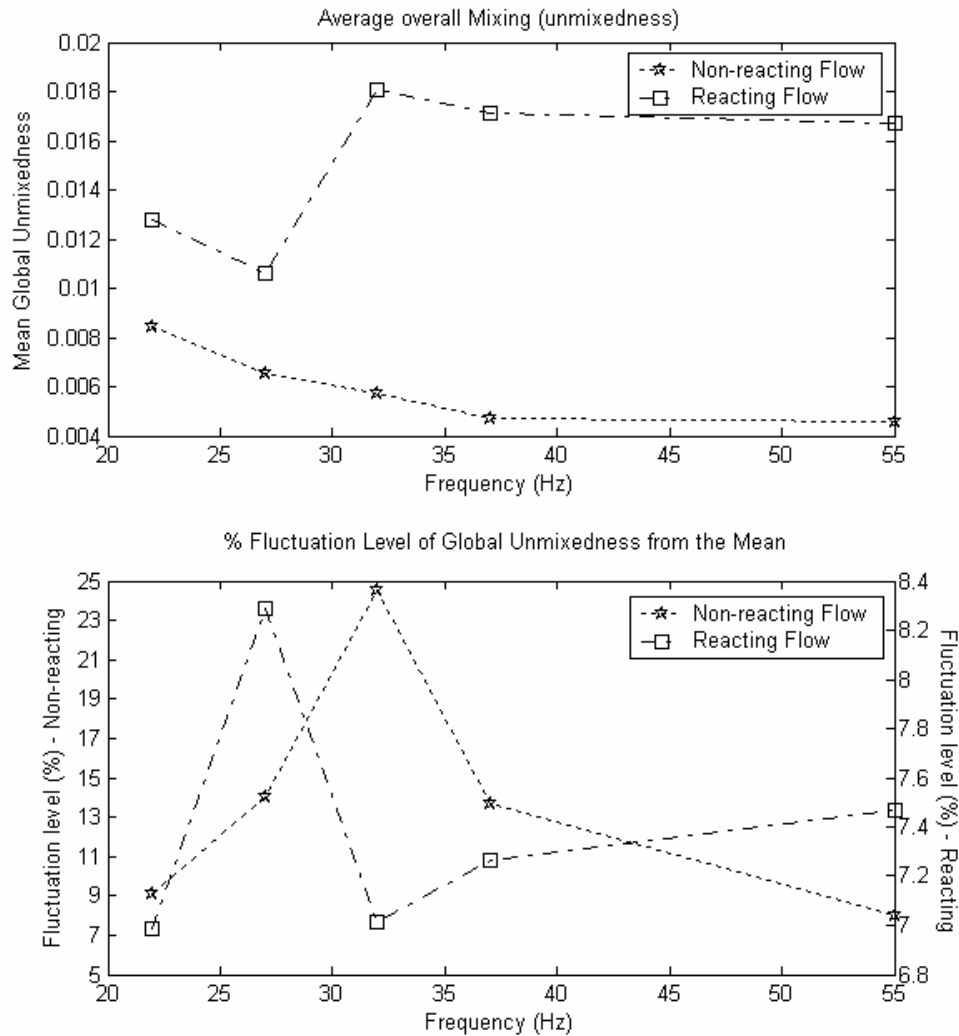
**Figure 3.20. Power density spectrum of fuel mixture fraction for 32Hz, reacting flow (from Fernandez et al. 2003).**

Figure 3.20 is a 3-D view of the power density spectrum; radial location versus the Fourier transforms of the time series data at each location versus intensity of each frequency at each radial location (Fernandez et al. 2003). The data was taken at the neck of the eductor block, upstream of the current imaging region. It is shown that there is a very strong peak in the mixture fraction oscillations in response to an imposed acoustic field which confirms the acoustics-induced mixture oscillations to be discussed later in this section in detail (see Figure 3.22). This particular plot is for a 32 Hz, reacting flow. Of particular interest is the very strong peak at 32 Hz, the driving frequency for this case. Similar peaks are evident in all of the acoustically forced cases, according to the authors

(Fernandez et al. 2003), corresponding to the driving frequency. This indicates that strong coupling occurs between the acoustic field and the mixing layer.

Also, since no strong frequency preference is seen in the outer portion of the flow, where the strong shear mixing occurs (Figure 3.9 and 3.10), the coupling is not a strong function of the vortex shedding from the nozzle tip or the shear mixing in the mixing zone. The vortices are expected to be larger in size and play a role in producing oscillations in the local equivalence ratio in the outer flow region (along the boundary of the mixing and flame zones).

Figure 3.21 shows the behavior of mixing under each imposed acoustic oscillation. The presence of a flame makes a great difference in the degree of mixing. Its behavior is such that the role of combustion process in causing far less efficient mixing is observed from the comparison with the non-reacting case, where the only difference is the presence of flame. While the fuel/air mixing for the non-reacting cases show decreasing unmixedness, or enhanced mixing, with increasing frequency of imposed acoustic oscillations, the mixing for reacting cases worsens stepping up between 27 and 32 Hz. Here, the comparison between figures top and bottom show that the fluctuation level is related to the average overall unmixedness in the field for reacting flows. For the non-reacting cases, the level of fluctuation peaks at 32 Hz while the overall mixing tends to get better monotonously. The level of fluctuation in mixing is affected by the excitation frequency, but this is not directly related to the overall average mixing in the entire field for the non-reacting cases.



**Figure 3.21. Response of fuel/air mixing to the imposed acoustic oscillations : average of unmixedness (top), and relative fluctuation amplitudes (bottom) at each frequency.**

The absolute amplitudes of fluctuations are greater for reacting cases than non-reacting cases (see Figure 3.22) though their relative magnitudes (%) give greater values for the non-reacting cases due to the normalization.

While combustion process has a great effect on the mixing behavior, mixing is also affected by the phase of excitation. The phase dependence of the mixing behavior is

presented in Figure 3.22 which shows the oscillatory behavior of mixing at frequencies of 22, 27, 32, 37 and 55 Hz, with (left) and without (right) the flame. The sine waves in bold lines correspond to the imposed acoustic waves. Acoustic waves, assumed to be in pure single-frequency sine wave form, are used as the reference for determining the phase of the data collected and represented in bold lines in Figure 3.22.

Examining the trend, measurements show quite clearly that the mixture fraction oscillates at the same frequency as the acoustic driving frequency. This suggests either that both the mixture fraction oscillations and the flame oscillations are coupled directly to the acoustic forcing, or that the system has three-way coupling where, in addition to the acoustic coupling, the presence of oscillation in mixture fraction induces oscillations in the flame and/or oscillations in the flame induce or enhance mixture fraction oscillations. Lieuwen et al. (1998, 2001) argues that the oscillations in local mixing induce or strengthen oscillatory behavior in flame burning, as is seen here.

Conversely, the non-reacting flow cases show weaker mixture fraction oscillations than the reacting cases, implying that flame oscillations magnify the mixture fraction oscillations. This would imply a bi-directional coupling. It must be noted that, in this work, there are clear limitation in being able to compare to or support Lieuwen's conclusions. In this work, the oscillatory fuel/air mixing is not the input variable being modulated as it is in Lieuwen's work but is another output, just as the flame behavior, resulting from the imposed acoustic excitation.

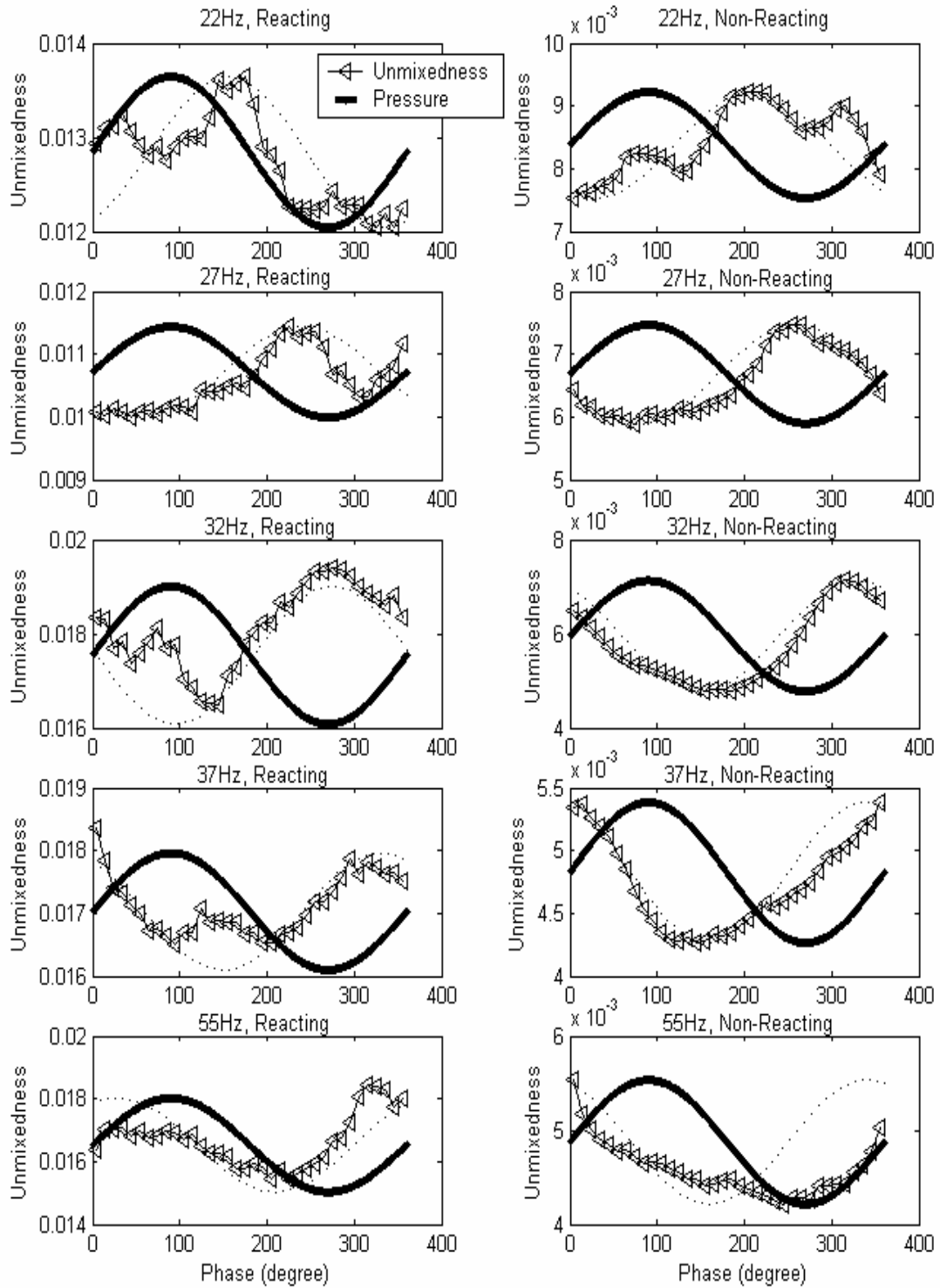


**Figure 3.22. Oscillatory behaviors of global mixing presented with reference acoustic wave.**

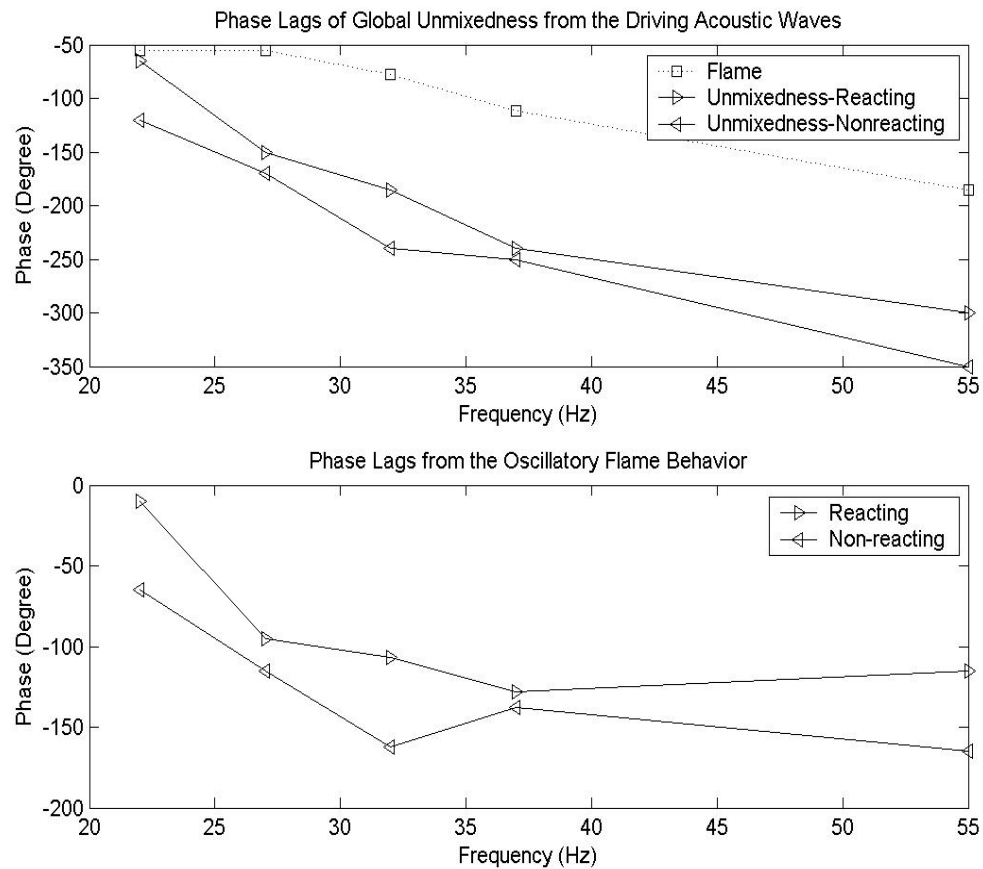


**Figure 3.23. Comparison of phase shifts of mixing and flame (Pun et al. 03) behaviors. Phase shift from the driving acoustic wave (top); from the oscillations in flame (bottom).**

Figure 3.23 shows a comparison of the phase shifts between the flame, the mixture fraction in reacting and non-reacting cases. There is a clear phase differences between reacting and non-reacting flow cases but the phase change with driving frequency follows the same trend for all three variables. When the differences in phase behavior between the flame and the mixture fraction are examined, especially at frequencies 27-55Hz (for reacting flow cases only), the phase difference is consistently 100-120 degrees (lagging)

or, 240-260 degrees (leading). It is not clear, at this point, why the phase differences are so consistent. Such uniformity with varying frequency implies a chemical time-scale that is independent of driving frequency, but nothing can be concluded without further investigation.

Phase lag also means that there exists time lag between oscillations in the flame region and the mixing region. Figure 3.24 (top) shows schematically the way time lags exist. Measured time lags are presented in the bottom of Figure 3.24. These are the delay between the fuel/air mixture fraction oscillations and the heat release rate oscillations. In this figure by Lieuwen et al (2001), the mixture fraction oscillation in the present work corresponds to  $\phi$ , the overall equivalence ratio, fluctuation at flame base.

It should be noted, however, that the measurements of mixing were not made in the same region where the combustion actually occurs, but in the region upstream of the flame due to the uncertainties in acetone fluorescence signal caused by high temperature in the flame region. These measured values of time lags are, thus, to be corrected by the travel time of fuel/air mixture stream between the mixing region and the flame region. But these processes actually need accurate measurements of the flow field using, for example, LDV or PIV methods.

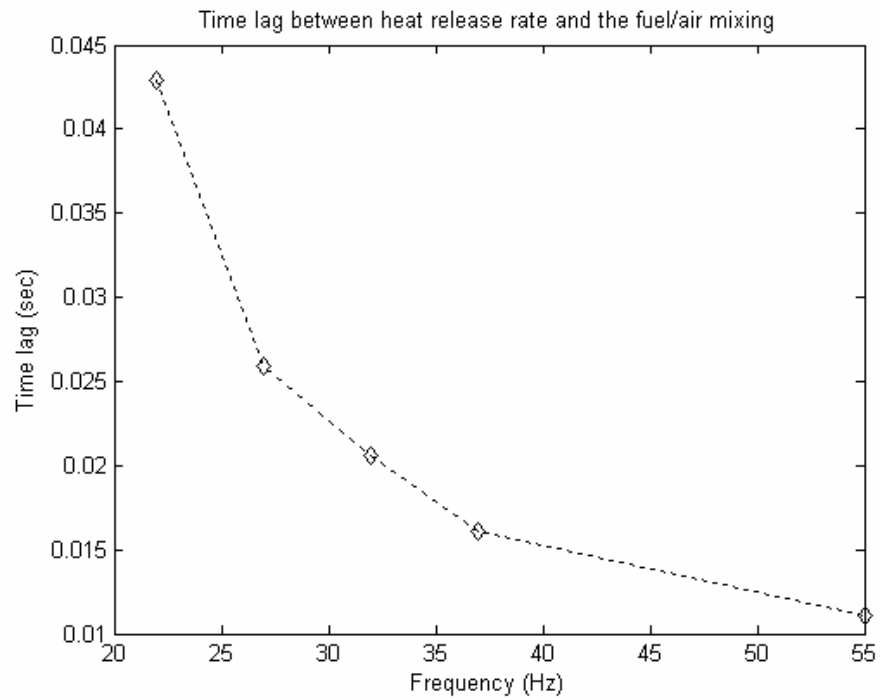
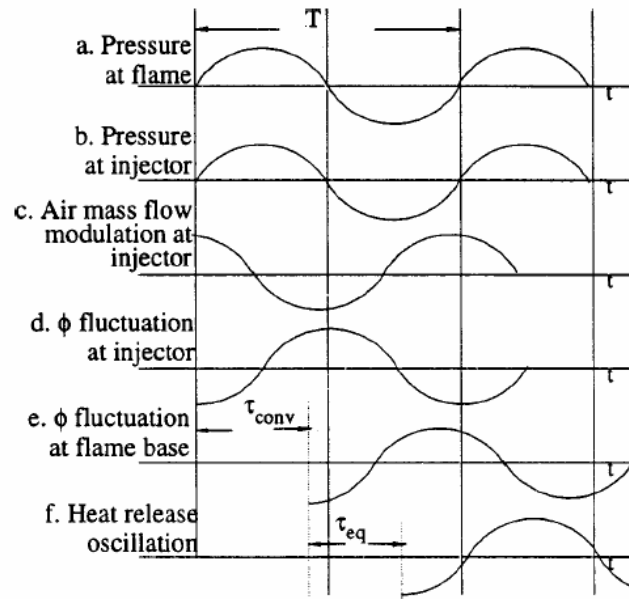
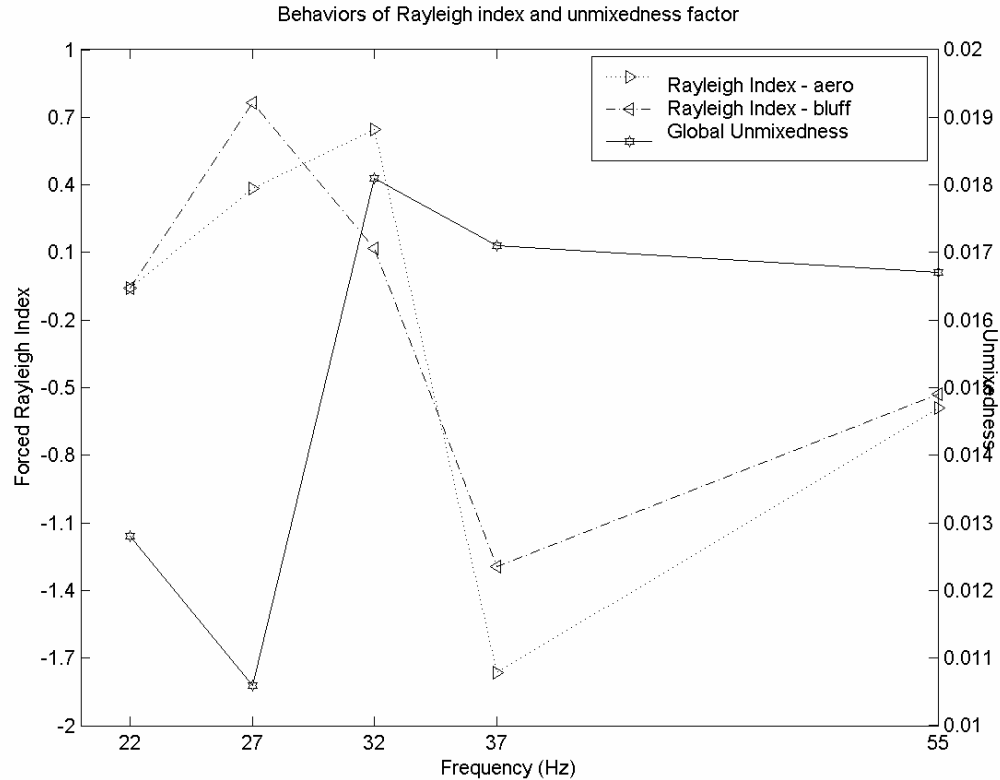


Figure 3.24. Time lags (top, Lieuwen et al. 2001) and measurements (bottom).



**Figure 3.25. Relationship between changes in mixing behaviors and flame response: Unmixedness factors & Rayleigh Indices.**

As mentioned above describing figure 3.21, the average overall unmixedness values and the fluctuation magnitudes of them have reverse relationship. In Figures 3.25 and 21, they are collated with the tendencies of Rayleigh indices at each of the frequencies. Here the aerodynamically stabilized burner (aero) is the same burner used for the current work, and the bluff-body stabilized burner (bluff) is a burner very similar to the ‘aero’ type burner with slight differences in geometry which was proven to be a bit more stable to the acoustic oscillations according to Pun et al. (2003).

Figure 3.25 shows that the global unmixedness behaves in opposite way as those of Rayleigh indices. The higher the unmixedness values, the less the mixing process is. Or,

the better the mixing occurs, the lower the unmixedness factors are. Figure 3.25 clearly shows that the acoustic wave gets amplified (positive values of Rayleigh index) for better global mixing while they tend to get damped for less effective mixing (negative Rayleigh index).

The behavior of fluctuation level shows more clearly that their behaviors agree such that, for instance, at frequencies where better mixing occurs with lower fluctuation level in mixing there are greater tendencies for amplifying the acoustic wave, and vice versa.

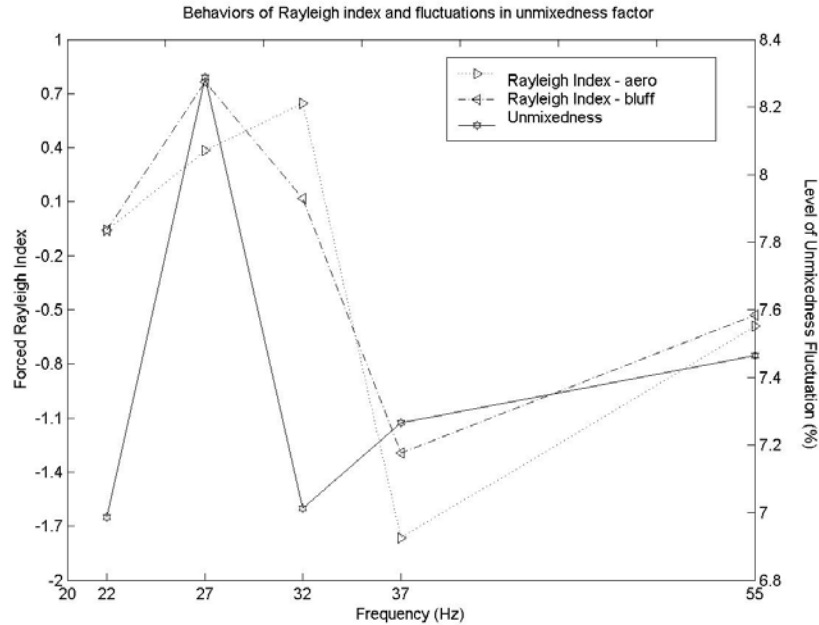


**Figure 3.26. Relationship between changes in mixing behaviors and flame response: fluctuations in mixing & Rayleigh Indices.**

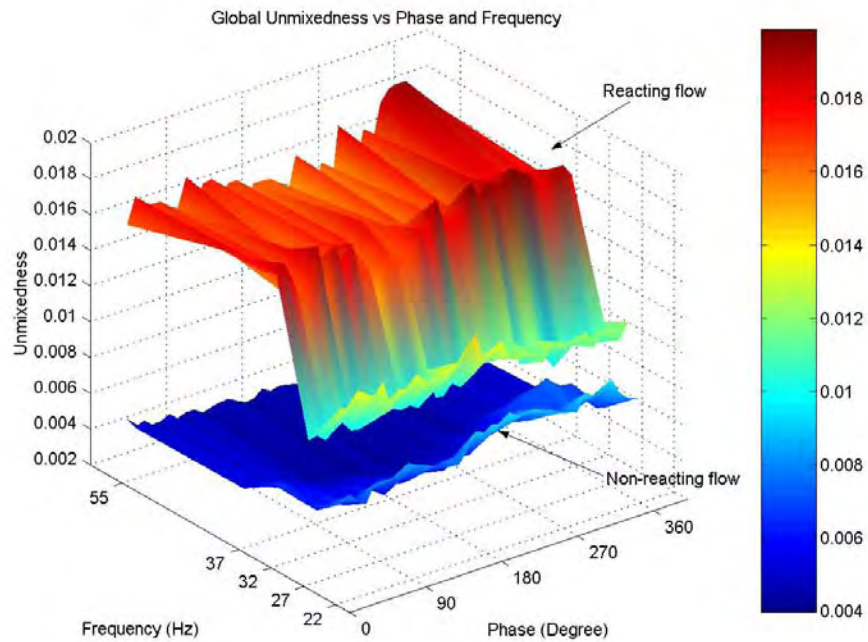


**Figure 3.27. 3-D representation of global unmixedness vs. excitation frequency and phase.**

The global unmixedness is plotted versus excitation frequency and phase during a cycle of excitation at each frequency in Figure 3.27. Much less effective mixing in terms of global unmixedness is observed in the presence of flame. Also the mixing at higher frequencies (32 ~ 55Hz) is much more affected by the presence of flame than at lower frequencies (22, 27Hz).

According to Figure 3.27, the combustion process alone causes large differences in the degree of mixing, lifting the unmixedness values up to a factor of 3 of those for the unexcited case. The increase in unmixedness with frequency for the reacting flow case seems to be due to interaction between the combustion process and the acoustic excitation; it is obvious when compared to the non-reacting case where the tendency is just the opposite.

Direct comparison of the curve shapes clearly shows that in reacting flow cases, the mixing fluctuates at higher frequencies than the imposed acoustic oscillations while still oscillating mainly at the imposed frequencies. On the other hand, non-reacting flow cases show only the oscillations at the imposed acoustic frequencies. Differences in the mixing behavior are caused by the thermo-acoustic coupling. The flame behavior is, in turn, expected to be affected by fluctuations in the mixing, or fluctuations in the equivalence ratio, in the mixing zone.

### **3.5 Summary**

Mixing is a significant factor in causing unstable combustion in systems that operate in a non-premixed or partially premixed combustion configuration and where the mixing occurs in the combustion chamber. The onset of unstable combustion for these systems is due very much in part to the presence of mixture fraction oscillations which are in turn the result of chamber acoustic oscillations.

The importance of the study of mixing lies, also, in the fact that many of the current approaches of active control schemes use the partial premixing as a means to actuate the combustion system. For example, high frequency valves imposing oscillations in the fuel injection in the main or secondary fuel feeding lines, and acoustic forcing from behind the fuel feeding line are used to modulate the fuel flow rate and overall equivalence ratio or degree of mixing (e.g., Cohen, 2001). So it would be important to understand how the dynamic behavior of mixing is related to the combustion dynamics because the flame behavior ( $Ra$ ) is closely related to the fluctuations in mixing. This work also provides a

set of observations of the behavior of the ‘modulated’ or disturbed fuel/air mixing due to the acoustic excitations.

The temporal unmixedness pattern reveals the breakdown of fuel/air distribution structure. It is shown that the breakdown of fuel concentration distribution is slower in the reacting flow cases, because of the flow field affected by the buoyancy of the hot product gases resulting in higher uncertainties in the mixing zone. The mean flow patterns keep the same structure downstream of the mixing region and as the flow progresses downstream, subsequent mixing reduces the variation in the distribution of fuel/air mixing.

Compared to the mixing in non-reacting flow cases, the reacting flow cases show thermo-acoustically and fluid dynamically coupled behaviors. It was found that less effective mixing occurs in the presence of flame. And the degree of mixing is affected by excitation frequency and the responses to each frequency differ from each other. The presence of a flame intensifies the oscillations present in the mixing zone. The heat release and induced buoyancy produced by the combustion process also play important roles in enhancing acoustic field-mixture fraction coupling. The increase in unmixedness with frequency for the reacting flow case seems to be caused by the interaction between the combustion process and the acoustic excitation, and it seems more plausible when compared to the non-reacting case where the tendency is actually in the opposite direction.

The acoustic-wave-induced oscillations in the overall mixing were clearly evident at all driving frequencies (22-55 Hz). The fluctuation in unmixedness means the fluctuations

in the degree of mixing. The result shows that there exists a very close resemblance between the relative amplitude of mixing fluctuation in the mixing zone and the Rayleigh index in the flame zone in their dependences on excitation frequencies. The greater average unmixedness and the fluctuation in its magnitude in the mixing zone occur at the same driving frequency as where the Rayleigh index is positive, and vice versa. This means that thermo-acoustic coupling (the Rayleigh index) and the degree of mixing (unmixedness) are strong functions of the excitation frequencies, and that the modulations imposed on the degree of mixing causes fluctuations in thermo-acoustic coupling. One can intuitively expect this phenomenon from the reasoning that the fluctuations in local degree of mixing cause fluctuating flame surface area, which is directly related to the heat release rate. A practically wide range of data, when completed, will give a good idea how the 'actuation' through fuel flow modulation should be directed.

Any unsteadiness in the process of combustion can be a source of sound, generating pressure and velocity fluctuations (Dowling 2000). When the sound waves are self-sustained by thermo-acoustic coupling inside combustors and gets positive feedback from the oscillating heat release rates, this leads to the growth of wave amplitudes leading to combustion instabilities. Mixing as shown in the present work can be a source of these instabilities. Also, a thorough study of the behavior of mixing will be beneficial for developing better actuation schemes for the efforts directed to the active control of combustion instabilities.

# Chapter 4

## Measurements of the Combustion

### Dynamics of a Swirl-Stabilized Burner

---

The global and local distribution of Rayleigh index, introduced in Appendix B, and the response functions are the main parameters to quantify and describe the combustion dynamics. The Rayleigh index quantifies the thermo-acoustic coupling, the interaction between the flame and acoustic waves, while the response function gives a measure of the system's reaction and the degree of sensitivity to outside disturbances. In this chapter, measurements of the thermo-acoustic coupling and flame responses are presented for a low-swirl burner, typical of new designs for the gas turbine industry. The purpose of the use of a swirl-stabilized burner is to extend the understanding developed in previous efforts (Pun et al. 2003) to more geometries, and in general to produce a clearer picture of the relevant dynamics. Higher driving frequencies (up to 400Hz) provide the basis for better understanding across a wider range of the system's operation. The use of the swirl burner also gives greater insight into the practical applicability of the methodology demonstrated.

## 4.1 Purpose

The objective of this part of the work is to determine the global and local values of the fluctuations of energy release rate with the use of OH Planar Laser-Induce Fluorescence (PLIF), and to demonstrate the experimental methodology. The measurements will provide the basis for constructing a model of the source term  $\dot{Q}'$  in equations developed in the Appendix B, a primary parameter of combustion dynamics. By 'primary parameter', it is meant that  $\dot{Q}'$  appears as a source of unsteady motions in the equations for flow in a combustor and therefore can be given a direct physical interpretation for a particular problem being considered. An accurate representation of  $\dot{Q}'$  is essential to understanding the presence of combustion instabilities, and accordingly how they can be either avoided or eliminated in practical systems. In general,  $\dot{Q}'$  must be known to analyze any problem of combustor dynamics (Culick, AFSOR final report, 2004).

Also, the behaviors of flames at different equivalence ratios are compared. Three different equivalence ratios, (0.5, 0.6, and 0.75) were used, which correspond to leaner, desired, and richer operation conditions for the swirl burner respectively. All three values of equivalence ratio are within the range.

The present work is based on the OH-PLIF measurement technique to image the flame region, to give phase-resolved flame behavior at each frequency with good spatial resolution. The response of the flame to the imposed acoustic field over the range of 22 – 400 Hz is then determined to provide data that is expected to serve as a starting point for combustion system designs, and for numerical estimations of combustor behavior up to

the higher practical levels (~5,000 Hz). OH-PLIF is expected to give the best temporal and spatial signal resolution at the present time, especially in comparison with the chemiluminescence technique (Pun, et al. 2003). In this work, the intensity of the OH-PLIF signal is considered linearly proportional to the amount of local/global heat release rate.

## 4.2 The Thermo-Acoustic Coupling

The main parameter to be considered is the Rayleigh index, a measure of energy transfer from the energy release by combustion process to the acoustics. Appendix B covers the main concepts and procedure for the derivation of this quantity. A simplified relation is obtained by further manipulations following Culick (1987):

$$(4.1) \quad \Delta E = \frac{\gamma - 1}{\gamma} \int dV \int_t^{t+\tau_n} \frac{p'}{\bar{p}} Q' d\tilde{t} ,$$

that is analogous to equation (B.34).

Following Pun et al. (2003), the forced Rayleigh index ( $R_f$ ) is obtained, eliminating dependence on specific gas composition. This involves normalization in time (t) by the corresponding the period ( $\tau_n$ ) for each excitation acoustic wave to give the non-dimensionalized time  $\xi$  ( $\xi \equiv t/\tau_n$ ):

$$(4.2a) \quad R_f = \int_0^1 \frac{p' q'}{p_{rms} \bar{q}} d\xi ,$$

where  $\xi$  is the non-dimensionalized time of a period of oscillations. In this work, the Rayleigh index is calculated using the following formula:

$$(4.2b) \quad \hat{R}_f = \frac{1}{36 \cdot p_{rms} \bar{q}} \sum_{bin=1}^{36} p'_{bin} q'_{bin} ,$$

where

$$(4.2c) \quad p'_{bin} = p_{bin} - p_{rms} , \text{ and } q'_{bin} = q_{bin} - \bar{q} .$$

Here, ‘bin’ indicate the phase bin, according to which the images are collected and processed;  $p_{bin}$  and  $q_{bin}$  are mean pressure and heat release rate in each phase bin.

The Rayleigh index is usually calculated in an indirect manner by means of chemiluminescence, or PLIF of OH or CH. Approximately, the radiation intensities from flame areas are proportional to the heat release rate. Of course, the proportionality differs with the method. For example, in chemiluminescence, the radiation intensity and the heat release rate have a linear relation (Pun et. al. 2002). However, it was shown Pun (2001) in his dissertation that the chemiluminescence technique is inferior to PLIF due to the integrated view of the control volume that smears the heat release distribution.

Perturbations (or outside disturbances) are emulated in various ways. Typically, actuators such as loudspeakers are used to excite the entire flow field (combustor) (Pun *et al* 2000, 2002; Chen *et al* 1993; Lawn, 2000; Paschereit *et al* 2000); or fuel injection is perturbed either by oscillating the mixture ratio in a diffusion flame (Sivasegaram *et al* 1995; Richards *et al* 1997; Papas *et al* 1999; Venkataraman *et al* 1999), or by oscillating the fuel/air mixture flow rate in premixed flames (Hantschk *et al* 2002). Vortex shedding inside swirl-stabilized combustors causes natural excitation of flames (Cadou *et al* 1998; Dowling 2000). In the present chapter, actuation by a pair of loudspeakers is used as illustrated in Figure 3.1.

### 4.3 OH PLIF

The greatest advantage to using laser-based measurements is the ability to provide non-intrusive, *in situ* measurements. The introduction of a physical probe will inevitably alter the flow-field, preventing precise measurements and sometimes even affecting the flow physics. Another difficulty is the survivability of a physical probe in a high temperature, high pressure combustion environment. The flexibility of laser-based techniques includes the capability of spreading the laser beam into a sheet. Planar laser-induced fluorescence (PLIF) can then be performed, yielding species information as a 2-D planar image, as opposed to LIF that resolves only a single point with each pulse. PLIF and LIF share the same physical principle, and actually the only difference lies in the fact that LIF is a point-wise measurement using a focused laser beam, while the laser beam is widened in height to give spatial resolution for PLIF. This technique has been used to measure a variety of chemical species in unsteady reacting flows, including OH as a measure of the heat release (Cadou *et al.* 1991; and Shih *et al.* 1996), and NO seeded fuel to measure the temperature field (Cadou *et al.* 1998). The first demonstration of 2D (planar) LIF of the hydroxyl radical in a flame was performed by Dyer and Crosley (1982).

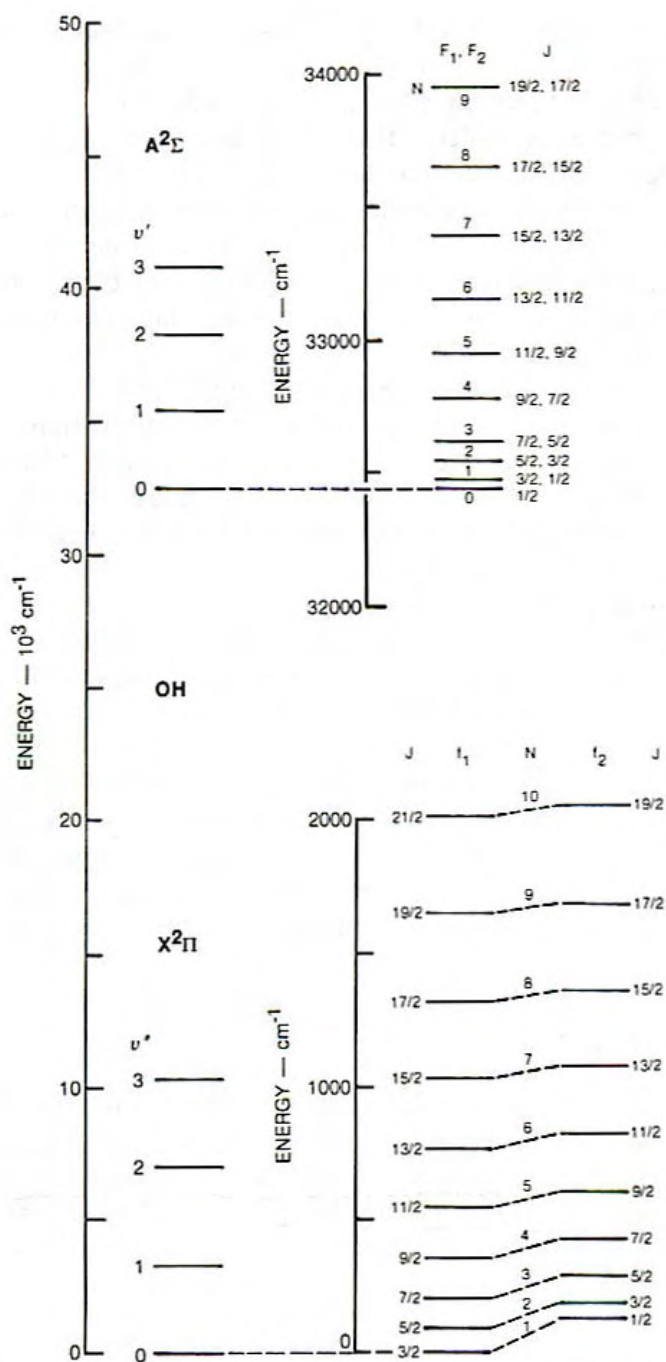
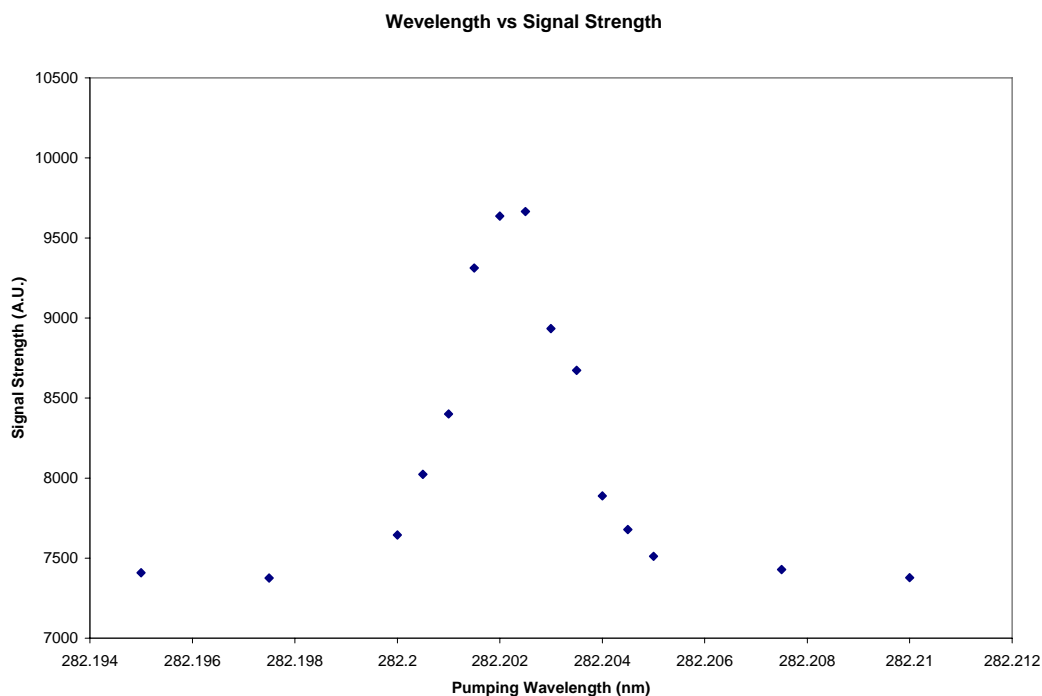
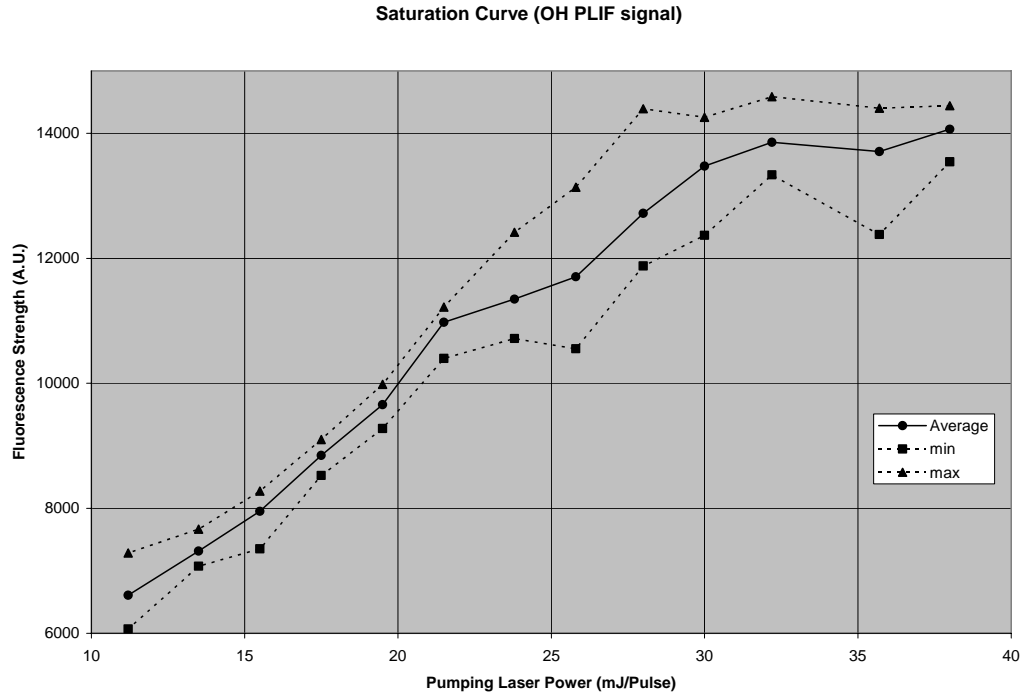


Figure 4.1. Energy levels of Hydroxyl radical (Eckbreth 1996).

Energy levels of the OH radical are shown in Figure 4.1. Based on this structure we know that to excite the hydroxyl radicals using the A-X (1,0) band will require a laser beam with wave number approximately  $36,000\text{ cm}^{-1}$ , which corresponds to around 280 nm. Since the absorption peak is narrow, wavelength scanning is required to find the absorption peak for this band in the vicinity of 280 nm. As shown in Figure 4.2, a peak appears in the emission spectrum, and in this case, 282.202 nm seems to be the right location to excite. The expected fluorescence signal is to be distributed in the range 300-320nm.



**Figure 4.2. The pumping laser scanning for (1,0) band of OH excitation.**



**Figure 4.3. Saturation of LIF signal to avoid the signal quenching.**

Figure 4.3 demonstrates the signal saturation dealt with in Chapter 2. In the current experimental configuration, the energy of the laser is 35 mJ/pulse with the imaging region 8.9 cm by 8.9 cm. The resolution of the images is 174  $\mu\text{m}$  by 174  $\mu\text{m}$ .

## 4.4 Experimental Configurations

The chamber and acoustics, the laser system, the data acquisition, the ICCD camera, and the control system are the same as described in Chapter 2 and 3. So here, only the distinctive features are noted and introduced.

### 4.4.1 Laser System for OH PLIF

The PLIF system is based on an Nd:YAG laser (Continuum Powerlite 9010) operating at 10 Hz, pumping a tunable dye laser (Continuum ND6000), which in turn drives a mixer/doubler system. The 532 nm beam pumps the dye laser, while excess energy at 1064 nm (energy not converted to 532 nm) is passed through a delay line. The mixer/doubler system was custom designed in cooperation with Dr. Sheng Wu of U-oplaz Technologies, for optimal energy conversion by special tuning of the BBO crystals (Wu et. al., 2000). Use of Rhodamine 590 for the dye laser in methanol optimizes conversion efficiency near 564 nm (~ 190 mJ/pulse), which is then doubled to approximately 282 nm to excite the A-X (1,0) band of OH (Dieke and Crosswhite, 1962). Energy in the vicinity of 35 mJ/pulse is provided by this system. This maintains fluorescence at the saturated regime. For schematic view of the PLIF system, see Figure 3.2.

#### **4.4.2 Filtering the PLIF Signal**

A LEO (Lattice Electro Optics) band pass filter (312.6F10-10, 1" diameter bandpass filter with FWHM 10nm, CWL 312.6nm) was attached in the ICCD camera to cut off all unnecessary signal and receive the fluorescence that is expected to be found around 300-320 nm region.

#### **4.4.3 Fuel/Air Feed System**

A Linde air flow meter/controller unit (18C-202-4125; ~ 50 slpm) and a Hastings flow meter/controller (HFC-203A; ~ 300 slpm) unit which was calibrated for the methane flow are used. The flow meters are calibrated with a Bios DryCal ML-500 calibration device

(volume flow rate). The input equivalence ratios into the premixer/burner unit (see Figures 4.5 and 4.6) are calculated from the calibration data (calibration was done in September, 2004), and then controlled for the duration of measurements.

In the present work,  $\phi = 0.5, 0.6,$  and  $0.75$  were used where  $\phi \sim 0.6 - 0.7$  is the recommended equivalence ratio by the designer (Dr. Robert Cheng, Lawrence Berkeley Livermore Laboratory) for the optimal performance of the burner. See Figure 4.4 for the schematic view of fuel/air feeding line, and Table 4.1 for operating conditions.

The volume flow rate is that of 90-150 SLPM (standard liters per minute), which corresponds to the exit velocity of 3-5m/s out of the nozzle, recommended by the designer. In the present work, the bulk axial velocity of 4m/s out of the nozzle has been used (see Table 4.1).

		<b>Fuel</b>	<b>Air</b>	<b>Fuel</b>	<b>Air</b>	<b>Fuel</b>	<b>Air</b>
<b>Equivalence Ratio</b>		<b>0.5</b>		<b>0.6</b>		<b>0.75</b>	
<b>Flow Rates</b>	<b>Volumetric (SLPM)</b>	<b>5.88</b>	<b>111.87</b>	<b>6.98</b>	<b>110.77</b>	<b>8.599</b>	<b>109.15</b>
	<b>Mass (g/s)</b>	<b>0.0653</b>	<b>2.237</b>	<b>0.776</b>	<b>2.215</b>	<b>0.0956</b>	<b>2.183</b>

**Table 4.1. Flow Rates.**

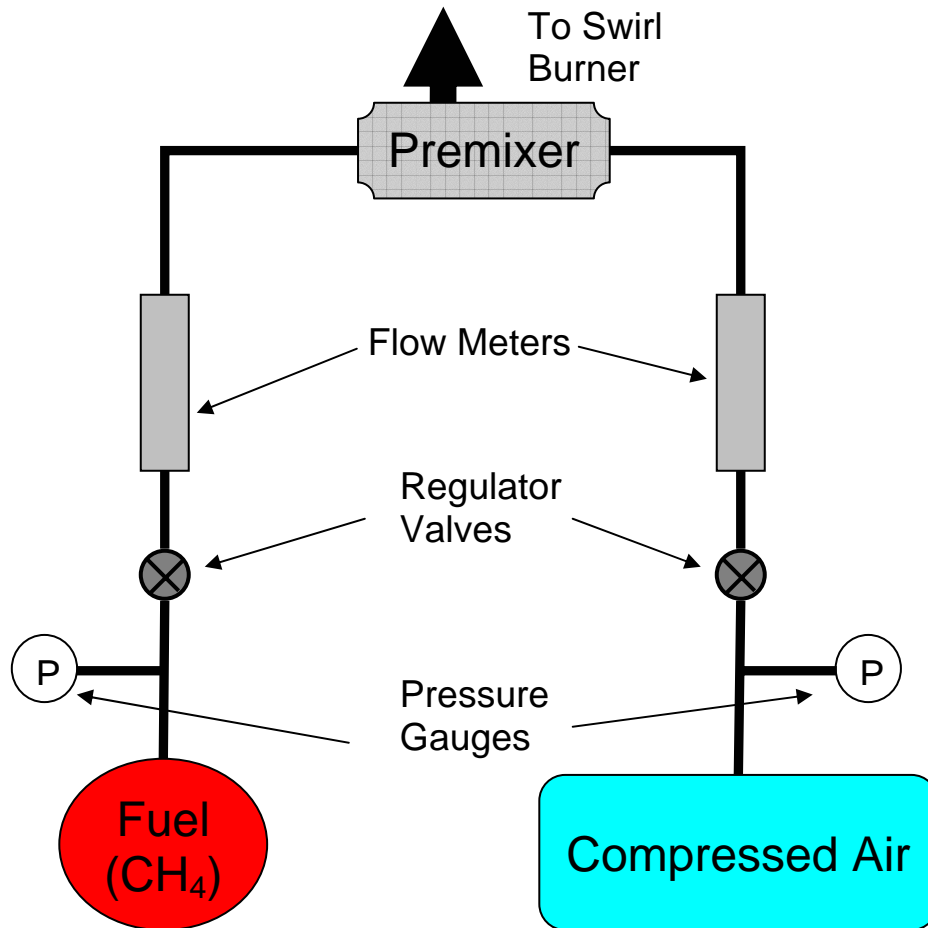
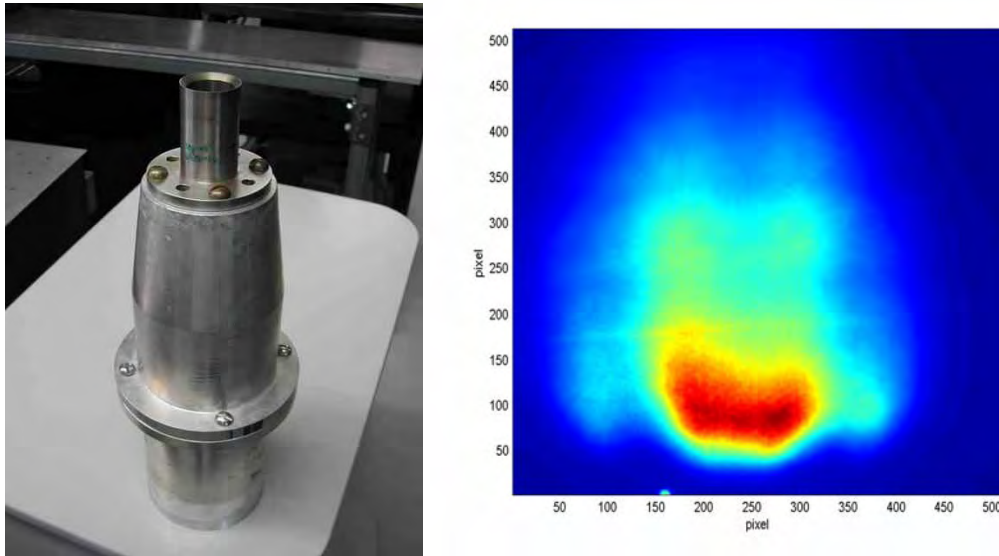
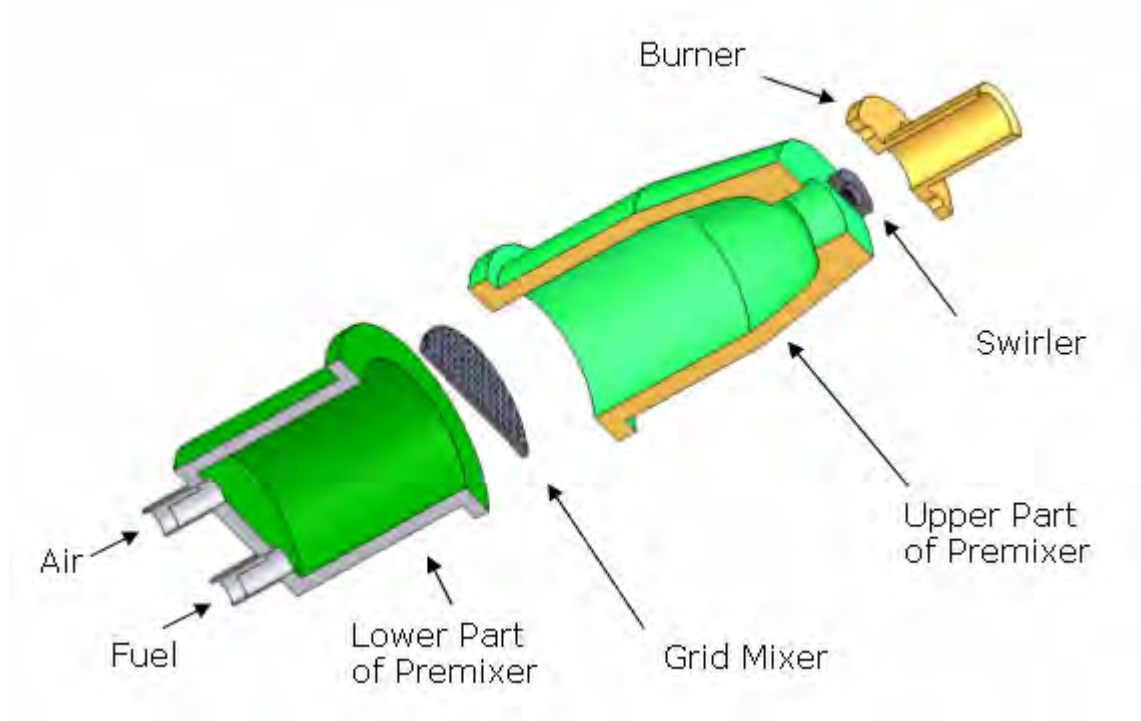


Figure 4.4. Diagram of the fuel/air feed system.

#### 4.4.4 The Swirl Burner



**Figure 4.5.** The swirl premixed burner installed on top of a pre-mixer (left); and the shape of the flame (averaged at 110Hz,  $\phi = 0.6$ , right).



**Figure 4.6.** The swirl burner assembly.

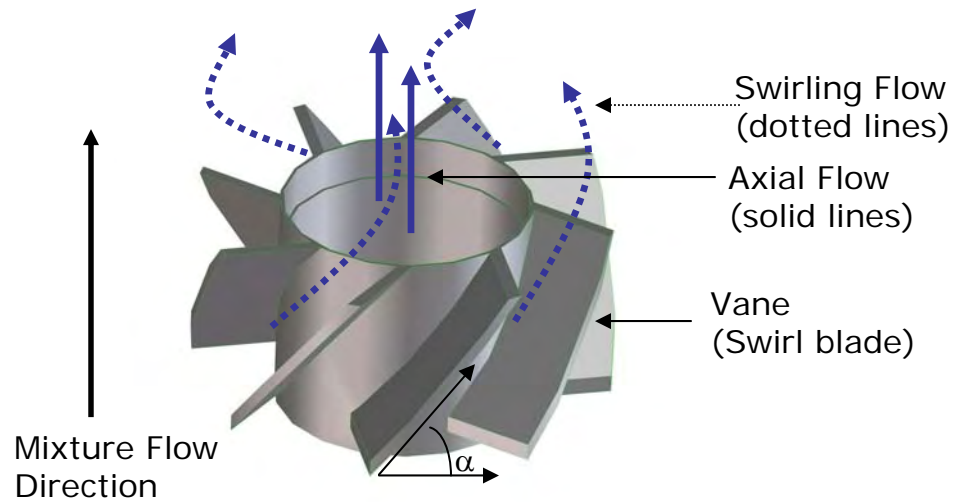


**Figure 4.7. The swirler.**

The burner shown in Figure 4.5 through 4.7 is a swirl stabilized burner with swirl number of around 0.7. The inner diameter of the swirl burner nozzle is 1 inch, the inside diameter of the premixer parts are 3 inches, and the total height of the assembly is about 18 inches. The swirler has small grid at the center enclosed by blades in the outer part (shown in Figure 4.7). There is another grid inserted between the upper and lower part of the premixer to enhance fuel/air mixing. There are 8 blades (vanes), each of which is approximately 1mm in thickness, around the center part (the grid core), and the angle ( $\alpha$ ) of the blades from the horizontal plane is approximately 65 degrees, the smaller the angle, the greater the swirl number. The aspect ratio, the ratio of the width of the swirling part to the radius of inner the axial flow part, is 1.0,  $\frac{1}{4}$  inch long respectively, and this ratio also affects the swirl number that the larger aspect ratio gives the greater swirl number, and vice versa.

Low-swirl burner uses small air jets to swirl the premixed flow inside the burner tube. The swirl leaves the center core flow undisturbed and produces a divergent flow above the burner exit. Flow divergence provides a highly effective means for stabilizing lean premixed combustion because it enables the flame to settle where the local velocity equals the flame speed (Cheng et. al. 1999).

## **4.5 Experimental Procedure**

### **4.5.1 General Procedure**

1. Laser preparations
  - Optimize the mixer/doubler tuning crystal angles for maximum energy conversion.
  - Check the laser beam profile and power. Leave for 15 minutes to reach steady state.
2. Set gas streams
  - Cooling air for the acoustic drivers.
  - Nitrogen purge gas through ICCD camera.
  - Turn on the ventilation pump.
  - Open valve for fuel/air stream, and direct the stream to the corresponding flow controllers.
  - Light up the flame right after the opening of the valve
  - Check the fuel and air stream stability.
3. Optical alignment

- Check the laser beam path with cards with lowered laser power at each point of beam deflection to ensure that the beam is directed in the right way.
  - Focus the ICCD camera on a card in the test section. Ensure the laser sheet is passing through the probed volume cleanly and focused at the center.
4. Beam profile calibration
- Minimize laser energy throughput using the wave plate. Set camera gain to 100, and gate width to 1  $\mu$ s with 1-2 ns delay.
  - Allow laser sheet to impinge on fluorescent card and acquire the beam profile with the ICCD camera, placing card in three different positions (left, center, right).
  - Return camera gain to 200, and gate width to 100 ns and wave plate inside the mixer/doubler to allow maximum laser energy throughput.
5. Prepare devices.
- Set acoustic driver power on controller, and activate drivers.
  - Turn on oscilloscope to monitor each and every signal.
6. Perform runs (duration approximately 3 minutes).
- Start LabView data acquisition program (main DAQ program and gating signal delayer).
  - Start WinView camera imaging software, typically taking 300 images (limited by system memory).
7. End experiments
- LabView and WinView routines end automatically
  - Turn off fuel and air, extinguishing the flame.

- Turn off acoustic drivers.
8. Repeat experiment.
    - Repeat steps 6-8 until more than 1800 images or more have been acquired at a particular test condition.
  9. Change experimental conditions.
    - Change the frequency driving acoustic wave.
    - Repeat steps 4 through 8 until experimental session is complete.
  10. Shutdown systems.
    - Shut off the laser.
    - Turn off the ventilations and other related devices.
    - Store acquired data – burn DVDs for post-processing and archival.

#### **4.5.2 Post-processing**

Images are taken at random pressure phases, with the camera gating signal being recorded by the data acquisition system along with the pressure signal so as to enable appropriate post-processing. Post-processing involves sorting of images by the phases of imposed acoustic oscillations, creating phase-averaged images, and normalizing based on laser intensity and other quantities.

Each image is read and tagged with its phase bin information, fluctuating pressure, and mean pressure values. After sorting and classifying images according to the corresponding phase information, quantities of interests such as the Rayleigh index, the heat release rate fluctuations, and the local/global flame responses are calculated.

## 4.6 Results

Main features of the combustion dynamics, especially the thermo-acoustic coupling (the Rayleigh index) and the heat release rate behavior are presented in the following five categories: pressure and heat release rate behavior; local distribution of Rayleigh index; global Rayleigh index (Rayleigh index of the entire control volume); local response; and the global response of the combustion process. As the heart of the thesis work, this chapter presents measurements with precision, and a general experimental procedure for determining the dynamic response of the flame and the combustion dynamics.

The global thermo-acoustic coupling (global Rayleigh index) and combustion responses (magnitude and phase shift) are the measures of the dynamic behavior of combustion systems and do not require spatial resolution for their measurement. Hence, measurement of these global quantities is often done with simpler light measuring devices (e.g., PMT, photodiodes, and the like). The global quantities give an indication of how a specific type of combustion system and combustor geometry would behave, but if local variables are not measured the results are burner and geometry specific.

One of the key aspects of this work has been the use of spatially resolved measurement techniques. Since the local response is a function of only local parameters (e.g. velocity, pressure), it is possible to apply these values to specific points in any combustor configuration. When all of the relevant flow field variables, such as velocity field, temperature, and thermo-acoustic coupling, are collected, the resulting data will be directly applicable to all other combustion systems. In this sense, the local Rayleigh

index, along with local responses, is a clear and useful way of quantifying and describing the local combustion dynamics.

#### **4.6.1 Combustor Pressure and Heat Release Rate**

A pair of acoustic drivers (loudspeakers) create pressure and velocity oscillations in the combustion chamber (see Figure 3.1). The intensity or the peak-to-peak of the pressure wave inside the chamber is  $0.1 \pm 0.01$  % of atmospheric pressure, the same level as in the work described in Chapter 3. Except for 22 Hz, which is approximately the minimum possible frequency produced by the current MacKie amplifier and the feedback controller, the Fast Fourier Transformed pressure signals are very clean and demonstrate the repeatability and reliability of the conditions generated for these experiments. See the left hand side of Figure 4.8 and refer to Appendix D for the remainder of the data.

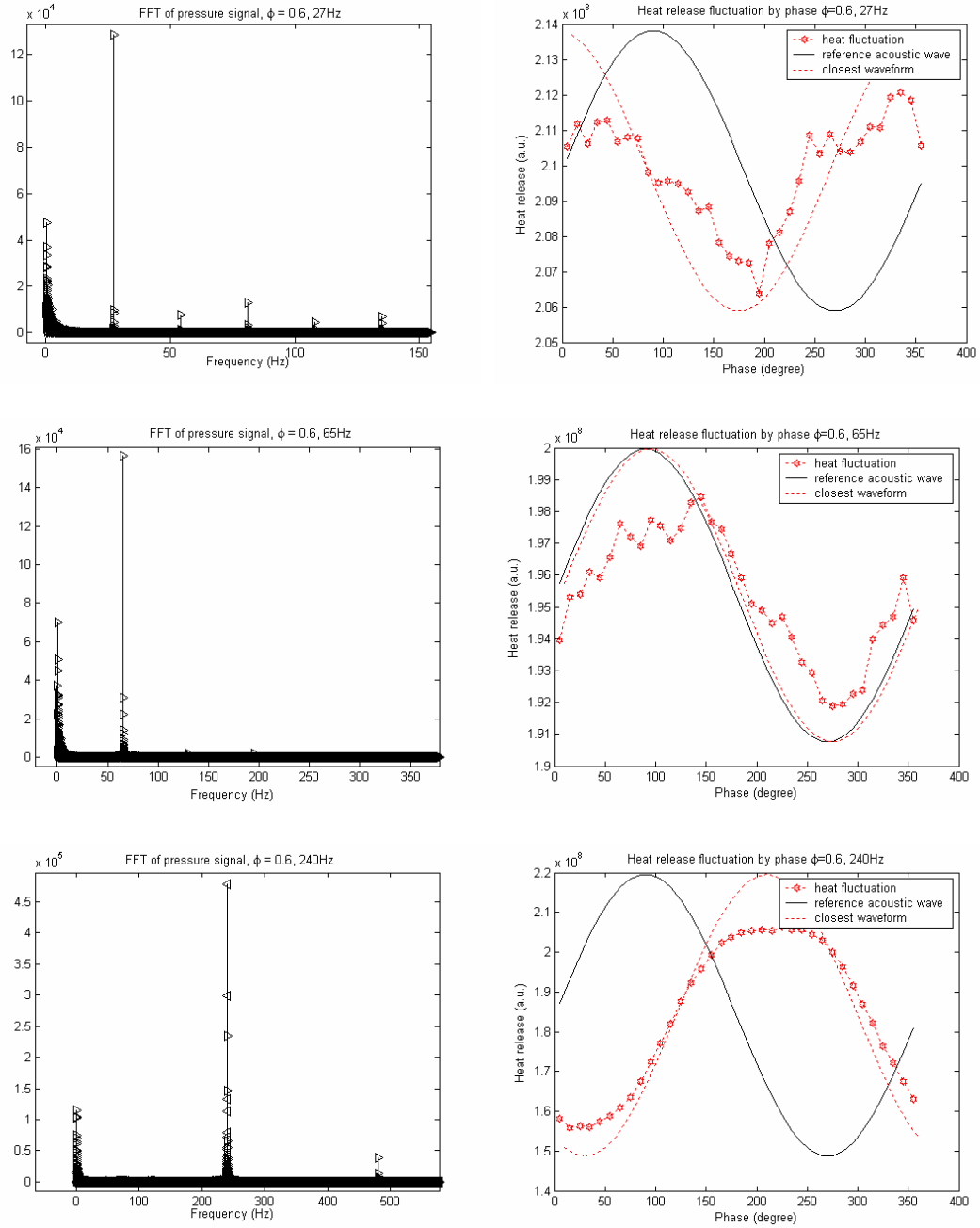


**Figure 4.8. FFT of the pressure signal (left) and heat release fluctuation (right)**

**at  $\phi = 0.6$ , for excitation frequencies 27, 125, and 240 Hz.**

The change in heat release rate is assumed to be proportional to the change in OH concentration, and this is quantified by recording and then processing the intensity of

each pixel in each OH-PLIF image, as discussed in Chapter 2 and section 4.2.2. The acoustic oscillations induce oscillatory flame behavior (Pun et al., 2003) and this fluctuation is captured by means of phase-binning; the mean intensities in each bin averaged over the images belonging to the bin show oscillatory behaviors, see the right hand side (RHS) of Figure 4.8.

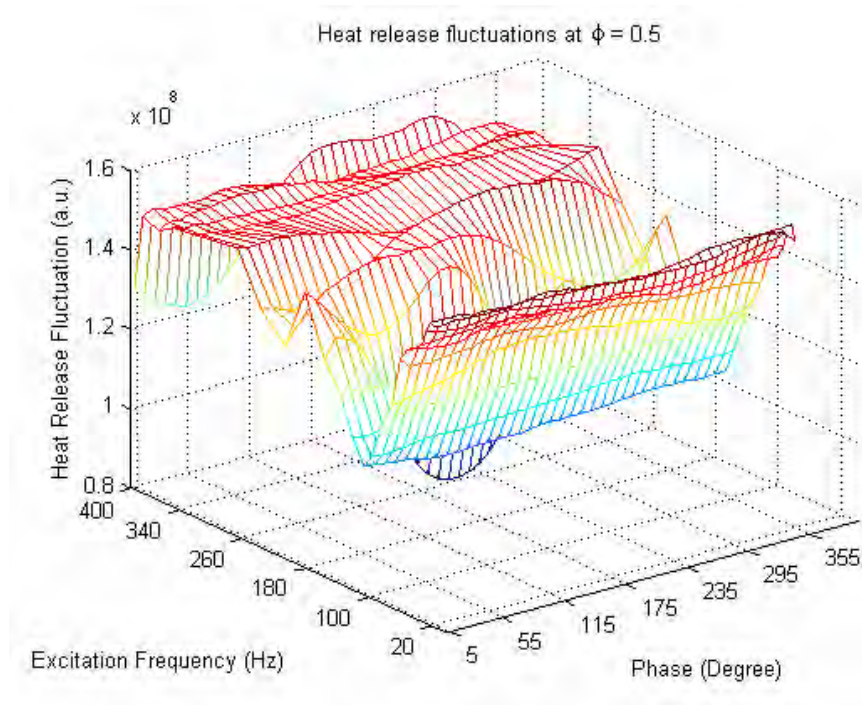


**Figure 4.9. Heat release fluctuation at  $\phi = 0.5$  as a function of excitation frequency and phase during one cycle of the imposed acoustic wave.**

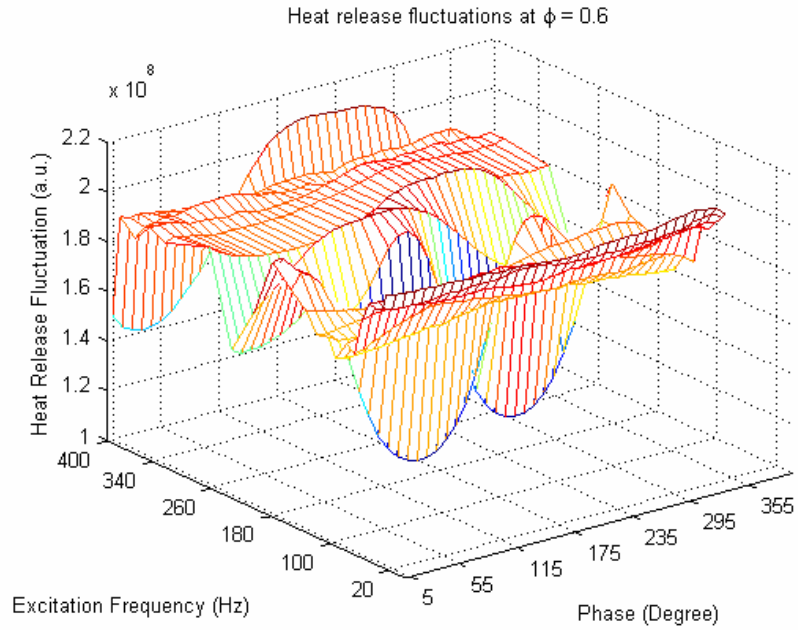


**Figure 4.10. Heat release fluctuation at  $\phi = 0.6$  as a function of excitation frequency and phase during one cycle.**

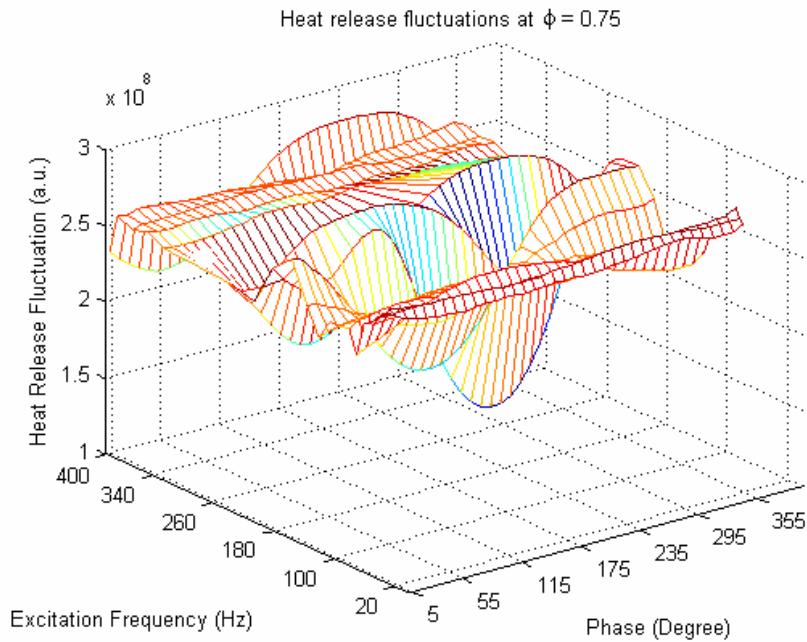


**Figure 4.11. Heat release fluctuation at  $\phi = 0.75$  as a function of excitation frequency and phase during one cycle.**

The fast Fourier transformed (FFT) signal (left hand side of Figure 4.8) shows the behavior introduced in Chapter 3. The turbulent flame that has many uncertainties and (probabilistically) random processes induce this low frequency feature that looks like 'f(x) = 1/x' graph. The right hand side of Figure 4.8 shows that the heat release rate fluctuates at each corresponding excitation frequency with a certain phase difference, implying that the acoustic excitation induces fluctuations in the rate of heat release. The amplitude of the normalized heat release rate fluctuations is one or two orders of magnitude greater than the normalized pressure fluctuations.

Figures 4.9 through 4.11 are summaries and juxtapositions of the heat release fluctuation over all excitation frequencies (22-400Hz) and phase, for equivalence ratios 0.5, 0.6, and 0.75. The rest of the data are given in Appendix D.

#### **4.6.2 Local Distribution of the Rayleigh Index**

The Rayleigh index is calculated using equation 4.2. The local distribution of Rayleigh index is given in Figures 4.13 through 4.15. As discussed in section 4.2, the positive region (red or warm-colored) indicates the region where the energy is positively fed back to the acoustic wave thus magnifying the amplitude of the acoustic waves at that frequency.

Figure 4.12(b) is the axial velocity distribution adapted from Cheng et al. (2000) using a swirl burner very similar to the one used in the present work. The distribution was normalized according to the appropriate scale (radius of the burner), then rescaled to be

compared with the current experimental configuration. The velocity was measured 5 mm above the burner, indicated as the thick black arrow (the relative height scaled appropriately) at the bottom of Figure 4.12(a). According to Figure 4.12(b), the axial velocity peaks at approximately  $r/R = 1.0$  where  $r$  is the distance from the center and  $R$  is the radius of the burner. Then the velocity drops very sharply at around  $r/R = 1.2$  to  $1.5$ . This region is where the maximum velocity gradient is located so that strong shear mixing between the inner flow and the outer flow (no flow in the current work) occur. In this shear mixing region, it is expected that vortex structures form along the zone due to the differences in flow properties such as the axial velocity and combustion driven density distribution.

It seems that the thermo-acoustic coupling (the Rayleigh index) is affected by or linked to the shear layer instability (the Kelvin-Helmholtz Instability (KHI)). Some numerical simulations showed that vortex ring structures grow in the jet boundary (Menon et al. 2004 and Perucho et al. 2004). The driving force for formation of this vortical structure is the axial component of the fluctuating flow velocity due to the acoustic excitations (Menon et al. 2004) and the flow field shearing with the outer flow.

Figures 4.13 through 4.15 show ‘circular patterns’ in the spatial distribution of the Rayleigh index in the region that are expected to be the shear mixing zone from the comparison with the axial velocity distribution (Figure 4.12(b)). These patterns are supposed to be ring type toroidal structures, considering the fact that the patterns are symmetric. So from here and on, this structure will be referred to as ‘toroidal structure’ or a ‘toroid’.

Each toroidal structured zone is characterized by the same sign of Rayleigh index thus forming islands of similar tendency toward instability. It is in the leaner part of the flame that the toroidal structures are observed. And where it is lean, it is more susceptible to the combustion instabilities because the values of the Rayleigh indices are larger. The right hand side of Figure 4.5 shows the global average of the flame. The toroidal structure is located in the shear zone where the fuel/air mixture is mixed with the outer air flow, then becoming further leaner, thus forming the weaker heat release rate zone at the boundary flame. Though the flame intensity is greater toward the center (RHS, Figure 4.5), the central region is not much affected by the exciting acoustic waves, in terms of the Rayleigh index (Figures 4.13 through 4.14) and the magnitude of the flame response (Figures 4.26 through 4.28). The greater part of the flow is the axial component ('low' swirl). Thus the greater part of energy is released in the center region. Yet the major contribution toward instability and flame response comes from the flame boundary, where the leaner portion of the flame is more heavily affected by the imposed acoustic oscillations.

The toroidal structure at the flame boundary widens outward with increasing equivalence ratio, as can be seen from comparison among Figures 4.13 through 4.15. The toroid widens outward to find locations where the mixture ratio is 'leaner', thus more susceptible to instabilities, while the central core part is not much narrowed inward by the growing toroidal structure.

The spatial frequency (the wave number) of the toroids occurrence is a strong function of excitation frequency (Figure 4.22). If this is actually the vortex structure (to be verified by flow field variable measurements in future work), then it means that each vortex structure formed due to the shear layer mixing (e.g., associated with a Kelvin-Helmholtz instabilities) is highly sensitive to the acoustic excitation. That is, the vortex structure created by the shear mixing are modulated by the imposed acoustic excitations and can be said to be the main factor determining the combustion response for this kind of low-swirl burner configuration.

Another interesting phenomenon is that the size of the structure becomes smaller and smaller until the acoustic excitation reaches a given frequency ( $\sim 100$  Hz). The number of toroidal patterns in the flame region indicates the frequency of the 'toroid' formation (or it may be the vortex shedding frequency) in the flow field. As shown in Figures 4.13 through 4.15, that frequency increases with acoustic driving frequency; this tendency is not dependent upon the equivalence ratio. Values of the local Rayleigh index were extracted along the peaks and troughs of the toroids formation as shown in Figure 4.12(a) by the thick dotted line. Figures 4.16 through 4.21 show how the spatial distribution of toroids fluctuates along the flame boundary (the shear mixing zone). There are two main features: 1) the wave number of the fluctuation gets higher with frequency to some asymptotic value (approximately  $35 \text{ m}^{-1}$ , see Figure 4.22); 2) the amplitude of oscillations decreases as the flow advances downstream.

If the toroidal structure in the distribution of local Rayleigh index is related to the vortex structure due to Kelvin-Helmholtz Instability, then the increase in the wave number to a certain asymptotic value in Figure 4.22 could be related to the 'lock-on' phenomena. This is a phenomenon that occurs where the vortex shedding due to the flow structure is interfered with by imposed vibrations such as acoustic driving, leading to a change in the vortex shedding frequency from the naturally observed one to a frequency closer to that of the excitation. The sudden transition of the wave numbers from the low frequency excitations (22-100 Hz) to the higher frequencies ( $> 100$  Hz) implies that the lock-on mode may exist in the low frequency region. Also, if the vortical structures coincide with the Rayleigh index distribution, which is very likely according to the numerical simulations by Menon et al. (2004), then it means not only that the 'lock-on' exists at low excitation frequencies, but also that the thermo-acoustic coupling (Rayleigh index) is itself coupled strongly to the vortical structures.

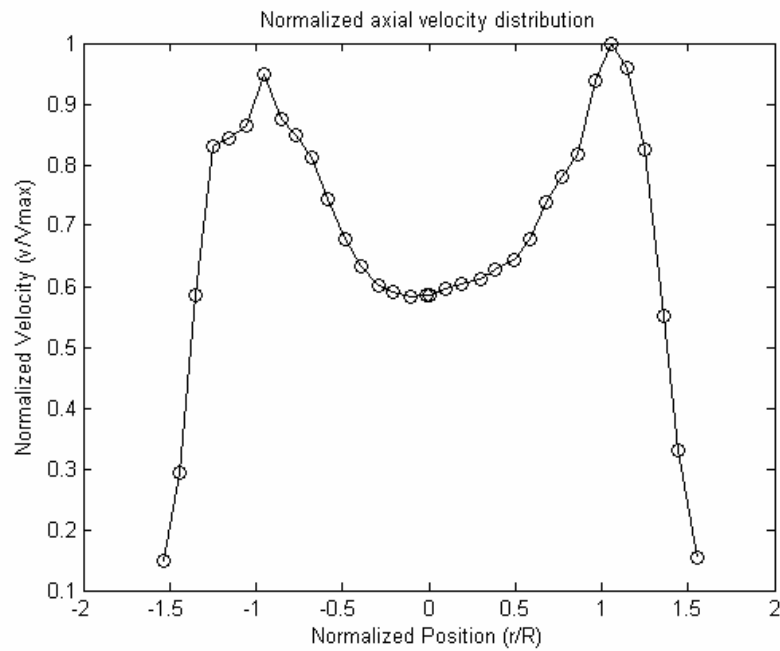
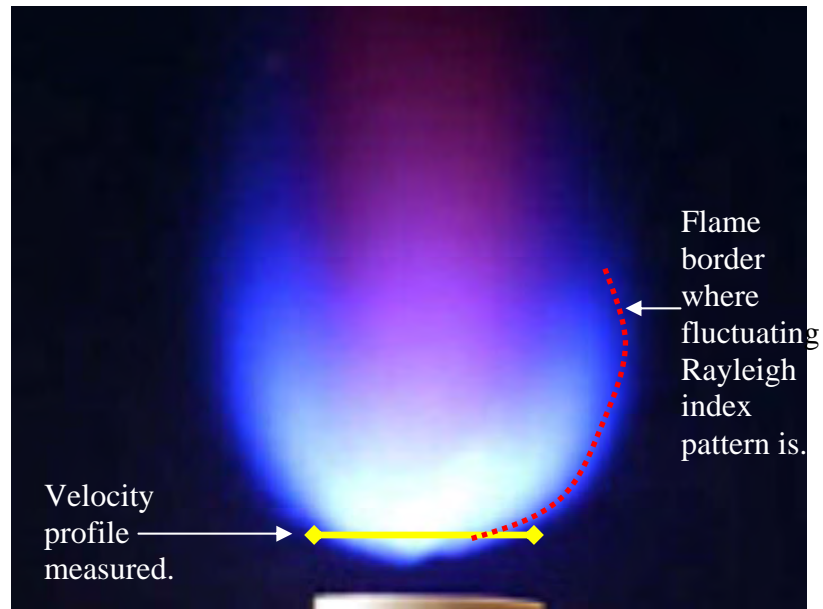


**Figure 4.12. Sketch of the swirl flame. The actual shape of the swirl flame where the fluctuating Rayleigh index is read along the dotted red line (top); the axial velocity distribution measured at the solid yellow line in the top figure (bottom), adapted from Cheng et al., 2000.**

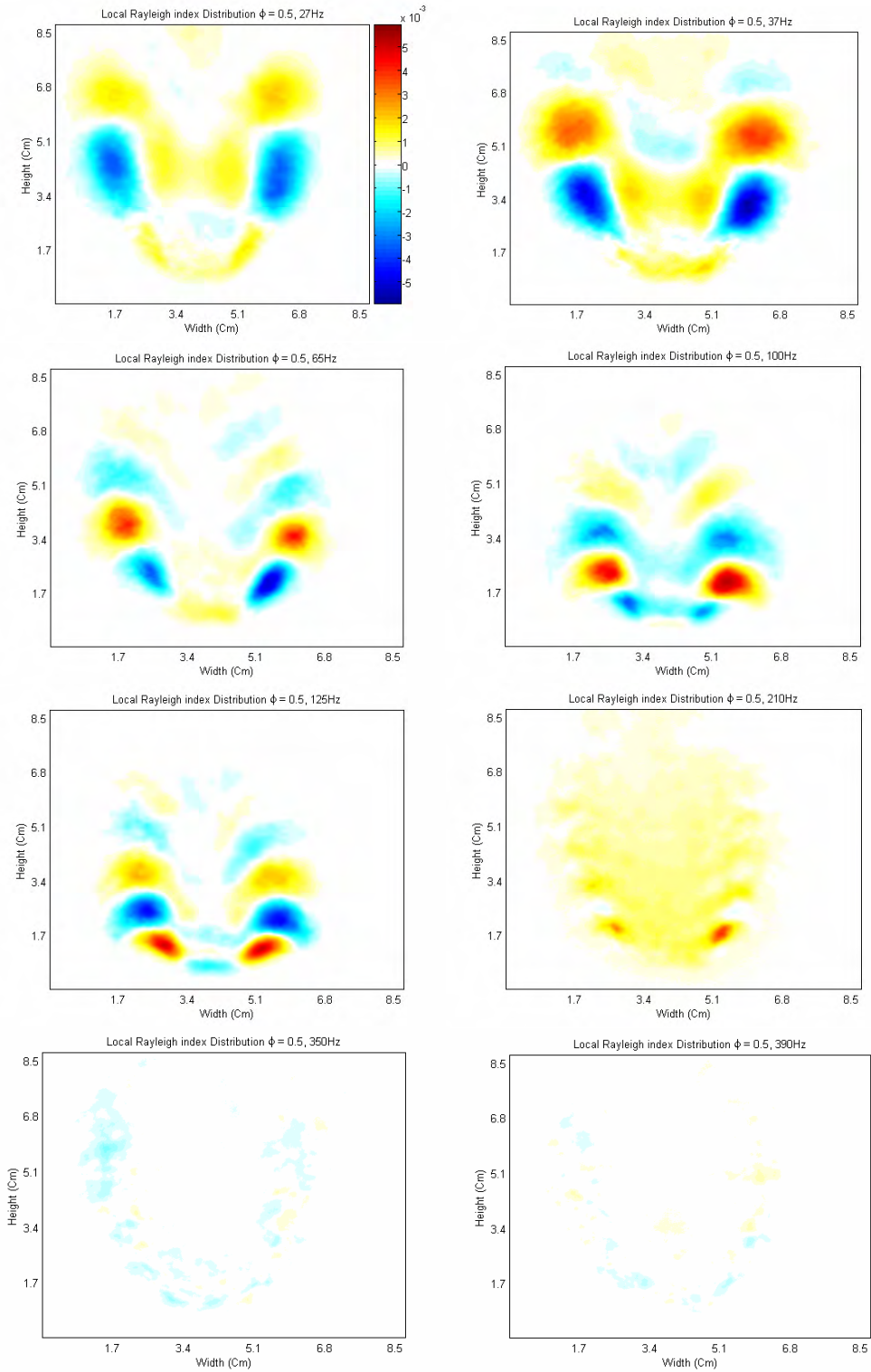


**Figure 4.13. Local distribution of Rayleigh index at the center plane of the flame,  $\phi = 0.50$  (at selected frequencies; refer to Appendix D for the remainder of the data)**

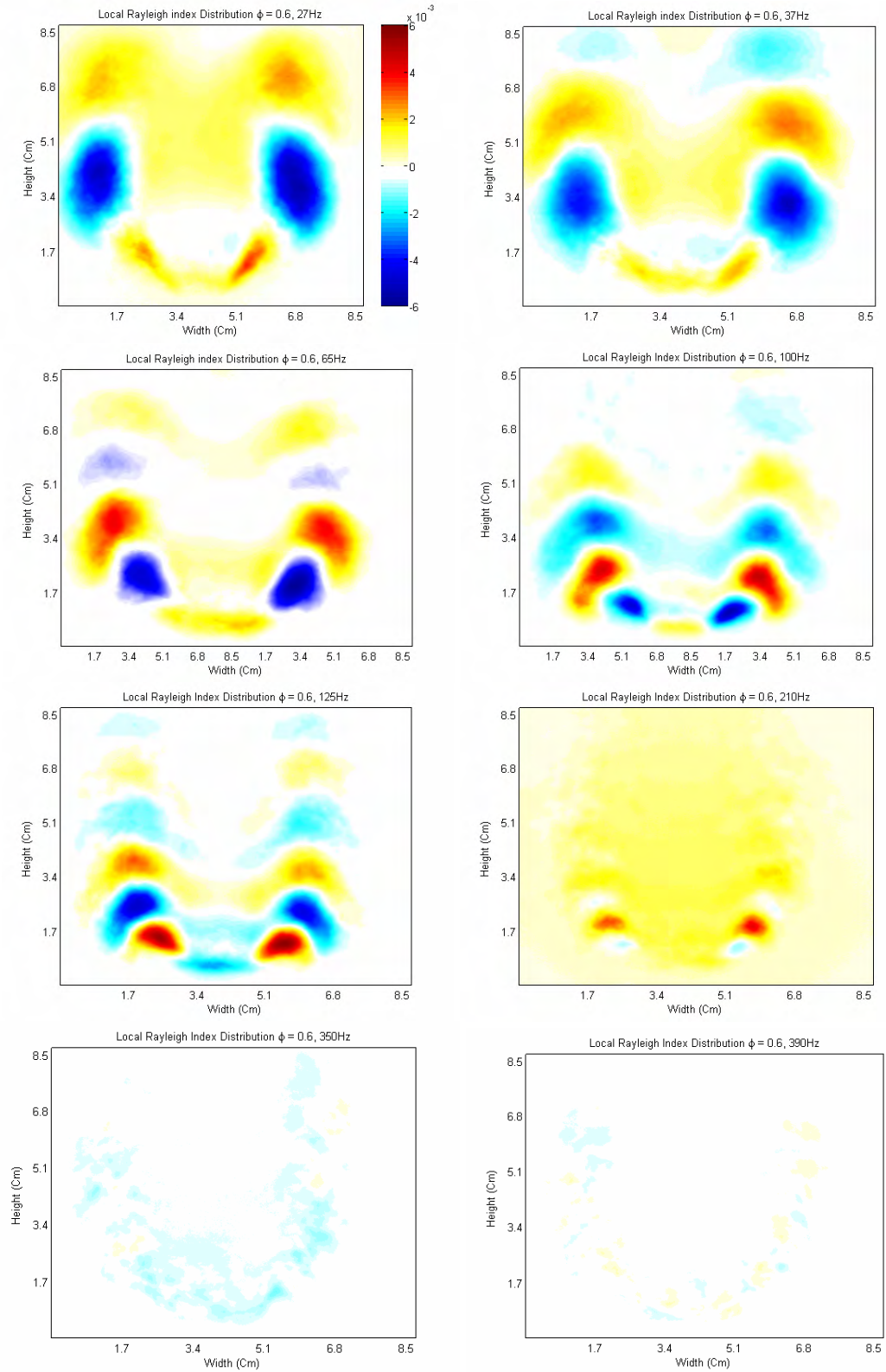


**Figure 4.14. Local Distribution of Rayleigh index at the center plane of the flame,  $\phi = 0.60$  (at selected frequencies; refer to Appendix D for the remainder of the data)**

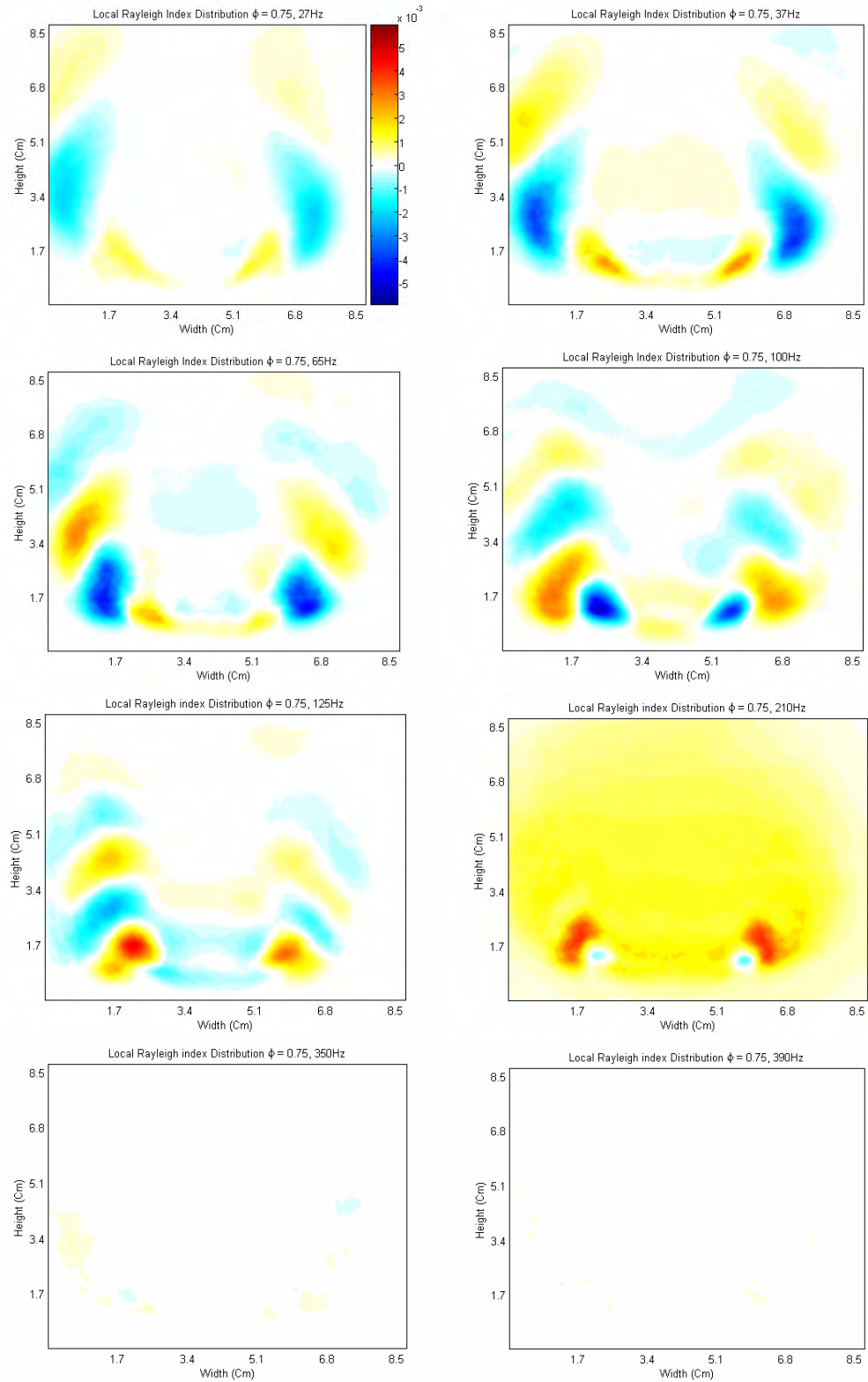


**Figure 4.15. Local distribution of Rayleigh index at the center plane of the flame,  $\phi = 0.75$  (at selected frequencies; refer to Appendix D the remainder of the data)**

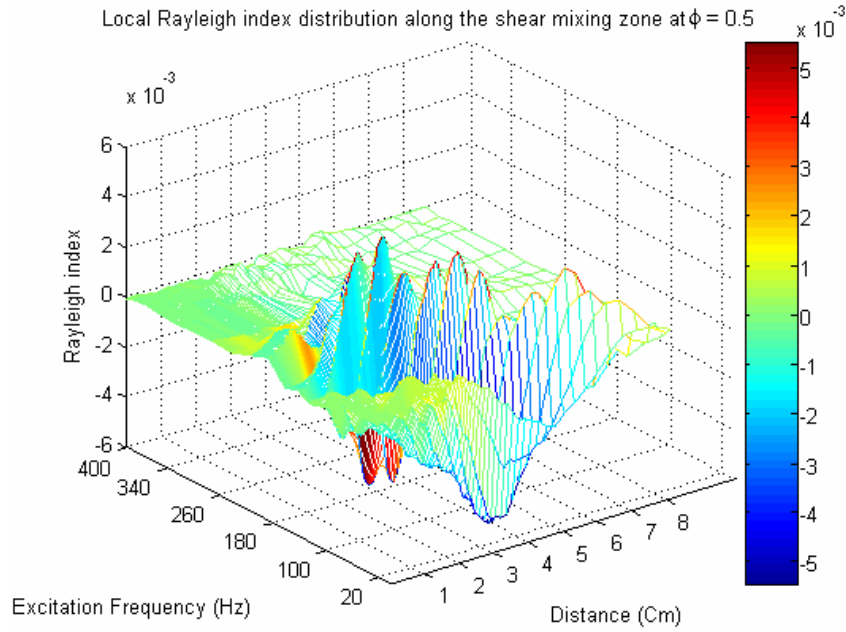


**Figure 4.16. Local Rayleigh index distribution as a function of frequency,  $\phi = 0.50$ .**

**(Distances in Figures 4.16 through 4.18 are along the flame border, see Figure 4.12)**

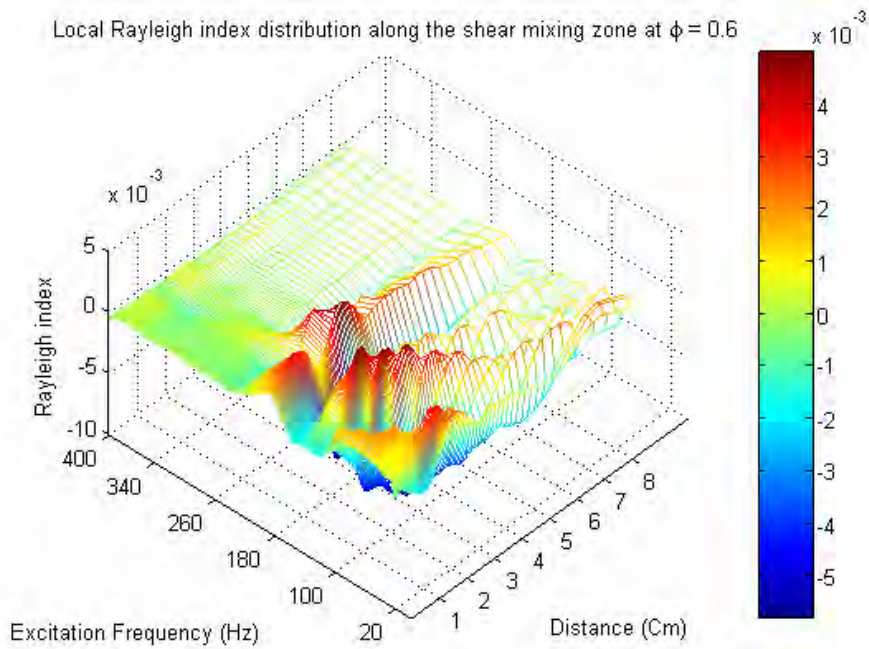


**Figure 4.17. Local Rayleigh index distribution as a function of frequency,  $\phi = 0.60$ .**

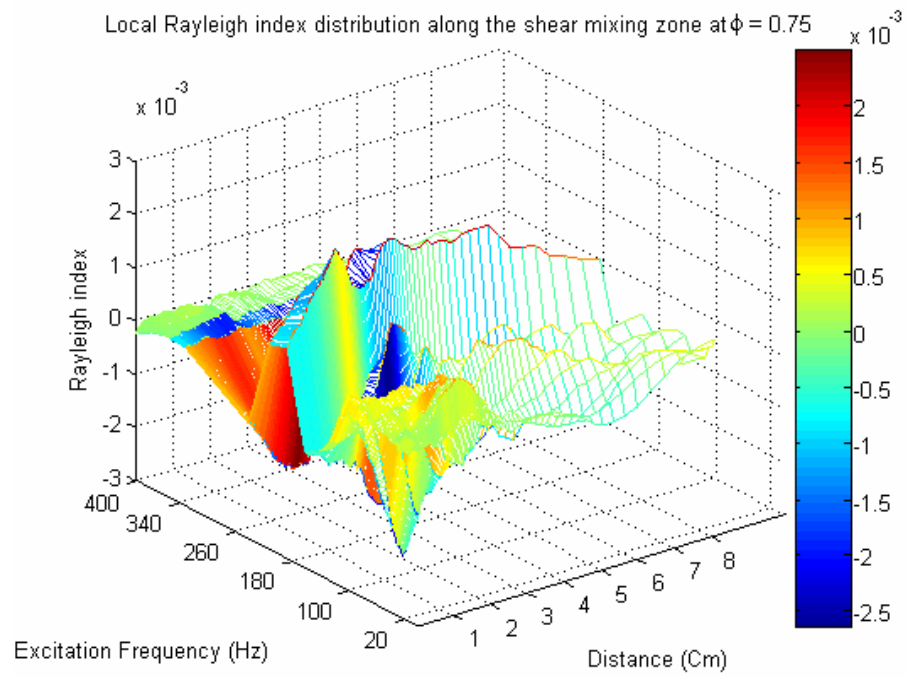


**Figure 4.18.** Local Rayleigh index distribution as a function of frequency,  $\phi = 0.75$ .

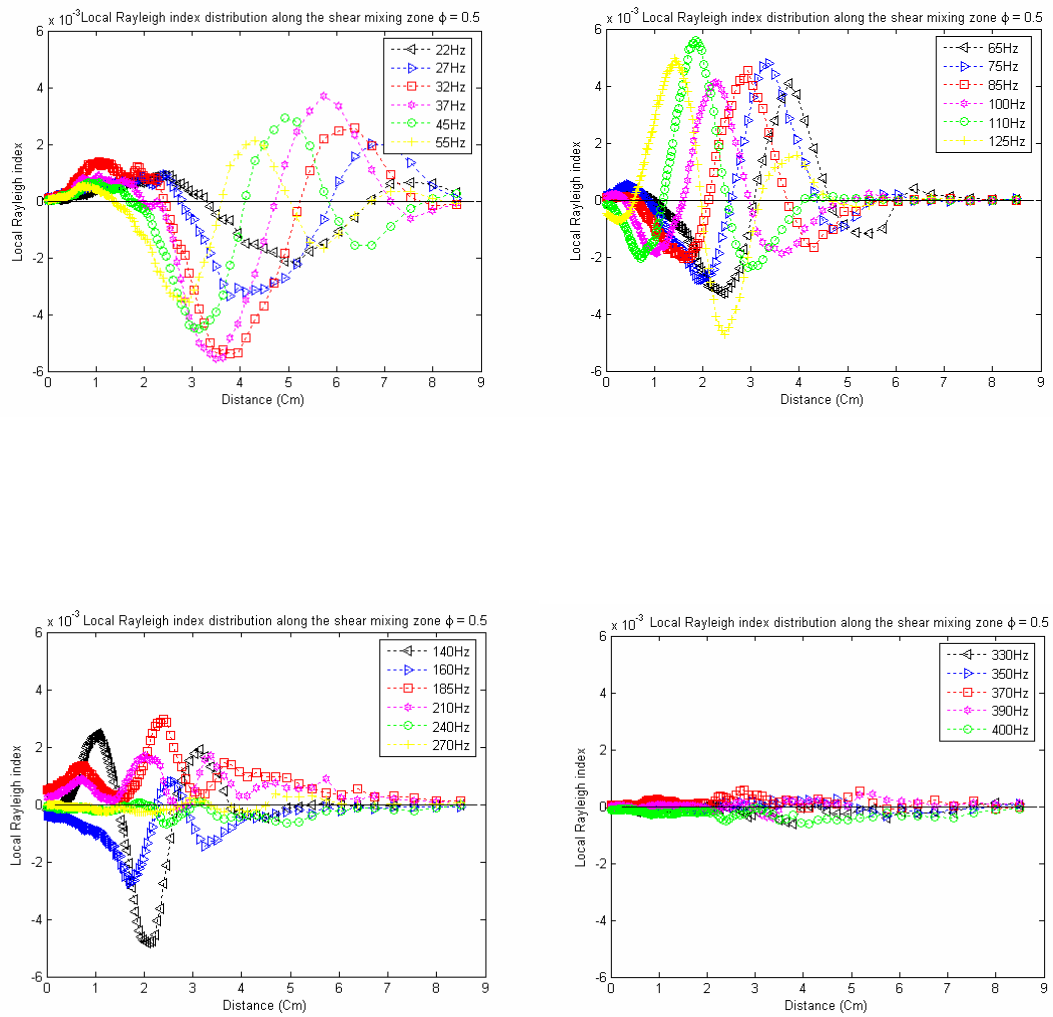


**Figure 4.19. Local Rayleigh index distribution along the flame boundary at each frequencies,  $\phi = 0.5$ .**

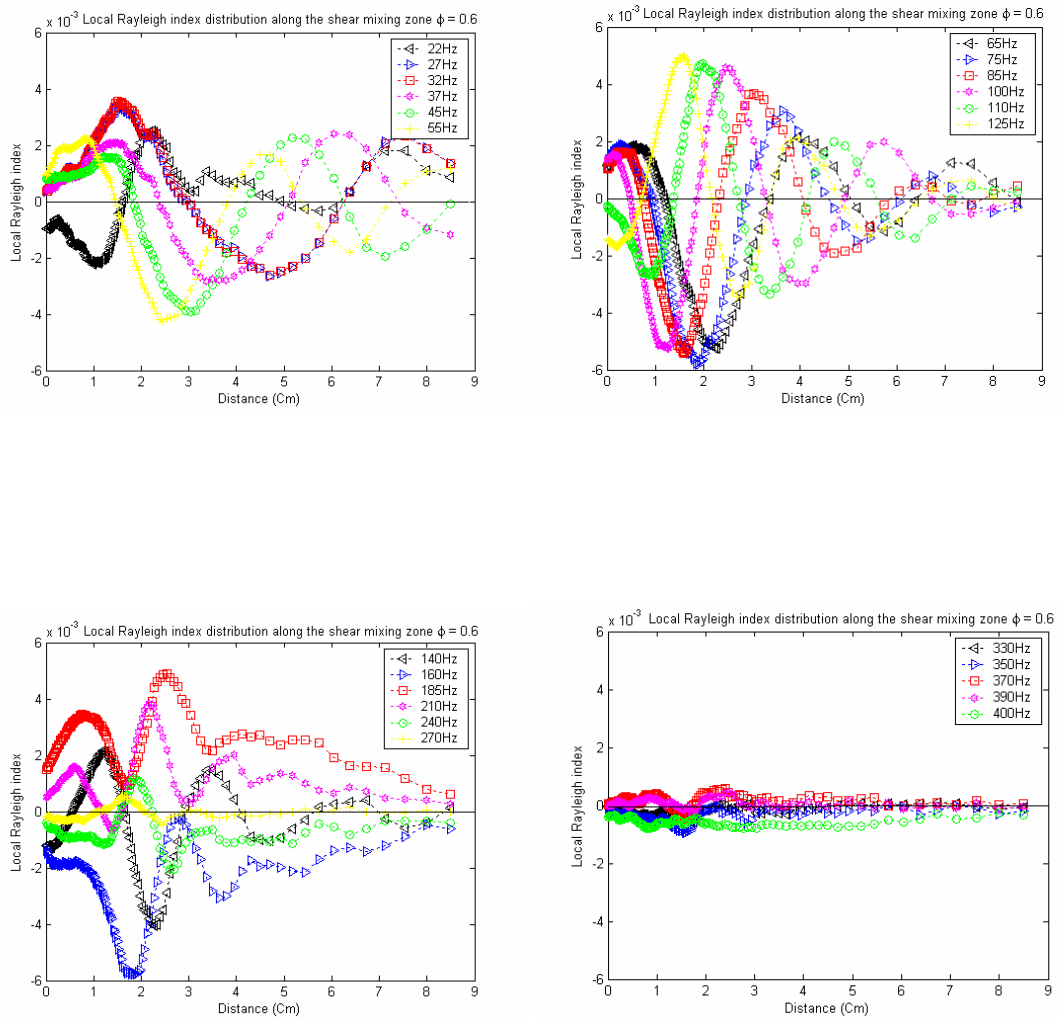


**Figure 4.20. Local Rayleigh index distribution along the flame boundary at each frequencies,  $\phi = 0.6$ .**

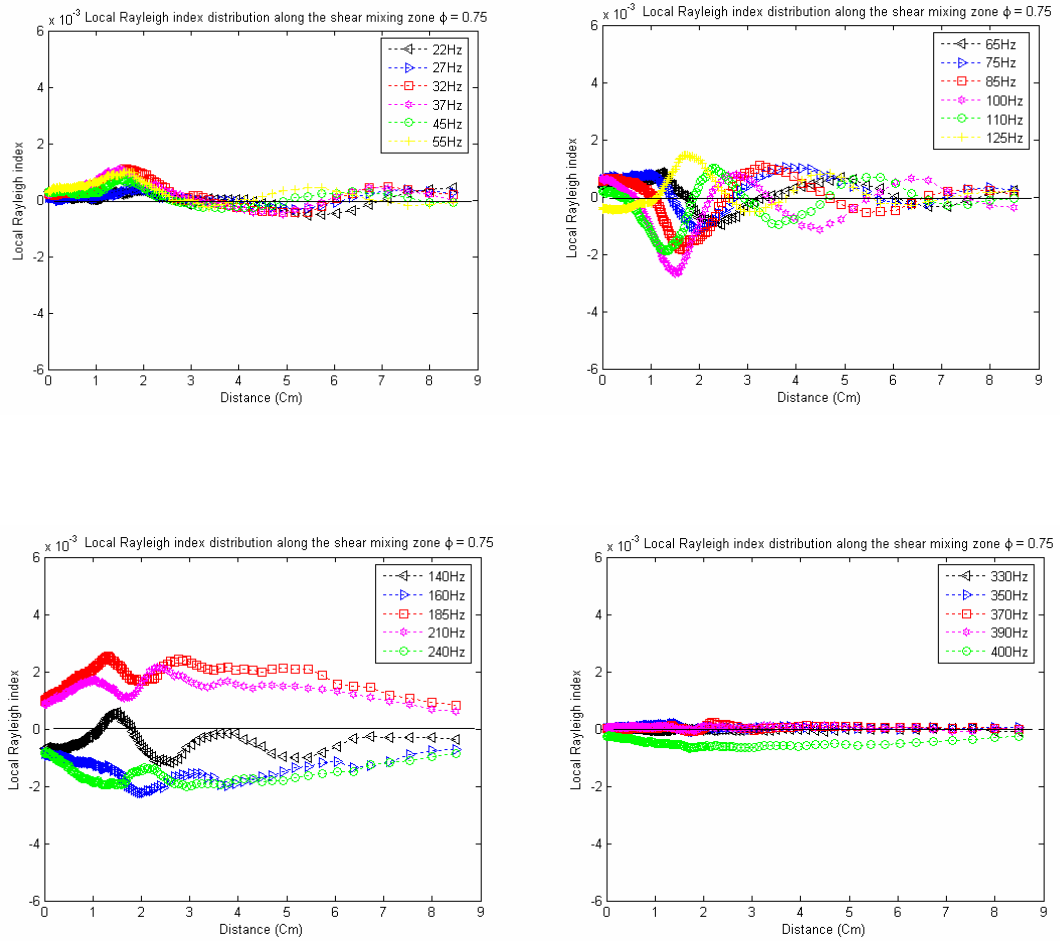


**Figure 4.21. Local Rayleigh index distribution along the flame boundary at each frequencies,  $\phi = 0.75$ .**

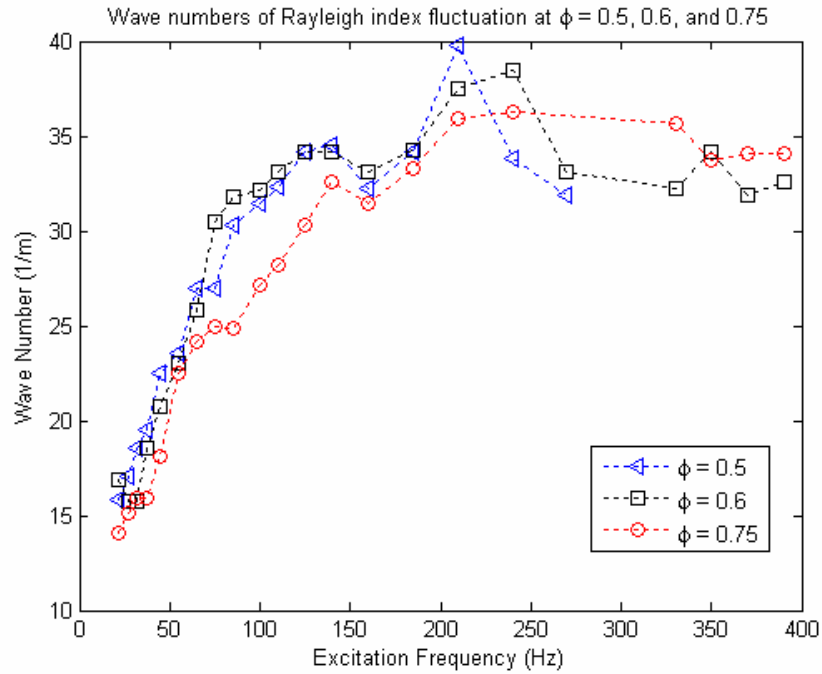


**Figure 4.22. Wave numbers of Rayleigh index fluctuation along the flame boundary.**

### 4.6.3 Global Rayleigh Index

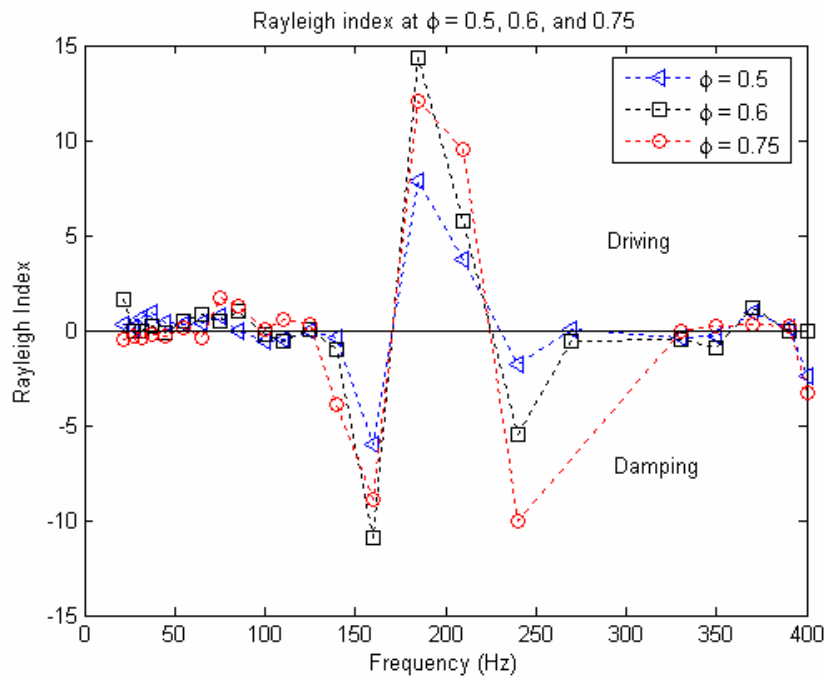


**Figure 4.23. Global Rayleigh index (vs. excitation frequency).**

The global Rayleigh index is a measure of the overall stability at a certain excitation frequency. This is obtained by integrating the normalized factor  $\frac{p'q'}{p_{rms}\bar{q}}$  over the control volume (over the whole image for these experiments). The pressure in the combustion chamber changes in a bulk fashion, ensuring that the pressure values,  $p'$  and  $p_{rms}$ , are valid across the whole image. The variables  $q'$  and  $\bar{q}$  are then calculated from the intensity at each pixel of the images.

Figure 4.23 shows the behavior of the global Rayleigh index, showing where the flame is expected to be stable and where it is not. The current measurements show that at frequencies of 150 to 240Hz, there are local frequency ranges where huge damping ( $Ra < 0$ ) and driving ( $Ra > 0$ ) effects are found.

Figure 4.23 also shows consistency in the measurements that the behaviors at the three different equivalence ratios (0.5, 0.6, and 0.75) agree with one another. This means the measurements method employed here is quite reliable and reproducible. Figure 4.24 also demonstrates how reliable the measurement method is, in terms of tendencies in the magnitudes and phase-shifts at different equivalence ratios. This helps achieve one of the major objectives of this work, to develop and demonstrate a way of measuring combustion dynamics with reasonable reliability.

#### **4.6.4 Global Flame Response**

The response of flame is of great importance to study in that this gives the idea how the system would react to outside disturbances (see Figure 1.3 and 1.5). Following Pun

(2003), the response of the flame is given by,

$$(4.3) \quad C_R = \frac{q' / \bar{q}}{p' / \bar{p}}.$$

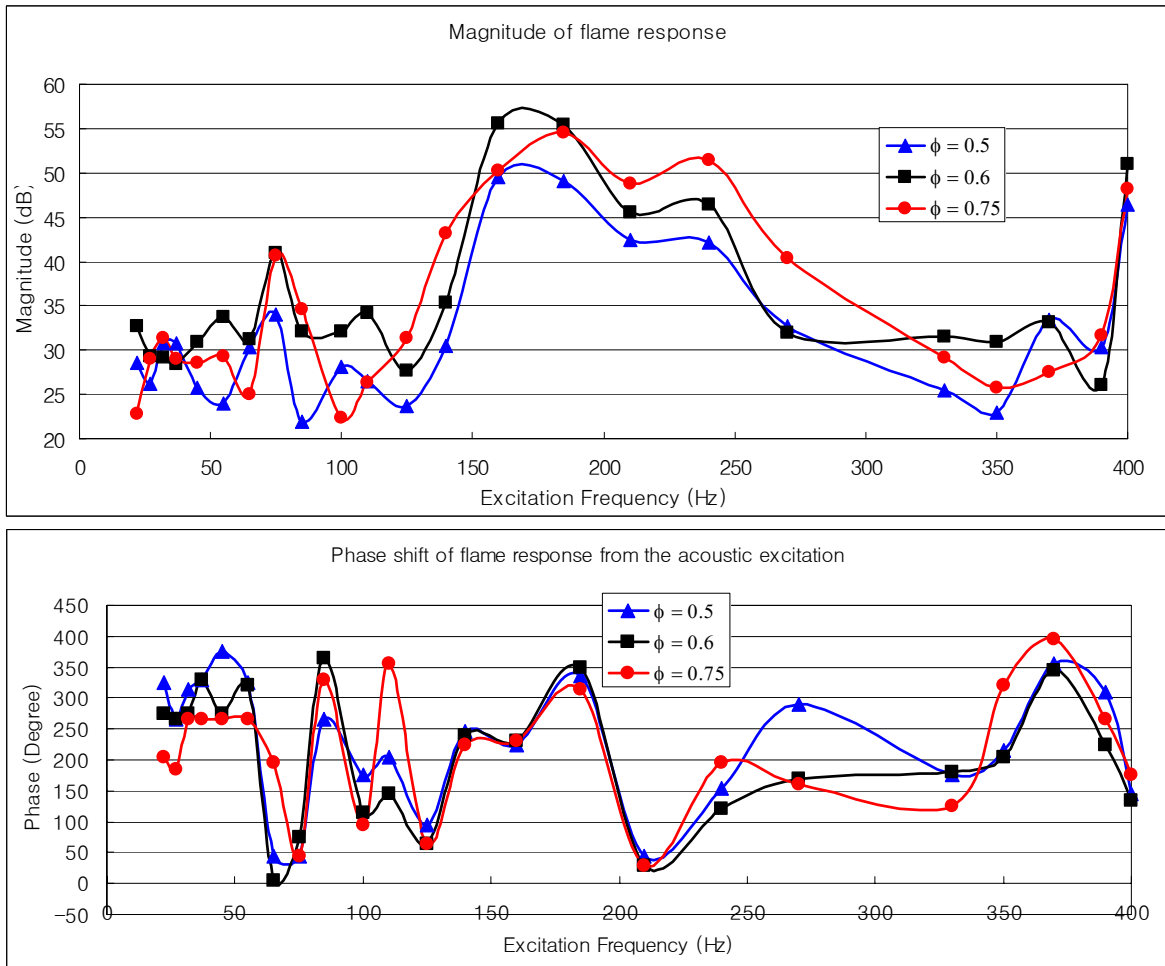


**Figure 4.24. Magnitude (top), and phase shift (bottom) of flame response.**

As mentioned in the previous section (4.5.3), the bulk motion of the acoustic wave gives the value for pressure fluctuation and local averaged pressure, while the measurements made and presented in Figure 4.8 give the values for the heat release. Here, the magnitude is in decibels (dB), which is the logarithm of equation 4.3 multiplied by 20.

The phase shift is measured from the phase of exciting acoustic waves; positive values mean that the peak of the heat release fluctuation is shifted to the right of the peak of the acoustic waves.

Figure 4.24 shows the magnitude and phase shift of the global response; that is, these results show the response of the flame to acoustic oscillations integrated over the imaged domain. For the three different equivalence ratios (0.5, 0.6, and 0.75), the response of the flame is almost identical, varying very slightly with excitation frequency. The role of swirl is best shown by the fact that for three different equivalence ratios, the global quantities (the Rayleigh index and flame responses) are not affected significantly, meaning that the swirl ensures more stable and consistent performance of the system within the range of equivalence ratio. The phase shift shows significant frequency dependence, but negligible dependence on the equivalence ratio.

Comparing Figures 4.23 and 4.24, it is found that the region with large absolute global Rayleigh indices coincides with the region where the flame response is far greater (note that the magnitude is in log scale!) than at other places (160 – 240 Hz). It seems clear that the global Rayleigh index is closely related to the global response of flame.

Using a basic acoustic analysis, the combustor geometry (open-closed end condition) gives a resonant standing wave of approximately 120 Hz at the flame temperature (1800 K), or lower for the averaged temperature along in the chamber. The acoustic resonance mode is expected to be a sharp, narrow peak, which is avoided in this measurement. So,

the plateau in Figure 4.23 (approximately from 150 to 250Hz is not supposed to be the combustor resonance mode, but, rather, it indicates the zone where the flame is thermo-acoustically unstable, and hence much more sensitive to the outside disturbances than at other frequencies.

It is no surprise, from the definition of the Rayleigh index, that the phase shift of the flame response is close to zero (or 360 degrees) where the Rayleigh index has a maximum value (e.g. at 185 Hz). Since it follows that when the heat release fluctuation has a phase shift of  $\phi$ ,

$$(4.4) \quad p'_n \propto \sin(w_n t), \text{ or } \text{Im}(e^{i w_n t})$$

and

$$(4.5) \quad q'_n \propto \sin(w_n t - \phi), \text{ or } \text{Im}(e^{i(w_n t - \phi)})$$

then

$$(4.6) \quad Ra \propto \int \sin(w_n t) \cdot \sin(w_n t - \phi_n), \text{ and the magnitude, } C_R \propto |e^{i\phi}| \sim 1,$$

and the Rayleigh index is a function of the phase shift ( $\phi$ ). The magnitude of the flame response has the same trend as that of the Rayleigh index, since the amplitude of  $p'$  is regulated by the feedback controller to a certain degree (approximately 0.1 % of atmospheric pressure). So, when  $p'$  is constant, only the way the amplitude of heat release rate fluctuation ( $q'$ ) matters.

#### 4.6.5 Local Distribution of Flame Response

Using equation 4.3, the local response of the flame is calculated in the same manner as the global responses. The primary difference is that instead of integrating over the entire

imaged region, the values at each pixel are used. The local maximum of the Rayleigh index coincides with the phase shift of 0 or 360 degrees, while the local minimum coincides with the phase shift of around 180 degrees (see Figure 4.25).

Comparing Figures 4.13 through 15 and Figures 4.26 through 28, we can conclude that 1) the local magnitude distribution is concentrated in the shear mixing zone which is along the flame boundary, 2) the local phase distribution coincides with local peaks (at 0 or 360 degrees) and troughs (at 180 degrees) of Rayleigh index. 2) is a bit redundant considering the definition of Rayleigh index that when in phase Rayleigh index goes positive (and toward the maximum), and vice versa. The magnitude of the local flame response is of greater interest. In section 4.6.4, it was shown (from Figures 4.23 and 4.24) that where there's a large absolute value of Rayleigh index the flame's response to the disturbance at that region (frequency) gets larger, irregardless of whether the acoustic wave dampens ( $Ra < 0$ ) or amplifies ( $Ra > 0$ ) at that frequency. This can be explained in the same way as in the previous section. The same tendency is confirmed by comparison of Figures 4.13 through 15 and Figures 4.26 through 28 (or refer to Figure 4.25 for an example). The magnitude of local response decays exponentially, the same way as the local Rayleigh index does along the flame boundary.

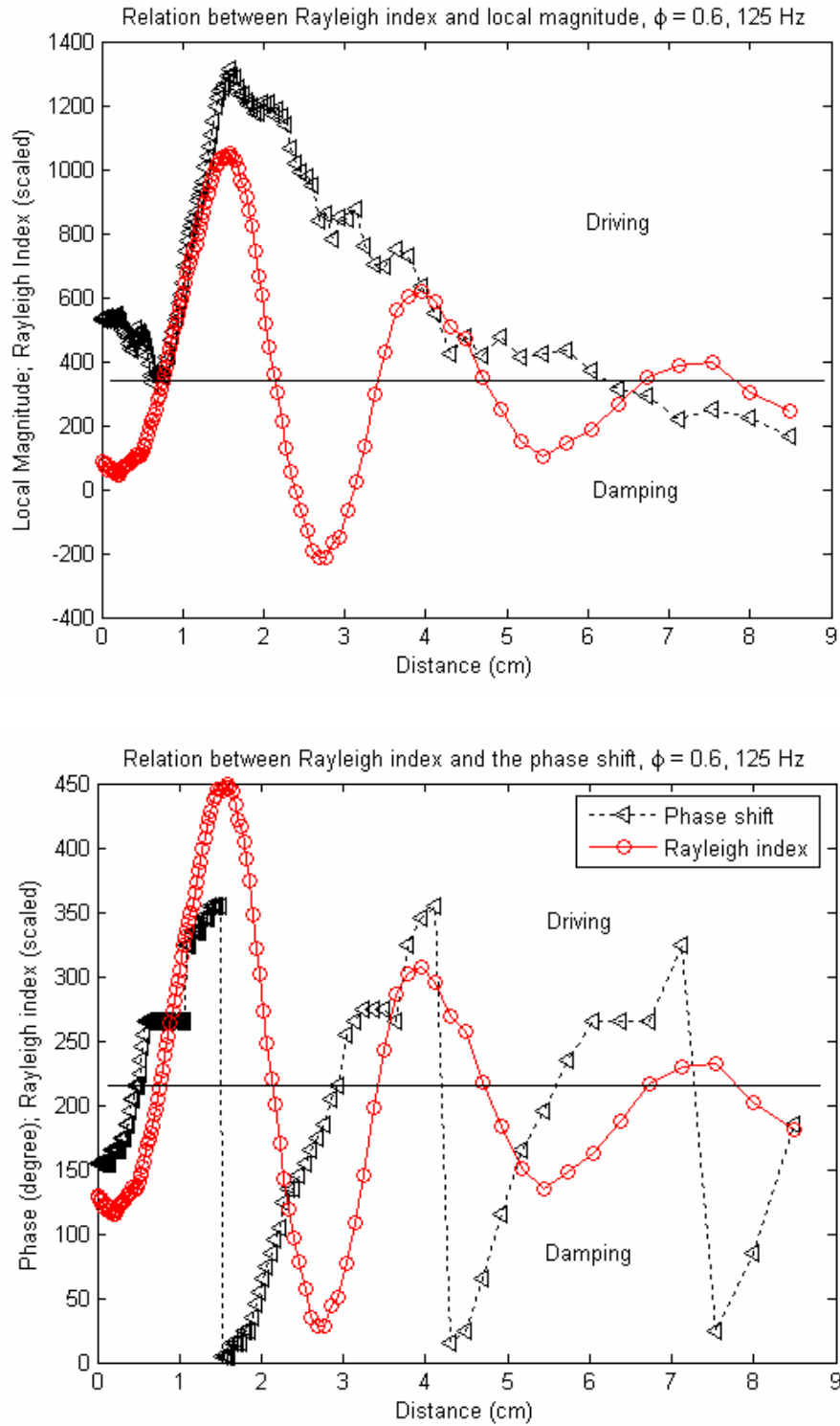


**Figure 4.25.** An example of relevance between the phase shift and Rayleigh index.

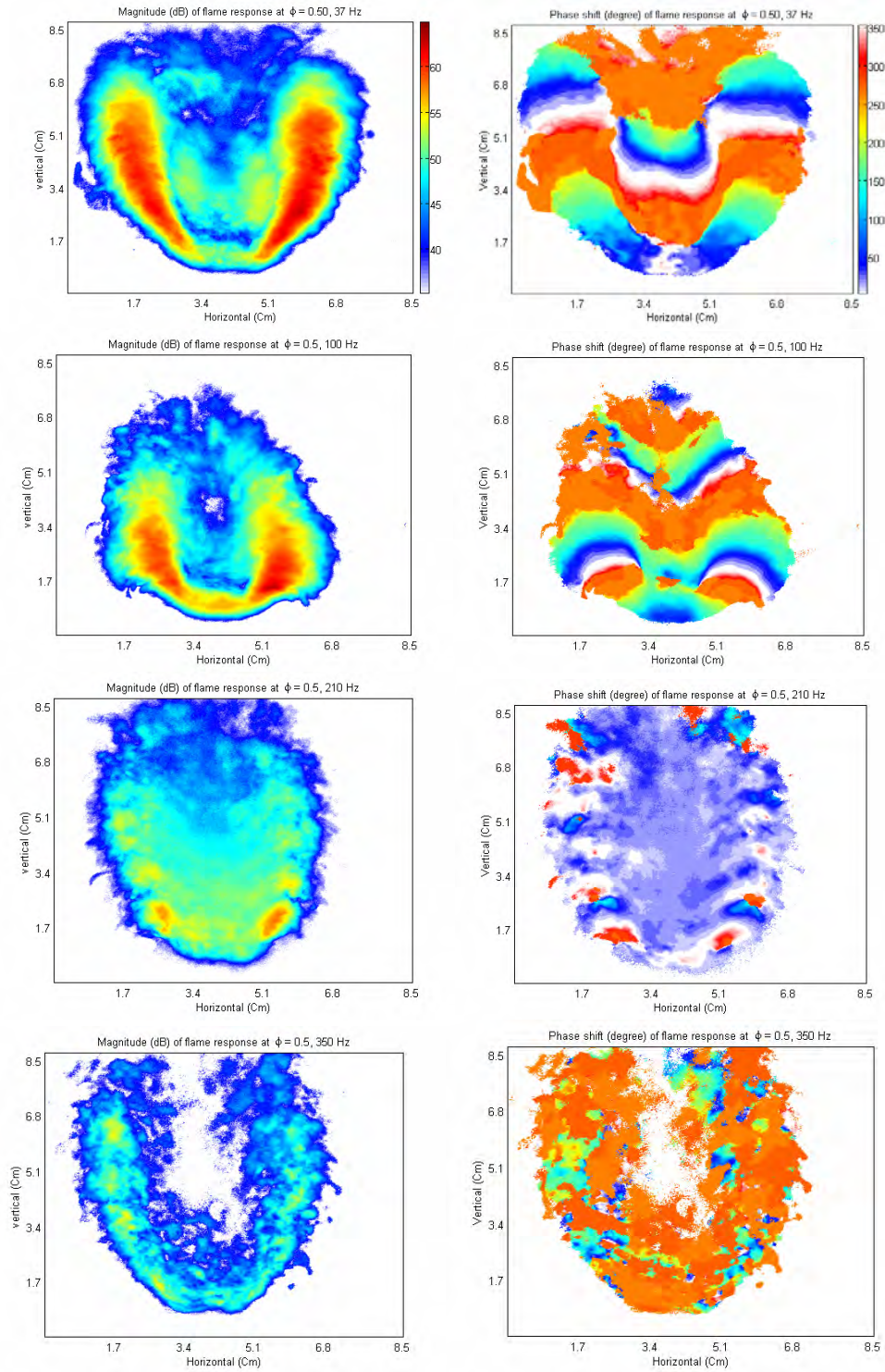


**Figure 4.26. Magnitude (left), and phase shift (right) of flame response,  $\phi = 0.5$  (at the center plane of the flame).**

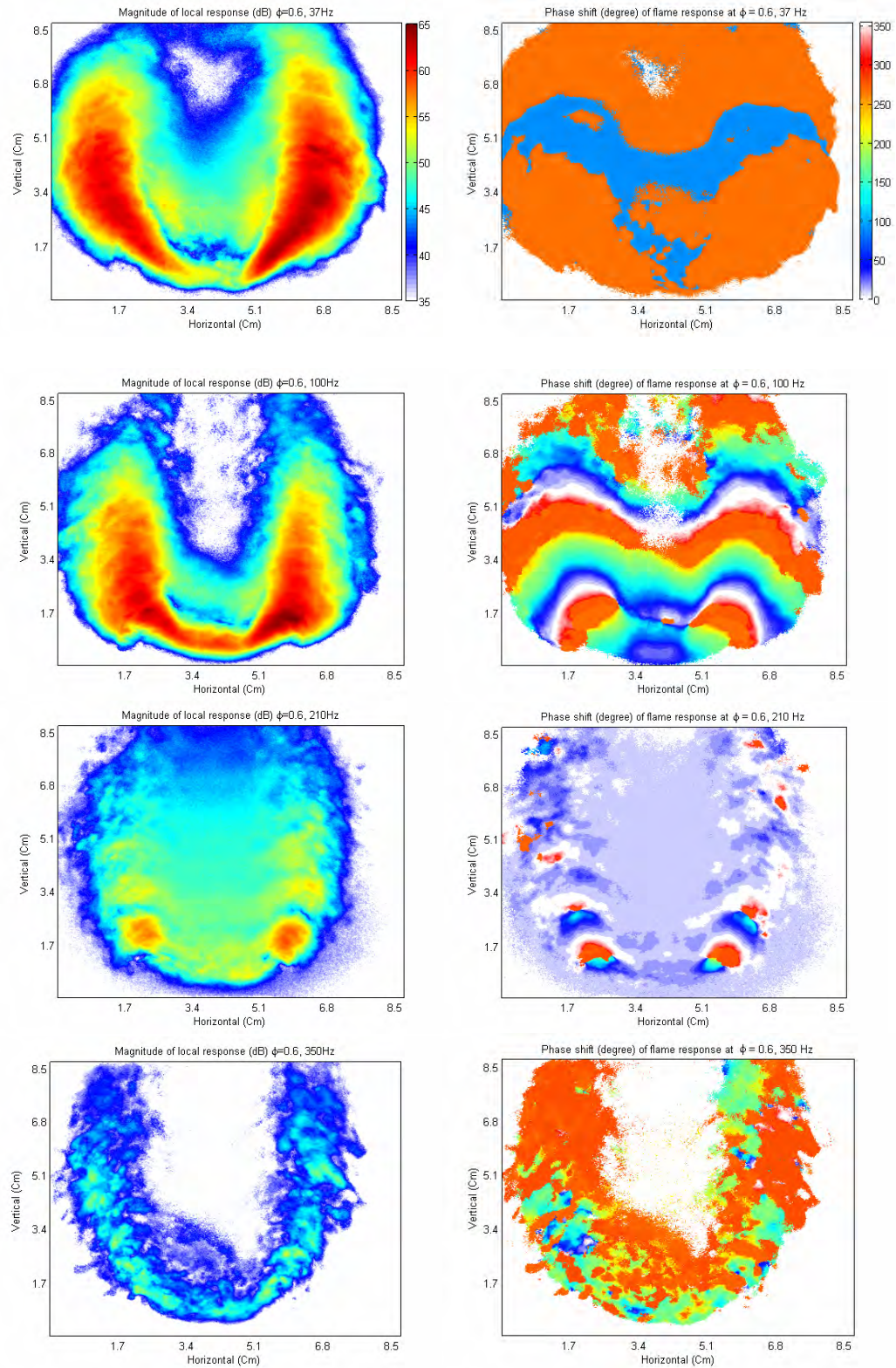


**Figure 4.27. Magnitude (left), and phase shift (right) of flame response,  $\phi = 0.6$  (at the center plane of the flame).**

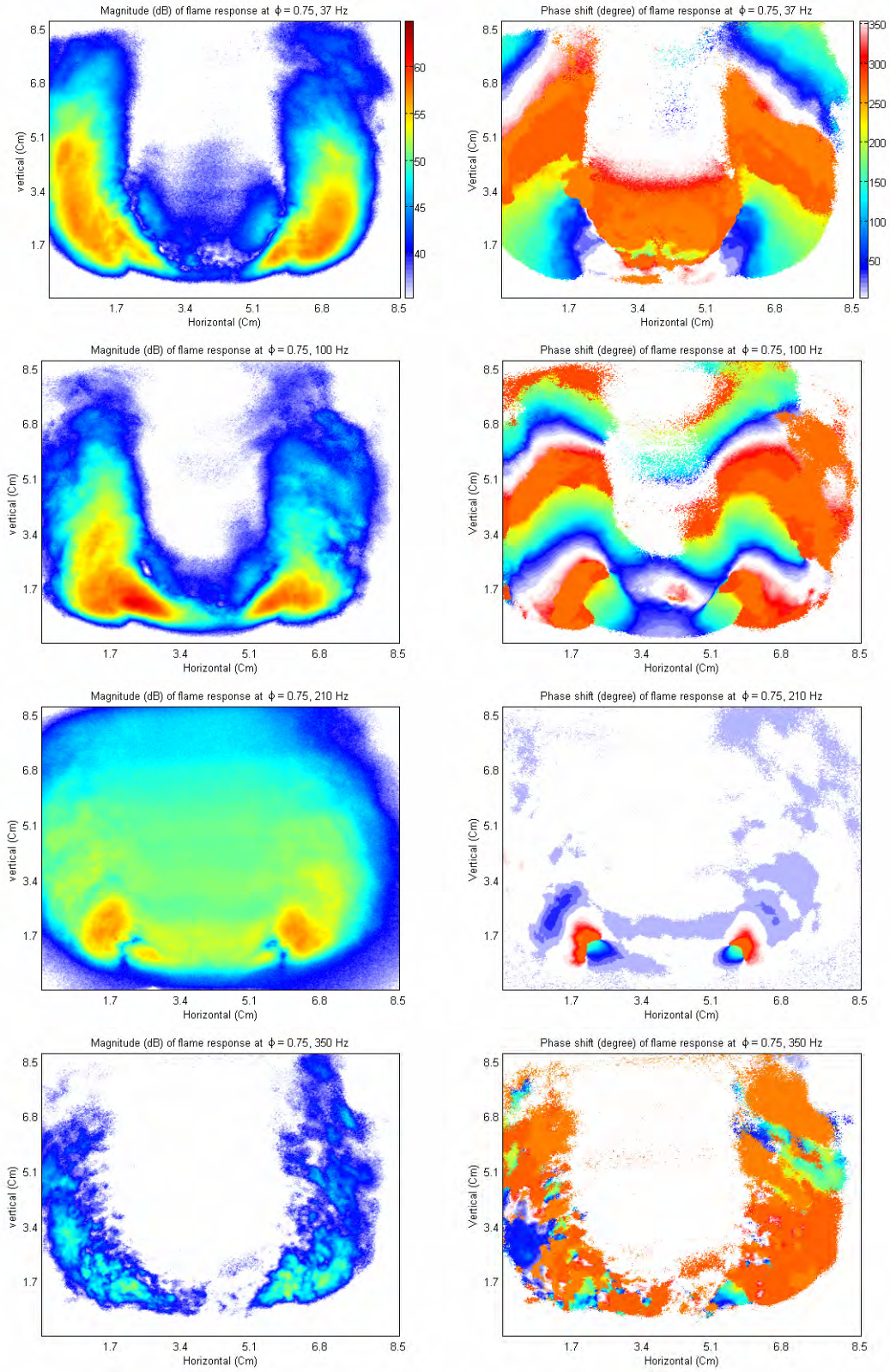


**Figure 4.28. Magnitude (left), and phase shift (right) of flame response,  $\phi = 0.75$  (at the center plane of the flame).**

## 4.7 Summary

This part of the thesis is intended to 1) provide a general experimental procedure to precisely quantify the dynamic response of combustion under the real combustion environment; 2) obtain practically-applicable data such as the global and local flame responses, using a commercially available type of swirl burner; 3) investigate the phenomena that have significant effects on determining the dynamic behavior of combustion systems, the thermo-acoustic coupling, and response of the flame to outside disturbances. This work was performed with a low swirl burner that uses small air jets to swirl the premixed flow inside the burner tube, leaving the center core flow undisturbed and produces a divergent flow above the burner exit. Flow divergence provides a highly effective means to stabilize lean premixed combustion because it enables the flame to settle where the local velocity equals the flame speed. To examine flame stability and behavior, a high degree of heat release fluctuation ( $\sim 10\%$  amplitude of the mean value) was induced by imposing pressure fluctuations (where only  $\sim 0.1\%$  mean amplitude was required). The frequency dependence of the fluctuation level and the phase shift of fluctuations were evident from the data presented. The phase shift, measured as the phase lag from the imposed acoustic waves, is a parameter of great importance in determining the stability and response of the combustion dynamics.

The local Rayleigh index distribution has a very distinct feature: it has a series of donut-like structures (toroids) distributed along, presumably, the shear mixing zone. Thermo-acoustic coupling is significant in the lean region, near the flame boundary, and where the shear entrainment of ambient air further dilutes the already lean initial fuel/air mixture.

At the flame boundary, shear mixing lowers the local equivalence ratio into the unstable zone (as depicted in Figure 1.2) while keeping it high enough to sustain the flame. The toroids widen with increasing equivalence ratio, growing outward (not inward) to reach locations, 'leaner' and more susceptible to instabilities. The toroidal structure does not seem to result directly from swirl since it is expected that the structure would then be asymmetric, following the spiraling flow field. Yet, the structures are perfectly symmetric over all conditions (excitation frequencies and equivalence ratios). This leads to the conclusion that the driving force for the formation of this structure is not the swirling tangential and radial flows, but, rather, the axial component of the flow field shearing with the outer flow (air in this case). Also, these structures appear to be a strong function of excitation frequencies, with a possible lock-on mode at low frequencies.

It is found that the region with large absolute global Rayleigh indices coincides with the region where the flame response is far greater than other places (160 – 240 Hz). The combustor geometry gives a resonant standing wave of approximately 120 Hz which is outside of this high response region. In the vicinity of 400 Hz, the absolute value of the Rayleigh index increases, and so does the magnitude of the flame response, which seems to be approximately the second mode.

The role of swirl is best shown by the fact that for three different equivalence ratios (0.5, 0.6, and 0.75), the global quantities (the Rayleigh index and flame responses) are not affected significantly meaning that the swirl ensures more stable and consistent performance of the system.

Three different equivalence ratios were tested for this configuration; however the equivalence ratio dependencies in any of the parameters are very weak in the current range ( $\phi = 0.5 \sim 0.75$ ). This is because the swirl creates a wider range of stably operational equivalence ratio, allowing the flame to remain stable at very low equivalence ratio.

The three equivalence ratios (0.5, 0.6, and 0.75) are in the mixture range where the flame responses can be treated almost the identically. It also can be concluded that the experimental methods gives quite reliable measurements providing repeatable results from the comparison of the three different equivalence ratio cases.

# Chapter 5

## Further Study of Swirl Burner

### Combustion Dynamics

---

In this chapter, as an extension of the study on combustion dynamics in the previous chapter, the dynamic behavior of a swirl burner is studied, with two different types of swirlers under atmospheric and elevated combustor pressure of 1.5 atmospheres. For this, a new combustion chamber that can hold up to 5 atmospheres has been constructed. The range of excitation frequency is from 37 Hz to 110 Hz which is allowed by the current experimental configuration. This work is intended to give insight into the design parameters of practical combustion systems, and to be the beginning of an effort to extend the availability of the experimental approach described in the previous chapter to more practical uses. Comparisons are made among the data taken at several different conditions to investigate how the dynamics change with varying conditions.

## 5.1 Introduction

To extend the applicability of the experimental methods introduced and developed in the previous chapter, it is necessary to make the experimental conditions as close to the real combustor conditions as possible.

Higher combustor pressure is an important improvement in our experimental configuration, which is achieved, thanks to the development of a high pressure chamber, which is introduced in the next section. In many practical combustion systems, especially gas turbine applications, higher overall combustor pressures occur so that it becomes an important experimental subject to investigate the effect of higher combustor pressure on the combustion dynamics. Low swirl burners are gaining popularity in practice nowadays for various advantages such as low pollutant (NO<sub>x</sub>) formation due to the lowered flame temperature by the lean-burn schemes, high fuel efficiency, and wider range of stable operation in the lean-burn schemes.

In this chapter, as a beginning of an effort to improve the practicality of the experimental methods being developed throughout this thesis work, the effect of higher combustor pressure, up to 1.5 atm for the present time, is studied. Also, two different types of swirlers are used to study how the different swirl conditions change the combustion dynamics of the system.

Though the same experimental procedures and apparatus as in the previous atmospheric work are employed, more improvement and refinement of the experimental

configurations are required to be optimal for the current setting (the high pressure chamber and its acoustic characteristics). Pressurization of the new combustor, at this time, was possible only up to 2 atmospheres, and approximately 1.5 atmospheres (22.2 psi) has been used for this work; the restriction has been set by safety concerns. One and a half atmospheres is not a high enough pressure to worry about the LIF signal quenching due to the high pressure (signal drop is around 5%, Kobayashi et al. 2002), so in this work, high pressure signal quenching is not considered. This work presents the up-to-date status of the experimental methods and the measurements as a result.

Two different types of swirler have been used. One (swirler A) has been described in the previous chapter (Figure 4.7); the other one (swirler B) is expected to have a narrower range of equivalence ratio for stable operation than swirler A due to its lower swirl number (Figure 5.1). The operating ranges are somewhat different for the both swirlers that the window of operating range for a stable combustion is narrower for the newer one shown in Figure 5.1 (swirler B). Due to this difference in stable operation range, comparisons are made between slightly different overall equivalence ratios. Data has been acquired with the conditions for the old swirler (swirler A), equivalence ratio 0.50 (1 bar), 0.63 (1, 1.5 bar); and for the new swirler (swirler B), 0.55 (1, 1.5 bar).

This work, as an extension of the previous chapter, presents an experimental procedure for determining features of combustion dynamics, extended knowledge of combustion dynamics in wider variety of operating conditions. Data have been taken with two types of swirler designs.

## 5.2 Experimental Configurations

The overall experimental set-up is composed of five significant parts: 1) the laser system, 2) the optics and optical pathway, 3) the burner assembly (premixer, burner, swirler, and gas feeding system), 4) the combustion chamber with acoustic drivers and the controller, 5) data acquisition system. Of these, the swirler, the premixer, and the combustion chamber are the distinct features of the current work. For the rest of the apparatus, refer to previous chapters (Chapter 2, 3, and 4).

### 5.2.1 The Swirler

Figure 5.1 shows the new swirler (swirler B). The vane angle,  $\alpha$ , is 65 degrees the same as the old swirler (swirler A, Figure 4.7). The aspect ratio (ratio of screen radius,  $r$ , to the whole radius,  $R$ ) is 0.8 for swirler B, while it is 0.5 for the swirler A, providing swirl numbers of 0.5 to 0.55 for the swirler B compared with 0.6 to 0.7 for the swirler A.

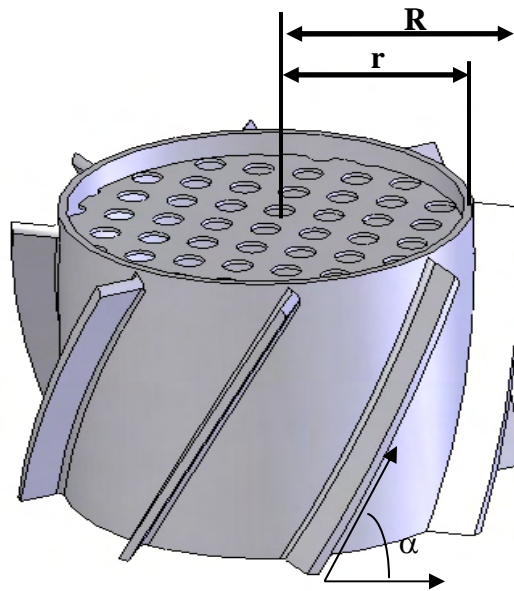


**Figure 5.1. The new swirler (swirler B).**

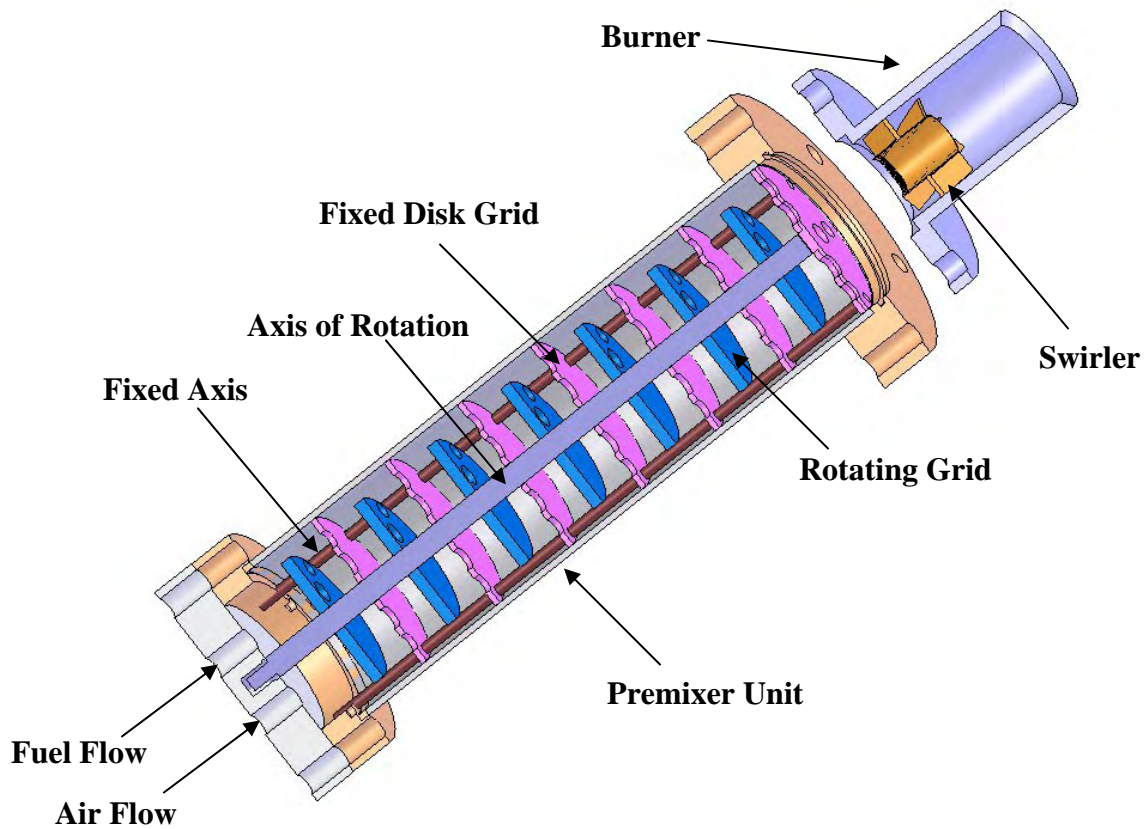


**Figure 5.2. Premixer, burner, and swirler assembly (designed by Y. Huang, University of Iowa).**

According to the contributor (Dr. Robert Cheng, Lawrence-Berkeley Livermore national laboratory), the swirl numbers can be changed by changing the blockage ratio of the center screen (the grid structure at the center, shown in Figure 5.1). The outer diameter ( $2R$ ) is one inch, which fits in the burner whose inner diameter is 1 inch, and the swirler is held on to the burner by a screw.

### 5.2.2 Premixer and Burner

Figure 5.2 shows the premixer/burner assembly. The premixer is a custom designed one with rotating disk grid that can be turned to regulate the degree of premixing. When the holes of rotating and fixed disk grids are in line, it is expected that the least amount of premixing occurs, and when they are 90 degrees from each other, the greatest amount of premixing is expected. For the present work, the holes are set to be in line as a start.

The premixer is an 8.12 inch long cylindrical pipe section, with 0.035 inch wall thickness and 1.88 inch inner diameter. The disk grids are 1.57 and 1.87 inches in diameter for the rotating and fixed ones, with 0.08 mm thickness for both. The sizes of the grid holes are 0.2 and 0.25 inch in diameter for both disks' outside and inside holes respectively, and each disk has 4 grid holes.

The fuel and air feeding rate is shown in Table 5.1, and the calibration charts are given in Appendix C.

<b>Swirler A (Figure 4.7)</b>		<b>Fuel</b>	<b>Air</b>
<b>Equivalence Ratio</b>		<b>0.5</b>	
<b>Combustor Pressure (bar)</b>		<b>1.0</b>	
<b>Flow Rates</b>	<b>Volumetric (SLPM)/Flow meter Reading</b>	<b>6.170 /13.41</b>	<b>117.4 /356</b>
	<b>Mass (g/s)</b>	<b>0.0686</b>	<b>2.349</b>

<b>Swirler A (Figure 4.7)</b>		<b>Fuel</b>	<b>Air</b>	<b>Fuel</b>	<b>Air</b>
<b>Equivalence Ratio</b>		<b>0.63</b>			
<b>Combustor Pressure (bar)</b>		<b>1.0</b>		<b>1.5</b>	
<b>Flow Rates</b>	<b>Volumetric (SLPM)/Flow meter Reading</b>	<b>7.460 /16.00</b>	<b>112.4 /341</b>	<b>7.460 /16.00</b>	<b>112.4 /341</b>
	<b>Mass (g/s)</b>	<b>0.0829</b>	<b>2.249</b>	<b>0.124</b>	<b>3.374</b>

<b>Swirler B (Figure 5.1)</b>		<b>Fuel</b>	<b>Air</b>	<b>Fuel</b>	<b>Air</b>
<b>Equivalence Ratio</b>		<b>0.55</b>			
<b>Combustor Pressure (bar)</b>		<b>1.0</b>		<b>1.5</b>	
<b>Flow Rates</b>	<b>Volumetric (SLPM)/Flow meter Reading</b>	<b>7.235 /15.59</b>	<b>125.2 /380</b>	<b>7.235 /15.59</b>	<b>125.2 /380</b>
	<b>Mass (g/s)</b>	<b>0.0804</b>	<b>2.505</b>	<b>0.121</b>	<b>3.758</b>

**Table 5.1. Flow Rates.**

### 5.2.3 High Pressure Chamber

The new high pressure chamber is shown in Figure 5.3 and 5.4. The combustion chamber is made out of stainless steel sections and a stainless steel top that gives closed end acoustic condition, and is connected to pressure regulator valves at the top section. The horizontal or 'arm' sections house a pair of loudspeakers (Crystal CMP-12, 4 ohm resistance) on each side. The exhaust port is connected to the motor-controlled regulator valves that regulate the mean pressure inside the combustor by adjusting the opening of the valves.

The speakers are 12 inches in diameter and powered by a 2600 W power amplifier (MacKie M2600) that is capable of generating 1300W per channel (we have two channels-one on each end of the chamber) thus allowing maximum of 650W per speaker. A function generator (Wavetek 171) provides the input signal in to the controller which conditions and feeds the signal into the MacKie amplifier (see Chapter 4 for the controller). Nitrogen cooling and purging is used to keep the speakers from high temperature and moisture; a co-flow in the chamber, also nitrogen, is used as shown in Figure 5.3 (H). This system prevents excessive heat transfer to the chamber wall, keeping the entire system from unexpected heat failure.

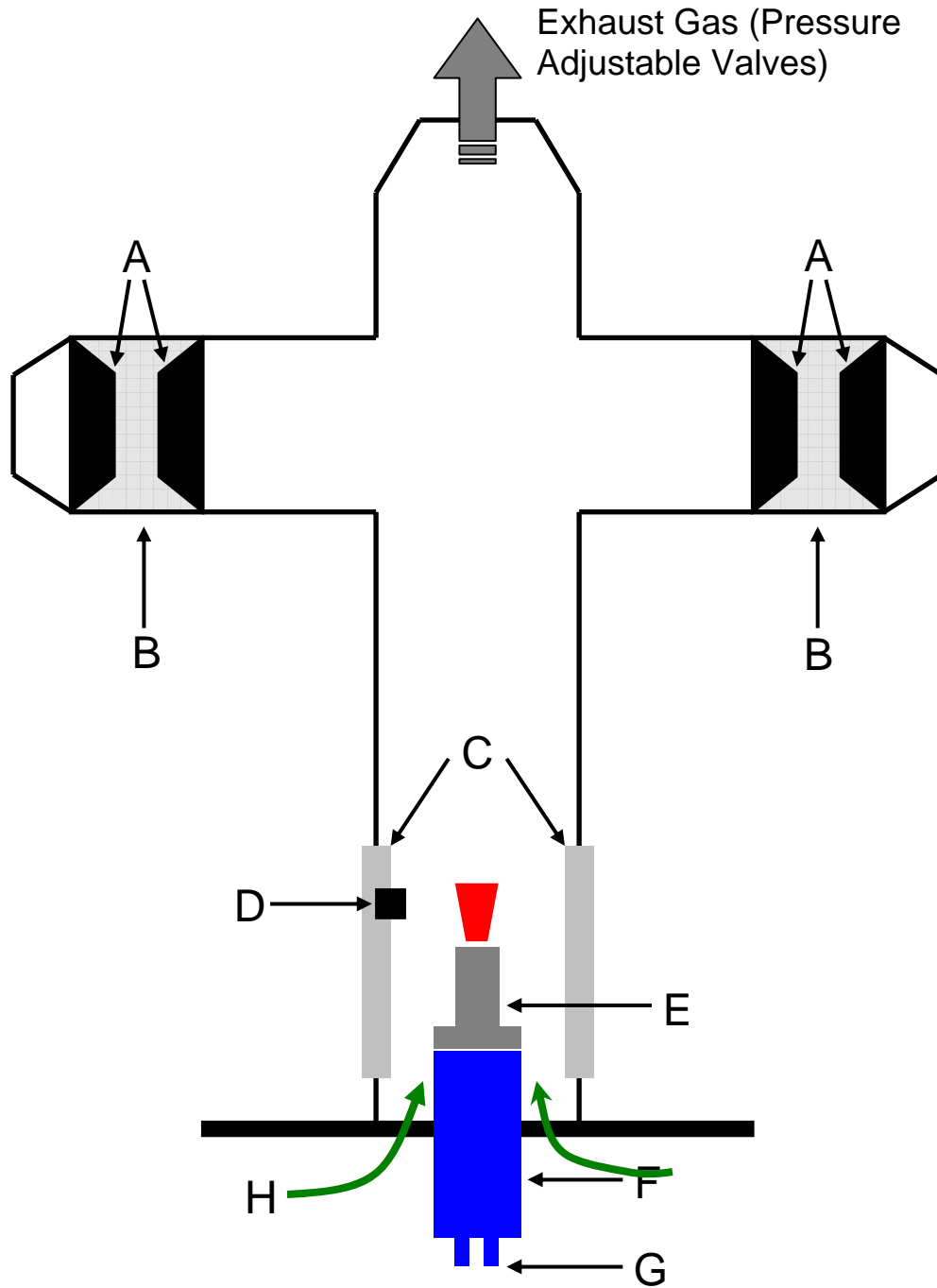
The chamber pressure is controlled by three motorized valves installed in the laboratory, Seamans Center, University of Iowa (supervised by Prof. Al Ratner in the Department of Mechanical and Industrial engineering). By controlling the amount of valve opening, the mean pressure inside is increased to a desired level (up to 1.5 atmospheres, in this

experiment). Pressurization and decompression must be performed very slowly to keep the mean pressure level inside the chamber at quasi-steady state to prevent mechanical failures (e.g., quartz windows and connection parts) due to the sudden pressure change.

The amplitude of the fundamental driving mode (the acoustic waves) is actively controlled by custom-designed electronics, which measure the pressure in the acoustic chamber at the burner with a pressure transducer (PCB 106B50), and appropriately scale the power output of the speakers. The signal from the transducer is notch-filtered to ensure the intended driving mode is correctly amplified or attenuated.

The piezoelectric pressure transducer (106B50) is located at the height where the flame sits. This transducer features high sensitivity (493.3 mV/psi) and stable thermal characteristics. A PCB model 482A16 power supply and amplifier, with the gain set at 100, powers the transducer.

For the optical access, quartz windows have been used, for better transmission of UV lights. The sizes of the windows are 12 inches by 1.5 inches for the laser beam sides, and 12 inches by 6 inches for the imaging sides. A  $\frac{1}{4}$  inch thick quartz window is capable of standing up to 2 atmospheres, and one inch thick windows can hold up to 5 atmospheres at least. In this experiment, the  $\frac{1}{4}$  inch thick windows are used. The imaging resolution is  $159\ \mu\text{m}$  by  $159\ \mu\text{m}$  ( $174\ \mu\text{m}$  by  $174\ \mu\text{m}$  for the work in Chapter 4) with the size of imaged area 7.5 cm by 8.1 cm.



- |                        |                     |                        |
|------------------------|---------------------|------------------------|
| A: Loudspeakers        | B: Speaker Section  | C: Quartz Window       |
| D: Pressure Transducer | E: Swirl Burner     | F: Adjustable Premixer |
| G: Fuel/Air Inlets     | H: Nitrogen Co-flow |                        |

**Figure 5.3. High Pressure Chamber (Diagram).**

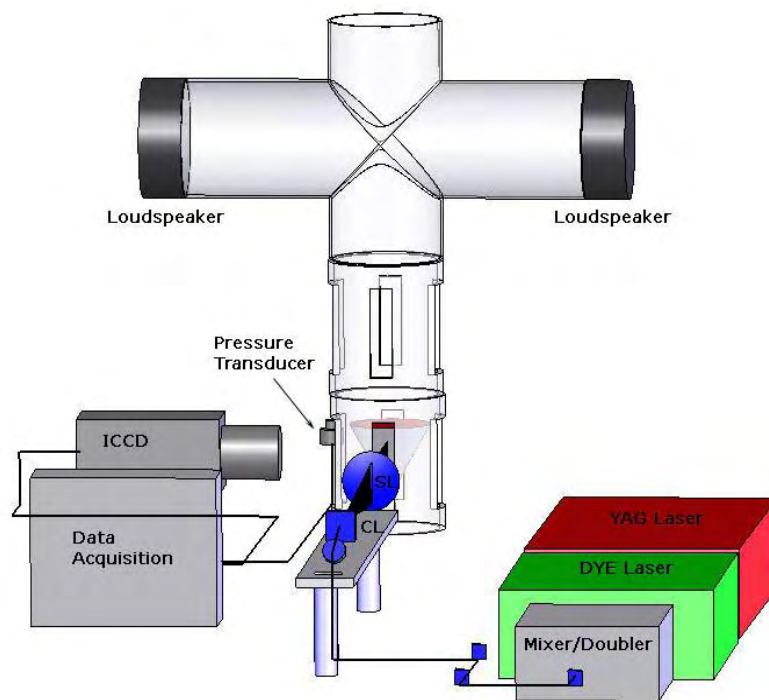


**Figure 5.4. High Pressure Chamber. The experimental layout (top); and a photo of the actual chamber (bottom, construction by Ratner Group, University of Iowa).**

### 5.2.4 Data Acquisition

The computer used in the data acquisition system consisted of an AMD Athlon™ 64, 2.0 GHz processor with 1 GB RAM and 160 GB of total hard drive space. Installed in the computer is a NI-DAQ 6024 PCI (National Instrument) 16-bit data acquisition boards capable of 4 differential channel measurements capable of up to 100 kHz. The channels are given to: pressure, camera gating signals, and time. Also in the same computer is the PCI controller card for the Princeton Instruments ICCD camera. The software used for the data acquisition is National Instruments LabView 7.0 for pressure and gating signals, and Princeton Instrument WinView32 for image acquisition.

## 5.3 Experimental Procedure

This work involves pressurizing and decompressing the combustion chamber, which requires a cautious and slow preparation and wrap-up processes for each set of experiment. The rest of the general procedure is almost identical to the one described in the previous chapter.

1. Laser preparations
  - Optimize the mixer/doubler tuning crystal angles for maximum energy conversion.
  - Check the laser beam profile and power. Leave for 15 minutes to reach the steady state.
2. Set gas streams
  - Cooling air for the acoustic drivers.

- Nitrogen purging gas through ICCD camera.
  - Turn on the ventilation pump.
  - Open valve for fuel/air stream, and direct the stream to the corresponding flow controllers.
  - Light up the flame right after the opening of the valve
  - Check the fuel and air stream stability.
3. Optical alignment
- Check the laser beam path with cards with lowered laser power at each point of beam deflection to ensure that the beam is directed in the right way.
  - Focus the ICCD camera on a card in the test section. Ensure the laser sheet is passing through the probed volume cleanly and focused at the center.
4. Beam profile calibration
- Minimize laser energy throughput using the wave plate. Set camera gain to 100, and gate width to 1  $\mu$ s with 1-2 ns delay.
  - Allow laser sheet to impinge on fluorescent card and acquire the beam profile with the ICCD camera, placing card in three different positions (left, center, right).
  - Return camera gain to 200, and gate width to 100 ns and wave plate inside the mixer/doubler to allow maximum laser energy throughput.
5. Pressurize the combustion chamber.
- Close two of the three motorized valves completely.

- Close the one remaining open valve very slowly, trying to increase the mean pressure inside the chamber quasi-steadily. Monitor the pressure gauge and the flame all the time.
  - Wait for more than 5 minutes to see that the mean pressure inside the chamber is fixed and in steady state at a desired pressure.
  - No need for this step for atmospheric experiments.
6. Prepare devices.
    - Set acoustic driver power on controller, and activate drivers.
    - Turn on oscilloscope to monitor each and every signal.
  7. Perform pre-runs (duration approximately 3 minutes).
    - Start LabView data acquisition program (main DAQ program and gating signal delayer).
    - Start WinView32 camera imaging software, typically taking 300 images (limited by system memory).
  8. End experiments
    - LabView and WinView32 routines end automatically
    - Turn off fuel and air, extinguishing the flame.
    - Turn off acoustic drivers.
  9. Repeat experiment.
    - Repeat steps 6-8 until more than 1800 images or more have been acquired at a particular test condition.
  10. Change experimental conditions.
    - Change the frequency driving acoustic wave.

- Repeat steps 4 through 8 until experimental session is complete.

#### 11. Decompress the combustion chamber.

- Leave the two closed valves at this point.
- Open the valve that was used to regulated the combustor pressure in step 5 very slowly. It is not recommended to open the valve abruptly, since sudden drop of pressure may cause mechanical failures.
- No need for this step for atmospheric experiments.

#### 12. Shutdown systems.

- Shut off the laser.
- Turn off the ventilations and other related devices.
- Store acquired data – burn DVDs for post-processing and archival.

## 5.4 Results and Discussion

Experiments have been performed where the swirler sustains the flame stably. For the swirler A, the equivalence ratio range of stable operation is wide ( $\phi \geq 0.5$ ) so data has been taken at  $\phi = 0.5$  and  $0.63$ , and pressurization was attempted at  $\phi = 0.63$  where the flame is most stably sustained at the elevated pressure (1.5 atm). For swirler B, the window of the equivalence ratio range for stable operation is far narrower than swirler A due to the weaker swirl,  $\phi = 0.55$  was used for stably sustaining the flame. Technical problems arise in pressurizing the combustion chamber; especially, due to the response time of the flow controllers it is harder not to lose the flame at other equivalence ratios than those suggested here at this point.

As in Chapter 4, the local distribution of Rayleigh index (the thermo-acoustic coupling) and response of flame (magnitude and phase) are calculated from the measurements. Also, the global parameters of the entire control volume (here, the imaged area) are calculated as important parameters to describe the characteristics of the given combustion system.

Swirlers are the essential part of the swirl burner system that determines the performance of the burner by changing the flow field. In this work, two different types of swirlers are used, and comparisons were made to show the effects of swirler design and elevated pressure inside the combustor.

#### **5.4.1 Distribution of Local Rayleigh Index**

Local Rayleigh index distributions are shown in Figures 5.5 through 5.9. In the figures presented, there are alternating Rayleigh index distributions at the boundary of the flame zone at relatively higher frequencies (85~110 Hz, irregardless of the flow condition).

As discussed earlier in Chapter 4, the toroidal structure seems to form due to the shear mixing between the higher speed flow in the flame region which dilutes the fuel/air mixture at the flame boundary leading to lower local equivalence ratios and greater susceptibility toward instabilities. And the distribution of alternating chunk of local phase shift, possibly due to the vortex pairs shed from shearing flows (the axial mixture flow and the outer flow), creates the alternating Rayleigh index pattern (described as the toroidal structure in this work) and the region of consistently high magnitude of local

flame response (Figures 5.14 through 5.23). It seems that the toroidal structures occur where the vortex forms due to the shear mixing, or the Kelvin-Helmholtz instability (KHI) mechanism at the boundary of the flame, though it remains to be seen whether these structures coincide with the vortex formation with the use of velocity field measurements. However, as shown earlier in Figure 4.12, the location of the toroidal patterns coincides with the maximum gradient in the axial velocity distribution such that the structure is located in the region of maximum shear, or the shear mixing region between the inner jet and outer fluid flow. This supports the arguments above that the significant Rayleigh index pattern is related to the shear mixing phenomena.

The structure in the flame boundary (Figures 5.5 through 5.9) is not as clear as in the data presented (Figures 4.13 through 4.15) in the previous chapter due to the nitrogen co-flow which reduces the velocity gradient between inner and outer flow, thus reducing the intensity of shear mixing. Plus, after the shear mixing, the local mixing zone equivalence ratio does not drop significantly since the outer layer is mostly nitrogen, a layer of co-flow that encloses the flame, thus the less clear toroidal pattern (or no pattern at all at lower frequencies).

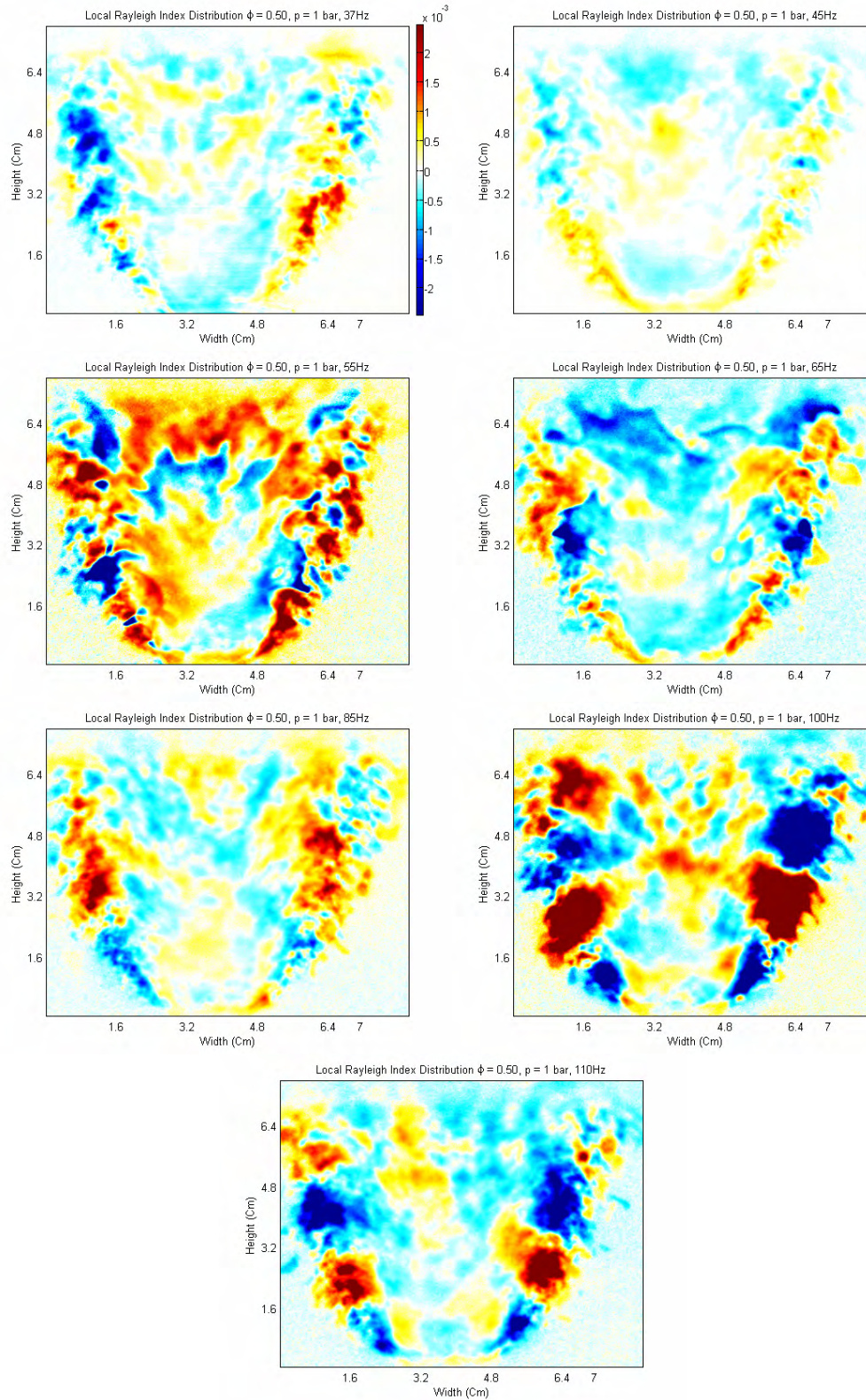


**Figure 5.5. Rayleigh index distribution, 1 atm,  $\phi = 0.50$ , swirler A.**

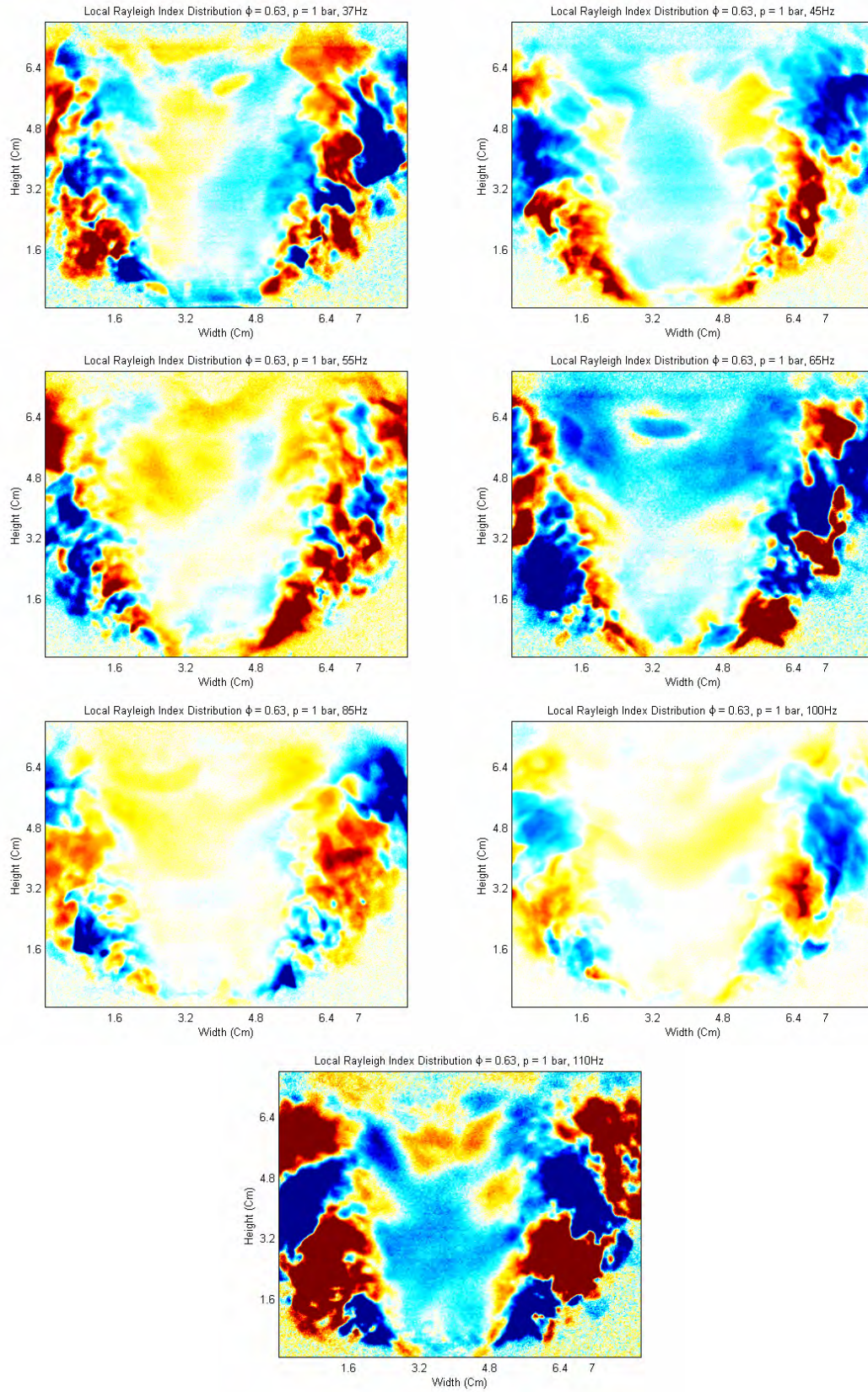


**Figure 5.6. Rayleigh index distribution, 1 atm,  $\phi = 0.63$ , swirler A.**

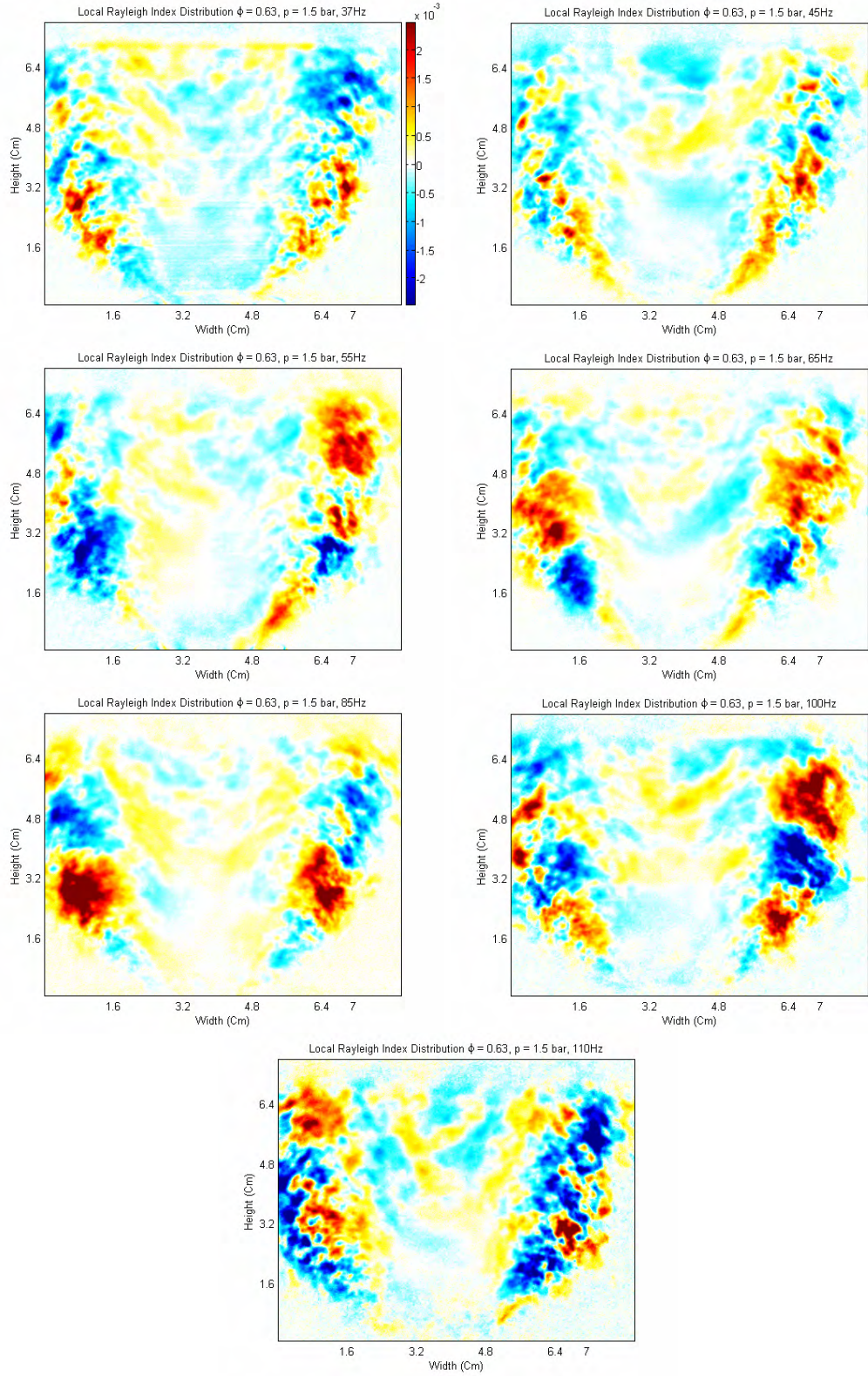


**Figure 5.7. Rayleigh index distribution, 1.5 atm,  $\phi = 0.63$ , swirler A.**

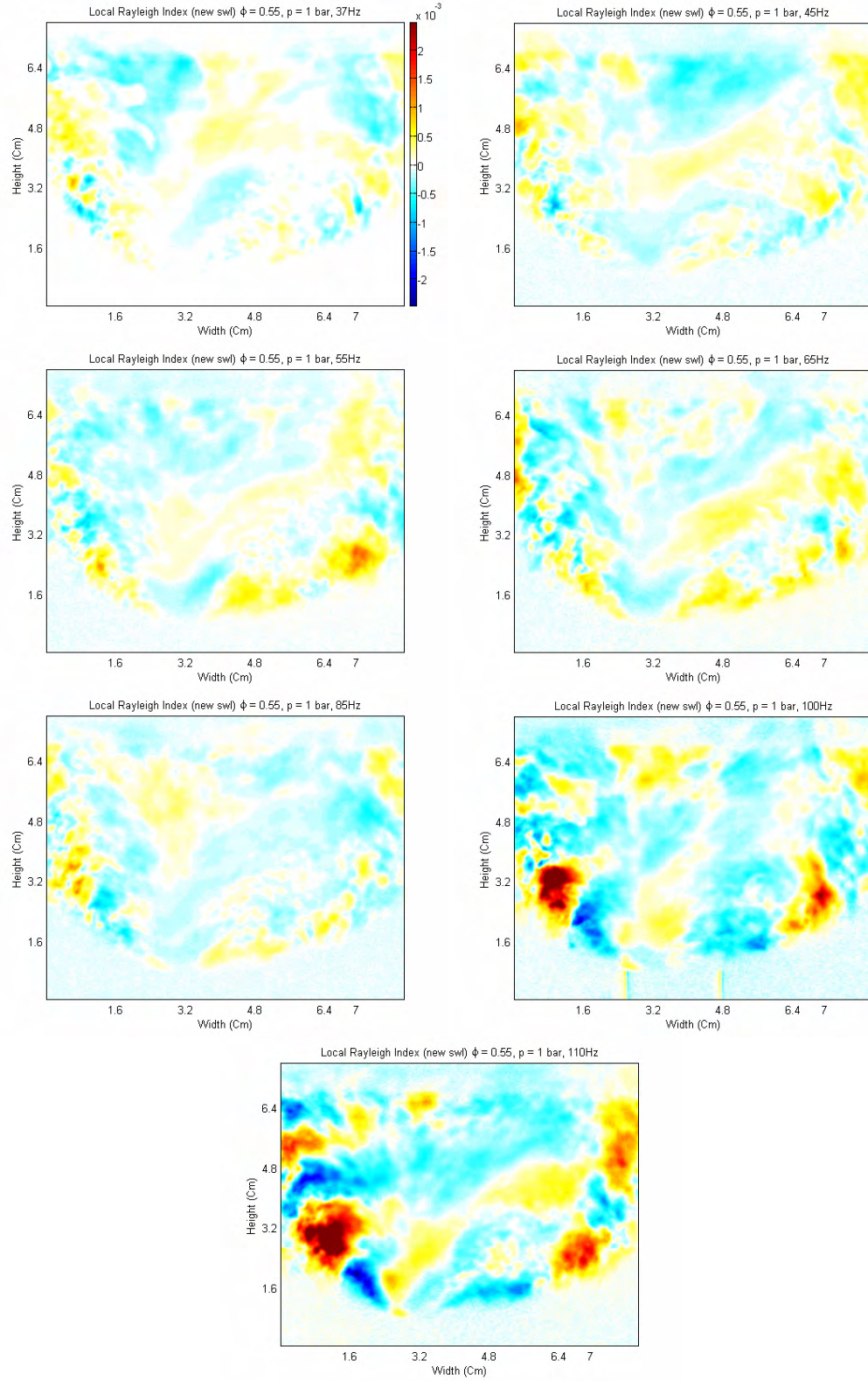


**Figure 5.8. Rayleigh index distribution, 1.0 atm,  $\phi = 0.55$ , swirler B.**

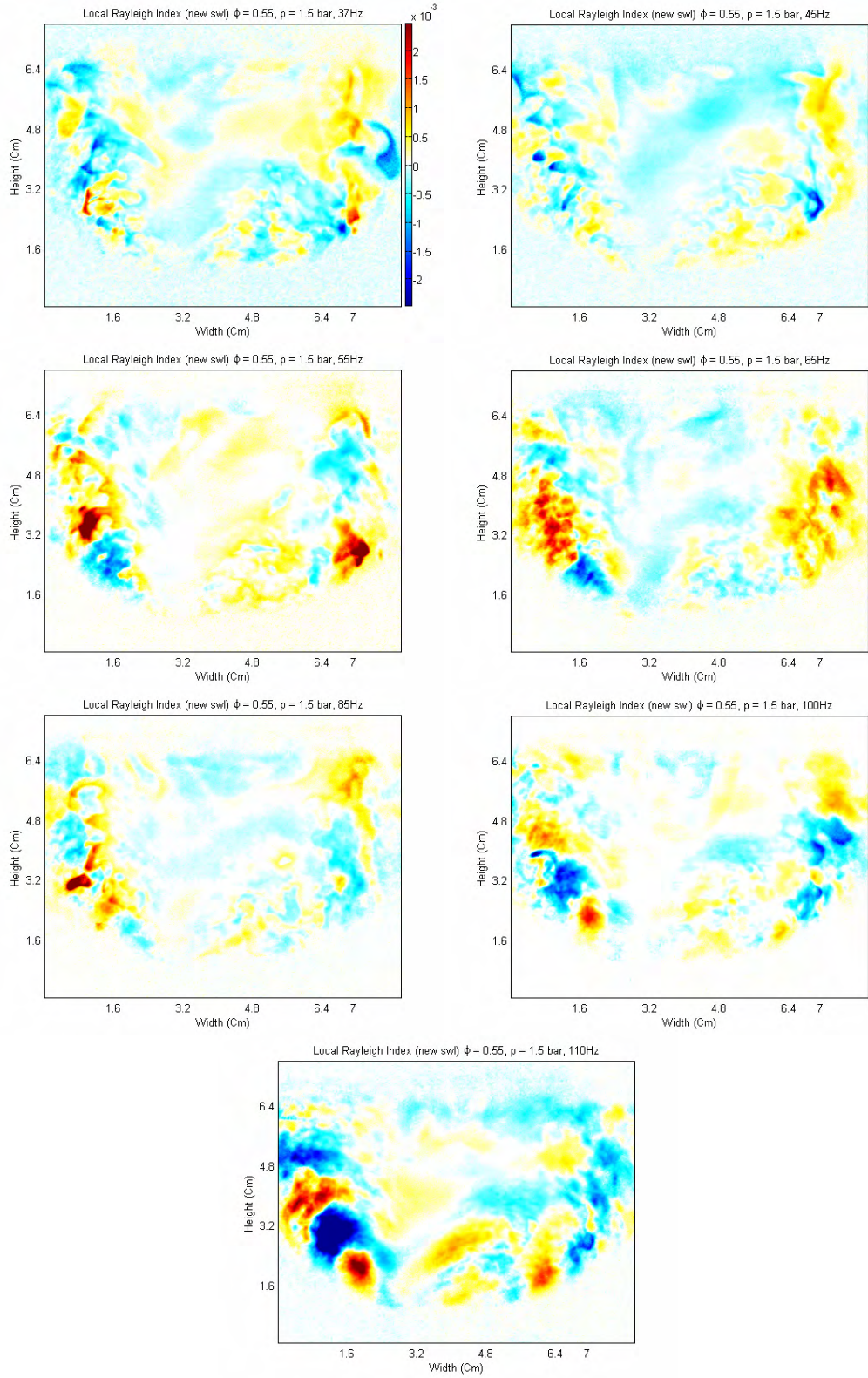


**Figure 5.9. Rayleigh index distribution, 1.5 atm,  $\phi = 0.55$ , swirller B.**

The data (Figure 5.5 through 5.9) confirms the observation made in Chapter 4 that the equivalence ratio does not affect the dynamics of combustion very much in the range of  $\phi = 0.5$  to 0.63 presented here for swirler A. The patterns of local Rayleigh index distribution do not show much difference for different equivalence ratios, though they still show strong dependence on the excitation frequency. Also, elevated combustor pressure (to 1.5 atmospheres) does not seem to affect the distribution of local combustion dynamics significantly from the comparisons between Figures 5.6 and 5.7 (swirler A), and between Figures 5.8 and 5.9 (swirler B). The distribution patterns of local Rayleigh index and local flame responses are not affected by the combustor pressure, while they show a strong dependence on the excitation frequencies.

Frequency is a dominant factor, according to the figures, in that the way the toroidal pattern is distributed is strongly dependent on the excitation frequency. At lower frequencies (e.g. 37 and 45 Hz), the structure is hard to recognize, while at higher frequencies (e.g. 100 and 110 Hz) the structure is obvious in all five different conditions tested. The higher frequencies seem to be coupled more to the behavior of combustion than the lower frequencies.

As in Chapter 4, the wave numbers of these alternating toroidal patterns are calculated along the shear mixing zone, showing that the wave number, the spatial frequency of the toroids occurrence, is dependent on the acoustic forcing frequency. The data presented in this chapter confirms the frequency dependence of the wave number such that it increases with increasing excitation frequency in the experimental range (37-110 Hz). Figure 5.10

shows the wave numbers versus the excitation frequencies for the five different experimental settings. The frequency dependence of the wave numbers is very similar to that shown in Figure 4.22 both quantitatively and qualitatively over the same range of excitation frequency.

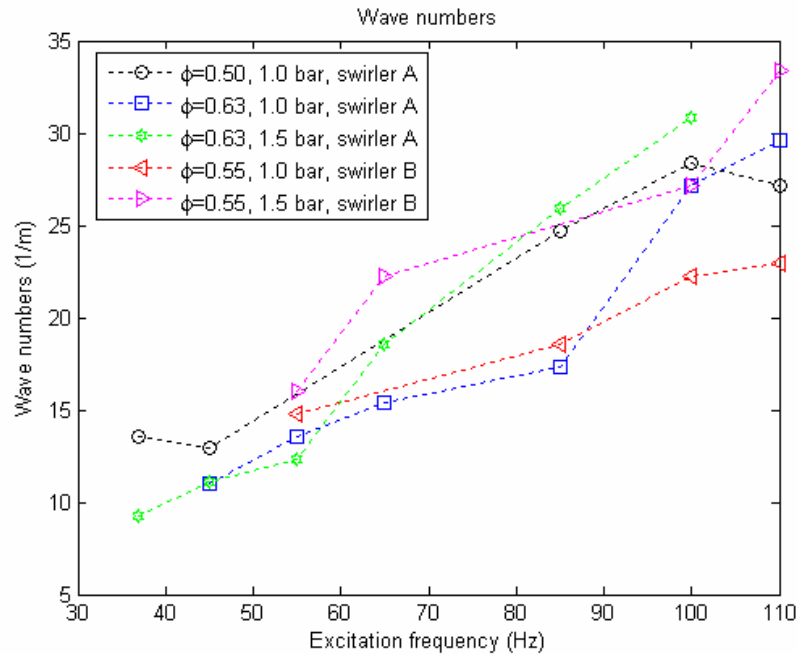


**Figure 5.10. Wave number distribution.**

Higher wave numbers are measured for higher combustor pressure. In Figure 5.10, the wave numbers are consistently higher for the 1.5 bar conditions (green for swirler A and magenta for swirler B) than for the atmospheric conditions (blue for swirler A and red for swirler B). The difference in wave numbers between atmospheric and pressurized conditions is very small at lower excitation frequency, and then it grows larger as excitation frequency increases. At higher pressure, the flame temperature goes higher due to the higher mass flow rate to sustain the flame, so the buoyant effect becomes larger, thus the gradients of velocity and other flow variables (e.g., density) at the flame

boundary get larger, giving higher degree of shear mixing and higher spatial frequencies of the toroids or, possibly, the vortex shedding frequency.

Different swirlers give different flow fields (compare Figures 5.5 to 5.7 (swirler A) with Figures 5.8 and 5.9 (swirler B)) since one swirler (swirler A) generates more centrifugal momentum than the other (swirler B). Due to the fundamental difference in the flow field variables (due to the difference in swirler design), comparisons can be made only with the global properties (not the local distributions) at this point (refer to the next section).

#### **5.4.2 Global Rayleigh Index and Flame Response**

Figure 5.11 shows the behavior of global Rayleigh indices with respect to the excitation frequency. The Global Rayleigh index is contributed mainly by the integrated local Rayleigh index. However, the local Rayleigh index distribution is meaningful in the flame boundary region, not at the center of the flame where most of the heat is released. So the global Rayleigh index is a measure of integrated effects of local Rayleigh index distribution, whose sign, on which the growth of the acoustic wave at that exciting frequency is dependent, is dependent on the domination of one phase shift region (around zero and 360 degrees or 180 degrees) over the other.

The Rayleigh index is shown to be a function of the excitation frequency, and the combustor pressure according to the data. However, the equivalence ratio seems to have very little effect on the Rayleigh index in the frequency range of 37 to 110 Hz. This is

confirmed by the top figure of Figure 5.11 in which the Rayleigh indices for  $\phi = 0.5$  and  $\phi = 0.63$  have quite identical behaviors. Also in Figures 5.12 and 5.13, along with Figures 4.23 and 4.24 in Chapter 4 confirm that the equivalence ratio is not a significant factor in determining the combustion dynamics. This is due to the fact that the swirl stabilizes the flame over a wide range of equivalence ratio producing a divergent flow above the burner exit. Flow divergence provides a highly effective means to stabilize lean premixed combustion because it enables the flame to settle where the local velocity equals the flame speed. Thus the swirl provides wider operational range of stable combustion in terms of the equivalence ratio, allowing combustion with better efficiency and less pollutant (NO<sub>x</sub>) formation.

Higher combustor pressure suppresses the sensitivity (in terms of flame response and the global Rayleigh index) of the flame to the outside disturbances (the acoustic forcing). This is found true for both types of swirlers (A and B, see Figure 5.11 and 5.12). The magnitudes of flame responses are lower for the pressurized cases, too.

One interesting point is that the phase shift behaviors are quite close to one another both quantitatively and qualitatively for the all five different conditions. So of the factors such as excitation frequency, elevated combustor pressure, the equivalence ratio, and the difference in the swirler design, only the frequency of the excitation plays a significant role in determining the phase shift of the global flame behavior. At lower frequencies (37-45 Hz), however, the phase shift is weakly dependent upon the combustor pressure and the type of swirler.

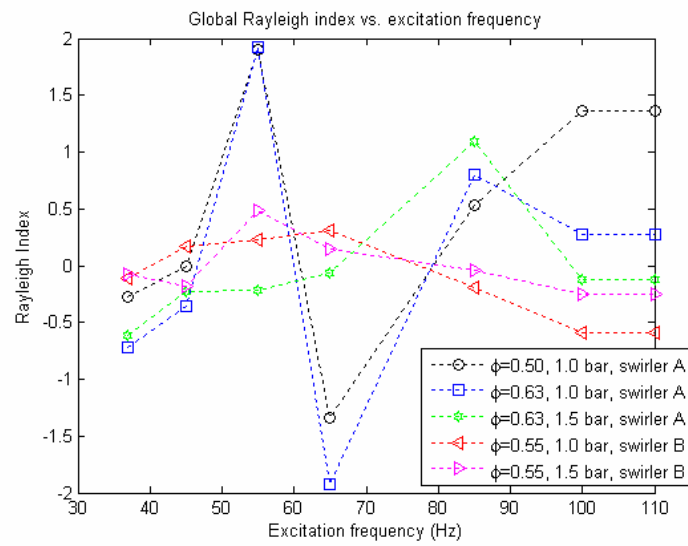
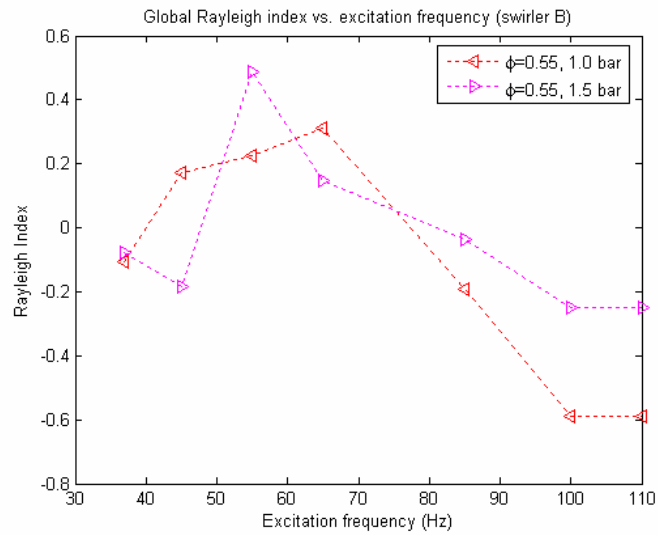
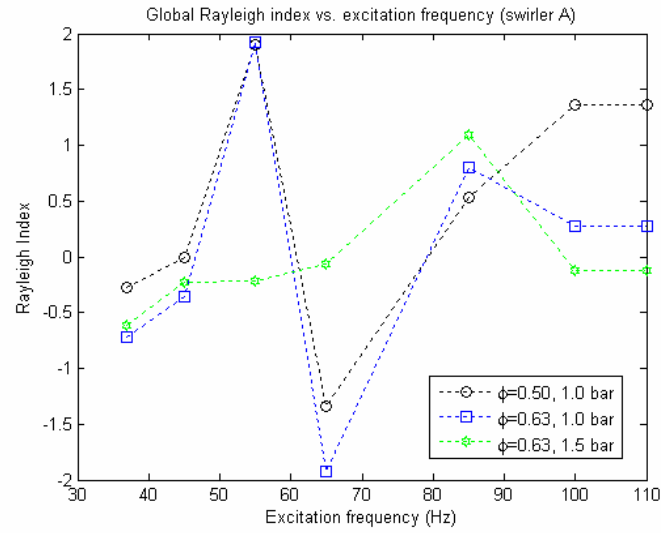
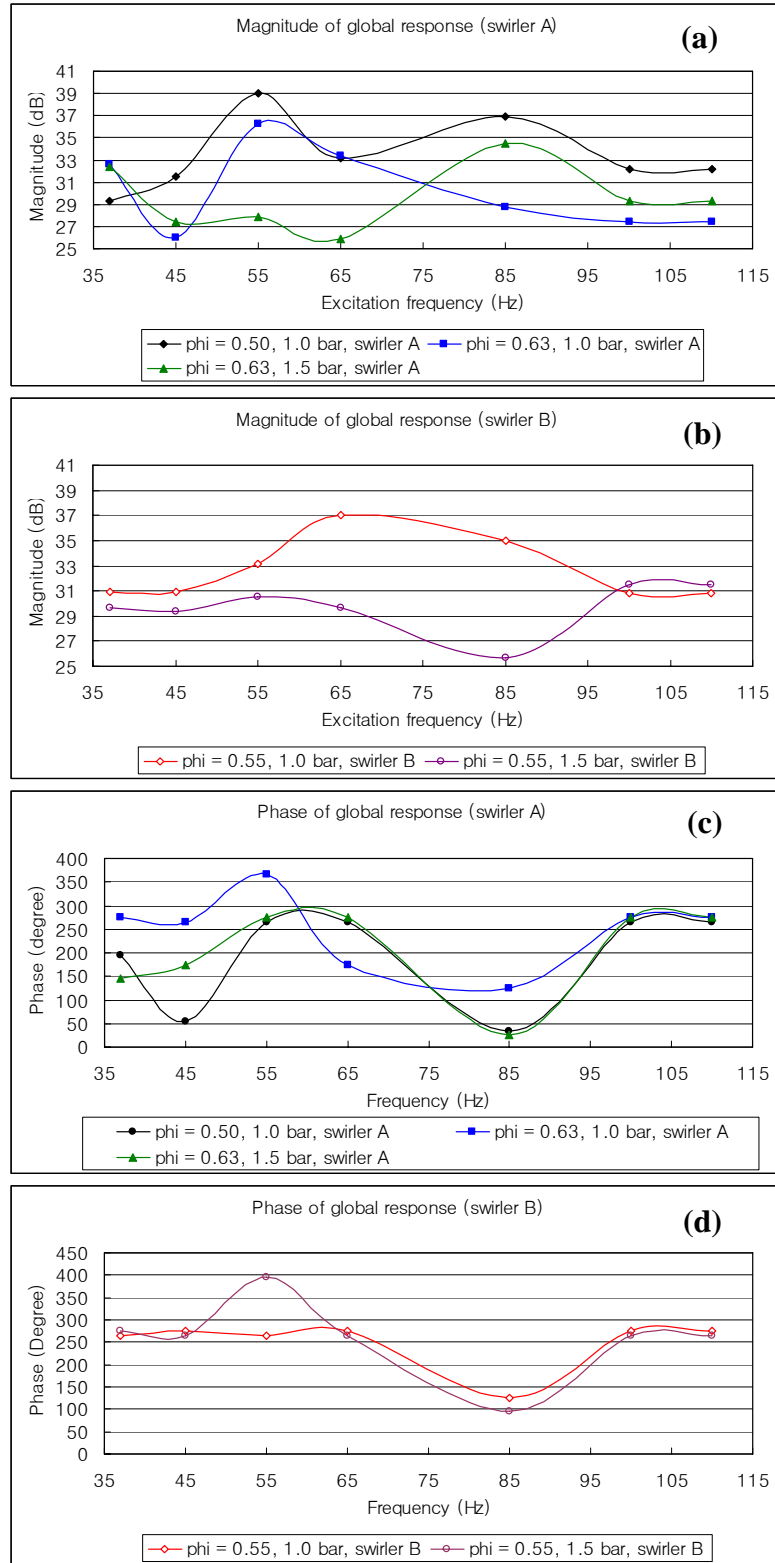
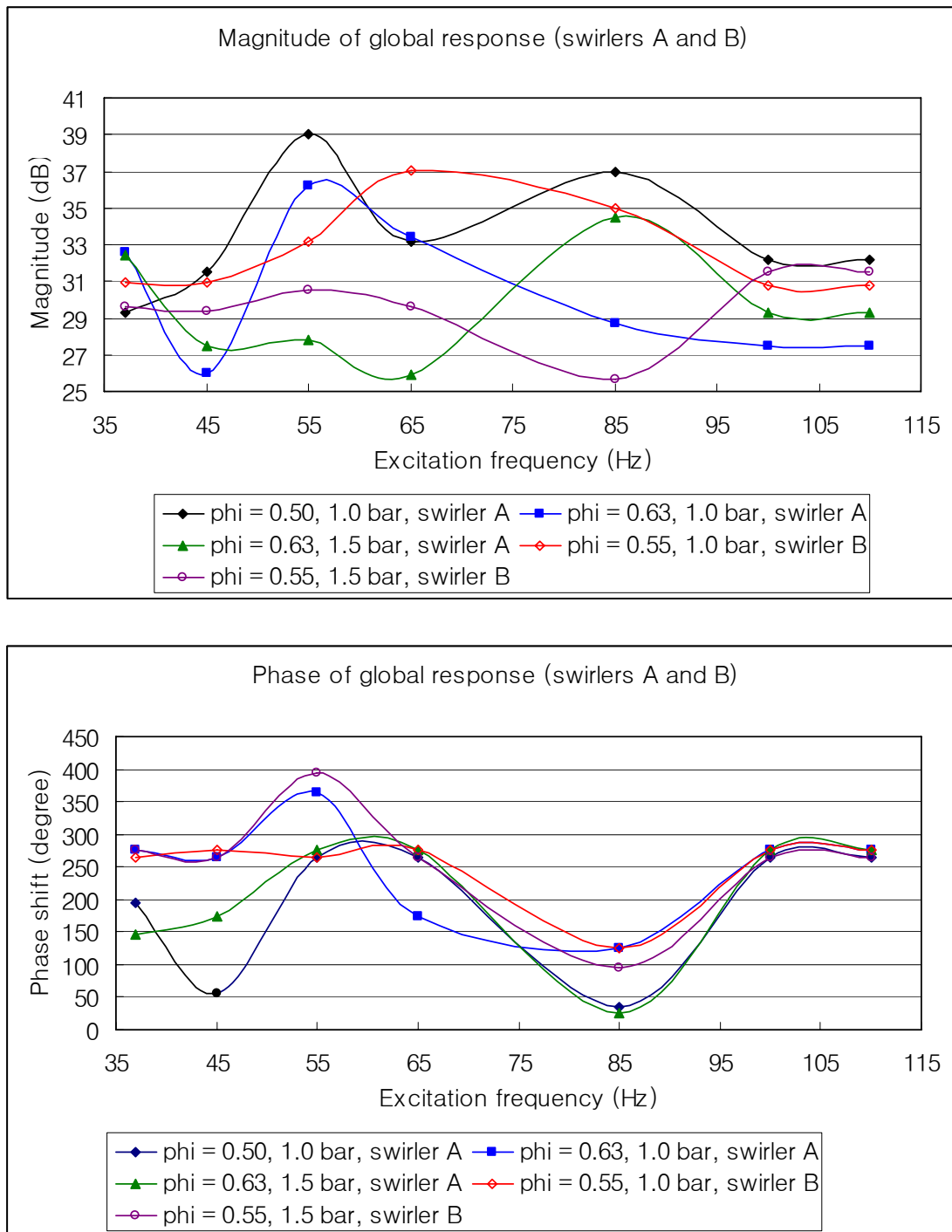


Figure 5.11. Global Rayleigh Index for swirler A (top), B (middle), and altogether.



**Figure 5.12. Global combustion response. Magnitude (a, b) and phase shift (c, d); swirler A (a, c) and swirler B (b, d).**



**Figure 5.13. Global combustion response (data for both swirlers A and B);  
magnitude (top) and phase shift (bottom)**

### 5.4.3 Distribution of Local Flame Response

Figures 5.14 through 5.23 are the local flame responses. Left hand sides are the local magnitudes, the right hand sides are the phase shift at each location. Magnitude is calculated taking the 20 times the log of 1-norm of equation 4.3 (i.e., in decibels, dB).

High values of magnitudes are distributed along the flame boundary, and this coincides well with locations of toroidal structures of the Rayleigh index distribution, except that the distribution of magnitude is horizontally wider than that of the Rayleigh index. Still, the magnitude is high where the local thermo-acoustic coupling (the Rayleigh index) is active (higher or lower than other regions). This confirms the reasoning that at the flame boundaries, mixing with outer flow due to the shear mixing decreases the local equivalence ratio thus causing the local flow to be more susceptible to instabilities.

As was observed in the previous chapter, the high magnitude of flame response is related to the greater amplitude in heat release rate fluctuations. And the Rayleigh index distributions follow those of the magnitudes of the flame responses, with the phase shift at each location determining the stability of the combustor (by alternating phase). This is the essential relationship between the Rayleigh index and the flame response.

Note that magnitudes less than 35 dB are not indicated in the figures.

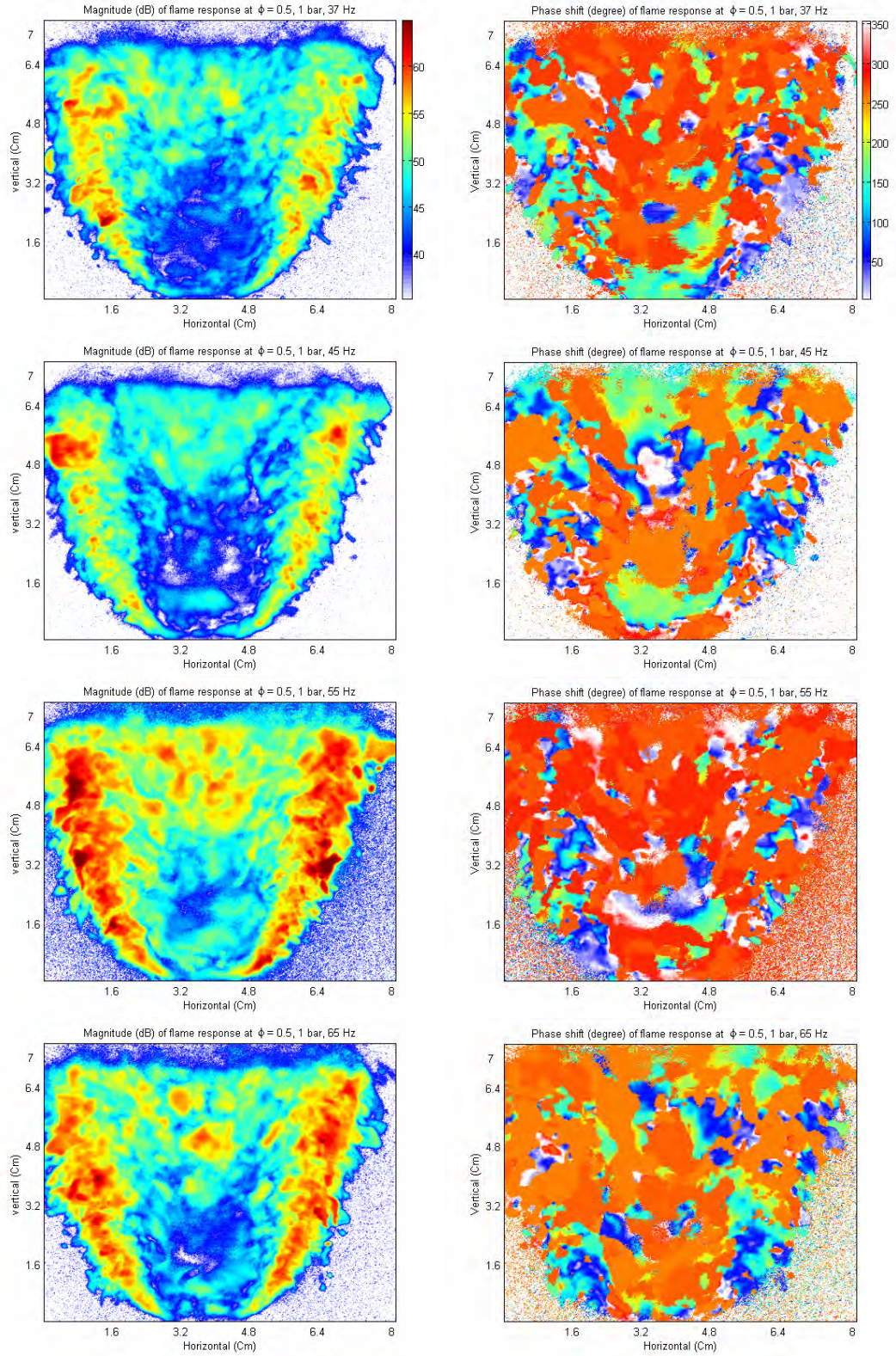


**Figure 5.14. Local response at 1.0 atm,  $\phi = 0.50$  with swirler A. Magnitude in dB (right hand side); phase in degrees (left hand side)**

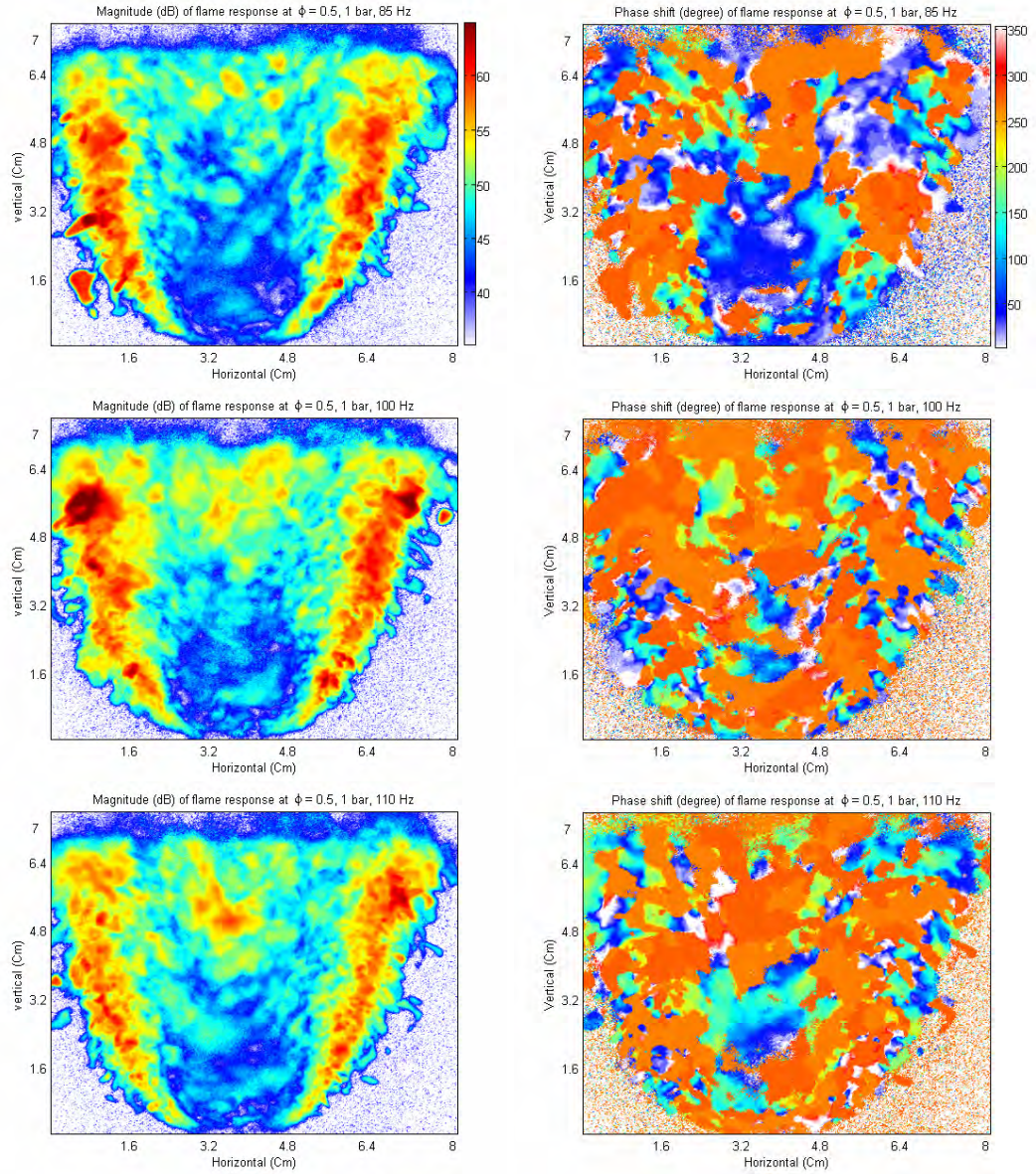


**Figure 5.15. Local response at 1.0 atm,  $\phi = 0.50$  with swirler A. Magnitude in dB (right hand side); phase in degrees (left hand side)**

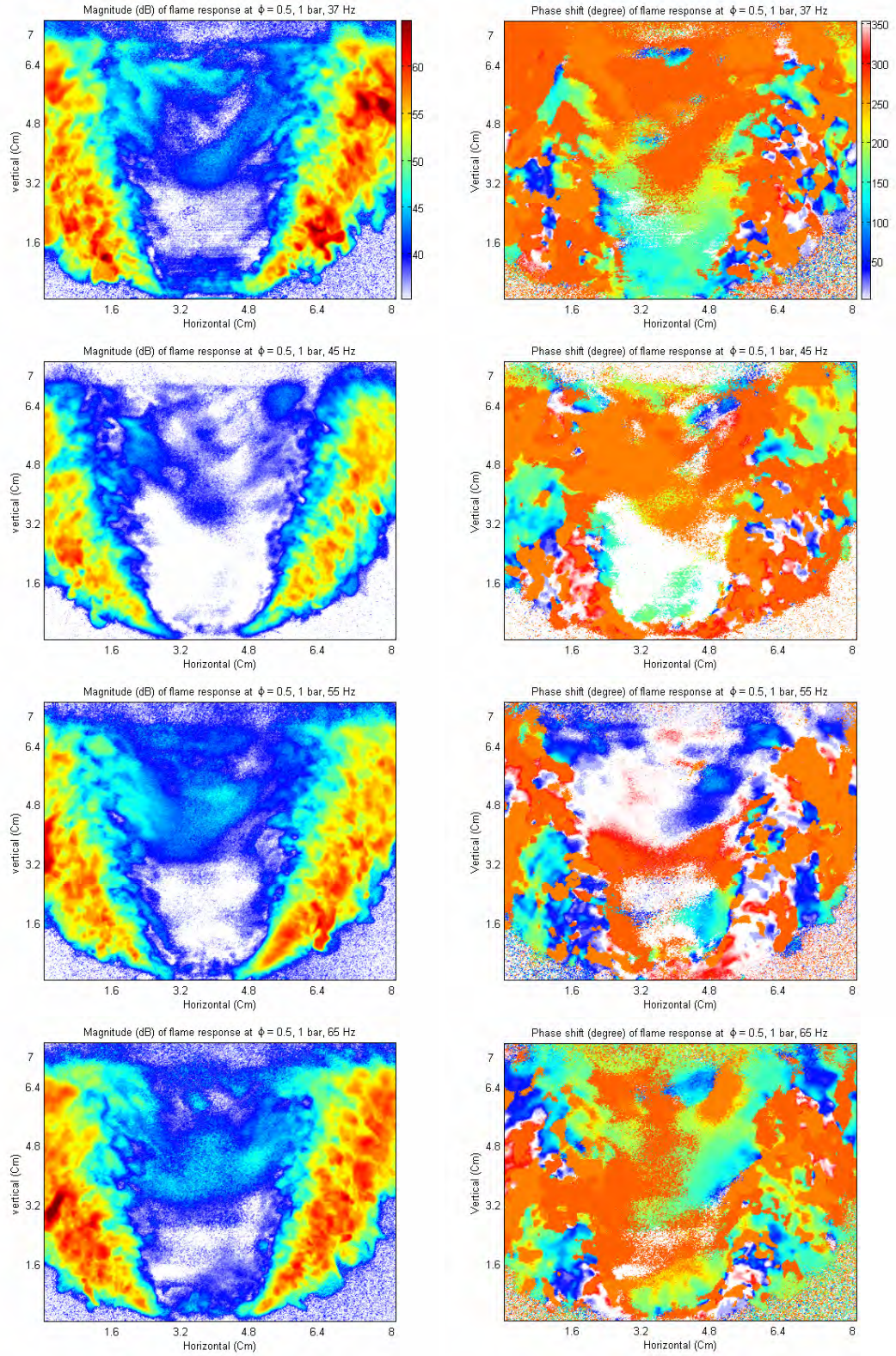


**Figure 5.16. Local response at 1.0 atm,  $\phi = 0.63$  with swirler A. Magnitude in dB (right hand side); phase in degrees (left hand side)**

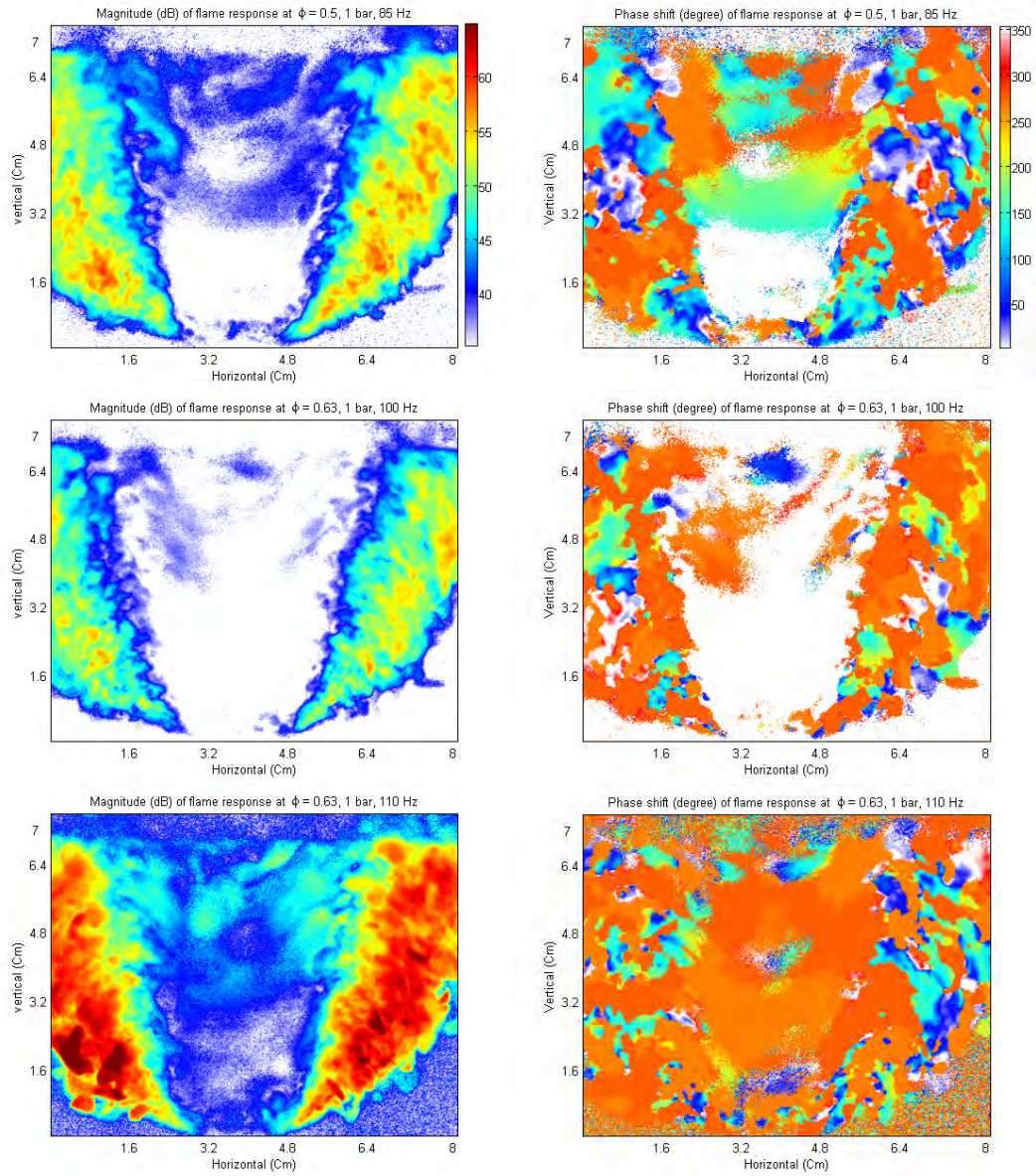


**Figure 5.17. Local response at 1.0 atm,  $\phi = 0.63$  with swirler A. Magnitude in dB (right hand side); phase in degrees (left hand side)**

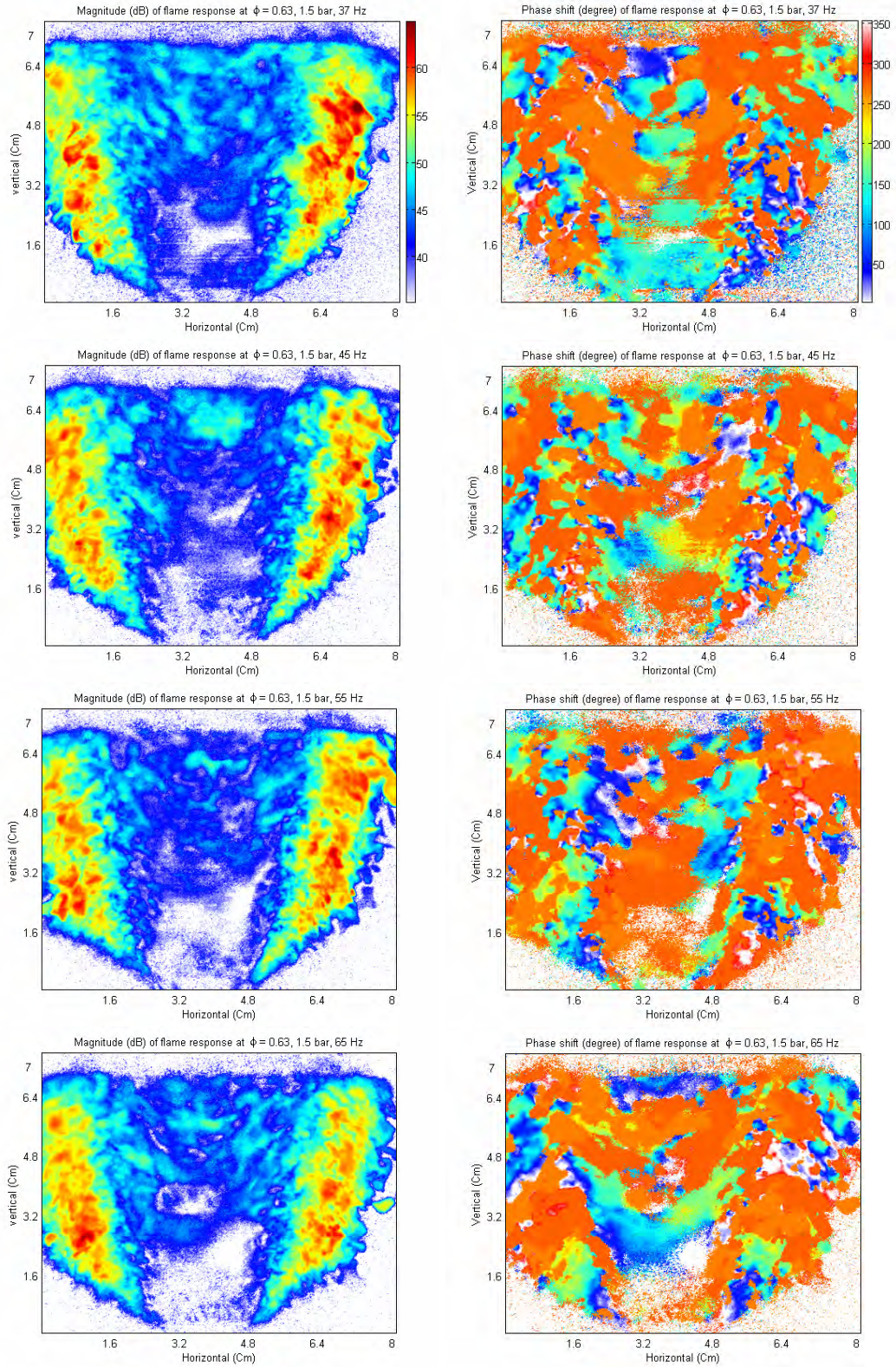


**Figure 5.18. Local response at 1.5 atm,  $\phi = 0.63$  with swirler A. Magnitude in dB (right hand side); phase in degrees (left hand side)**

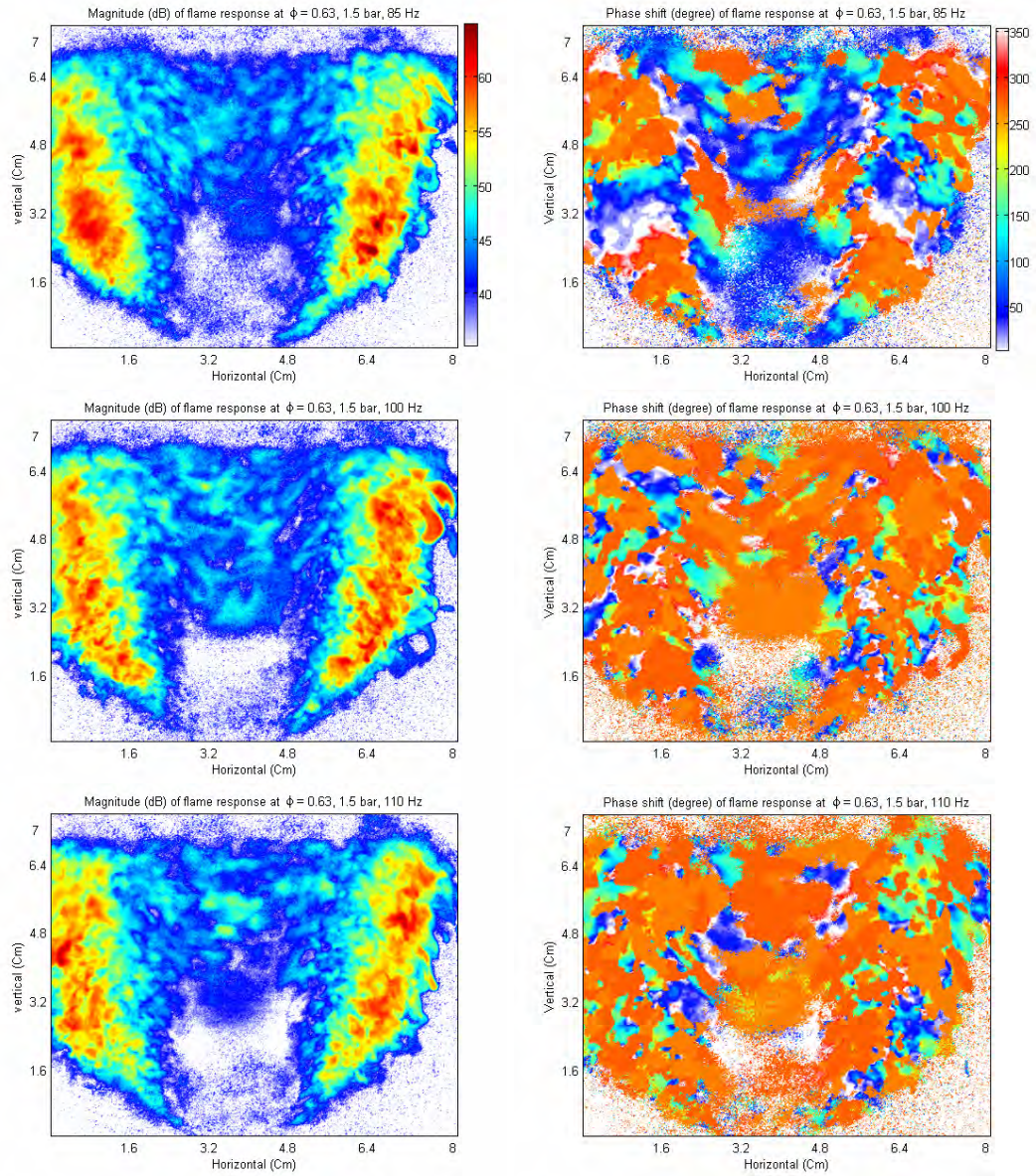


**Figure 5.19. Local response at 1.5 atm,  $\phi = 0.63$  with swirler A. Magnitude in dB (right hand side); phase in degrees (left hand side)**

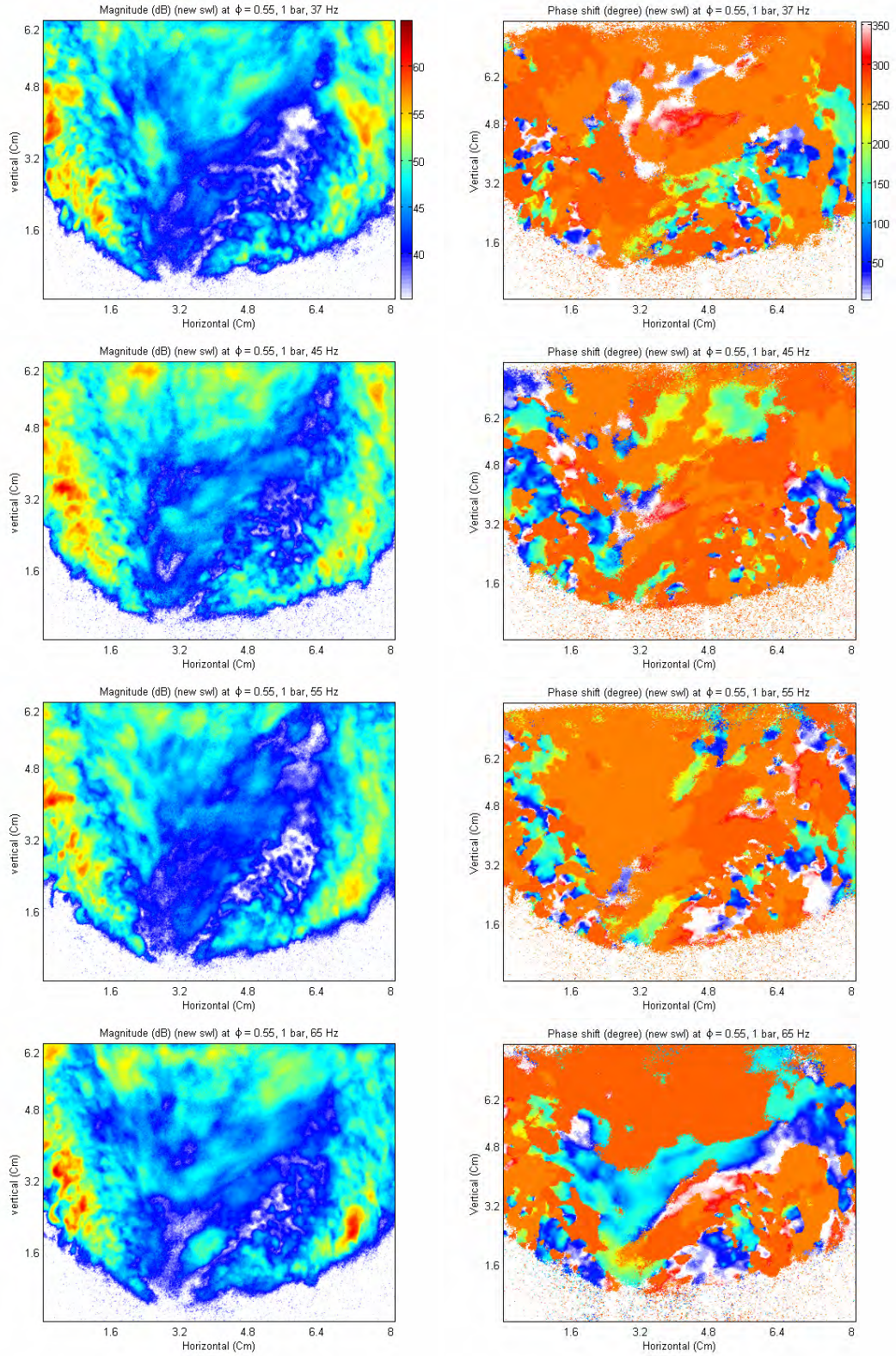


**Figure 5.20. Local response at 1.0 atm,  $\phi = 0.55$  with swirler B. Magnitude in dB (right hand side); phase in degrees (left hand side)**

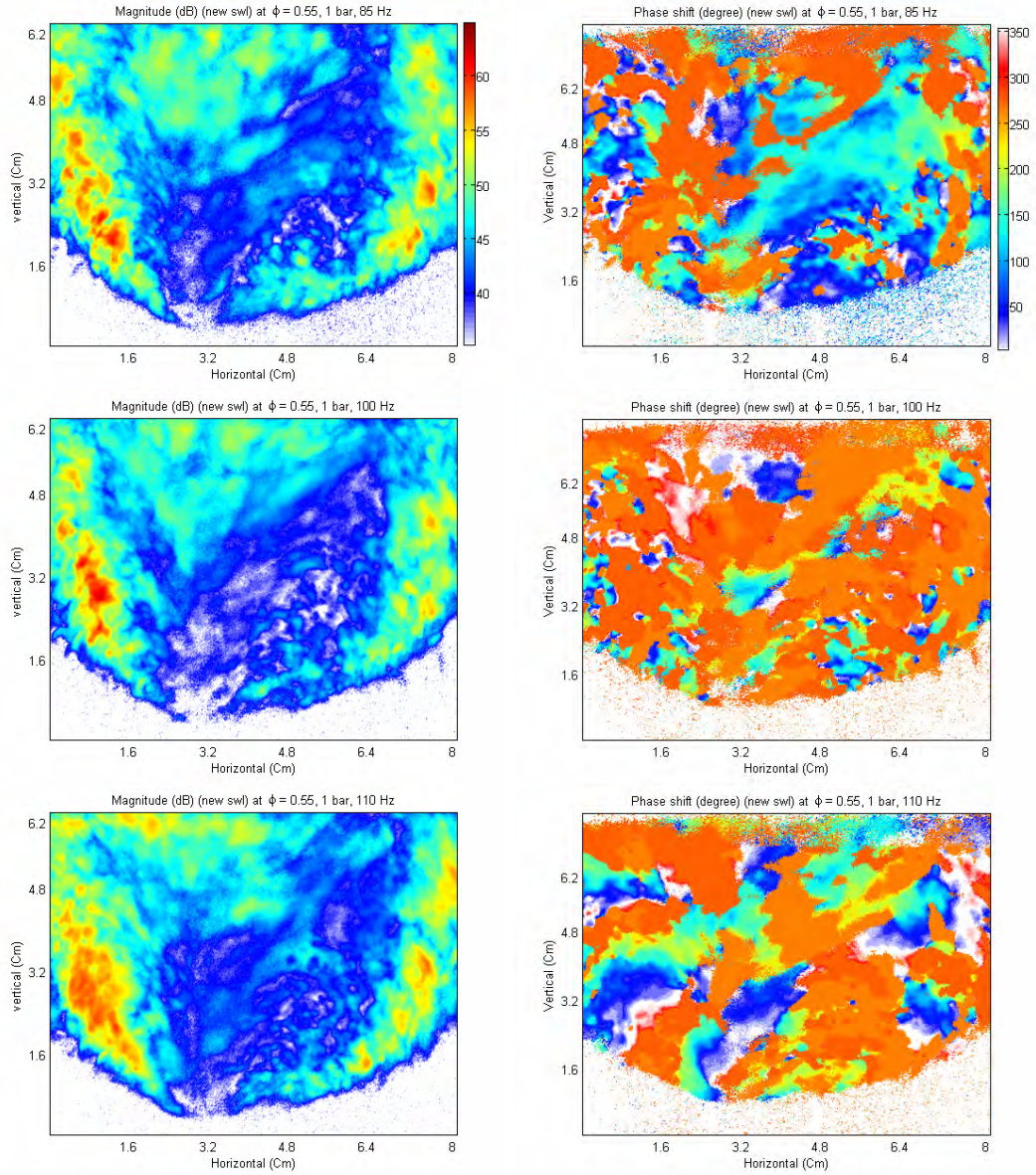


**Figure 5.21. Local response at 1.0 atm,  $\phi = 0.55$  with swirler B. Magnitude in dB (right hand side); phase in degrees (left hand side)**

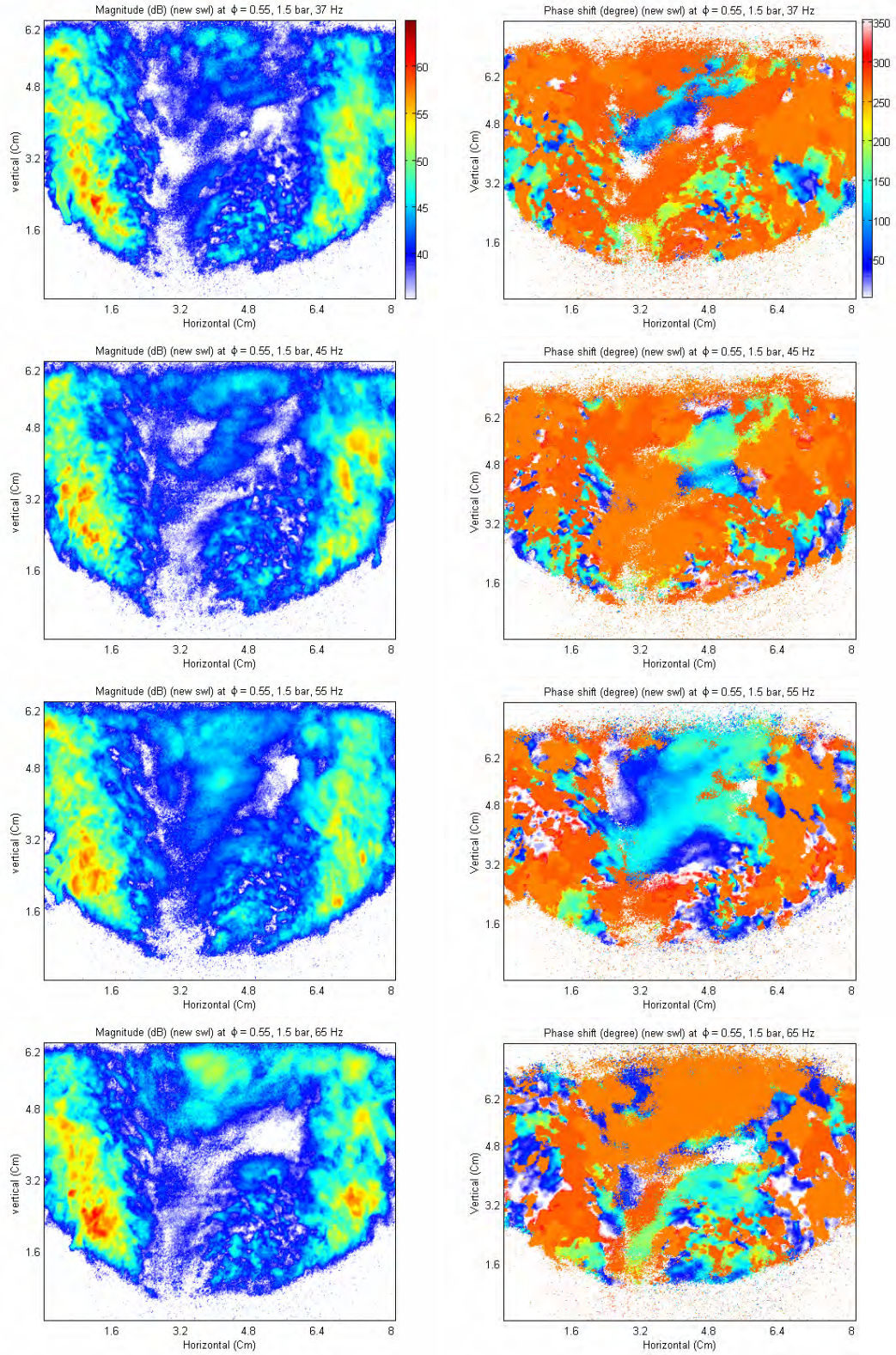


**Figure 5.22. Local response at 1.5 atm,  $\phi = 0.55$  with swirler B. Magnitude in dB (right hand side); phase in degrees (left hand side)**

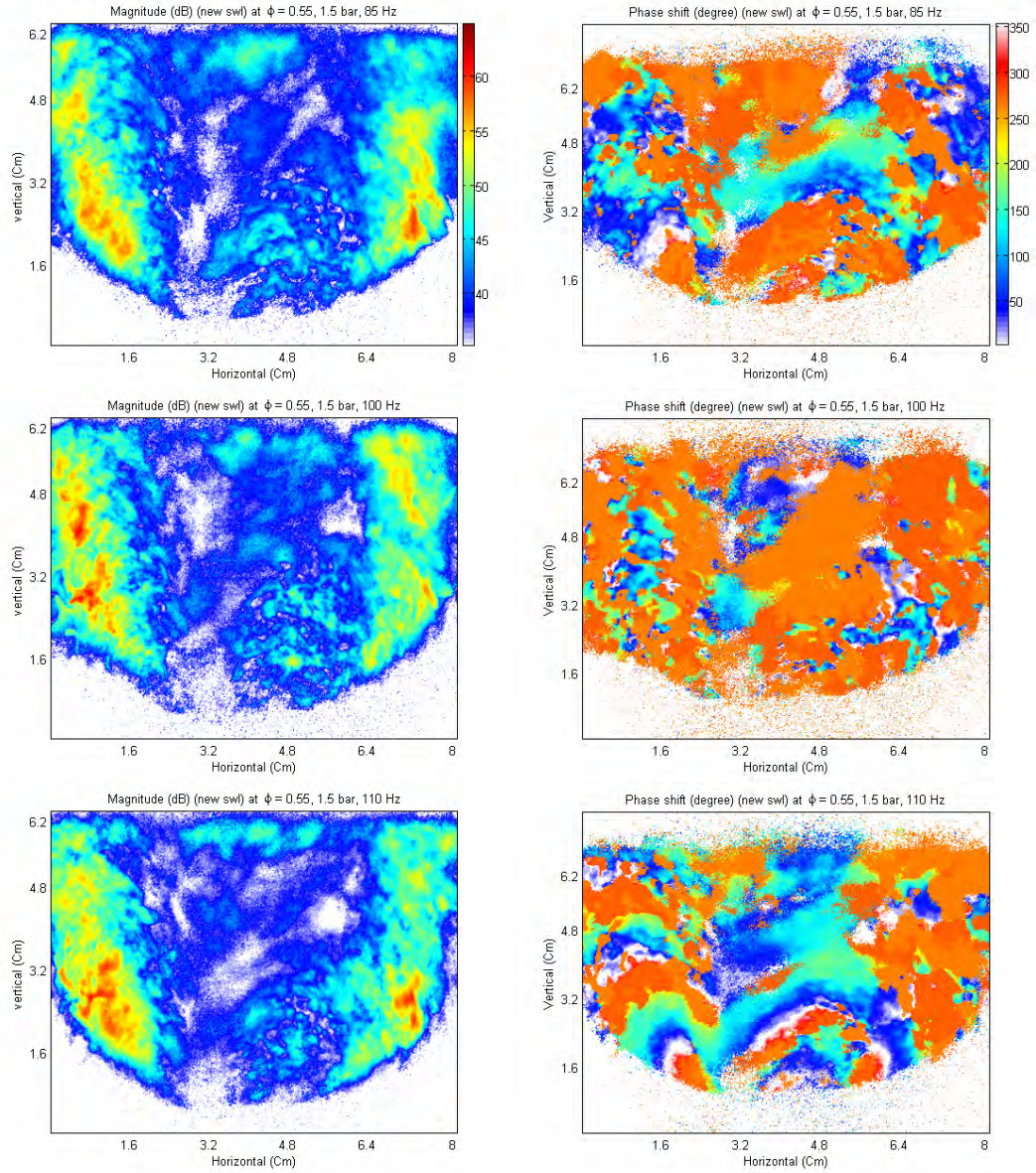


**Figure 5.23. Local response at 1.5 atm,  $\phi = 0.55$  with swirler B. Magnitude in dB (right hand side); phase in degrees (left hand side)**

## 5.5 Summary

For this work, the same technique that was developed and used in the previous chapter has been used. The agreements and tendencies in the data presented show that the technique is reliable.

Two different types of swirlers have been tested in a newly designed high pressure chamber, which is capable of holding up to 5 atm with the stable operational range of excitation frequency from 37 Hz to 110 Hz. This work presents the up to date status of the experimental methods and the measurements as a result. Pressurization, at this point, was possible only up to 2 atmospheres, and approximately 1.5 atmospheres (22.2 psi) has been used for this work. The measurements show good agreement among themselves in that the behavior of thermo-acoustic coupling (the Rayleigh index) and flame responses have the same tendency, while keeping distinct features specific for each of the five different settings (2 different swirlers).

Local Rayleigh index distribution shows that there are alternating Rayleigh index distributions along the flame boundary, which agrees well with the results in Chapter 4. The formation of this toroidal, alternating structure in the flame boundary is not as obvious as in the data presented in Chapter 4 due to the nitrogen co-flow, which reduces the velocity and other flow properties' gradient between inner and outer flow, the major driving force for vortex formation and shear mixing.

The global Rayleigh index is a function of the excitation frequency, and the combustor pressure according to the results, and is an integrated effect of the local thermo-acoustic

coupling (between  $p'$  and  $q'$ ). The local thermo-acoustic coupling effect is higher either positively (driving) or negatively (damping) along the flame border (shear mixing zone between the flame's axially moving properties and the ambient flow. And the global Rayleigh index is contributed mainly by this higher level of local thermo-acoustic coupling in the flame boundary, while the flame core region, though this is the part where most of the energy is released, does not show much involvement in determining the global stability of the flame at the given excitation frequency. The same is true with the global flame responses. All the major contribution to these global parameters come from the flame boundary where the fuel/air mixture gets mixed with entrained with outer flow due to the shear mixing (e.g., the KHI) leading to lower local equivalence ratio that is low enough to be far more sensitive to outside disturbances (or susceptible to combustion instabilities).

However, the input equivalence ratio seems to have very little effect on the Rayleigh index, and the flame response in the range that has been used for this work (0.5-0.63).

One interesting aspect of the global flame responses is that the phase shift behaviors are quite close to one another both quantitatively and qualitatively for the all five different conditions. So the excitation frequency is the dominant variable in determining the phase shifts of global flame responses with stronger effects than other factors such as the elevated combustor pressure, the equivalence ratio, and the difference in the swirler design.

Elevated combustor pressure seems to affect the combustion dynamics that the toroidal pattern in Rayleigh index distribution gets less obvious with higher pressure. Again, the excitation frequency has a dominant effect in the way the toroidal pattern is distributed over the control volume (the alternating frequency or the wave number, for example). The higher the excitation frequency, so is the wave number. The Rayleigh indices are lower for the higher pressure cases, and so are the magnitudes of flame responses.

Higher pressure seems to suppress the sensitivity of the flame to acoustic forcing (magnitudes of flame response), which is confirmed with both types of swirlers (A and B, see Figure 5.11 and 5.12), over the imposed acoustic frequencies (37-110 Hz). The magnitudes are lower for the higher pressures. The phase shift shows a tendency that it is dependent on frequency while not showing any apparent dependence on either the equivalence ratio or the type of swirler. They are almost identical except at the lower frequencies (37-45 Hz).

# Chapter 6

## Concluding Remarks

---

The complex chemistry and turbulent flow field makes it difficult to set up models that can be used in general, not just case-specific as is the current practice. Measurements of detailed local dynamics of combustion would facilitate the study of mechanisms leading to the combustion instabilities. Thus, in the study of combustion dynamics and instabilities, numerical and experimental approaches should go hand-in-hand to provide reliable data for assessing the stability and performance of combustion systems. An experimental approach provides the valuable verification ground along with the readily usable data, while a numerical approach provides data for use in the operational range where experimental approach is not practical if it can be corrected and verified by the measured data in the range where experiments are practical.

This thesis presents the current status of experimental measurements of combustion dynamics. The series of works described in this work converge to the subject of

developing experimental tools for measuring parameters that determines the combustion dynamics, namely the global and local values of thermo-acoustic coupling and flame responses.

As a main tool of the series of research, the effect of collisional quenching in the presence of quenching species ( $\text{CO}_2$ ) on fluorescence was studied. This study was carried out to investigate fundamental issues in laser-based diagnoses such as collisional quenching and signal saturation. The primary interest was to study the effect of quenching on  $\text{N}_2$  (mild quencher) and  $\text{CO}_2$  (strong quencher), and  $\text{CO}_2$  is shown to cause significant signal reduction, which requires the use of saturated LIF scheme. The benefits of saturating fluorescence are 1) there is no signal reduction due to the presence of quenching species, and 2) the signal is uniform over the control volume, thus giving better reliability to the measurements even for a pumping laser beam with a not-so-perfect beam shapes.

Mixing is an important factor affecting the stability and performance of combustion systems. Also, it is an important actuation tool in many contemporary works on the active control of combustion instabilities (Cohen et al. 2001, 2003). Fluctuations in mixing, and therefore the fluctuation in local/global equivalence ratios, are used for actively controlling the combustion systems without detailed knowledge of the dynamics of mixing. Especially in non-premixed or partially premixed combustion systems, mixing plays an important role in combustion dynamics. Numerically demonstrated by Lieuwen et al. (1998), oscillations in equivalence ratio (unmixedness, equivalent in non-premixed flame) are the main cause of oscillatory combustion behavior.

In comparison with the previous work by Pun et al. (2003), there exists a close relationship between the flame's response to imposed acoustic oscillations and the induced mixture fraction oscillations. The pressure oscillations cause oscillations in mixture fraction and the degree of local and global mixing in the flow field, which, further downstream, become the oscillating flame, since the oscillations in mixture fraction causes fluctuations in the flame surface area, eventually oscillating the heat release rates (Durox et al. 2005).

The result also shows that the presence of the combustion process alone causes far less efficient mixing compared to the 'cold flow' cases, and that the imposed acoustic oscillations create periodic behavior in the degree of mixing, which, to some extent, is also a function of the imposed frequency. According to the data, the level of fluctuations in mixing seems to be most directly related to the magnitude of the flame response function and the thermo-acoustic coupling (the Rayleigh index).

Also it is important to note that non-reacting flow acetone PLIF measurements still give the same physical structure of the distribution of unmixedness as that of the reacting flow. So it can still be used for qualitative approaches to observe the phenomena in reacting flows.

Appendix B presented a detailed derivation process of the thermo-acoustic coupling that is the interactions between the energy released from the combustion processes and the traveling acoustic waves, or the pressure fluctuations. This is the theoretical background for the measurements of thermo-acoustic coupling, quantifying one of the major aspects

of combustion dynamics. The formulations introduced in Appendix B define the kind of interaction between the combustion process and the traveling acoustic wave inside the combustors.

Combustion dynamics are measured in terms of the Rayleigh index and the flame response functions with the use of phase-resolved OH-PLIF. The purposes of this work are to 1) provide a general experimental procedure to precisely quantify the dynamic response of combustion under the real combustion environment; 2) to investigate the dynamics that has significant effects on determining the dynamic behavior of combustion system; 3) to obtain practical applicable data such as the global and local flame responses, using a commercially available type of swirl burner.

Use of a swirl burner gives better practical implication of the methodology demonstrated since there is growing popularity in industries for the fuel efficiency and environmental friendliness (less NO<sub>x</sub> produced due to the lowered flame temperature).

The thermo-acoustic coupling (the Rayleigh index) mainly occurred in the shear mixing zone. The toroidal pattern in the distribution of the local Rayleigh index seems that the coupling occurs where the vortices are, along the shear mixing zone that the Kelvin-Helmholtz instability is intertwined with the thermo-acoustic coupling. It is shown that 1) the toroidal thermo-acoustic coupling pattern occurs in the flame boundary where the local equivalence ratio is lower due to the shear mixing with the entrained air from the outer flow that the flame in that region is more expected to be more unstable (see Figure

1-2); 2) the phase shift of heat release (flame) fluctuation from the imposed acoustic wave seems to be very closely coupled to the vortices generated at the flame boundary due to the shear mixing (KHI) thus causing the alternating (toroid) structure; 3) the high magnitude of flame response (sensitivity to the outside disturbances) coincides with the high absolute value of Rayleigh index, the degree of thermo-acoustic coupling; 4) the way the thermo-acoustic coupling is distributed over the space is highly dependent on the excitation frequencies; 5) the measurements technique shows good resolution with reasonable reliability from the comparison of three different measurements conditions (equivalence ratio).

The region with large absolute global Rayleigh indices coincides with the region where the magnitude of flame response is far greater than other frequencies (160 – 240 Hz). The combustor geometry gives a resonant standing wave of approximately 188 Hz which approximately corresponds to the center of the excitation zone with high magnitude of flame response and the Rayleigh index. Also, in the vicinity of 400 Hz, the absolute value of the Rayleigh index increases, and so does the magnitude of the flame response, which seems to be approximately twice the resonant frequency. At resonant frequency of the acoustic cavity (longitudinal), the chamber, the heat release fluctuation peaks and so does the response (magnitude) of the flame. However, it is expected that the acoustic resonance occurs as a sharp peak not as the plateau over the range of frequency (150-250 Hz), so it is more likely that this is the unstable combustion regime due to the thermo-acoustic coupling, the combustion instabilities for the given system than a simple acoustic resonance phenomenon.

A new, high-pressure chamber was used for the measurements of combustion dynamics. As an initial approach, measurements were made at a slightly elevated pressure (~1.5 atm) at a moderate frequency range (30 – 110 Hz) to see how the higher ambient pressure affects the flame dynamics. Two different types of swirlers, thus creating two different types of flames, were tested and compared.

This work presents the up to date status of the experimental methods and the measurements as a result. The measurements show good agreement among themselves in that the behavior of thermo-acoustic coupling (the Rayleigh index) and flame responses follow the same tendency, while keeping distinct features specific for each of the five different settings (2 different swirlers).

The global Rayleigh index is a function of the excitation frequency, and the combustor pressure according to the results. However, the equivalence ratio seems to have very little effect on the Rayleigh index, and the flame response in the range that has been used for this work (0.5-0.63). Elevated combustor pressure seems to affect the combustion dynamics that the ‘toroidal pattern’ in Rayleigh index distribution becomes less obvious with higher pressure. The excitation frequency has a dominant effect in the way the toroidal pattern is distributed over the control volume (the alternating frequency or the wave number, for example). The higher the excitation frequency, the higher is the wave number. The Rayleigh indices are lower for the higher pressure cases, as are the magnitudes of flame responses.

Higher pressure seems to suppress the sensitivity of the flame to acoustic forcing (magnitudes of flame response), which is confirmed with both types of swirlers (A and B, see Figure 6-11 and 6-12). The magnitudes are lower for the higher pressures. The phase shift shows a tendency that it is dependent on frequency while not showing any apparent dependence on either the equivalence ratio or the type of swirler. They are almost identical except at the lower frequencies (37-45 Hz).

#### *Future Works*

For the immediate future, it is always the first priority to upgrade the experimental condition to a level that is closer to the real combustor situations. Pressurization is sometimes a big issue if the tested combustion system is a high pressure combustor such as the gas turbine engines. Use of a feedback controller system for regulating the combustor pressure is a consideration. Of course the fuel and oxidizer feeding system need to be upgraded for safety and economy as well. The acoustic system needs better power to eligibly create useful acoustic disturbances in the flow field. Higher excitation frequency is a great issue, too, and this effort requires a lot of work in refining and conditioning the acoustic system. Acoustic excitations up to the order of a kilohertz will be a great practical improvement.

Measurements of flow field variables such as velocity and temperature are needed for the completeness of the experimental tools suggested in the present work. It is very important to use non-intrusive tools, essentially laser based techniques like PIV technique.

A detailed study of photo-chemical effect that causes the over-saturation phenomena is a subject to study since the effect of over-saturation on the measurements precision and the reliability has not been thoroughly studied. This would give a 'rule-of-thumb' technical idea how much power is required for a specific situation of testing and for a reliable one. For this a very light-tight environment is required, along with very sensitive photo-diodes.

Measurement of mixing in the combusting region is an important problem. However, since measurements of mixing (Chapter 2) showed that the behaviors of the degree of mixing or 'un-mixing' (unmixedness) are not affected too much as to change the qualitative features, it would be helpful to perform a simple acetone PLIF approach on the swirl flows to study the distribution of the degree of mixing due to swirl.

# **Appendix A**

## **Laser Induced Fluorescence:**

### **An Introduction**

---

The experimental works presented in this thesis are based on laser induced fluorescence (LIF) technique. In this section, the general theoretical background, and some details related to the implementation of acetone PLIF are presented.

## A.1 Background

### A.1.1 Theoretical Background

Laser-induced fluorescence occurs with following steps.

1. The species is brought to an excited electronic state by a pump laser (Figure A.1).
2. The excited molecules then fluoresce by emitting photons and decaying to lower energy states.

Then the detection devices are used to take the photon-counts or images.

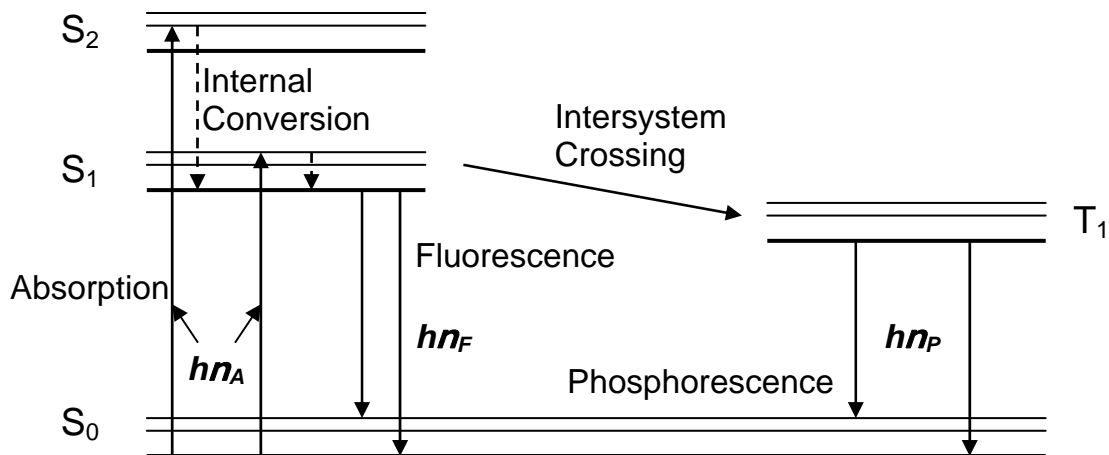


**Figure A.1. Jablonski Diagram.**

Measurements with laser systems are usually non-intrusive, and therefore do not affect the flow field. For the current research, laser induced fluorescence (LIF) have been used.

A brief schematic of how the technique works is shown in Figure A.1 (the Jablonski diagram).

Fluorescence is a two step process; an absorption (upward arrows) followed by spontaneous emission (downward arrows).

Here,

1) lines denote the vibrational levels;

2) 'Intersystem crossing': molecules in S1 state can also undergo a spin conversion to the first triplet state, T1. Emission from T1 is termed phosphorescence and is generally shifted to longer wavelength region (lower energy level) compared to the fluorescence signal. The conversion from the singlet to a triplet state is called the 'intersystem crossing'. Transition from T1 to the singlet ground state is forbidden, and as a result, rate constant for triplet emission is several orders of magnitude smaller than those for fluorescence. Molecules containing heavy atoms such as bromine and iodine are frequently phosphorescent. The heavy atoms facilitate intersystem crossing and thus enhance phosphorescence quantum yields (Eckbreth, 1996).

A typical LIF configuration is shown in Figure A.2, where the laser beam is split by the beam splitter (BS), then goes through spherical (SL) and cylindrical lenses (CL) to be focused at the right location (probing location, a point in this case). Then the signal is received by a charge coupled device (CCD) camera or a photo-multiplier tube(PMT), which is normally used to amplify the weak fluorescence signal.

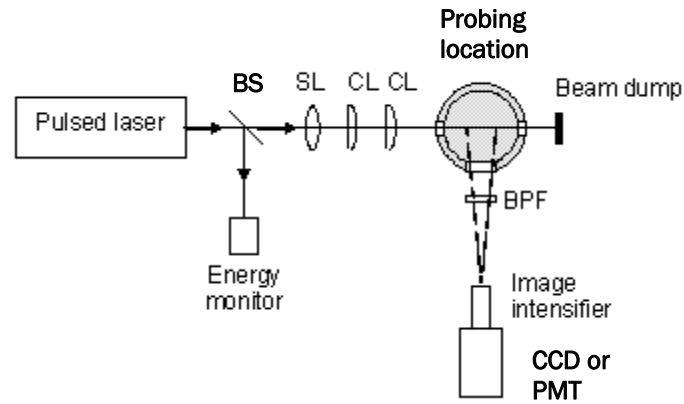


**Figure A.2. A typical experimental set-up for LIF measurements.**

According to Allen et al. (1995), the fluorescence signal can be modeled by a two-level steady state model, and is given by:

$$(A.1) \quad S_f = \eta \left( \frac{\Omega}{4\pi} \right) V_c I_v \left[ \frac{A_{eff}}{A + Q(\chi_P, P, T)} \right] \chi_j P_t \sum_i \left[ f_{B,i}(T) B_i g_i(\nu, P, T) \right]$$

where the symbols are as follows.

$\eta$	quantum efficiency of ICCD photocathode
$\Omega$	collection optics solid angle
$V_c$	collection volume of one detector pixel
$I_v$	laser spectral fluence
$A_{eff}$	effective Einstein coefficient for spontaneous emission
$A$	Einstein coefficient for spontaneous emission
$Q(\chi_P, P, T)$	electronic quenching rate
$\chi_j$	mole fractions of measured species j, in measurement volume

$Pt$	total gas pressure
$f_{B,i}(T)$	Boltzmann fraction of absorbing species in state i
$B_i$	Einstein coefficient for stimulated emission for transition i
$g_i(\nu, P, T)$	overlap integral (convolution of absorption and laser lineshape profiles)

For a given pressure and other parameters, we have a reduced form (A.2).

$$(A.2) \quad S_f^+(\lambda, T) \propto \frac{P}{T} \sigma(\lambda, T) \phi(\lambda, T)$$

where  $n_{\text{abs}}$ , the number density,  $\sigma$ , the molecular absorption cross section, and  $\phi$ , the fluorescence quantum yield are the temperature dependent parameters. Then for given pressure  $p$  and wavelength  $\lambda$ ,  $S_f(T)/S_f(300\text{K})$  can be calculated and plotted. This can be done over a range of temperatures so that the relative values can be mapped and used to evaluate temperature distribution.

### A.1.2 PLIF

Planar LIF (PLIF) is essentially the same technique as LIF, except that, as shown in Figure A.3, the beam is not focused on a point in space as in Figure A.2. Instead, the laser beam is widened, usually vertically, to a certain height, then refocused to keep the beam shape (a sheet).

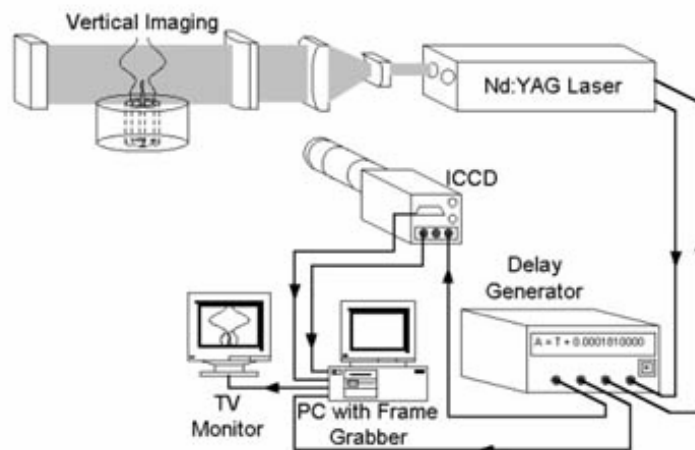


**Figure A.3.** Schematic diagram of Planar LIF (PLIF, adapted from world wide web, <http://rpl.snu.ac.kr/>).

## A.2 Characteristics of Acetone PLIF

Acetone ( $\text{CH}_3\text{-CO-CH}_3$ )'s molecular weight is 58.08 with melting point at  $-95^\circ\text{C}$ , and boiling point at  $56^\circ\text{C}$ ., ignition temperature around  $465^\circ\text{C}$ . depending on the mole fraction. Figure A.4 shows the temperature dependence of the saturation vapor pressure of acetone.

The graph fits to the equation :

$$(A.3) \quad \log_{10} P(\text{torr}) = 7.125267 - \frac{1214.208}{230.002 + T(\text{C})} .$$

Acetone PLIF uses UV laser sheet to excite the acetone molecules to the first excited singlet state (S1). Acetone is a broadband absorber in the UV (225 - 320 nm, see Figure A.5). Acetone molecules absorb relatively strongly, so many molecules are raised to the first excited singlet state, S1. This is the principal process that about 98% of excited state acetone molecules go back to the ground state without any emission; no radiation or fluorescence. About 1.8 % of the excited state molecules get excited to first triplet state,

T1, which requires spin changes. This state is lower in energy level than the first excited singlet state, S1, and relaxes back to the ground state either by collisional quenching or by *phosphorescence*. The remaining 0.2%, for vapor, relaxes through fluorescence (world wide web, <http://ae.gatech.edu/~comblab5/Optical/plif.htm>). As shown in Figure A.5, acetone fluorescence is broadband in UV to blue (visible) region. The phosphorescence is very strongly quenched by the oxygen, if it is included in the stream, so the phosphorescence is negligible in the experiments performed in the presence of oxygen.

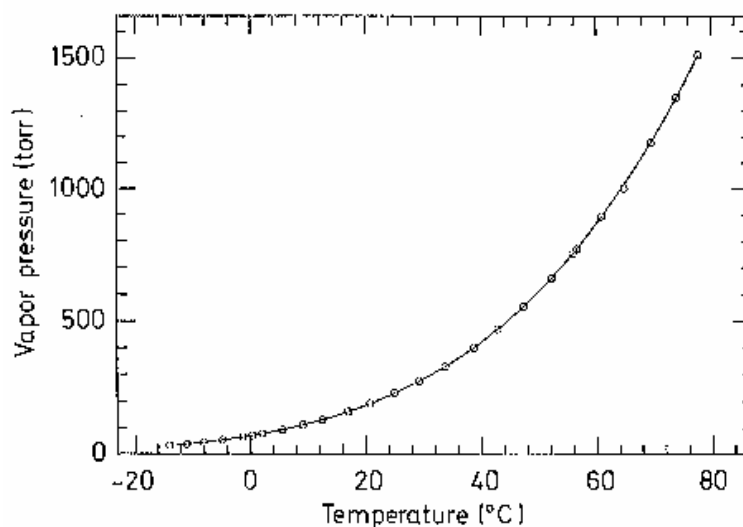


**Figure A.4. Acetone vapor pressure versus temperature (Lozano et al. 1992).**

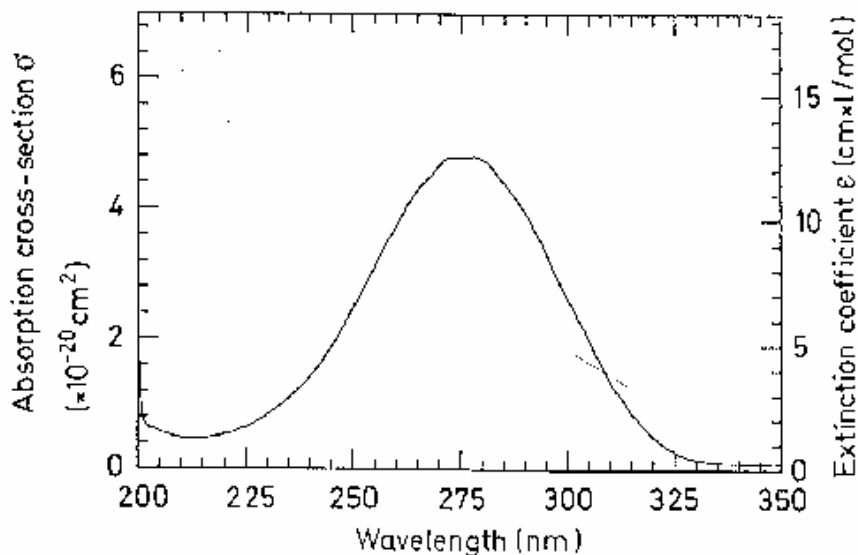


**Figure A.5. Acetone absorption spectrum corresponding to excitation from the ground state to the first excited singlet (Lozano et al. 1992).**

The primary dissociation process is given by



The free acetyl radical can recombine with another one to form a biacetyl molecule. This is responsible for the green biacetyl phosphorescence emission observed in some static cell acetone experiments (Lozano et al. 1992) which is negligible in current experiments since it occurs only for temperatures below 100 C, and originates from acetone triplets. For excitation wavelengths shorter than 312nm (our current set up is at 280 nm), the dissociation takes the alternative path



The biacetyl molecules, however, are known to be not affecting the flow, and the efficiency of fluorescence is very low when the excitation wavelength is lower than 320nm (ours, 280 nm), and the phosphorescence is quenched by oxygen as mentioned

above almost entirely. Plus, the phosphorescence from the biacetyl takes too much time ( life time of about 200 $\mu$ s), while acetone fluorescence takes only about 4 ns hence suitable only for very slow flows. Especially at 280 nm excitation, current setting, it has shown that the fluorescence life time is around  $1.7\pm 0.3$  ns (Lozano et al. 1992).

One of the very attractive features of acetone PLIF is that the relative fluorescence signal can be directly interpreted as the relative mole fraction of the species. The strength of the fluorescence signal, the vapor pressure of the species, and the excitation laser strength are in linear relationships (equation (A.1)). Figure A.6 shows the linearity of the acetone fluorescence w/r/t the incident laser energy intensity.

$$(A.5) \quad \begin{aligned} S_f(\lambda, T) &\propto E \bullet n_{abs}(T), \\ n_{abs}(T) &\propto p_{vap, acetone} \end{aligned}$$

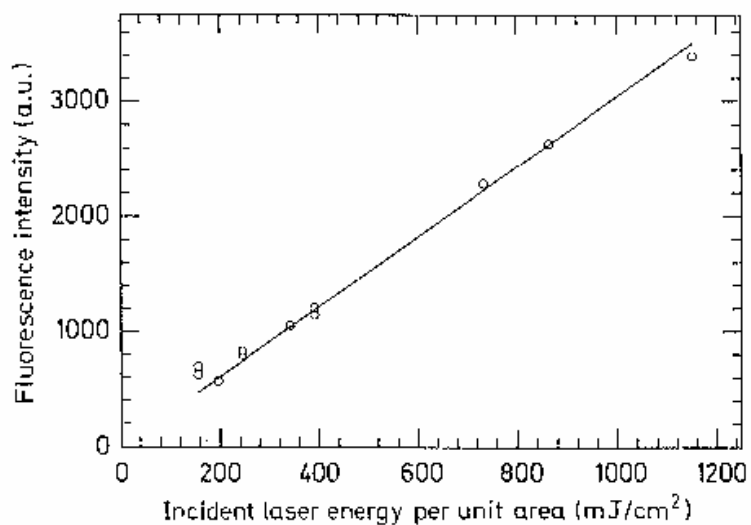


**Figure A.6. Relation between fluorescence signal and the intensity of laser excitation (Lozano et al. 1992).**

Figure A.7 shows the linearity between the acetone partial pressure and the fluorescence intensity.

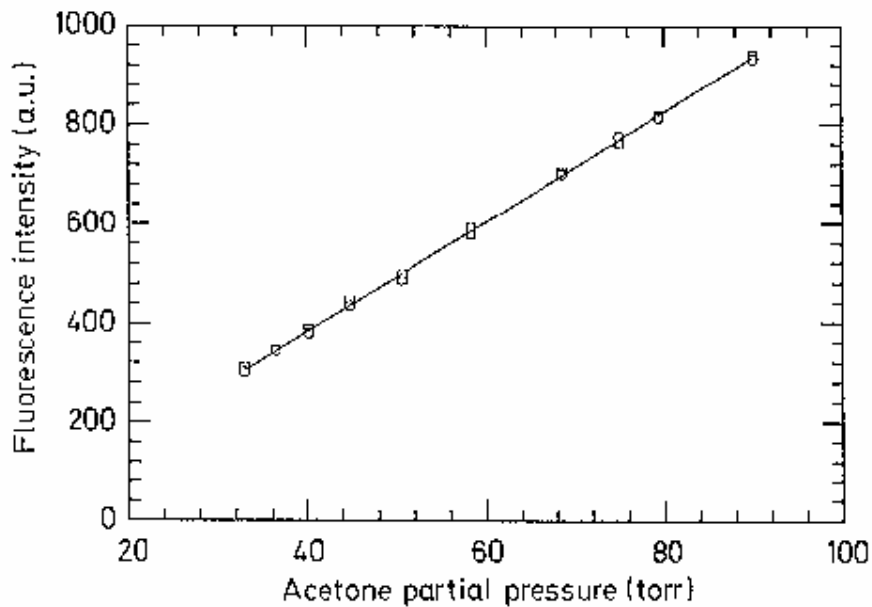


**Figure A.7. Relation between fluorescence signal and the intensity of laser excitation (Lozano et al. 1992).**

Collisional quenching rates vary with temperature and local gas composition, thus complicating the interpretation of PLIF signals when such quenching is significant. However for acetone PLIF, the collisional quenching is negligible, and the quantum yield is independent of molecular collisions, hence independent of temperature and local gas composition. So for concentration measurements, acetone fluorescence signal is very easy to handle.

# **Appendix B**

## **Introduction to the Rayleigh Index**

---

This chapter provides a brief introduction to the theoretical background for the measurements made and presented in the chapters 4 and 5 based on Culick (1975, 1976, 1981, and 1987)'s mathematical formulations. The commonly quoted observation of Rayleigh is taken as the starting point for this analysis and further formulations are developed based mainly on the over-three-decades worth of work of Culick. Finally, discussions on the significance of this approach and on its applications are given.

## **B.1 Introduction**

The interaction between the energy release in combustion processes and the acoustics accompanying those processes, the thermo-acoustic coupling, has been a great concern for many researchers working with combustors. Heat release and acoustics can both complement and interfere with each other, based on when the fluctuations in energy release and combustor pressure are in a proper phase (in- or out-of- phase). When the interaction is strongly positive, it tends to lead to unstable burning of flames (or even flame extinction) and growth of vibrations to an unacceptable levels. These structural vibrations and enhanced heat transfer rates can result in catastrophic system failure.

Lord Rayleigh gave the famous description of this phenomenon as following, the Rayleigh Criterion (Rayleigh, 1945, p. 226):

*If heat be periodically communicated to, and abstracted from, a mass of air vibrating (for example) in a cylinder bounded by a piston, the effect produced will depend upon the phase of the vibration at which the transfer of heat takes place. If heat be given to the air at the moment of greatest condensation, or be taken*

*from it at the moment of greatest rarefaction, the vibration is encouraged. On the other hand, if heat be given at the moment of greatest rarefaction, or abstracted at the moment of greatest condensation, the vibration is discouraged.*

Following this intuitive observation by Rayleigh, numerous attempts have been made to formulate and solve the phenomena analytically (Chu, B.-T., 1964, Putnam, 1964, 1971, Harrje et al. 1972, Culick, 1973, 1975, 1976, 1981, 1987, 1997, Zinn, 1986).

In the following sections the formulations leading to the so called Rayleigh index, a measure of energy transfer from the combustion energy release to the traveling acoustic waves in a cycle, is briefly shown. Discussions regarding these formulations and Raleigh's observation in connection with its significance in this series of work are also presented. The formulations presented here, as mentioned earlier, mainly follow the developments made by Culick over the past several decades (Culick 1976, 1987).

## **B.2 Mathematical Formulations**

### **B.2.1 Governing Equations**

The governing equations in the combustion chamber of some arbitrary geometry are:

$$(B.1) \quad \frac{\partial \rho}{\partial t} + u \cdot \nabla \rho = W$$

$$(B.2) \quad \rho \frac{\partial u}{\partial t} + \rho(u \cdot \nabla)u = -\nabla p + F$$

$$(B.3) \quad \frac{\partial p}{\partial t} + \bar{\gamma} p \nabla \cdot u = -(u \cdot \nabla)p + P$$

where (B.3) is obtained from the combination of (B.1), (B.2), and the ideal gas equation

$$(B.3a) \quad p = \rho \bar{R} T,$$

with  $\rho = \rho_g + \rho_l = \rho_g(1 + C_m)$  and  $C_m = \rho_l / \rho_g$ , such that

$$(B.4) \quad \bar{\gamma} = \frac{C_p + C_m C_l}{C_v + C_m C_l},$$

and

$$(B.5) \quad \bar{R} = \frac{(C_p + C_m C_l) - (C_v + C_m C_l)}{1 + C_m},$$

with  $\bar{R}$  being the mass-averaged gas constant.

The symbols  $W$ ,  $F$ , and  $P$  stand for the following:

$$(B.6) \quad W = -\rho \nabla \cdot u - \nabla \cdot (\rho_l \delta u_l),$$

$$(B.7) \quad F = \delta F_l + \delta u_l \omega_l,$$

$$(B.8) \quad P = \frac{\bar{R}}{C_v} [Q + \delta Q_l + \delta u_l \cdot F_l + \{(e_l - e) + \frac{1}{2}(\delta u_l)^2\} w_l - \bar{C}_v T \nabla \cdot (\rho_l \delta u_l)].$$

In this flow, the flow variables can be re-written as  $p = \bar{p} + p'$ ,  $u = \bar{u} + u'$ , and

$\rho = \bar{\rho} + \rho'$ , and when applied to equations (B.2) and (B.3), they become:

$$(B.9) \quad \bar{\rho} \frac{\partial u}{\partial t} + \nabla p' = -\bar{\rho} \{(\bar{u} \cdot \nabla) u' + (\bar{u} \cdot \nabla) \bar{u}\} - \rho (u' \cdot \nabla) u' - \rho \frac{\partial u'}{\partial t} + P',$$

$$(B.10) \quad \frac{\partial p'}{\partial t} + \bar{\gamma} \bar{p} \nabla \cdot u' = -\bar{u} \cdot \nabla p - \bar{\gamma} p' \nabla \cdot \bar{u} - u' \cdot \nabla p - \bar{\gamma} p' \nabla \cdot u' + P',$$

with

$$(B.11) \quad p' = \bar{R} (\rho' \bar{T} + \bar{\rho} T').$$

Here, up to the second-order terms have been kept. Differentiating equation (B.10) with respect to time and substituting (B.9) for  $\partial u' / \partial t$ , we get:

$$(B.12) \quad \nabla^2 p' - \frac{1}{\bar{a}^2} \frac{\partial^2 p'}{\partial t^2} = h,$$

with

$$(B.13) \quad \bar{a}^2 = \bar{\gamma} \bar{R} \bar{T}$$

where

$$(B.14) \quad h = -\frac{1}{\bar{a}^2} \frac{\bar{R}}{C_v} \frac{\partial Q'}{\partial t} + g,$$

where  $g$  denotes all possible fluid-dynamic effects other than heat release  $Q'$ .

The boundary condition for the above wave equation for the pressure fluctuations is:

$$(B.15) \quad \hat{n} \cdot \nabla p' = -f,$$

where  $f$  represents the local characteristics of the acoustic and fluid-dynamic boundary,

$$(B.16) \quad f = \bar{\rho} \frac{\partial u'}{\partial t} \cdot \hat{n} + \bar{\rho} \{ (u \cdot \nabla) u' + (u' \cdot \nabla) u \} \cdot \hat{n} + \bar{\rho} (u' \cdot \nabla) u' \cdot \hat{n} + \rho' \frac{\partial u'}{\partial t} \cdot \hat{n} - F' \cdot \hat{n}.$$

For spatial and temporal averaging, it is adequate to assume that the pressure and velocity fields are composed of normal modes  $\psi_n$  for the chamber geometry with time-varying amplitudes  $\eta_n(t)$ , such that

$$(B.17a) \quad p'(r_1, t) = \bar{p} \sum_{n=1}^{\infty} \eta_n(t) \psi_n(r_1)$$

$$(B.17b) \quad u'(r_1, t) = \sum_{n=1}^{\infty} \frac{\dot{\eta}_n(t)}{\bar{\gamma} k_n^2} \nabla \psi_n(r_1).$$

This assumption works well, as shown by numerical simulations (Culick, 1991, Culick and Yang, 1989), to when the fluctuating values reach 10% of the mean values, and often higher. The validation experiments to demonstrate these methods of obtaining quantitative values typically involves pressure fluctuations below 1 % of the mean value.

Substituting (B.17) in to (B.12) and performing spatial averaging, we get:

$$(B.18) \quad \frac{d^2\eta_n}{dt^2} + \omega_n^2\eta_n = F_n = F_n^Q + F_n^e,$$

with

$$(B.19a) \quad F_n = -\frac{\bar{a}^2}{\bar{p}E_n^2} \left\{ \int h\psi_n dV + \oint\oint f\psi_n dS \right\},$$

$$(B.19b) \quad F_n^Q = \frac{\bar{R}/C_v}{\bar{p}E_n^2} \int \psi_n \frac{\partial Q'}{\partial t} dV,$$

$$(B.19c) \quad F_n^e = -\frac{\bar{a}^2}{\bar{p}E_n^2} \oint\oint \psi_n g dV,$$

where  $E_n^2 = \int \psi_n^2 dV$ .  $F_n^Q$  denotes the effects of heat transfer from the combustion process, and  $F_n^e$  the rest.  $F_n$  depends nonlinearly on the amplitudes  $\eta_n$ , and equation (B.18) describes a system of coupled nonlinear oscillators.

Writing  $\eta_n(t)$  as

$$(B.20) \quad \begin{aligned} \eta_n(t) &= r_n(t) \sin(\omega_n(t) + \phi_n(t)) \\ &= A_n(t) \sin \omega_n(t)t + B_n(t) \cos \omega_n(t)t, \end{aligned}$$

$\eta_n$  accounts for the change in amplitudes, and shifts in phase differences and oscillating frequencies.

To obtain the general form of Rayleigh index, a measure of the amount of energy transfer from the combustion process to the acoustic waves, we attempt to calculate the energy and the differences in each cycle of the acoustic wave. The acoustic energy  $\mathcal{E}_n$  of  $n^{\text{th}}$  mode for a forced harmonic oscillator is given by:

$$(B.21) \quad \mathcal{E}_n = (\dot{\eta}_n^2 + \omega_n^2 \eta_n^2) / 2.$$

The energy flows to a particular mode at the rate of  $F_n \dot{\eta}_n$ , so the energy transfer during a period  $\tau_n = 2\pi / \omega_n$  is given by

$$(B.22) \quad \Delta \mathcal{E}_n(t) = \int_t^{t+\tau_n} F_n \dot{\eta}_n d\tilde{t}$$

### B.2.2 Linear analysis of Rayleigh's criterion for small amplitude motion

From the above equation (B.22), the linear stability of small-amplitude oscillations in the developing stages of oscillations can be simply dealt with. For linear acoustics, we assume relations such that:

$$(B.23a) \quad \eta_n = \hat{\eta}_n e^{i\bar{a}k_n t}$$

$$(B.23b) \quad F_n = \bar{F}_n e^{i\bar{a}k_n t}.$$

Then the equation (B.18), when (B.23) applied, yields:

$$(B.24) \quad k_n^2 = \frac{\omega_n^2}{\bar{a}^2} - \frac{\bar{F}_n / \eta_n}{\bar{a}^2},$$

where

$$(B.25) \quad k_n = \frac{1}{a}(\varpi_n - i\alpha_n)$$

From equation (B.24) we can draw conclusions as to the real and imaginary parts

$$(B.26) \quad \varpi_n^2 = \omega_n^2 - F_n^{(r)} / \eta_n,$$

$$(B.27) \quad \alpha_n = \frac{1}{2\omega_n} \frac{F_n^{(r)}}{\eta_n}.$$

So integration of equation (B.22) by parts, with the assumption that the value  $F_n \eta_n$  has almost negligible variations per cycle, we get:

$$(B.28) \quad \Delta \mathcal{E}_n(t) = - \int_t^{t+\tau_n} \eta_n \frac{dF_n}{d\tilde{t}} d\tilde{t},$$

with equation (B.23b) modified to polar form with  $\varphi$  being the phase shift:

$$(B.29) \quad F_n = |\overline{F}_n| e^{i(\overline{\omega}k_n t + \varphi)}.$$

Substituting (B.29) into (B.28) with a bit of manipulations, we reach the relation:

$$(B.30) \quad \Delta \mathcal{E}_n = \omega_n |\overline{F}_n| \frac{\tau_n}{2} \sin \varphi,$$

where by applying the result (B.27) that  $|\overline{F}_n| \sin \varphi = \hat{F}_n^{(i)} / \hat{\eta}_n = 2\omega_n \alpha_n$ , we get:

$$(B.31) \quad \Delta \mathcal{E}_n = 2\pi\omega_n \alpha_n.$$

Equation (B.32) concisely shows the Rayleigh's criterion, that if energy is added ( $\Delta \mathcal{E}_n < 0$ ) to the system then the acoustic mode grows since the growth constant,  $\alpha_n$ , is positive, and vice versa.

### B.2.3 Nonlinear Analysis of Rayleigh's Criterion

After a transient period of oscillations, ideally, the acoustics reach a limit cycle where the frequencies and magnitudes of oscillations do not vary over time. This is due to the nonlinearities present in dissipation effects in combustion dynamics and fluid flows.

With equation (B.19b) applied to equation (B.22), we obtain,

$$(B.32) \quad \Delta C_n = \frac{\bar{R}/C_v}{\bar{p}E_n^2} \int \left\{ [Q' \dot{\eta}_n]_t^{t+\tau_n} - \int_t^{t+\tau_n} \ddot{\eta}_n Q' d\tilde{t} \right\} \nu_n dV,$$

where it is assumed  $[Q' \dot{\eta}_n]_t^{t+\tau_n} \approx 0$ , and by setting

$$(B.33a) \quad \ddot{\eta}_n = \omega_n^2 \eta_n,$$

along with (B.17) and

$$(B.33b) \quad \bar{R}/C_v = \bar{\gamma} - 1,$$

we obtain a relation:

$$(B.34) \quad \Delta C_n = (\bar{\gamma} - 1) \frac{\omega_n^2}{E_n^2} \int dV \int_t^{t+\tau_n} \frac{p'_n}{\bar{p}} \frac{Q'}{\bar{p}} d\tilde{t}.$$

Equation (B.34) is a mathematical form of what was stated by Lord Rayleigh (1945).

The equation explains the implication of itself, since  $\Delta C \propto \int_t^{t+\tau} p' Q' d\tilde{t}$ , that the phase difference between the fluctuations in pressure and heat release are important in determining the stability of combustion system in the control volume.

Rayleigh's criterion is a measure of the rate of energy transfer from the combustion process, the heat, to the acoustic wave, a form of mechanical energy during a period of the frequency of acoustic wave. The energy release and subsequent heating in the flow

field cause differences in density and other related flow variables resulting in  $p-v$  work done to the flow field by the combustion process.

This coupling, between acoustic waves and heat release inside a combustor, is referred to as the ‘thermo-acoustic coupling’. Thermo-acoustic coupling is one of the most important quantities to be measured and analyzed for the study of combustion dynamics and its unstable behaviors.

In the chapters, Chapter 4 and 5, experimental methods to quantify the formulations developed here will be demonstrated. When enough data on thermo-acoustic coupling are collected (along with flow variables associated with them, though the measurements of the flow variables is out of the scope of this dissertation) the design process of combustion system will be greatly supplemented. Moreover, the active control of combustion will be enhanced with these new sets of data. The measurements of thermo-acoustic coupling with flow variables associated with them will also be a good starting point for numerical research when broader conditions where experimental efforts cannot yet reach.

# **Appendix C**

## **Flowmeter Calibration**

---

To control the fuel and air flow rates, two flow-rate controllers based on feed back control of the mechanical valves.

A Linde flow meter/controller unit (18C-202-4125; ~ 50 slpm) has been calibrated (Figure C.1), and used for regulating the flow rate of fuel (methane). The formula for converting the flow meter reading to the actual volume flow rate in standard liters per minutes (SLPM) are given as equation C.1.

$$(C.1) \quad \mathbf{SLPM (methane) = 0.4884 \times "flow\ meter\ reading" - 0.3782}$$

A Hastings flow meter/controller (HFC-203A; ~ 300 slpm) unit has been calibrated (Figure C.2), and used for the air flow rate control. The formula for conversion is given as equation C.2.

$$(C.2) \quad \mathbf{SLPM (air) = 0.2397 \times "flow\ meter\ reading" + 0.0735}$$

The flow meters calibrations were performed with Bios DryCal ML-500 calibration device (volume flow rate).

Calibration Chart for He-50SLPM Flow Controller (Sep 20, 2004)

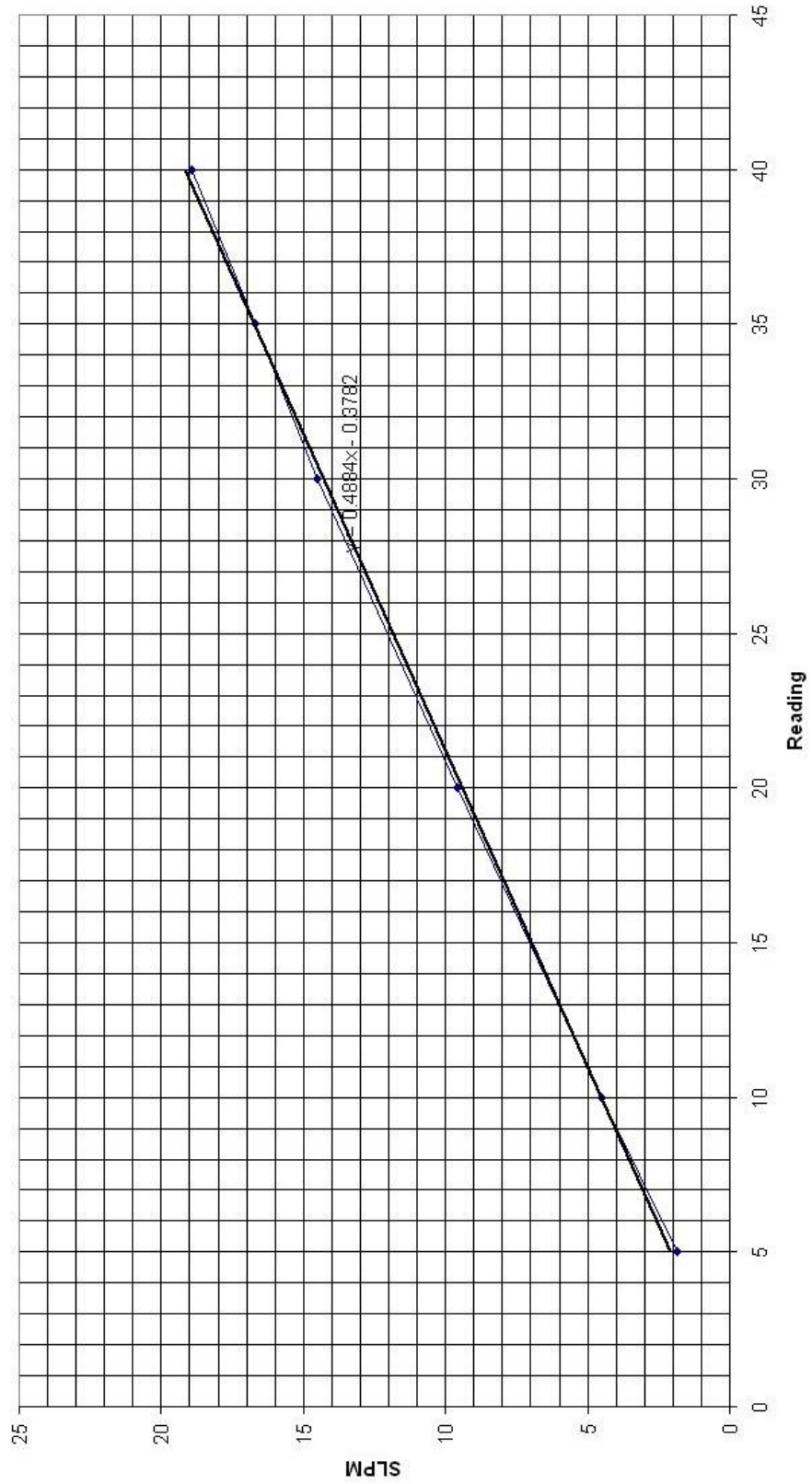
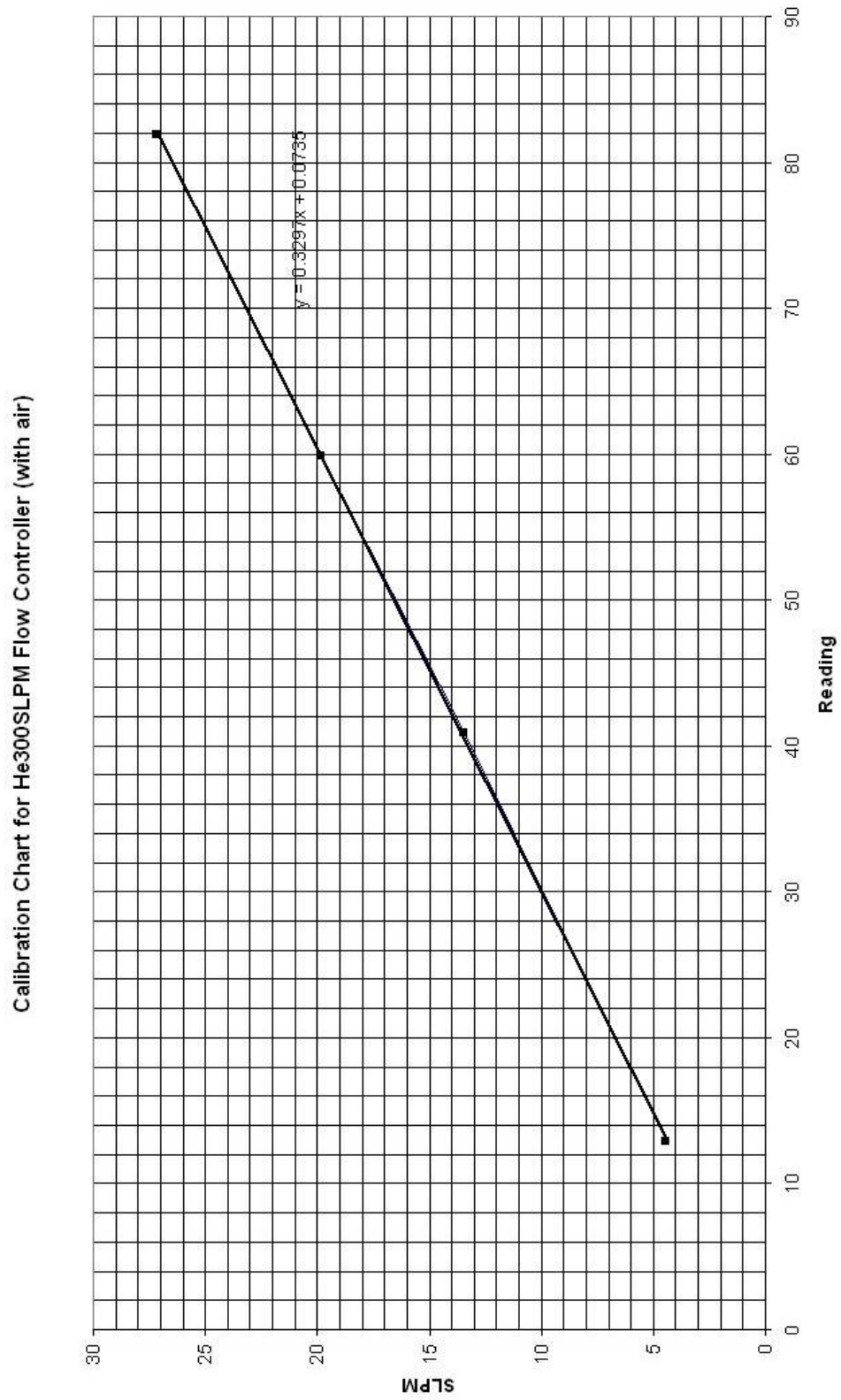


Figure C.1. Flow rate calibration for the fuel flow controller.



**Figure C.2. Flow rate calibration for the air flow controller.**

# **Appendix D**

## **Combustion Dynamics Data**

---

In this part, the measurements of combustion dynamics (the Rayleigh index and flame response) are presented that could not be included in Chapter 4 due to the massive amount of data. Except for those include in Chapter 4, the rest of the figures are presented here.

The first part, Figures D.1 through D.17, is the fast Fourier transformed pressure signal and the corresponding heat release fluctuations, corresponding to Figure 4.8. The figures in the second part, Figures D.18 through D.24, are distributions of local Rayleigh index, corresponding to Figures 4.13 to 4.15. Figures D.25 through D.40 consist the third part, the distribution of local flame responses corresponding to Figures 4.26 to 4.28.

The data presented here would serve as a basis (reference data) for the theoretical and numerical approach for determining the dynamic response of the combustion system.

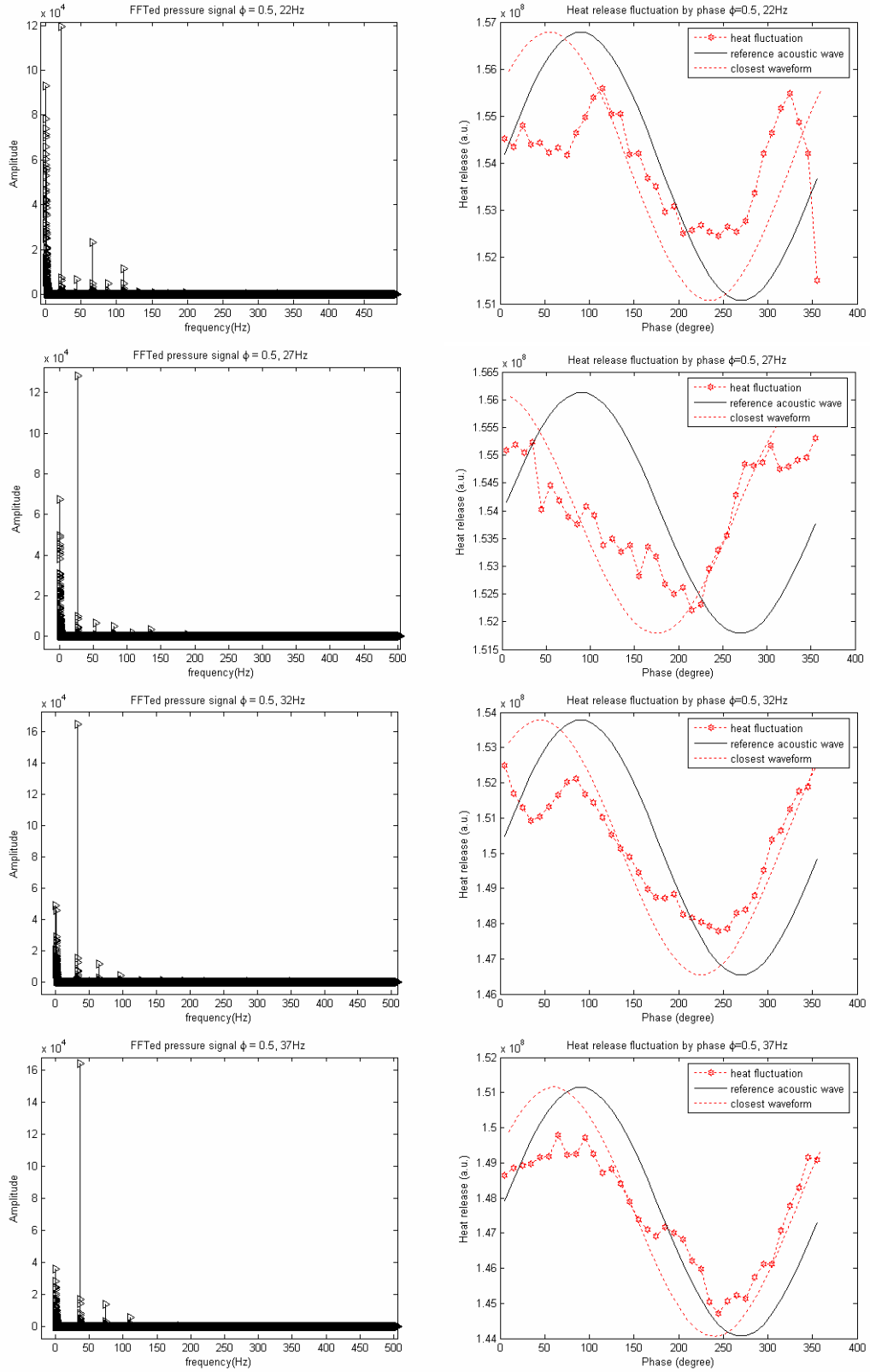
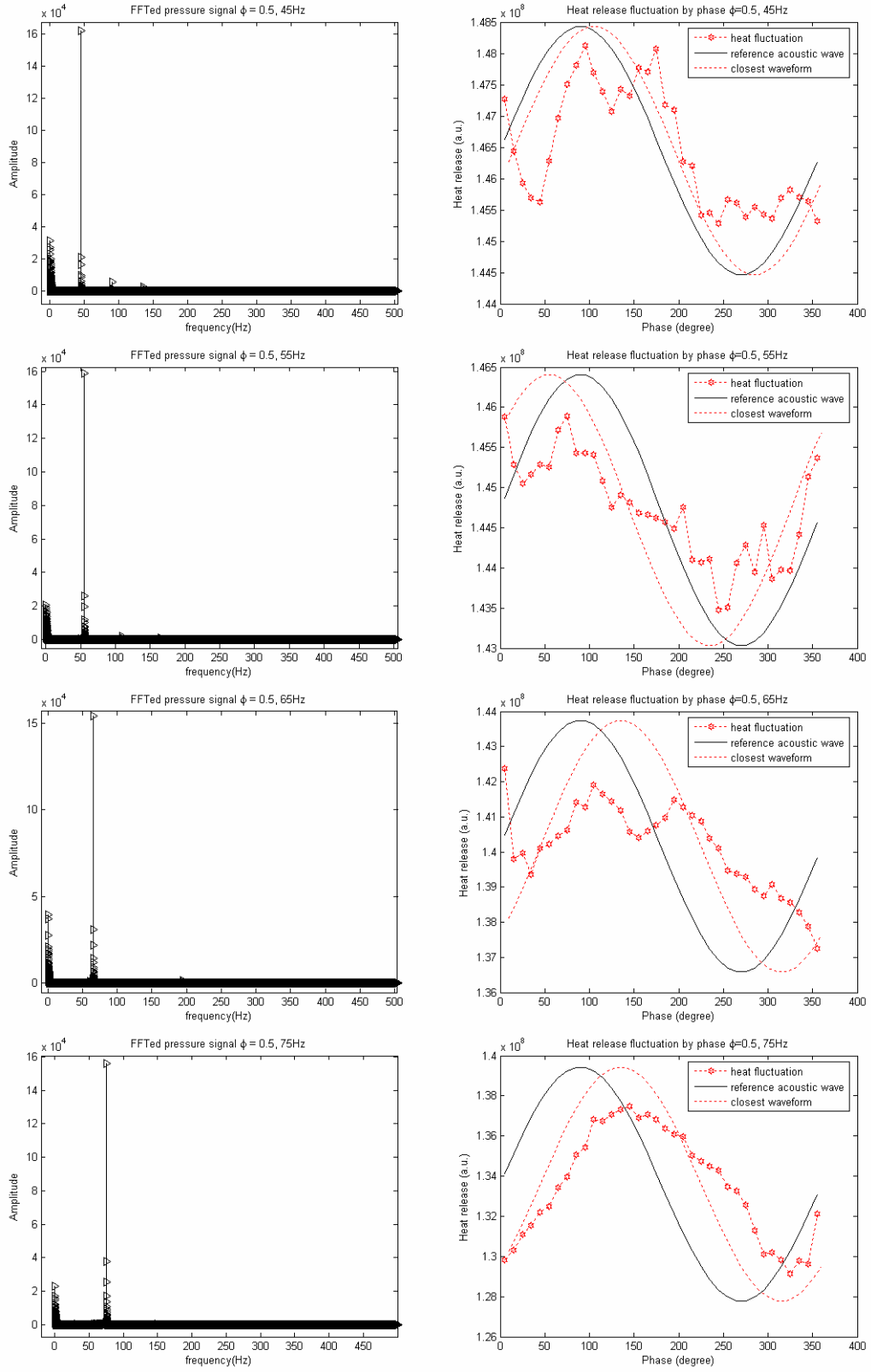


Figure D.1. FFTed pressure signal (left) and heat release fluctuation (right) at  $\phi =$

0.50



**Figure D.2. FFTed pressure signal (left) and heat release fluctuation (right) at  $\phi =$**

**0.50**

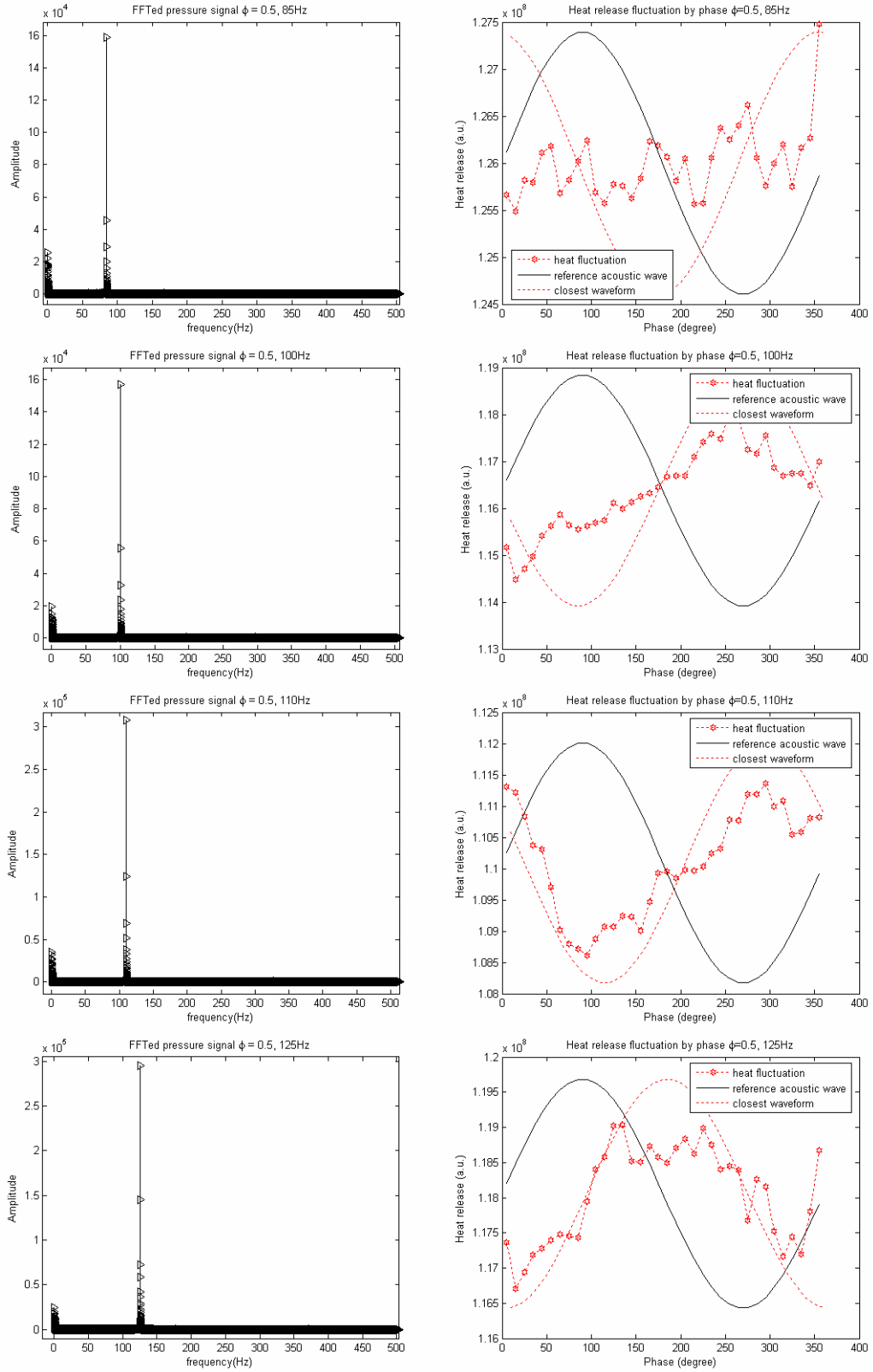


**Figure D.3. FFTed pressure signal (left) and heat release fluctuation (right) at  $\phi =$**

**0.50**

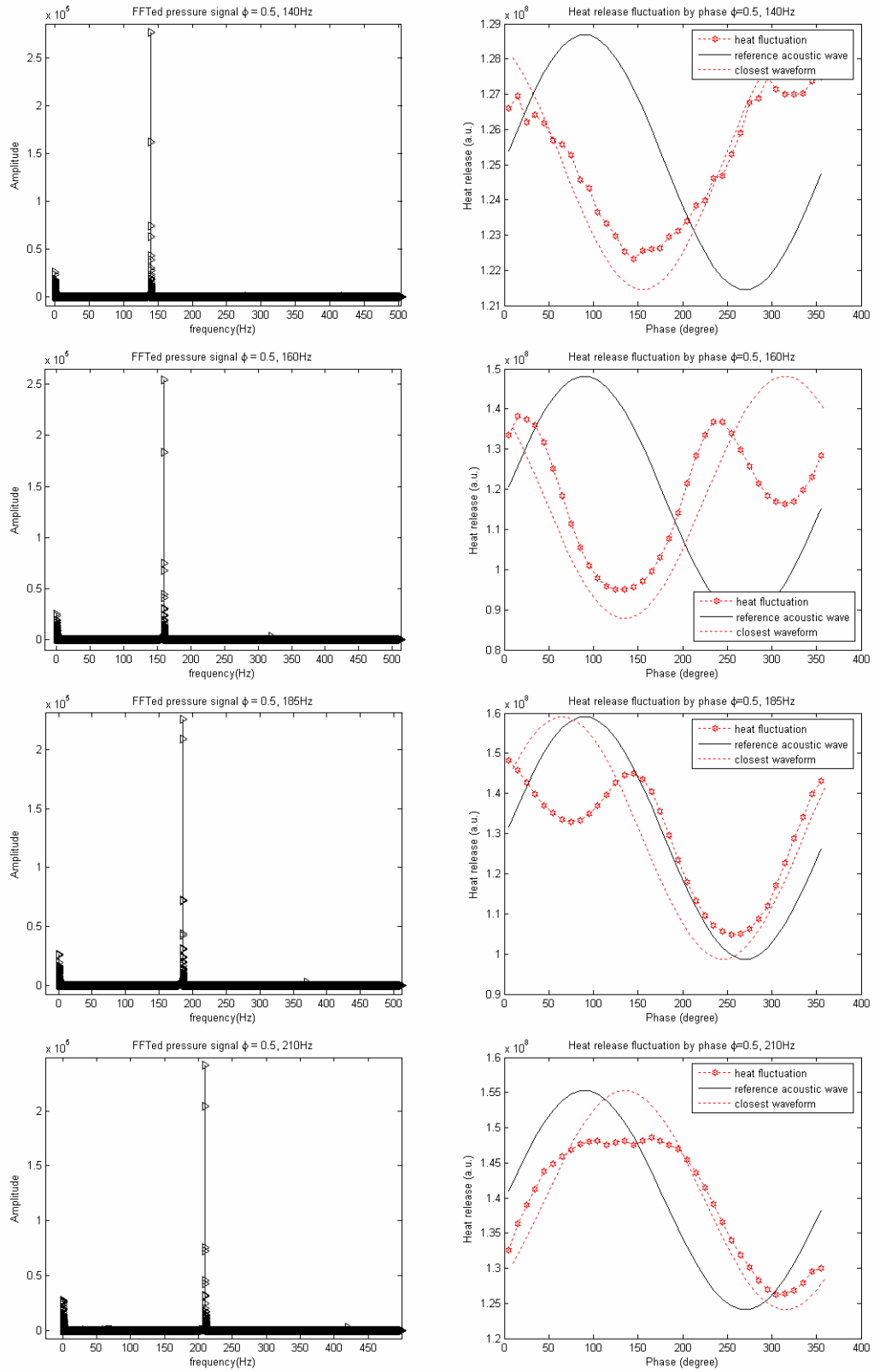
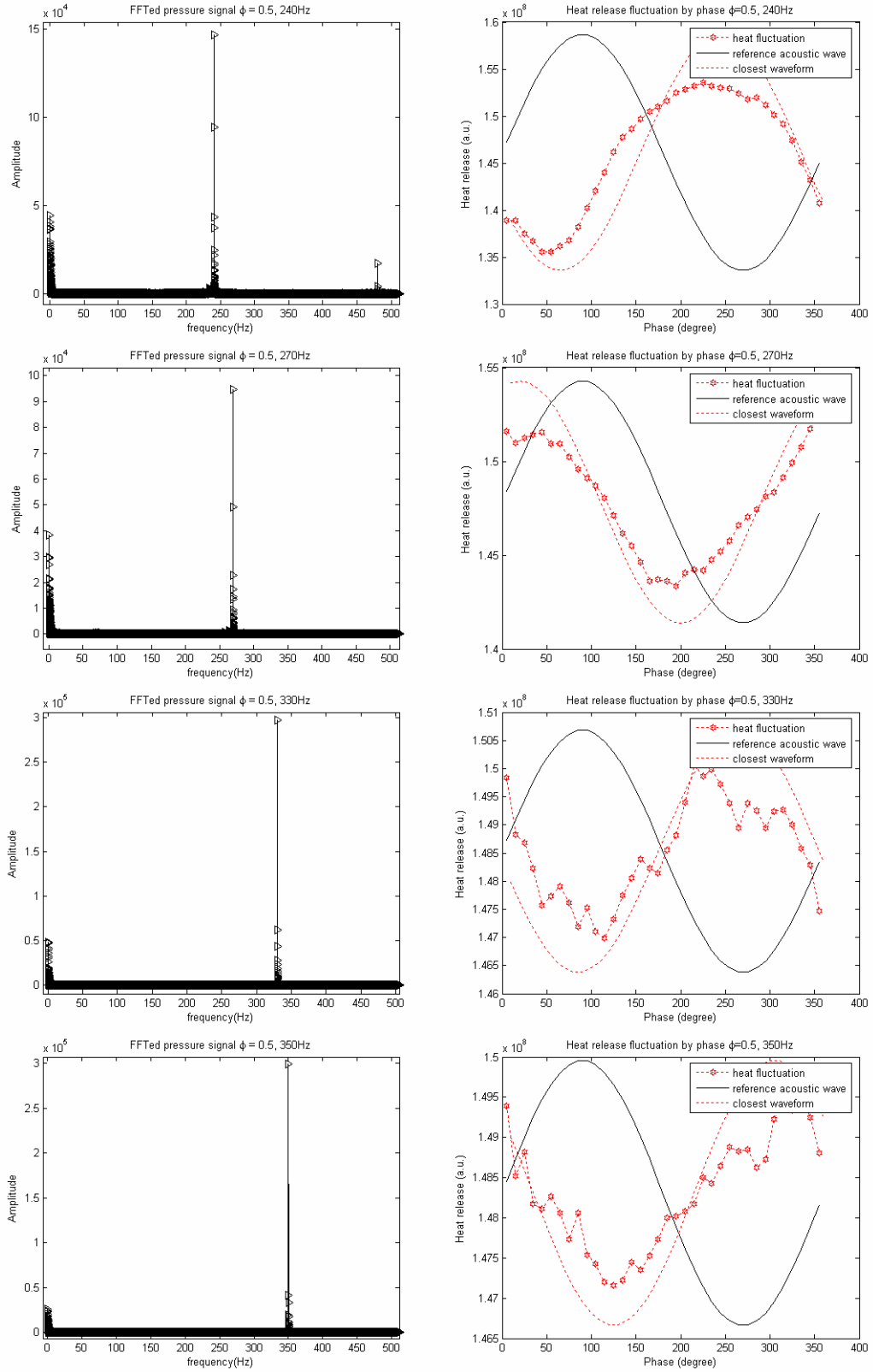


Figure D.4. FFTed pressure signal (left) and heat release fluctuation (right) at  $\phi =$

0.50



**Figure D.5. FFTed pressure signal (left) and heat release fluctuation (right) at  $\phi =$**

**0.50**

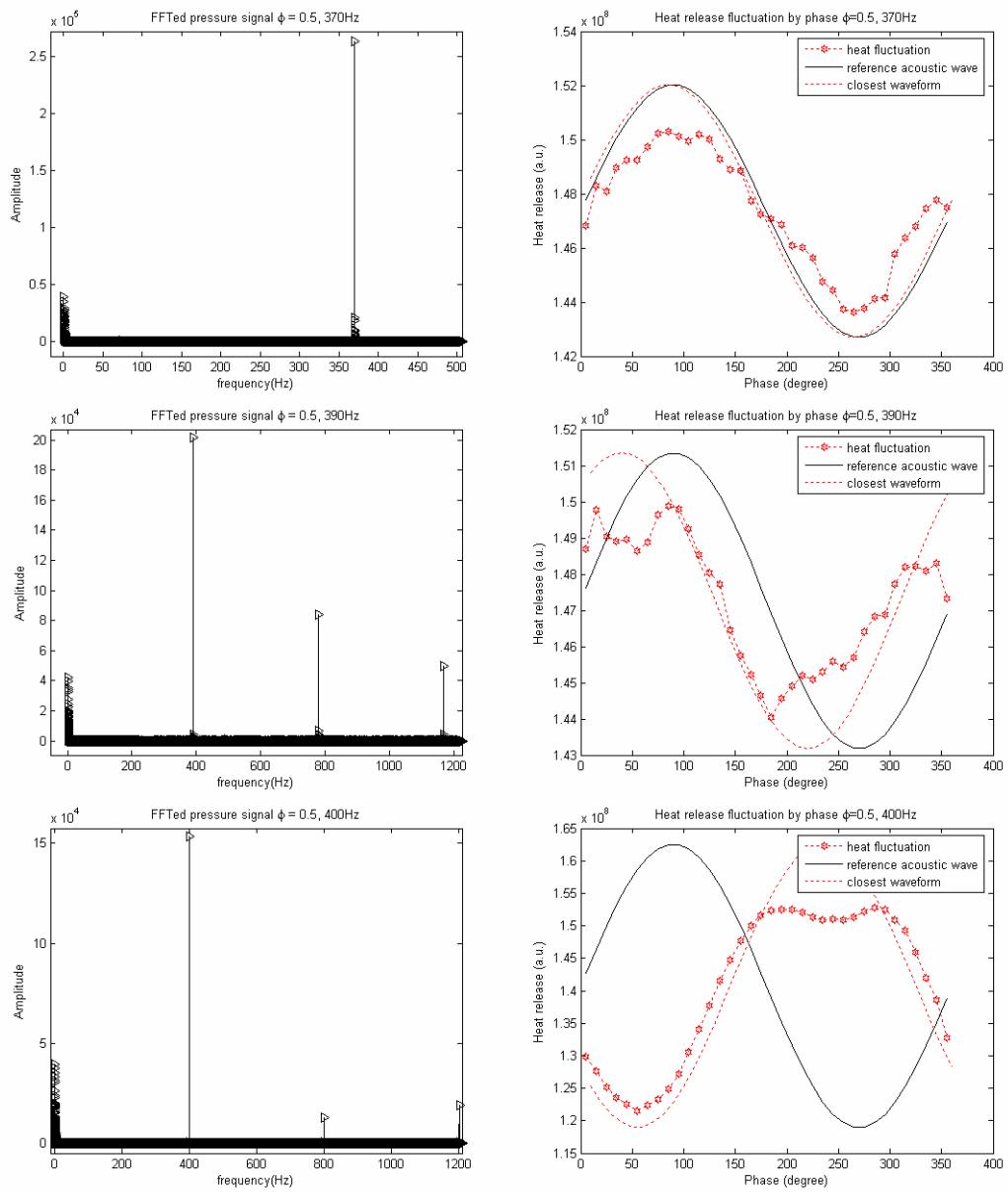


**Figure D.6. FFTed pressure signal (left) and heat release fluctuation (right) at  $\phi = 0.50$**

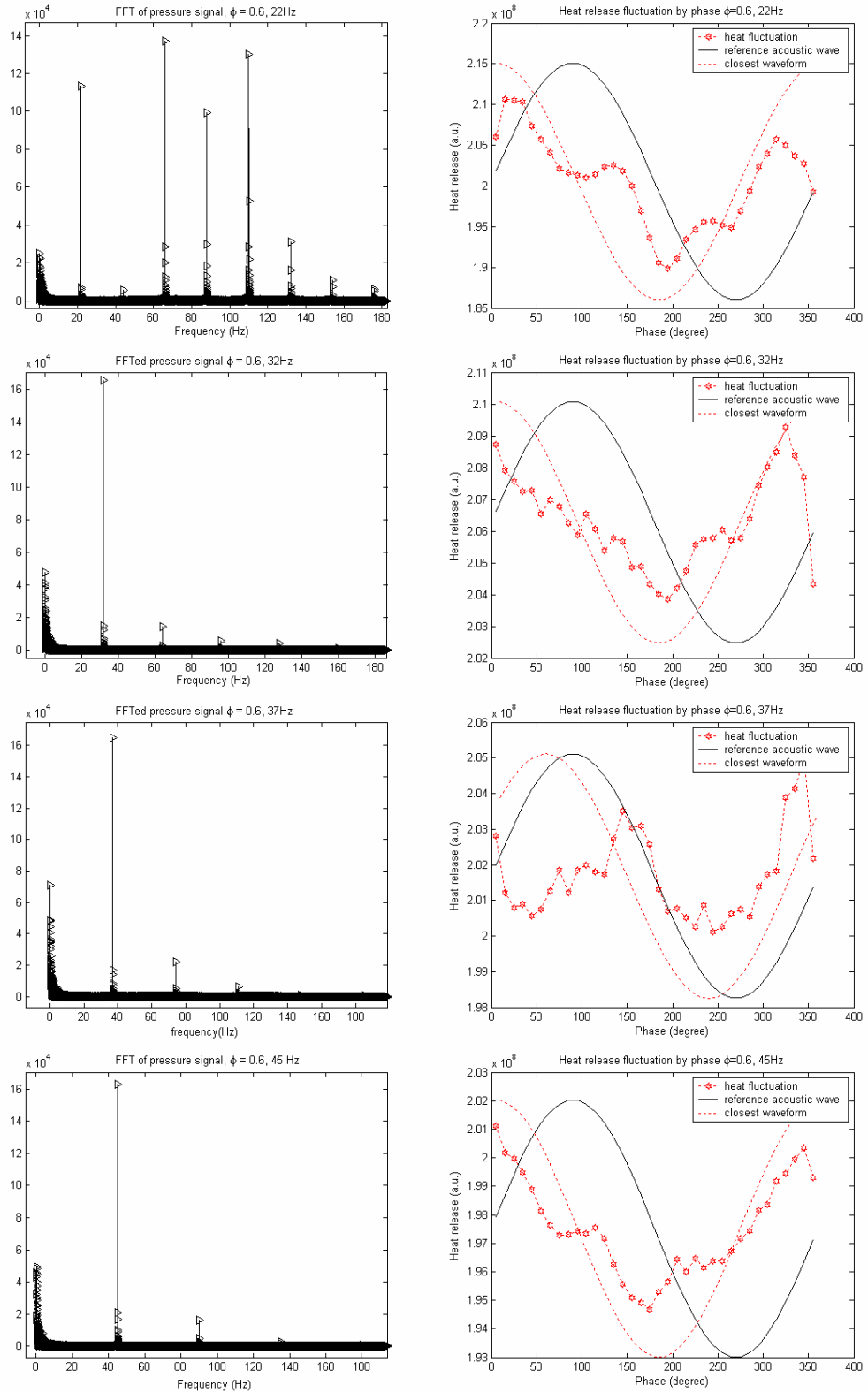


**Figure D.7. FFTed pressure signal (left) and heat release fluctuation (right) at  $\phi = 0.60$ .**

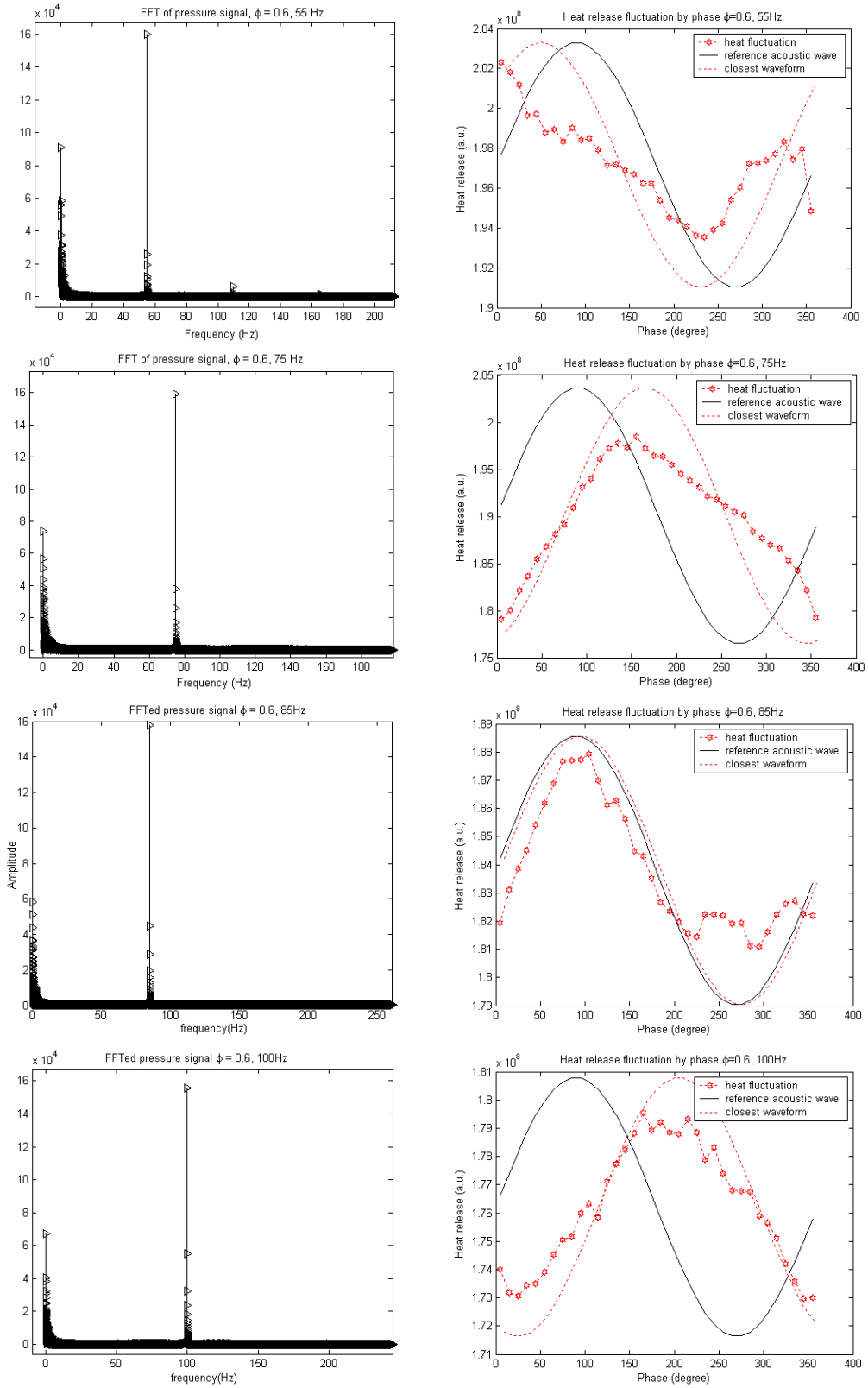
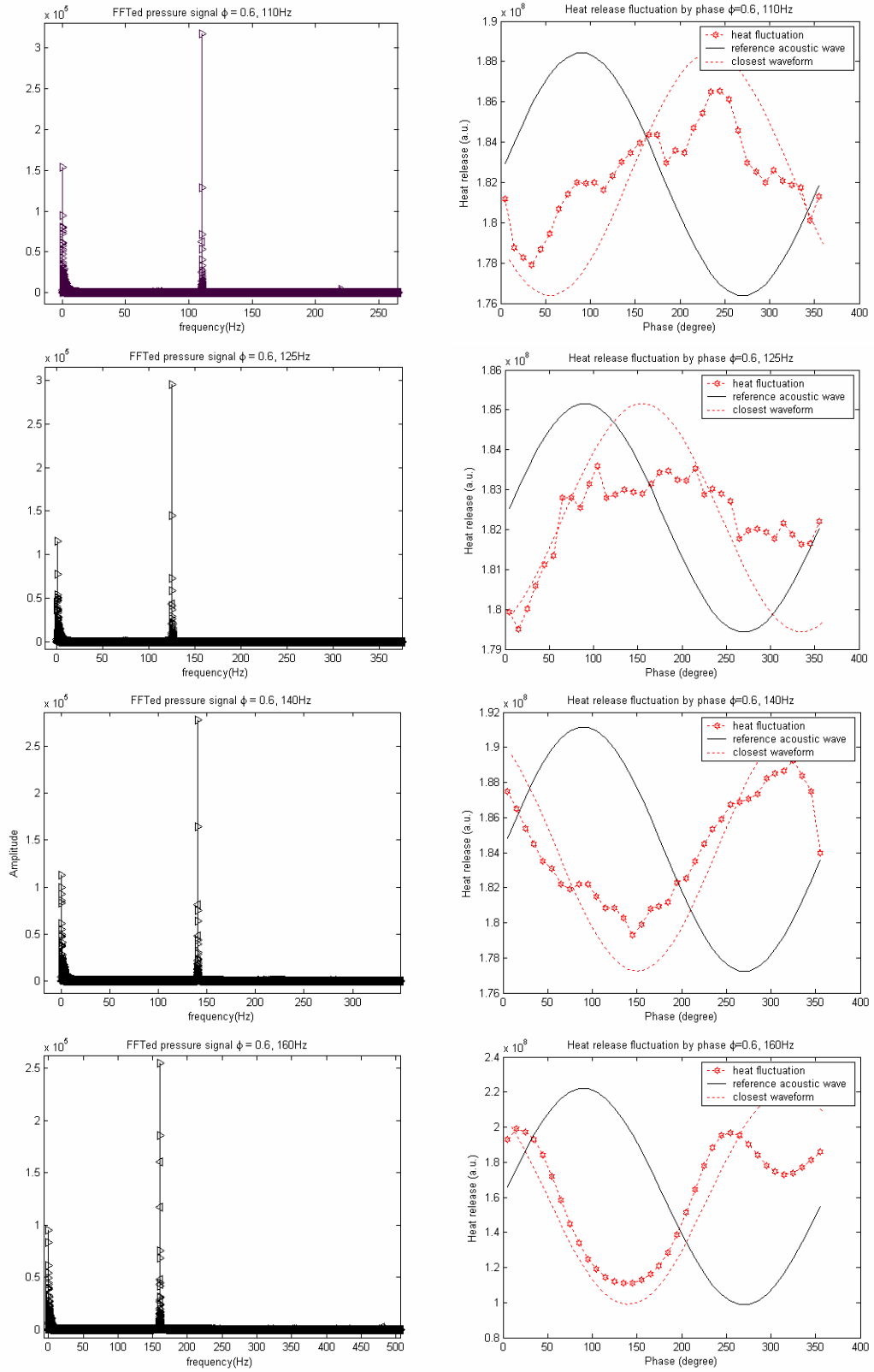
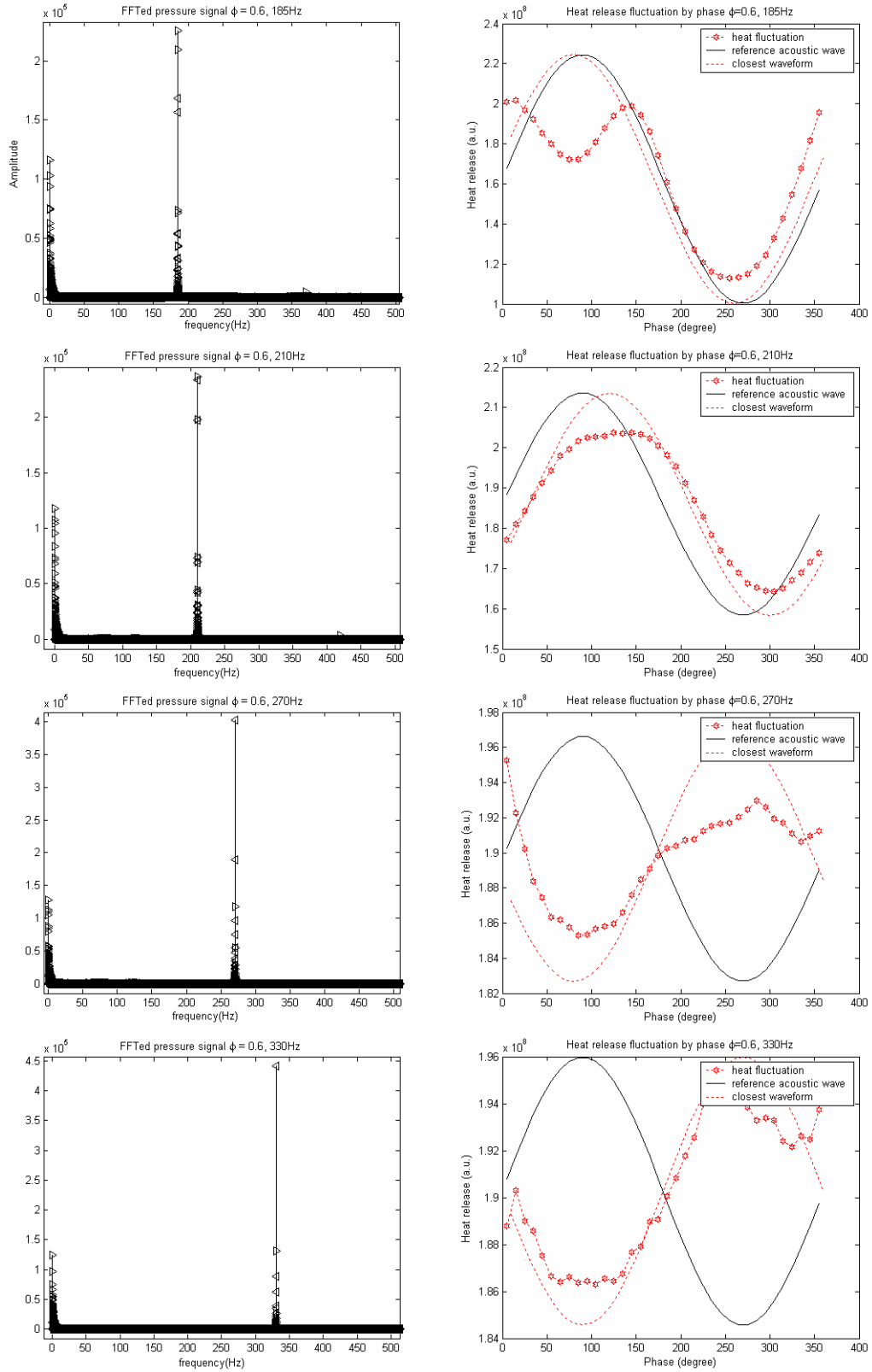


Figure D.8. FFTed pressure signal (left) and heat release fluctuation (right) at  $\phi = 0.60$ .



**Figure D.9. FFTed pressure signal (left) and heat release fluctuation (right) at  $\phi = 0.60$ .**



**Figure D.10. FFTed pressure signal (left) and heat release fluctuation (right) at  $\phi = 0.60$ .**

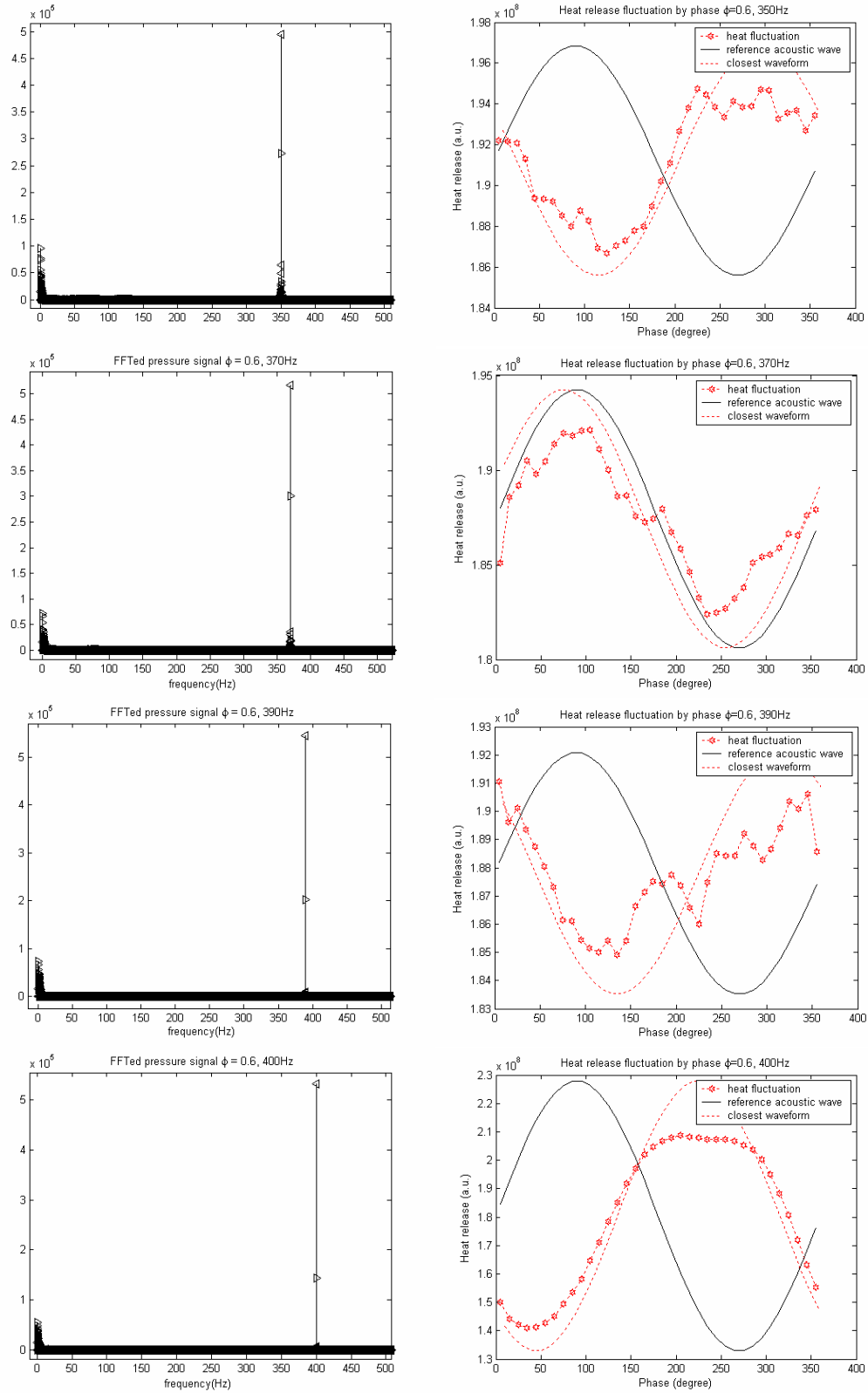


**Figure D.11. FFTed pressure signal (left) and heat release fluctuation (right) at  $\phi = 0.60$ .**

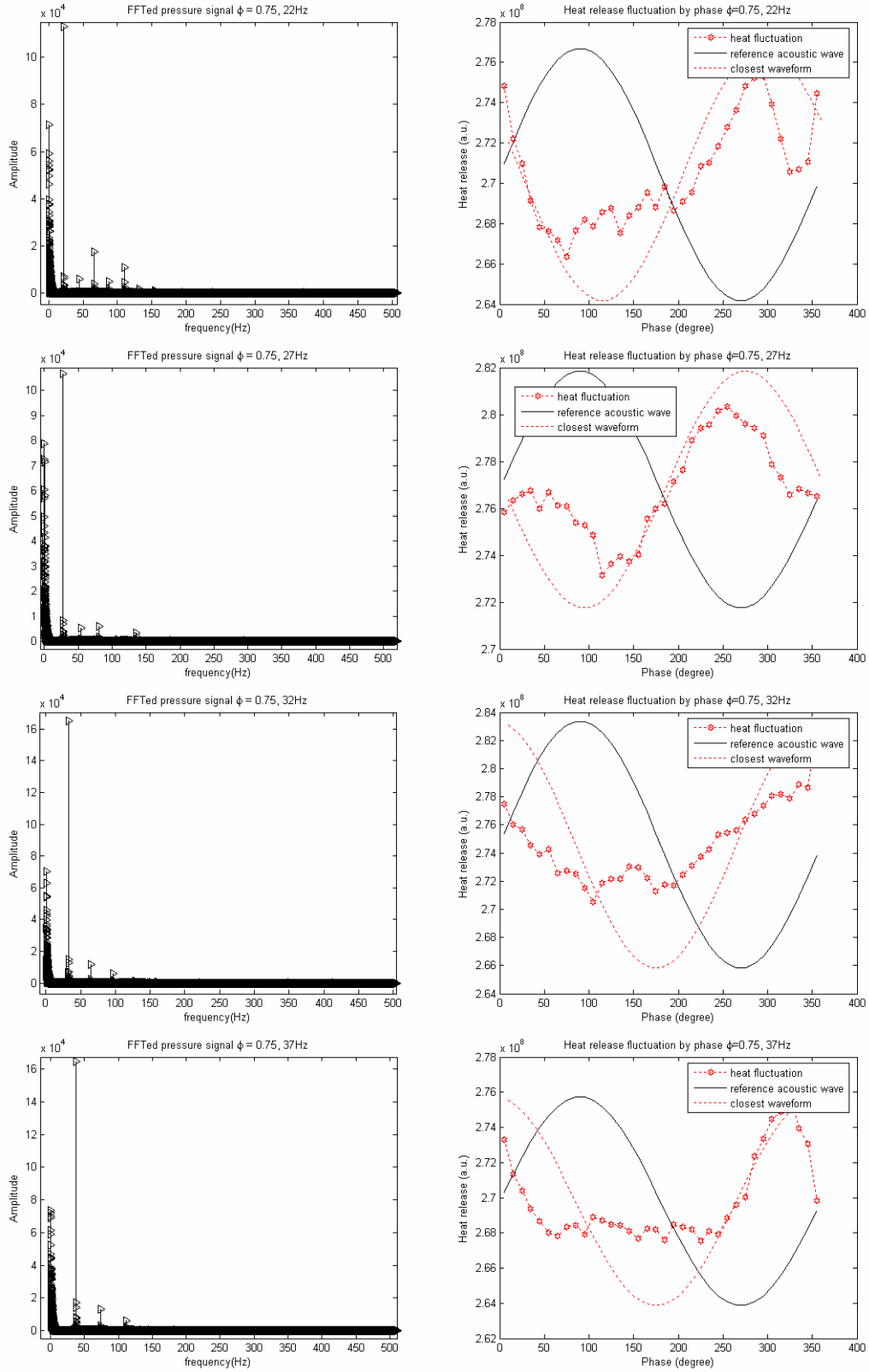


**Figure D.12. FFTed pressure signal (left) and heat release fluctuation (right) at  $\phi = 0.75$**

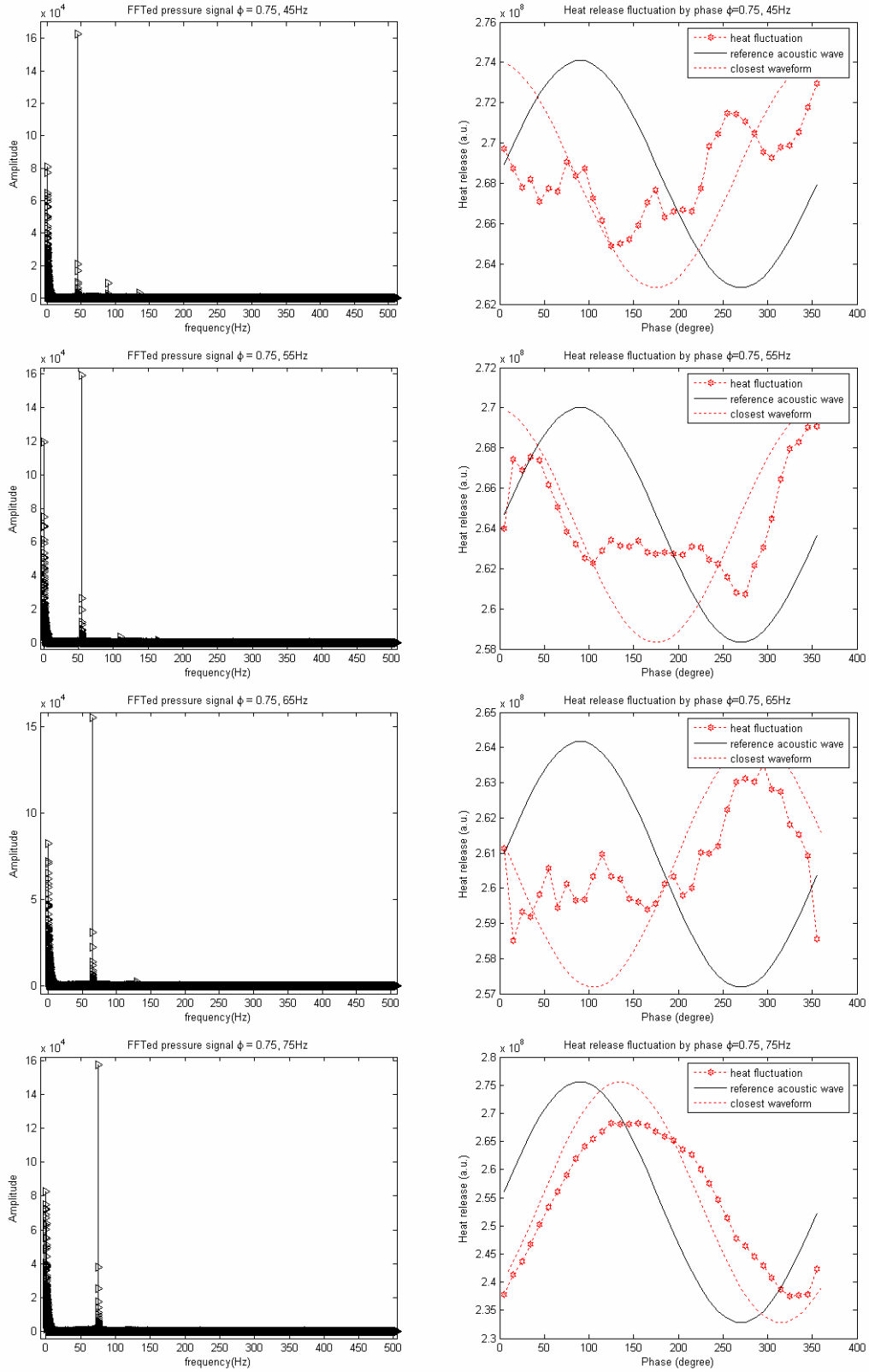
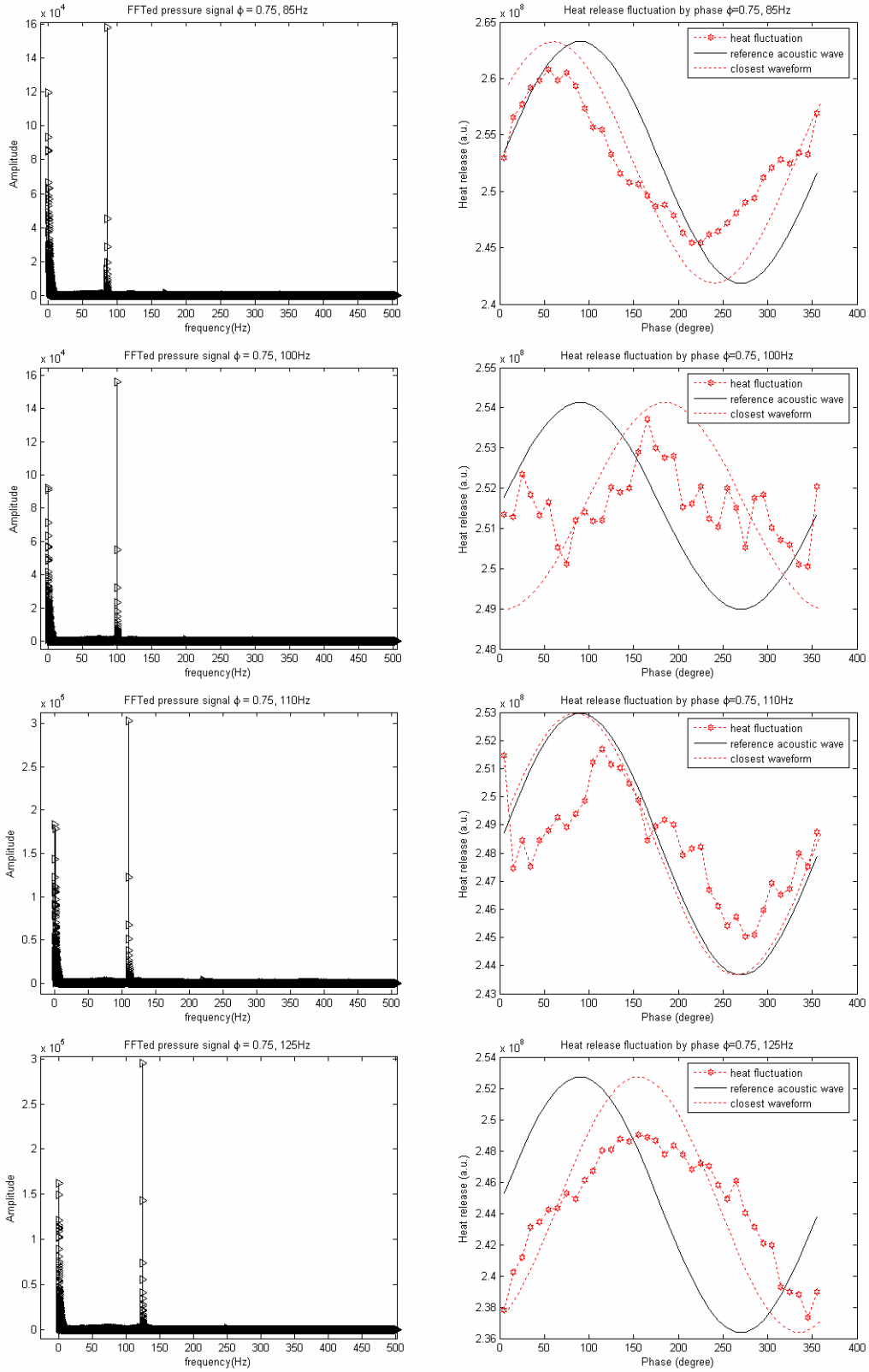
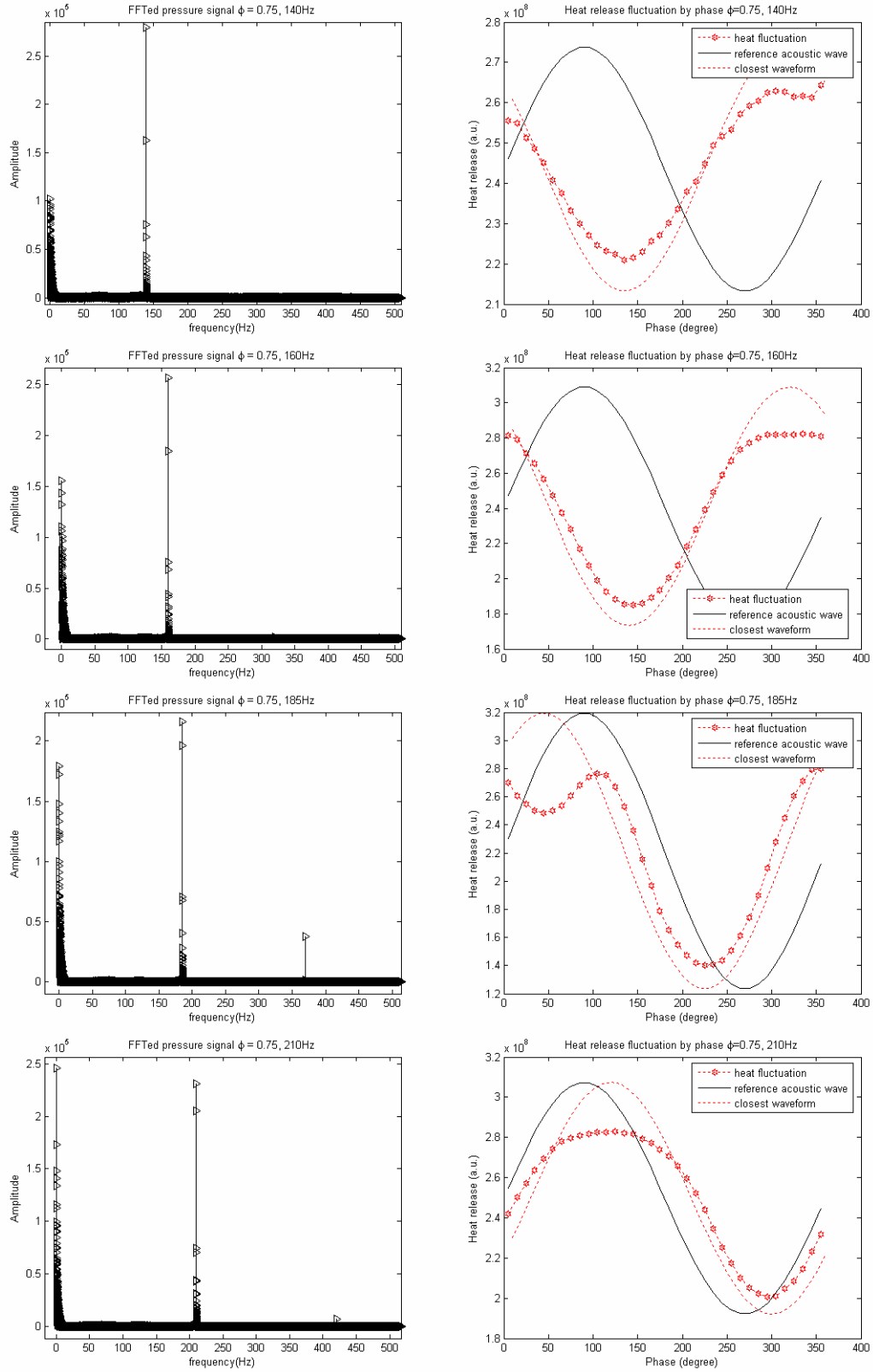


Figure D.13. FFTed pressure signal (left) and heat release fluctuation (right) at  $\phi =$

0.75



**Figure D.14. FFTed pressure signal (left) and heat release fluctuation (right) at  $\phi = 0.75$**



**Figure D.15. FFTed pressure signal (left) and heat release fluctuation (right) at  $\phi = 0.75$**

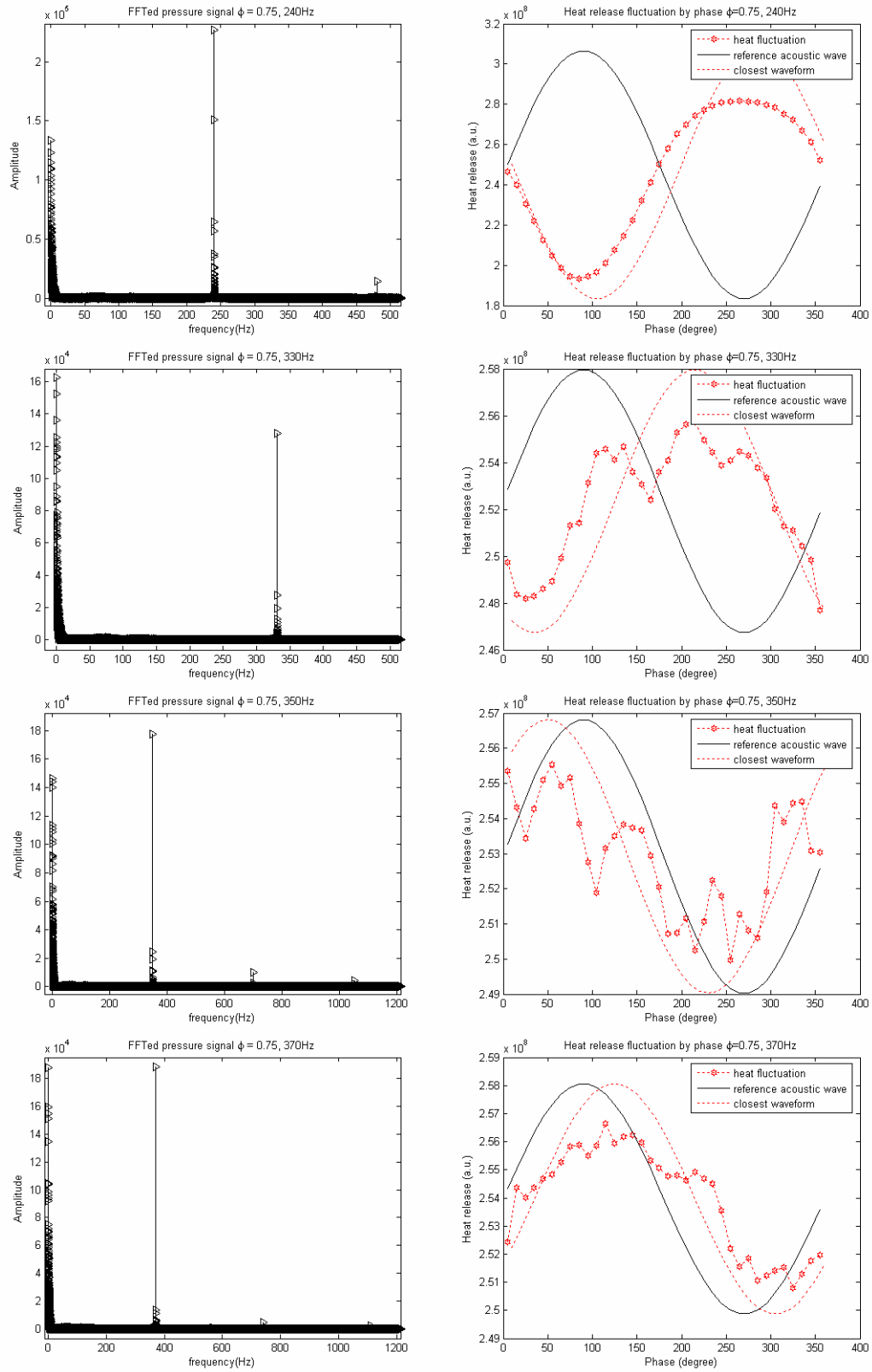


**Figure D.16.** FFTed pressure signal (left) and heat release fluctuation (right) at  $\phi = 0.75$

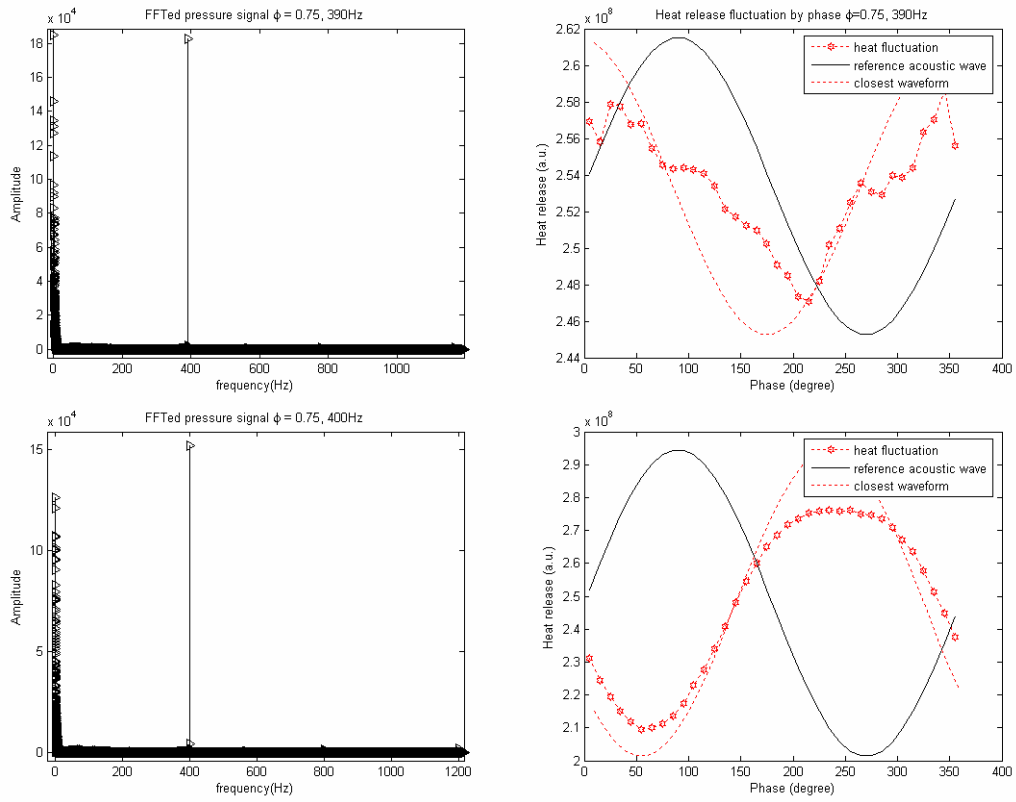


**Figure D.17. FFTed pressure signal (left) and heat release fluctuation (right) at  $\phi = 0.75$**

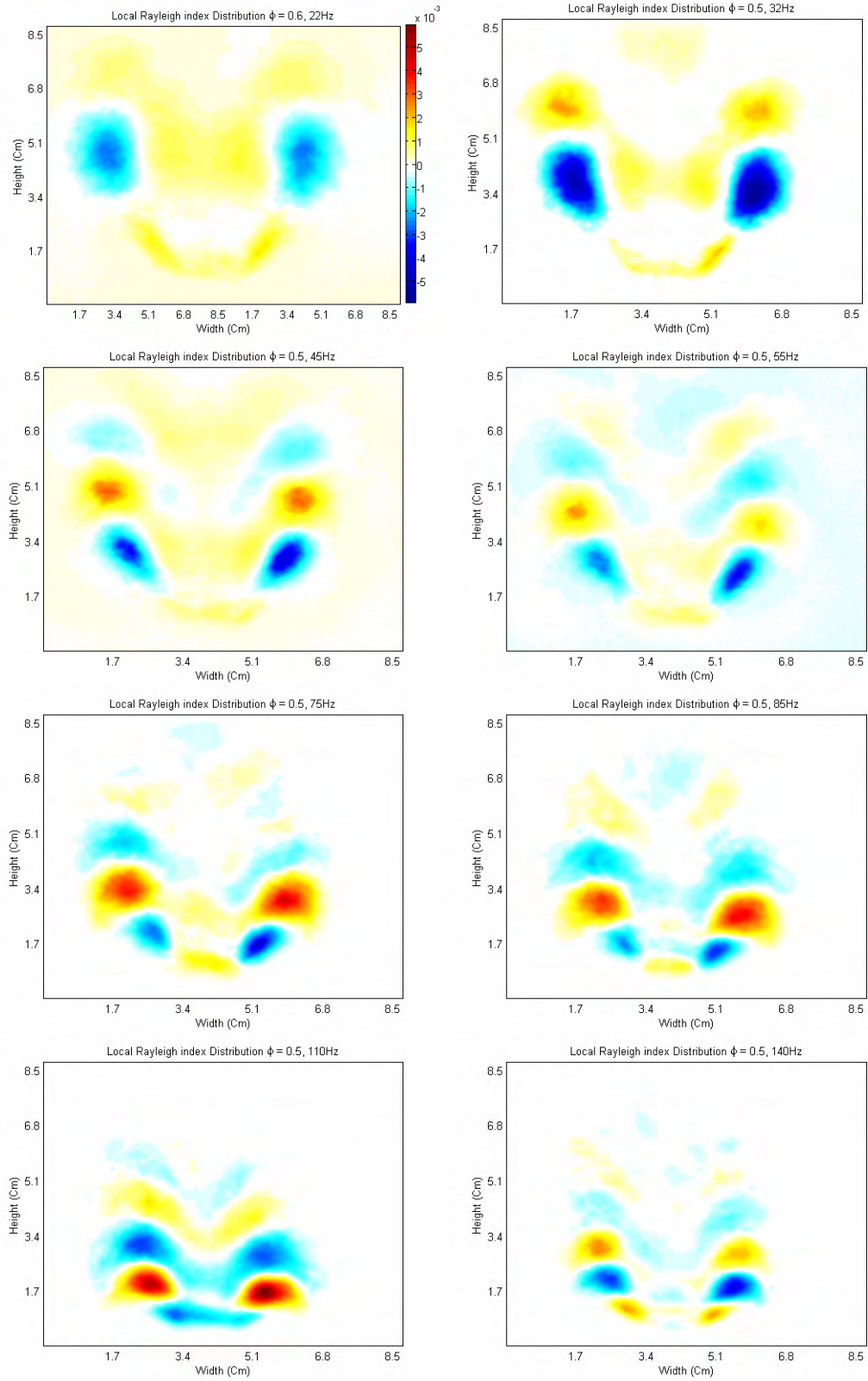


**Figure D.18. Distribution of local Rayleigh index,  $\phi = 0.50$ .**

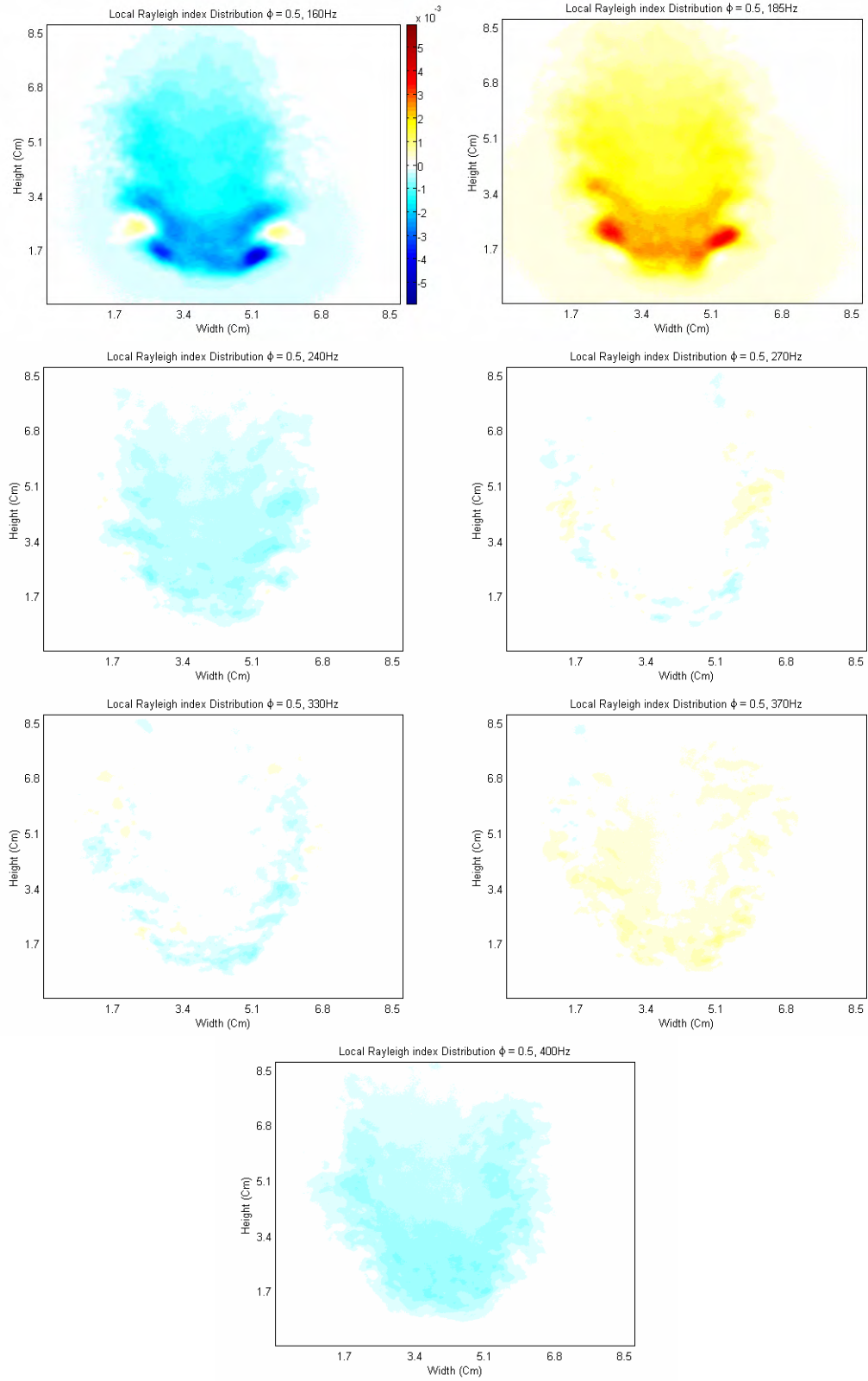


**Figure D.19. Distribution of local Rayleigh index,  $\phi = 0.50$ .**

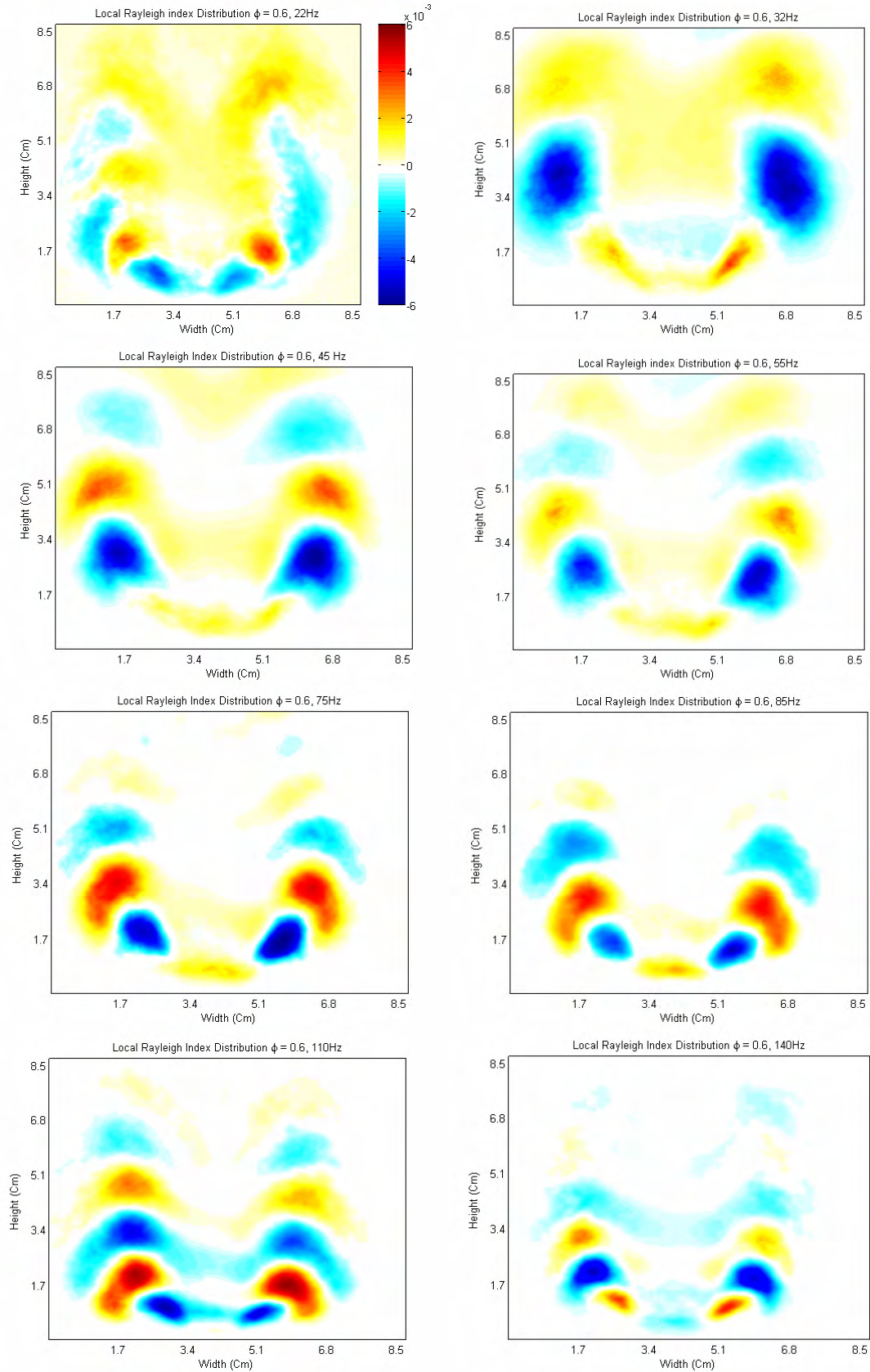


**Figure D.20. Distribution of local Rayleigh index,  $\phi = 0.60$ .**

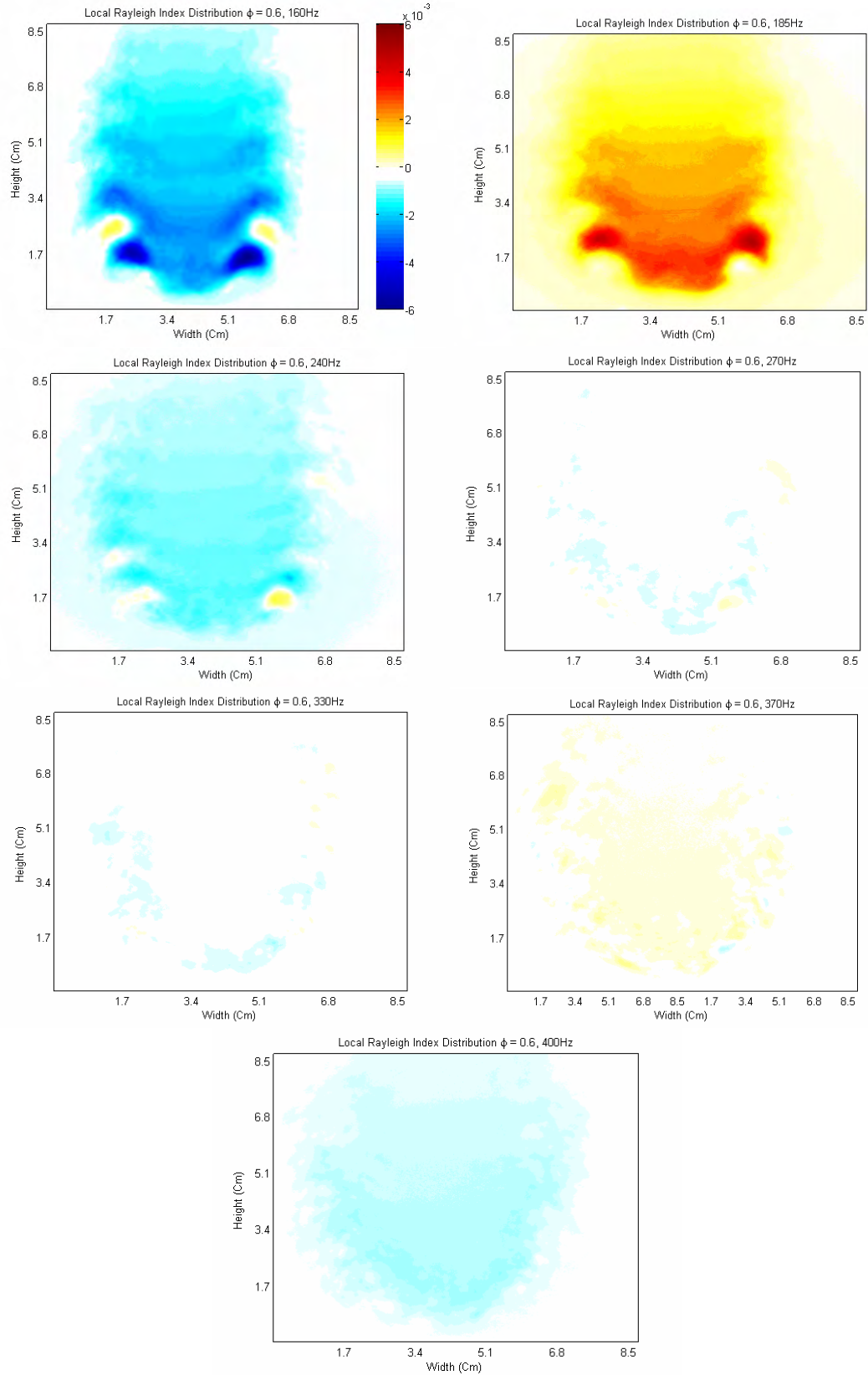


**Figure D.21. Distribution of local Rayleigh index,  $\phi = 0.60$ .**

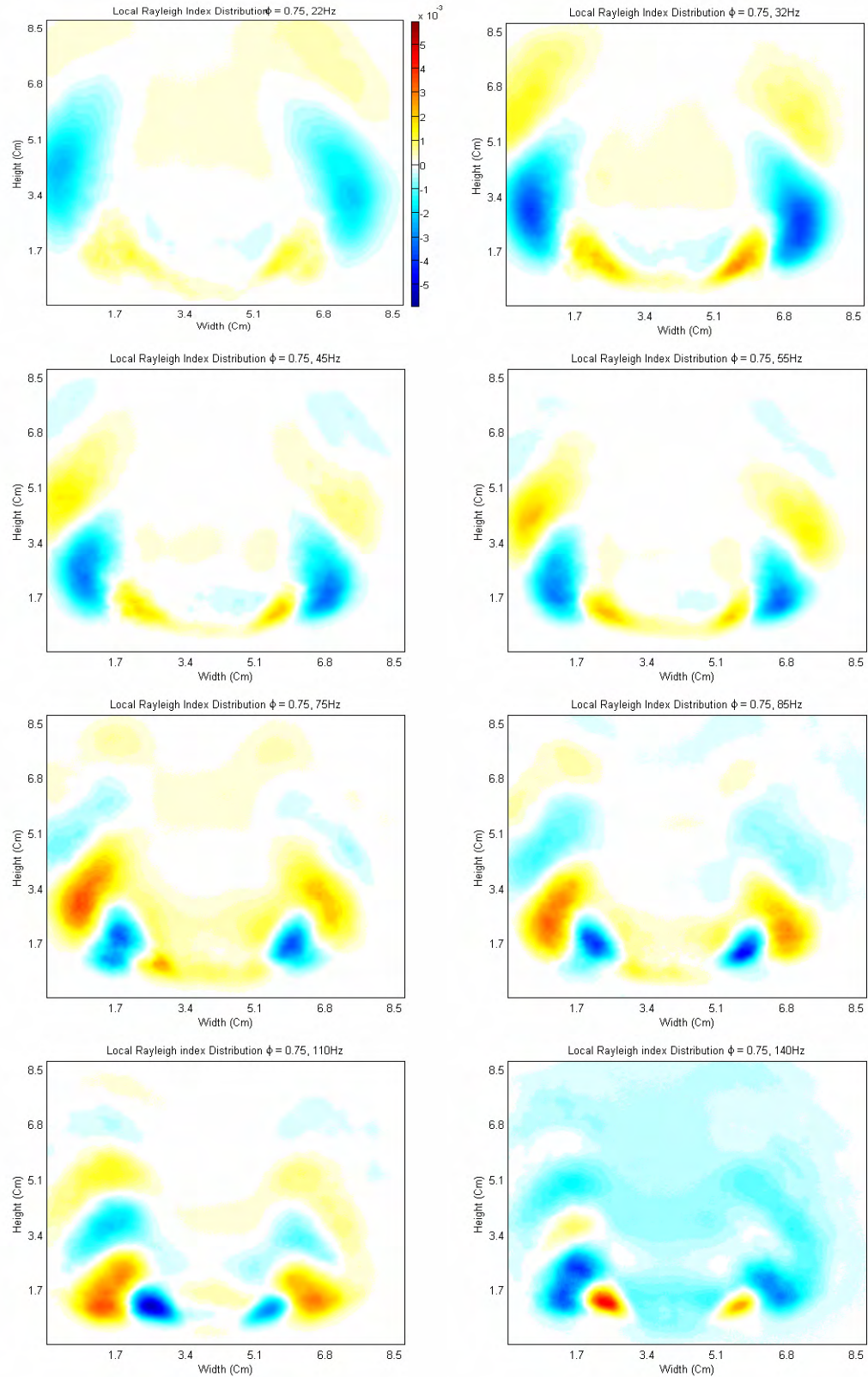


**Figure D.22. Distribution of local Rayleigh index,  $\phi = 0.75$ .**

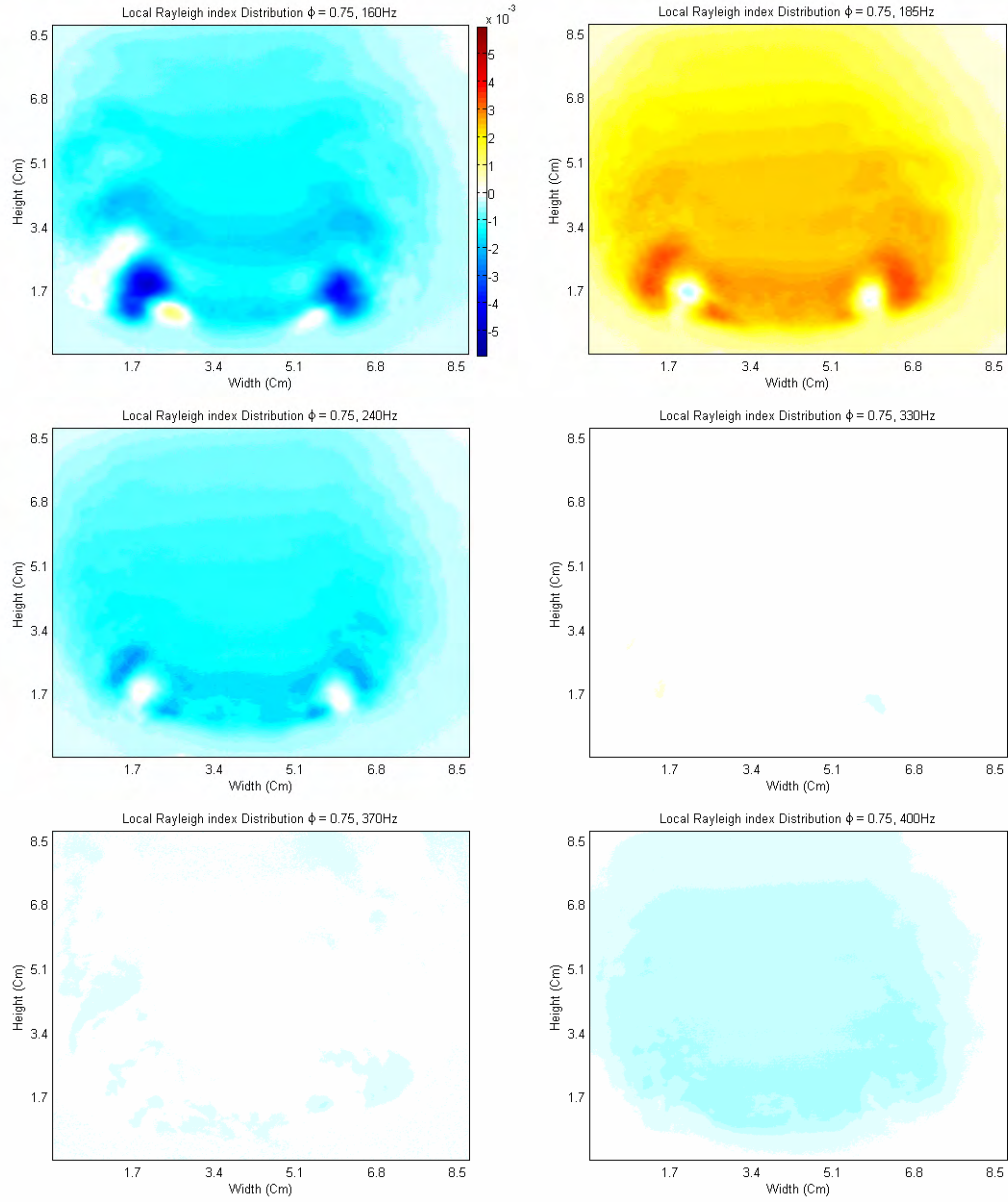


**Figure D.23. Distribution of local Rayleigh index,  $\phi = 0.75$ .**

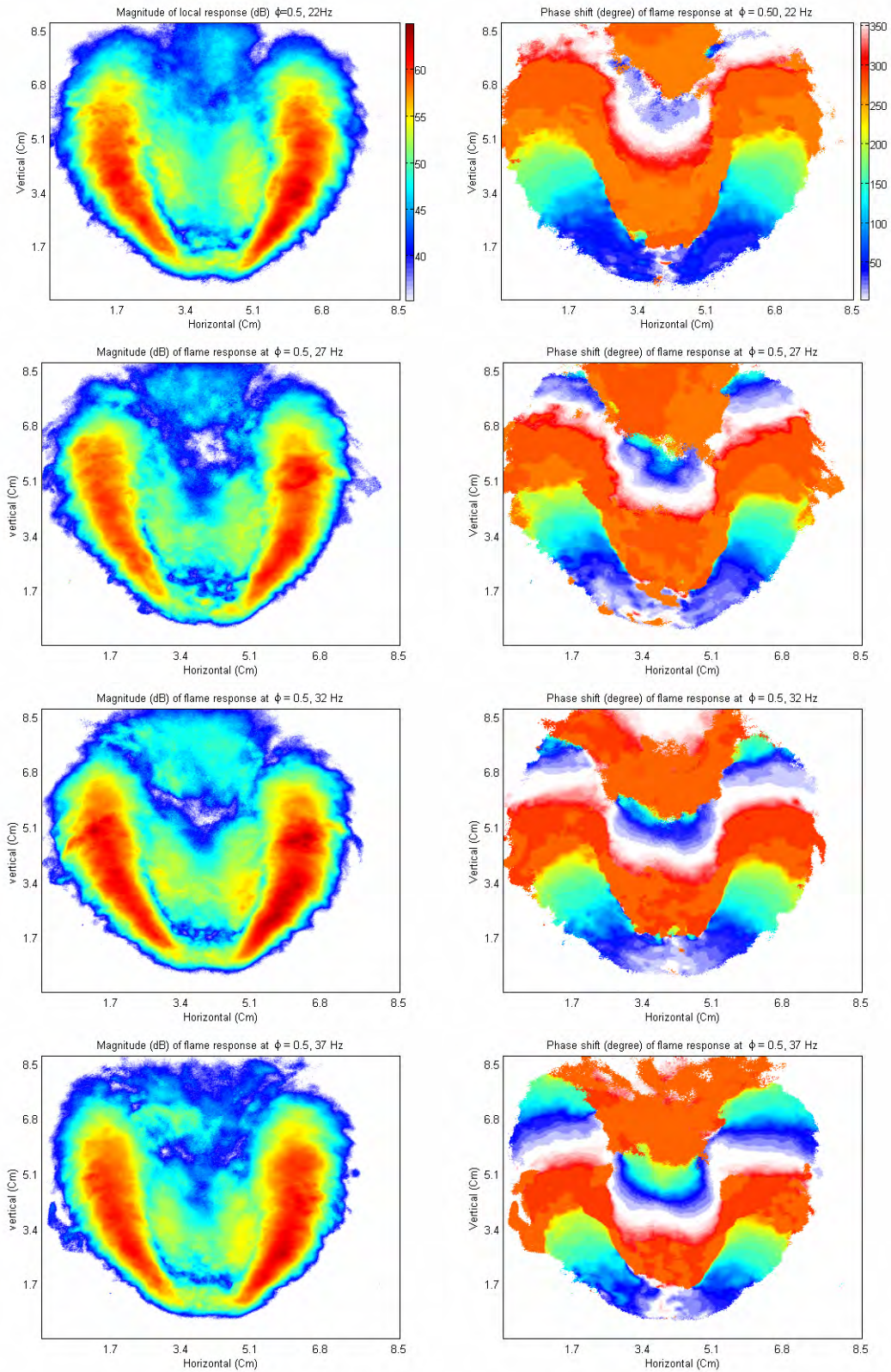


**Figure D.24. Local magnitude (left), and phase shift (right) of flame response,  $\phi = 0.50$ .**

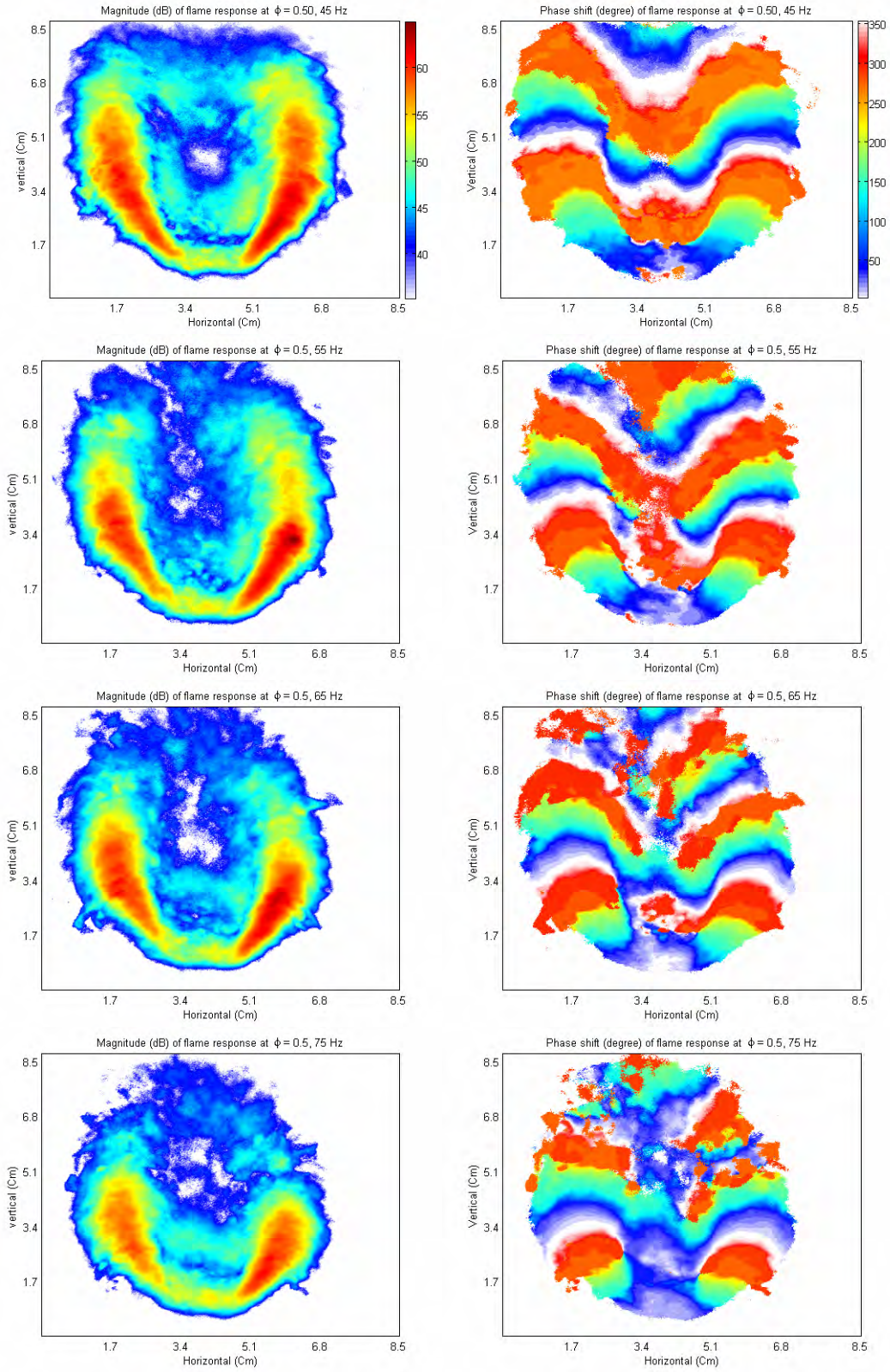


**Figure D.25. Local magnitude (left), and phase shift (right) of flame response,  $\phi = 0.50$ .**

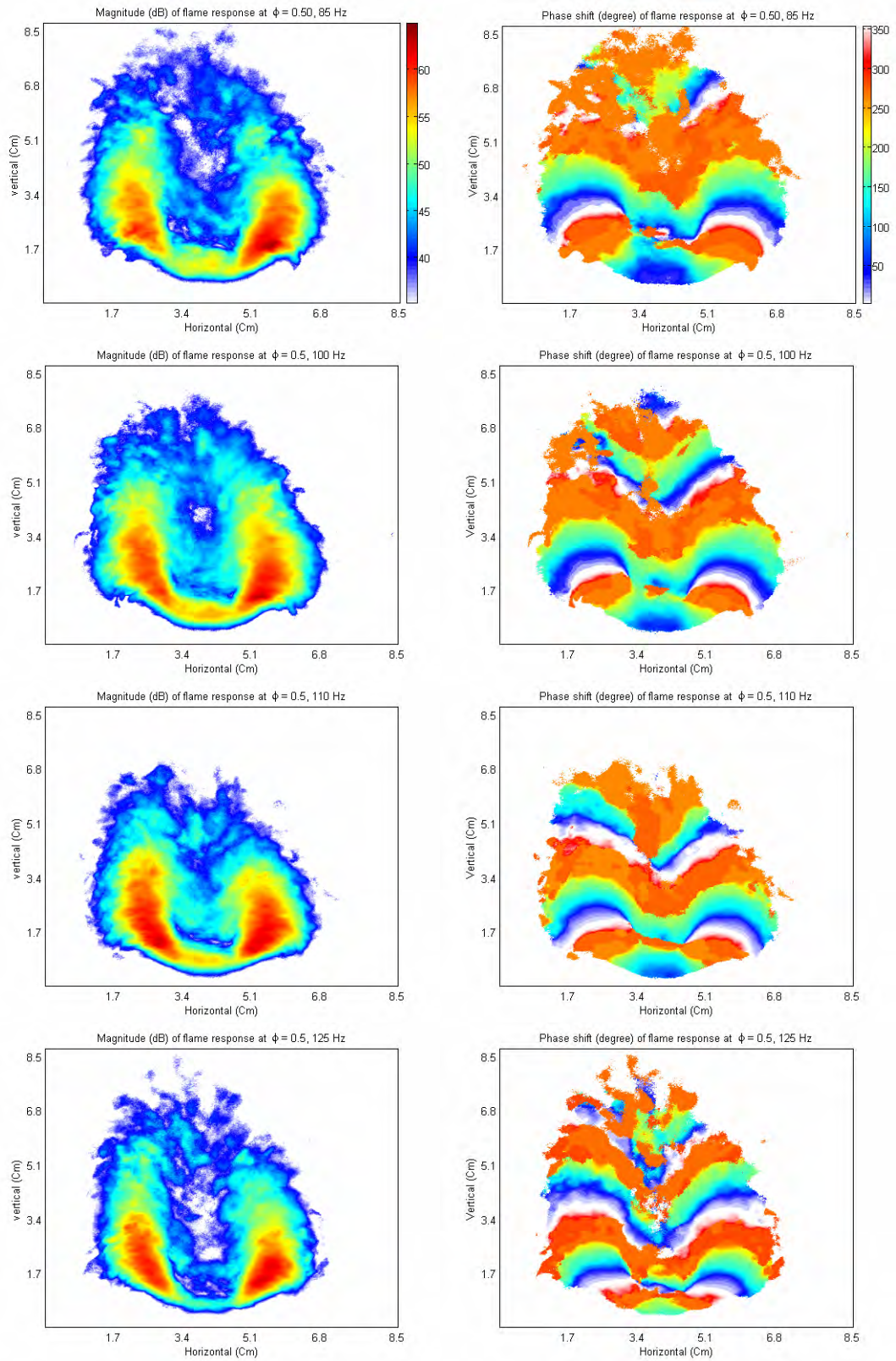
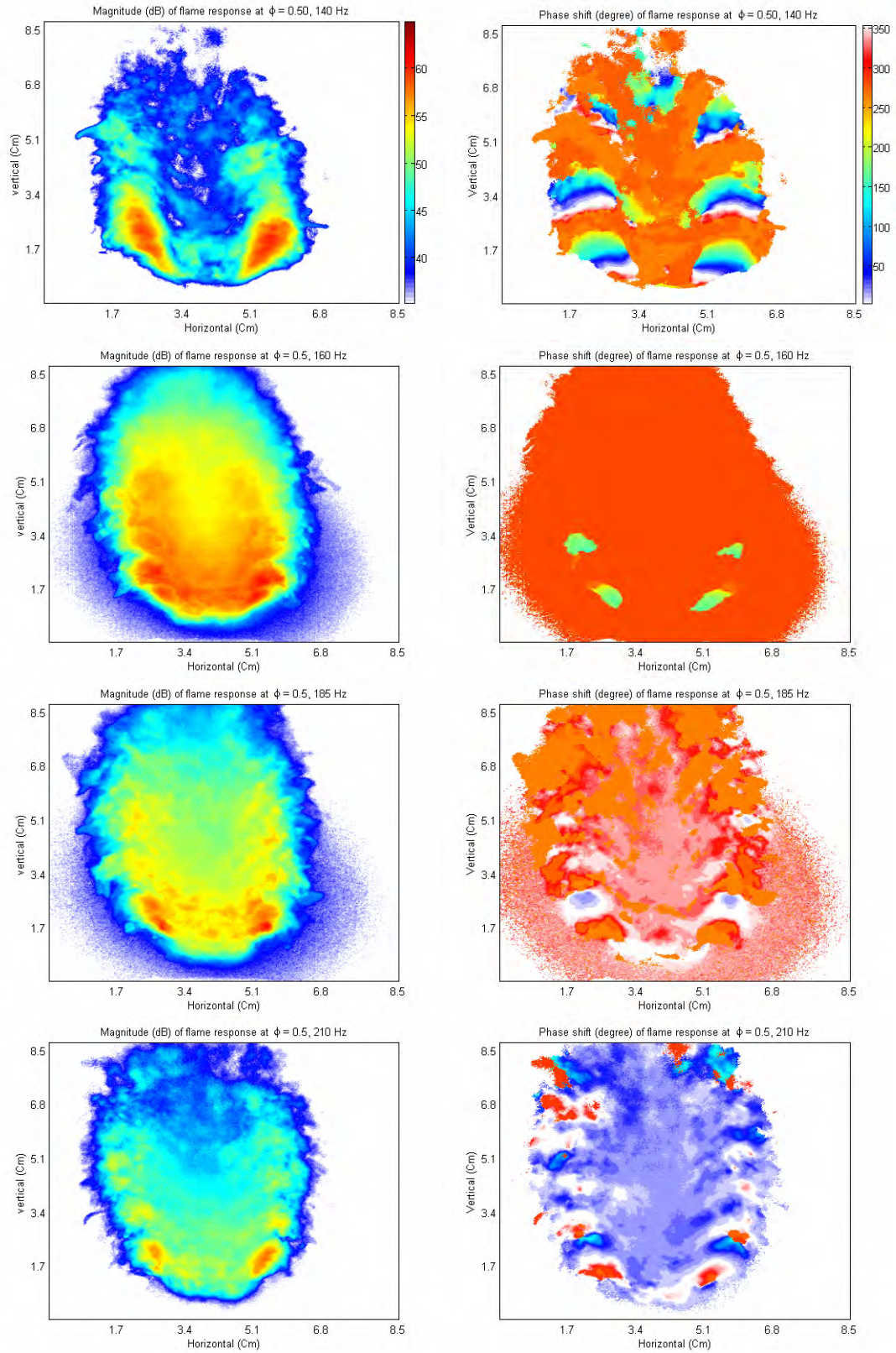
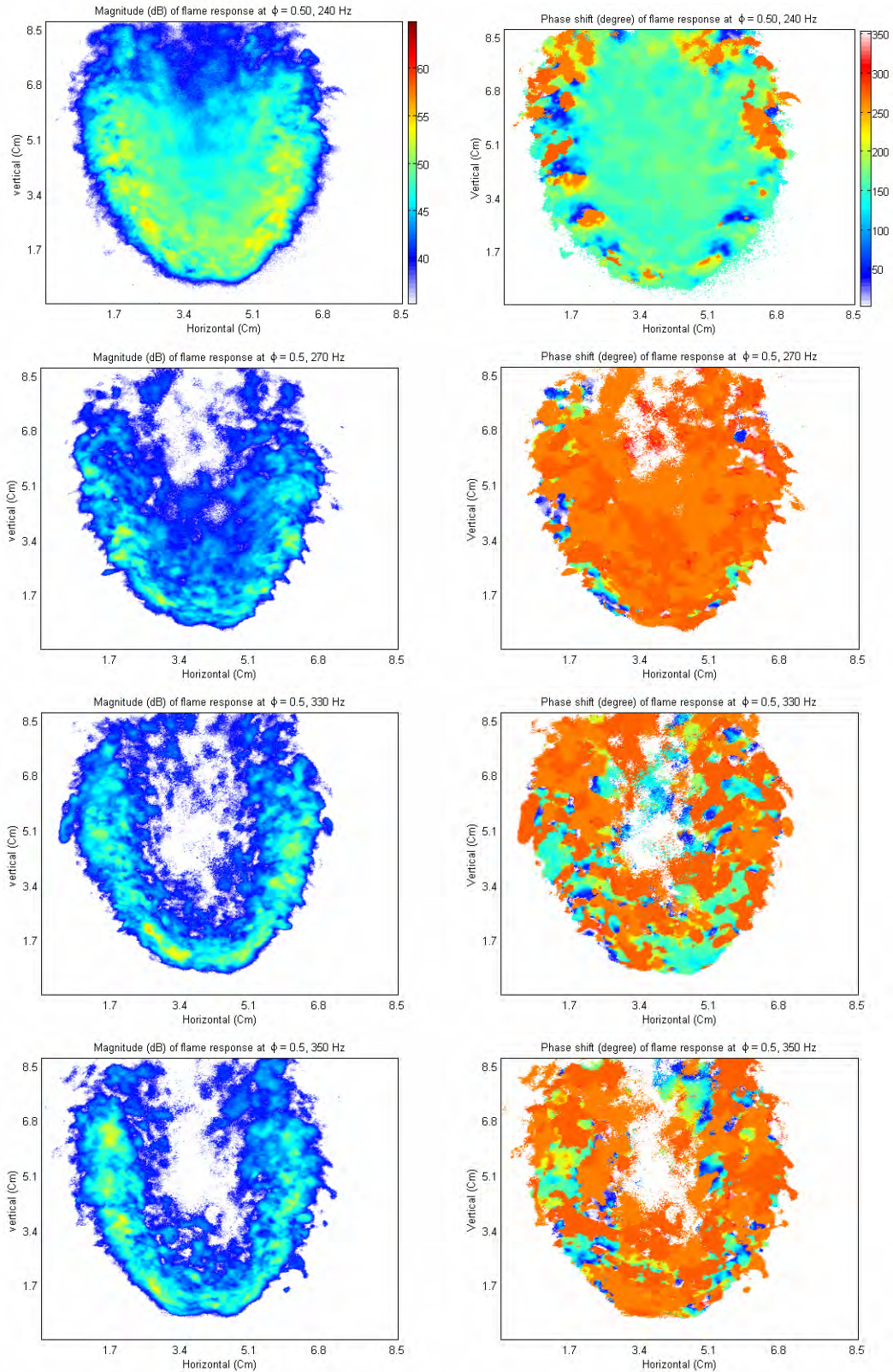


Figure D.26. Local magnitude (left), and phase shift (right) of flame response,  $\phi = 0.50$ .



**Figure D.27. Local magnitude (left), and phase shift (right) of flame response,  $\phi = 0.50$ .**



**Figure D.28. Local magnitude (left), and phase shift (right) of flame response,  $\phi = 0.50$ .**

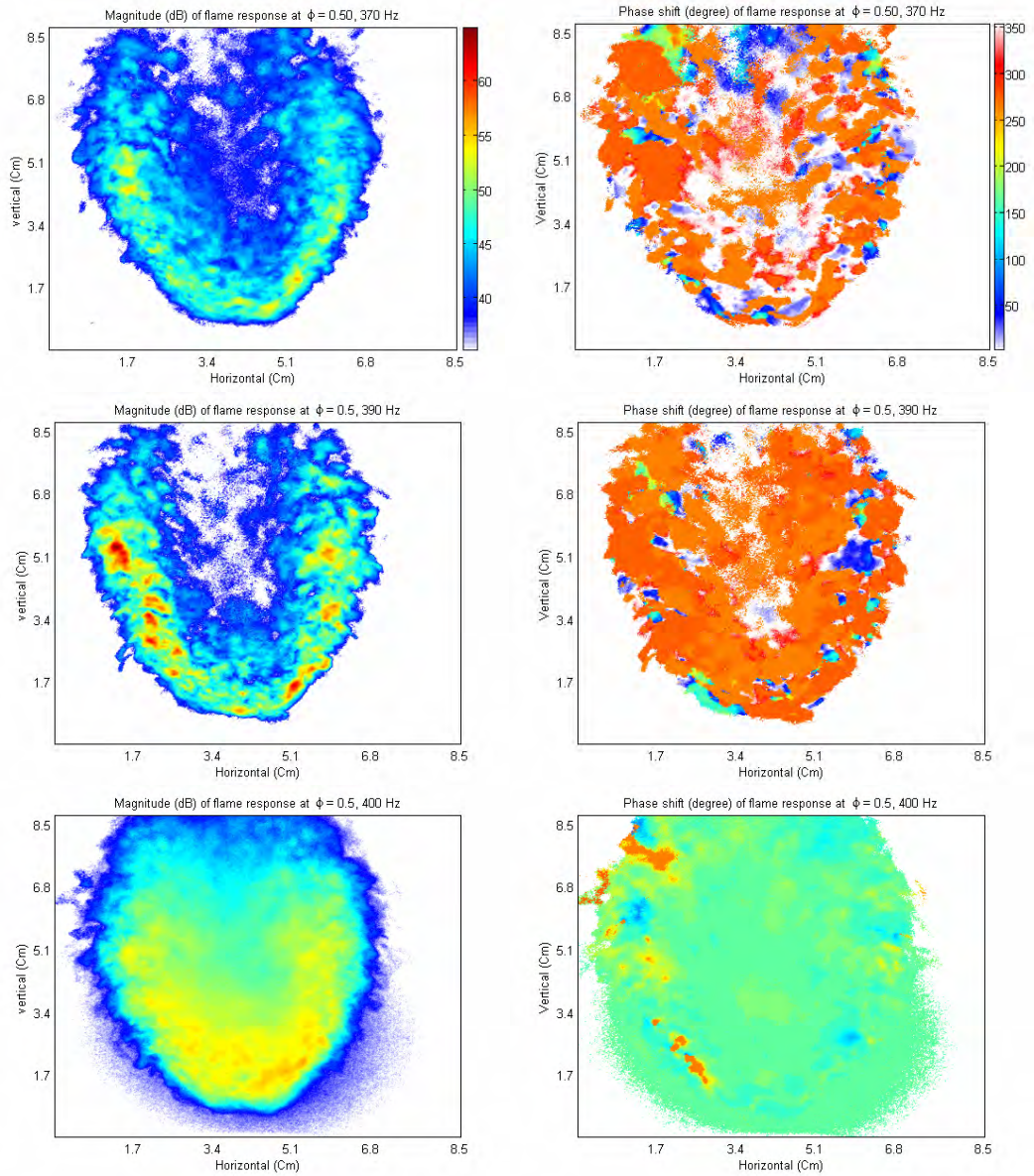


**Figure D.29. Local magnitude (left), and phase shift (right) of flame response,  $\phi = 0.50$ .**

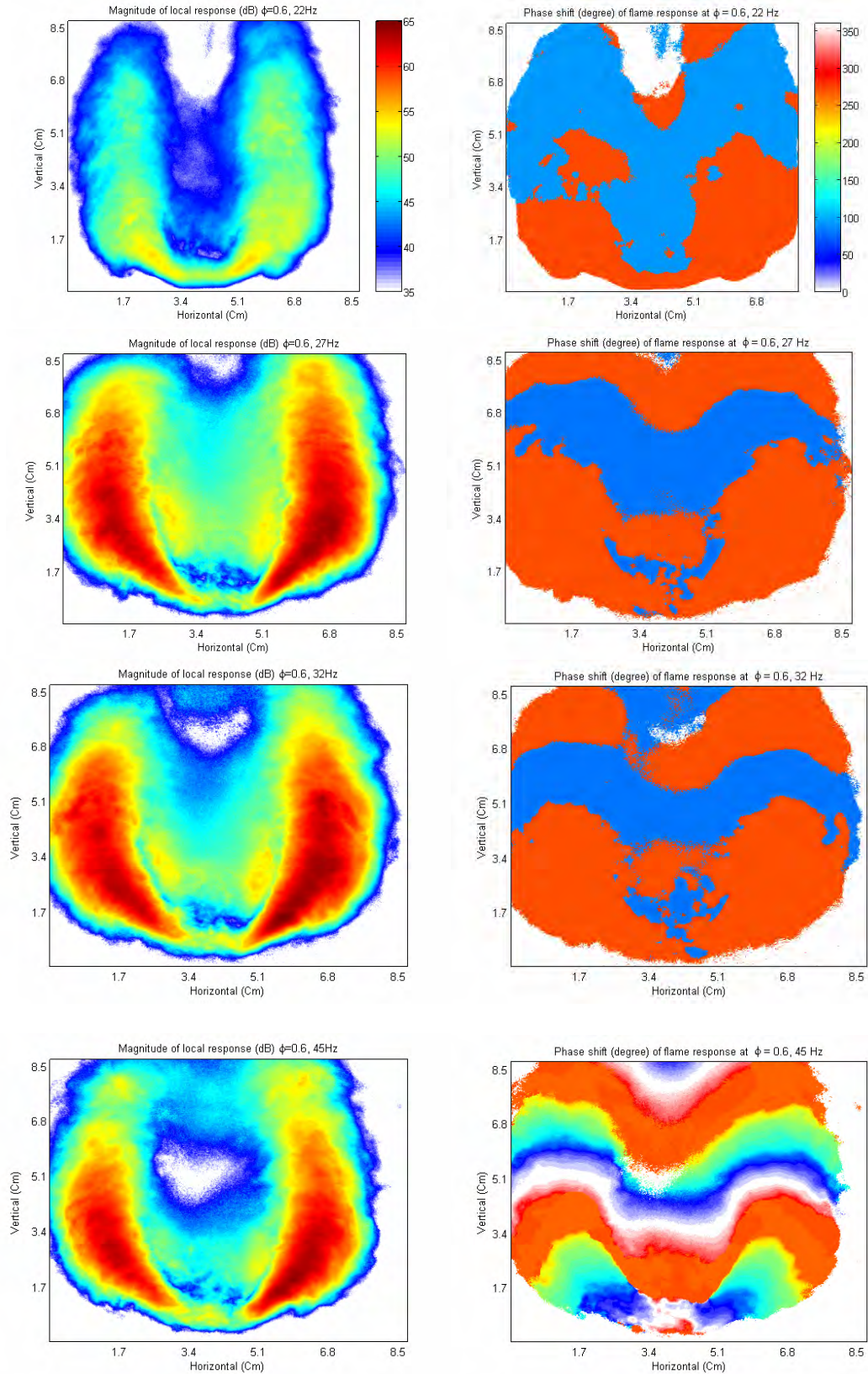


**Figure D.30. Local magnitude (left), and phase shift (right) of flame response,  $\phi = 0.60$ .**

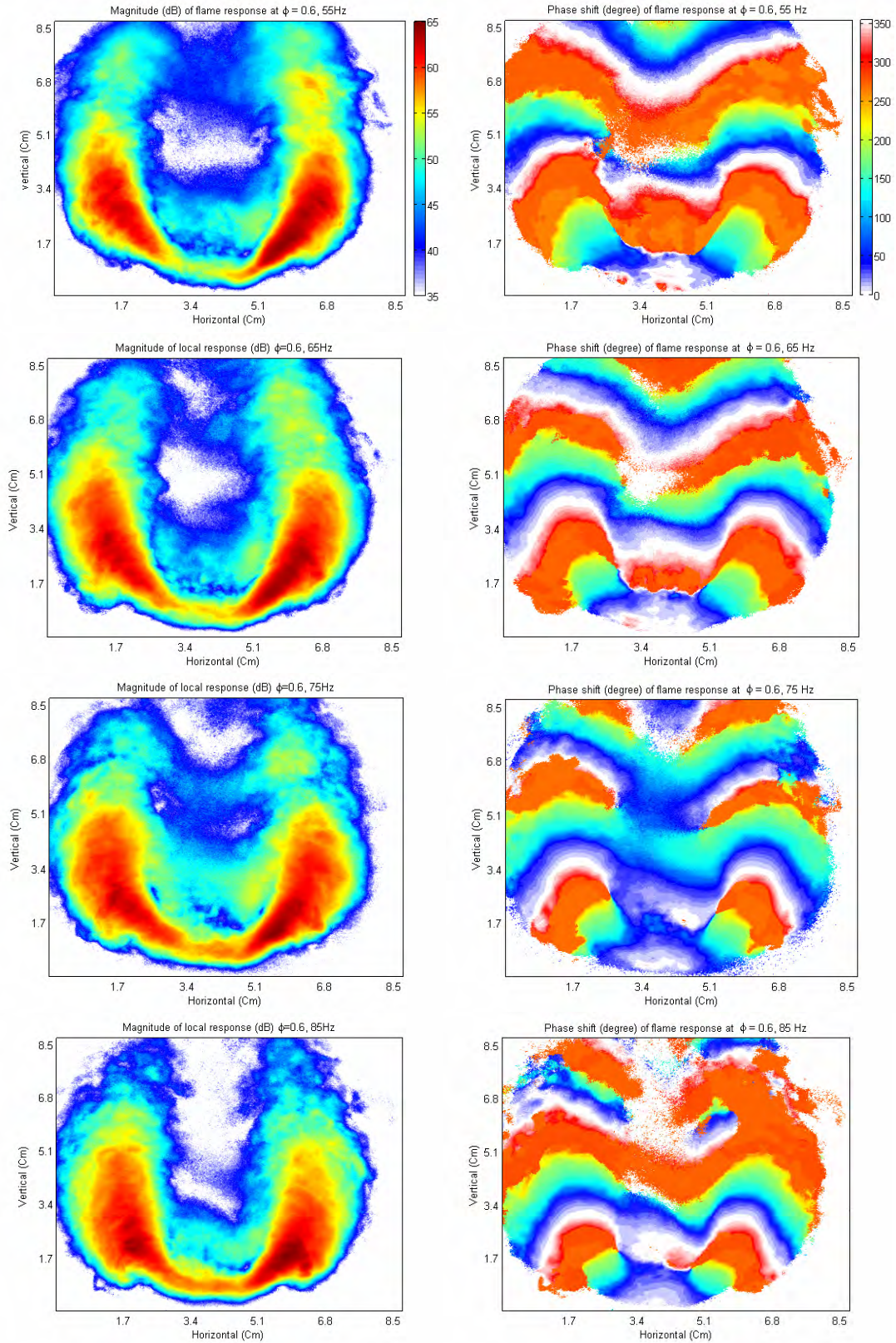


**Figure D.31. Local magnitude (left), and phase shift (right) of flame response,  $\phi = 0.60$ .**

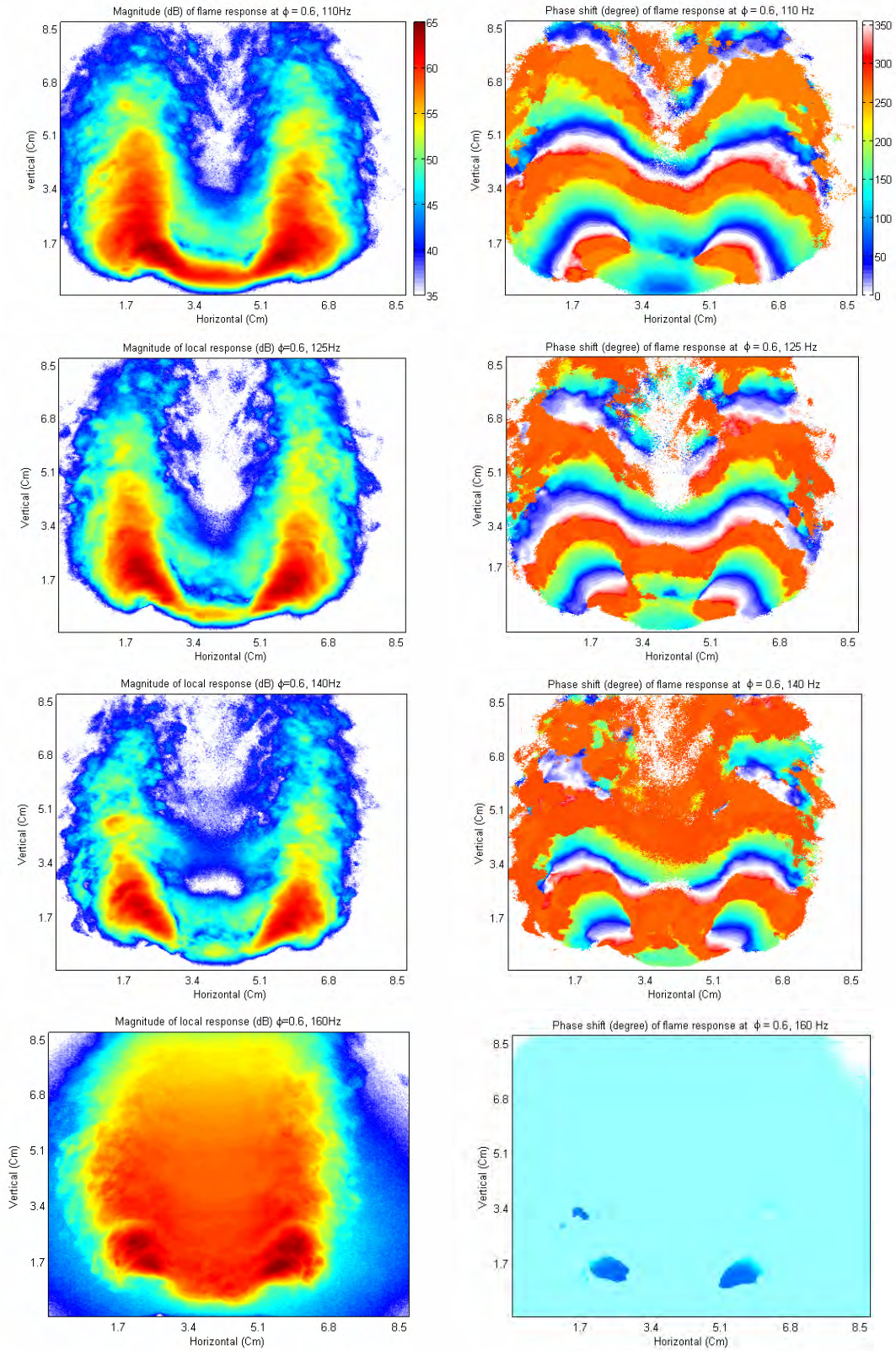


**Figure D.32. Local magnitude (left), and phase shift (right) of flame response,  $\phi = 0.60$ .**

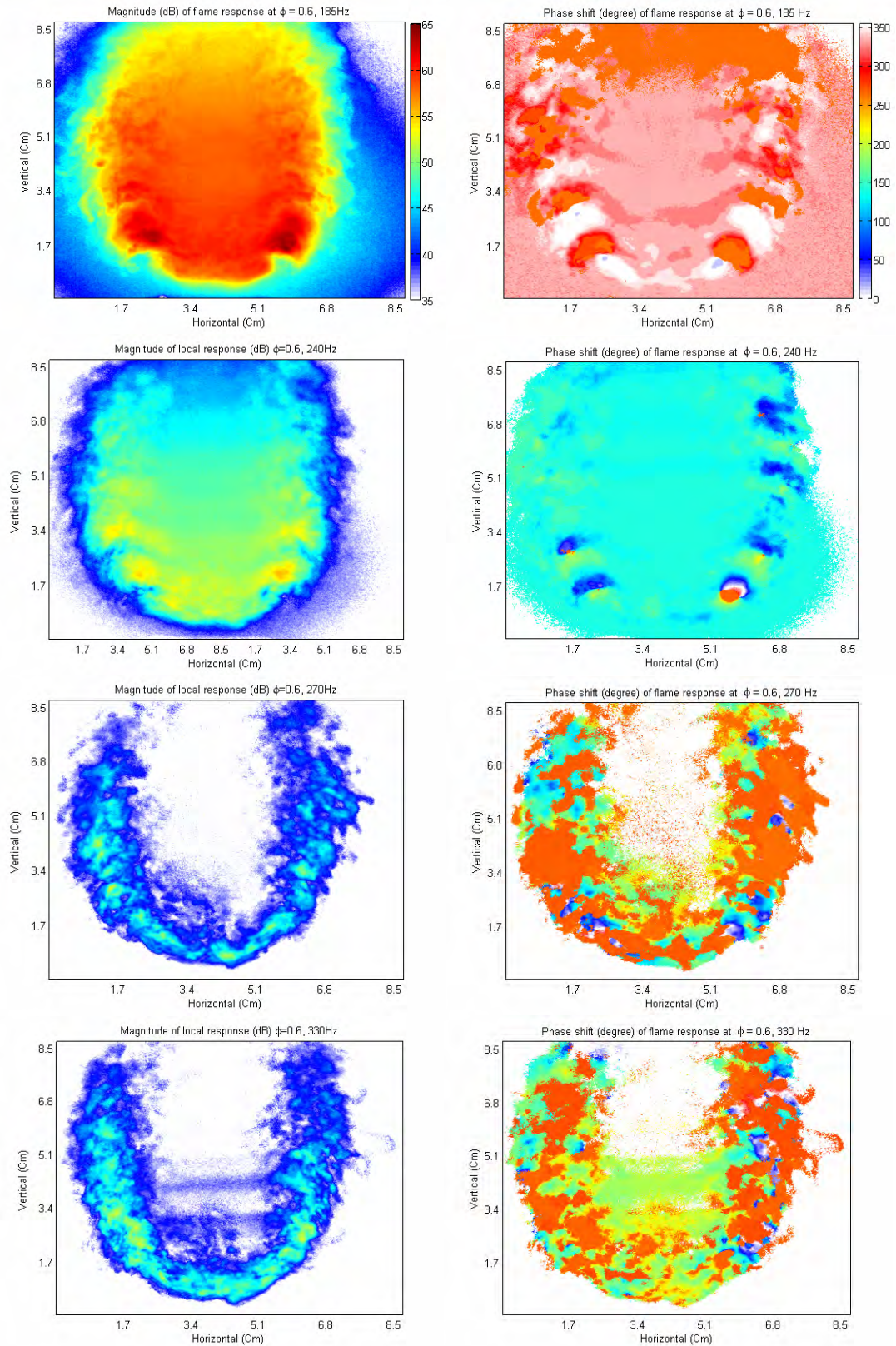


**Figure D.33. Local magnitude (left), and phase shift (right) of flame response,  $\phi = 0.60$ .**

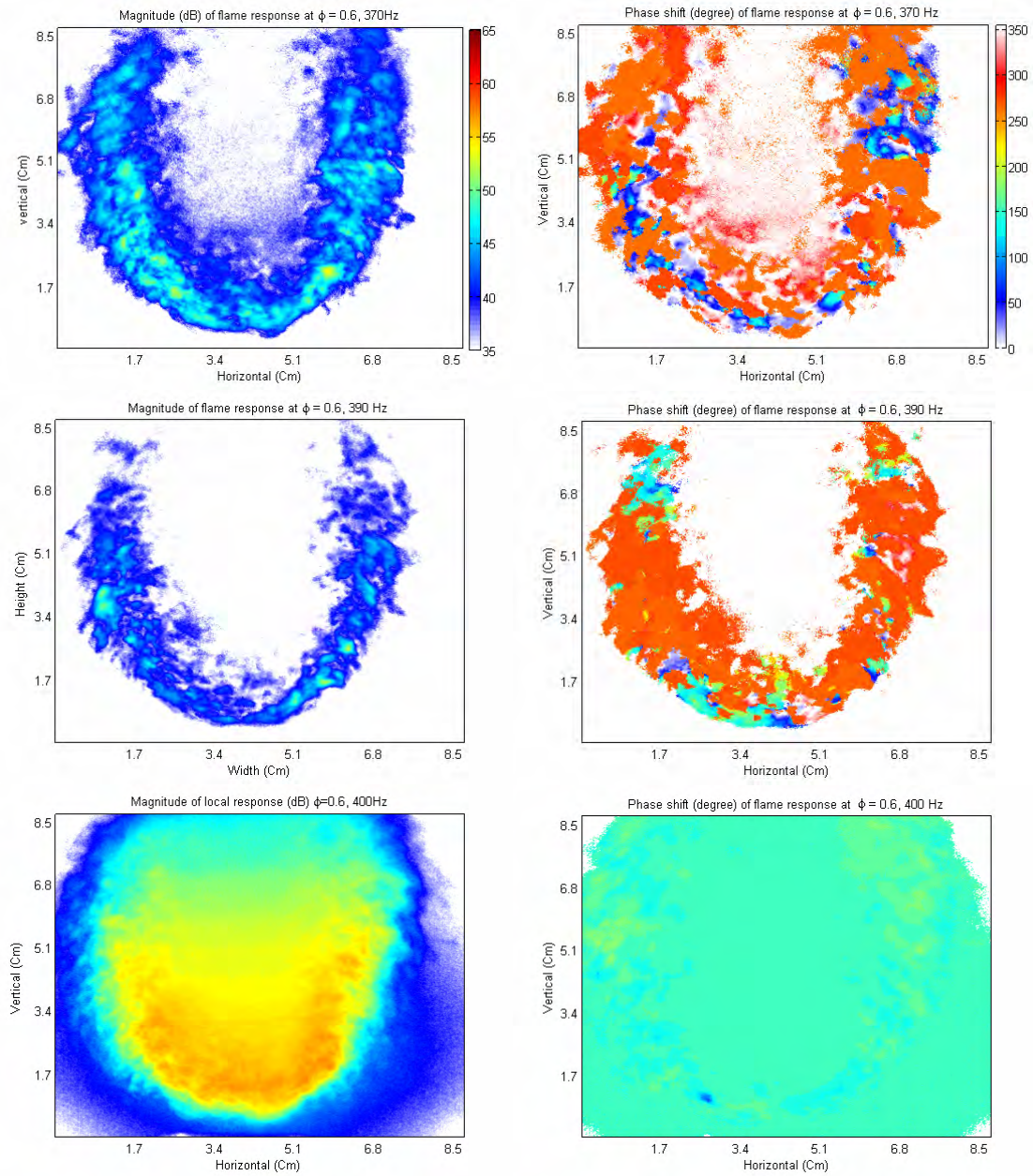


**Figure D.34. Local magnitude (left), and phase shift (right) of flame response,  $\phi = 0.60$ .**

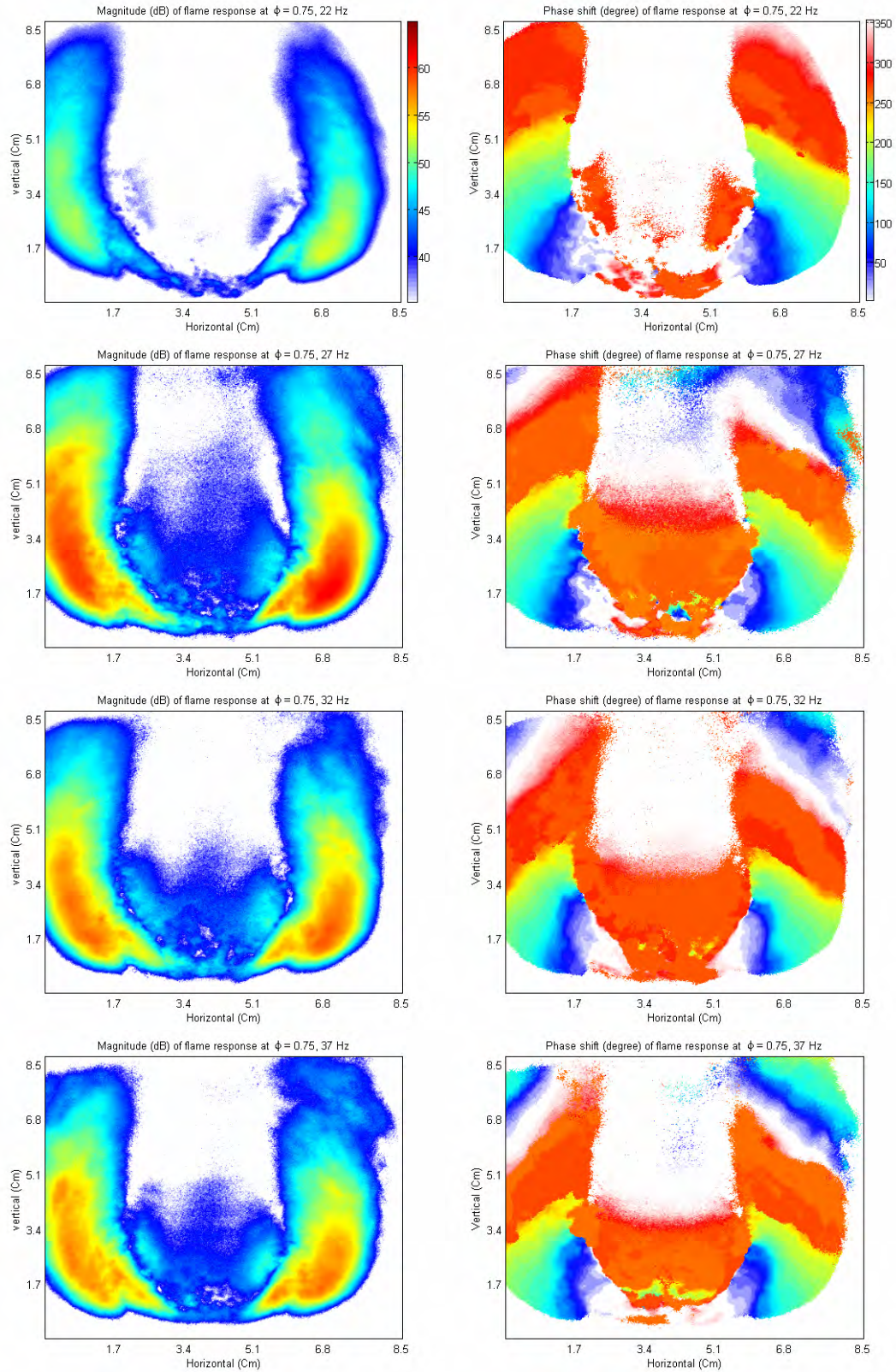
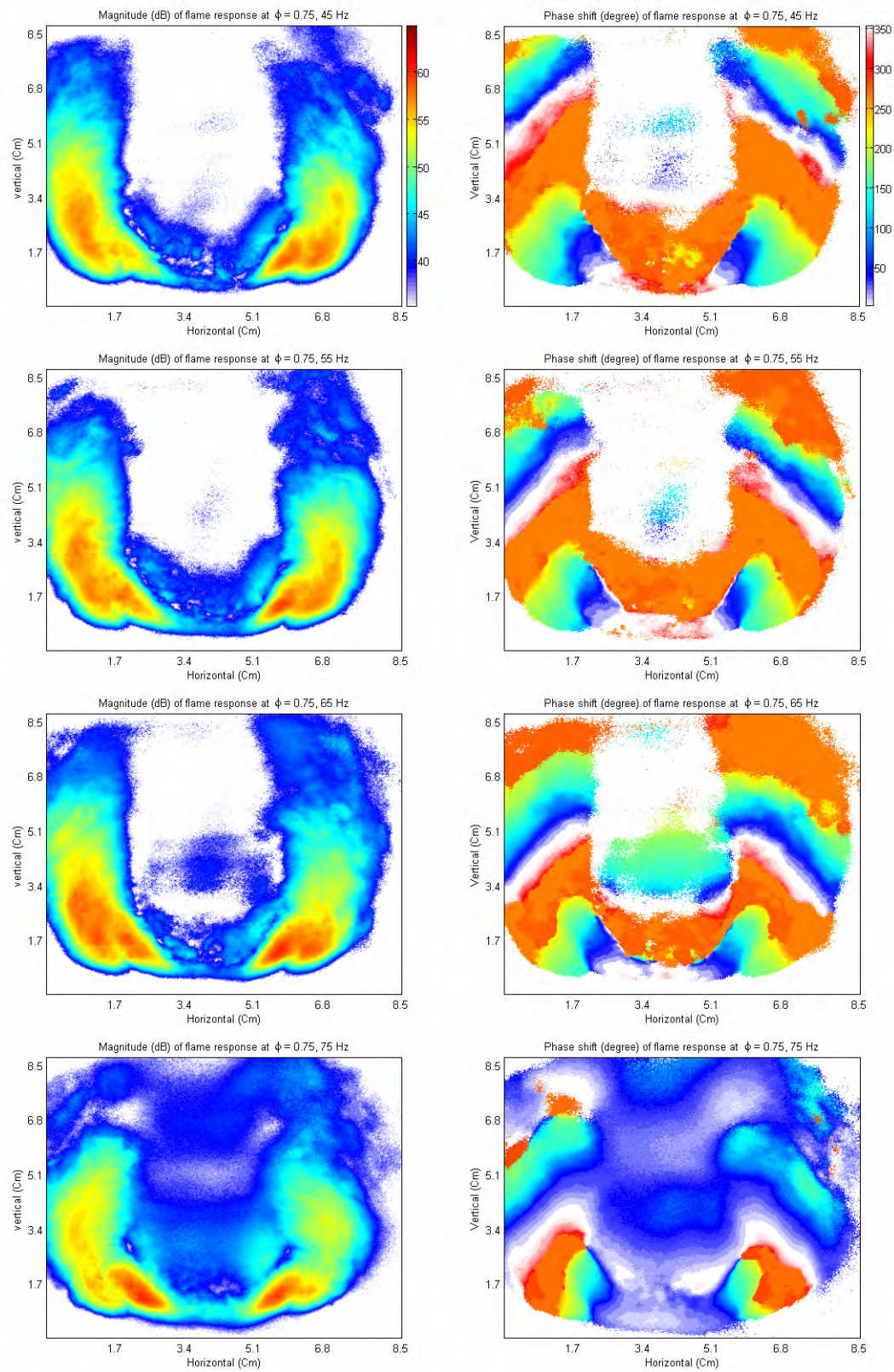
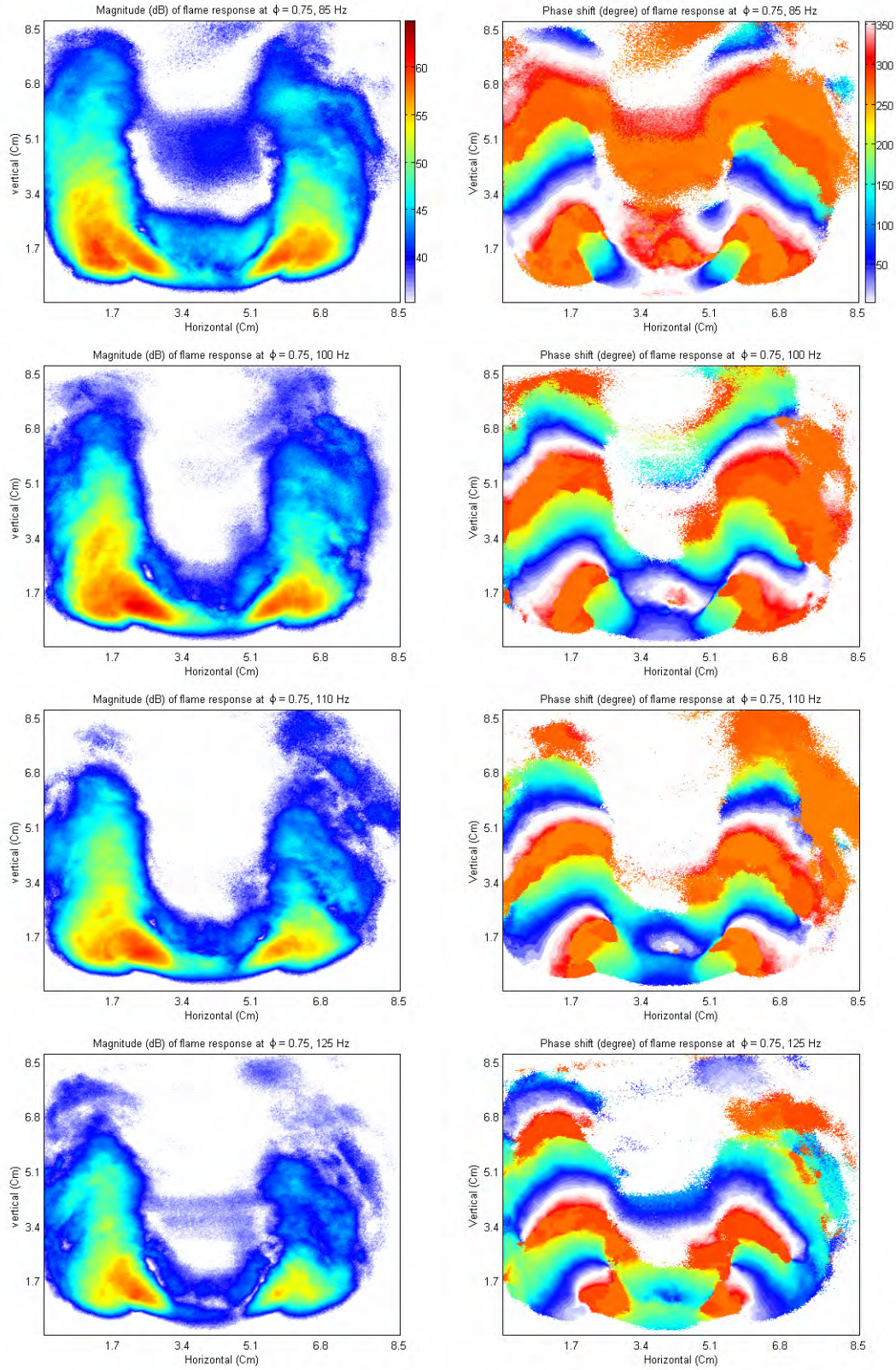


Figure D.35. Local magnitude (left), and phase shift (right) of flame response,  $\phi = 0.75$ .



**Figure D.36. Local magnitude (left), and phase shift (right) of flame response,  $\phi = 0.75$ .**



**Figure D.37. Local magnitude (left), and phase shift (right) of flame response,  $\phi = 0.75$ .**

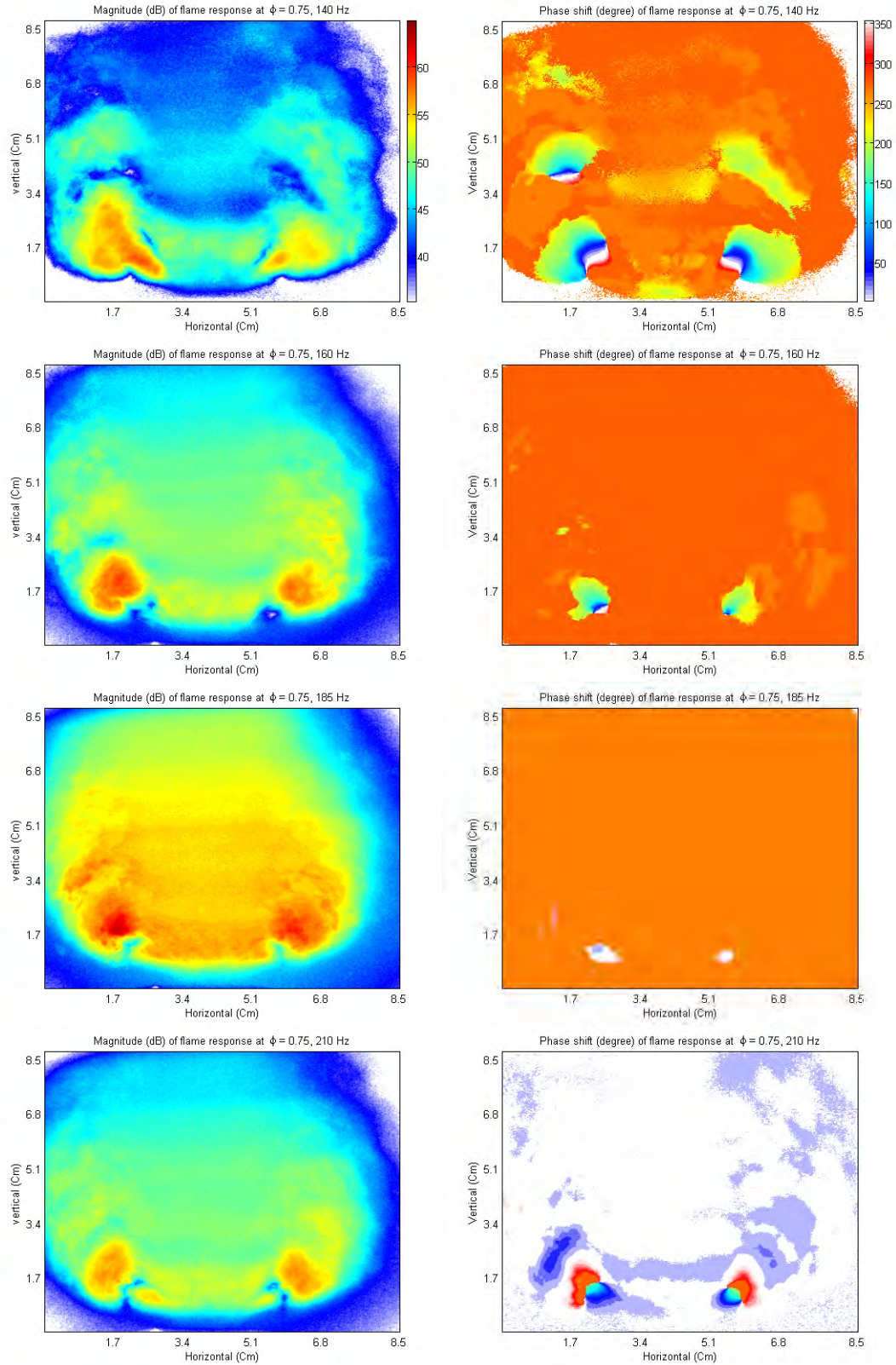


**Figure D.38. Local magnitude (left), and phase shift (right) of flame response,  $\phi = 0.75$ .**

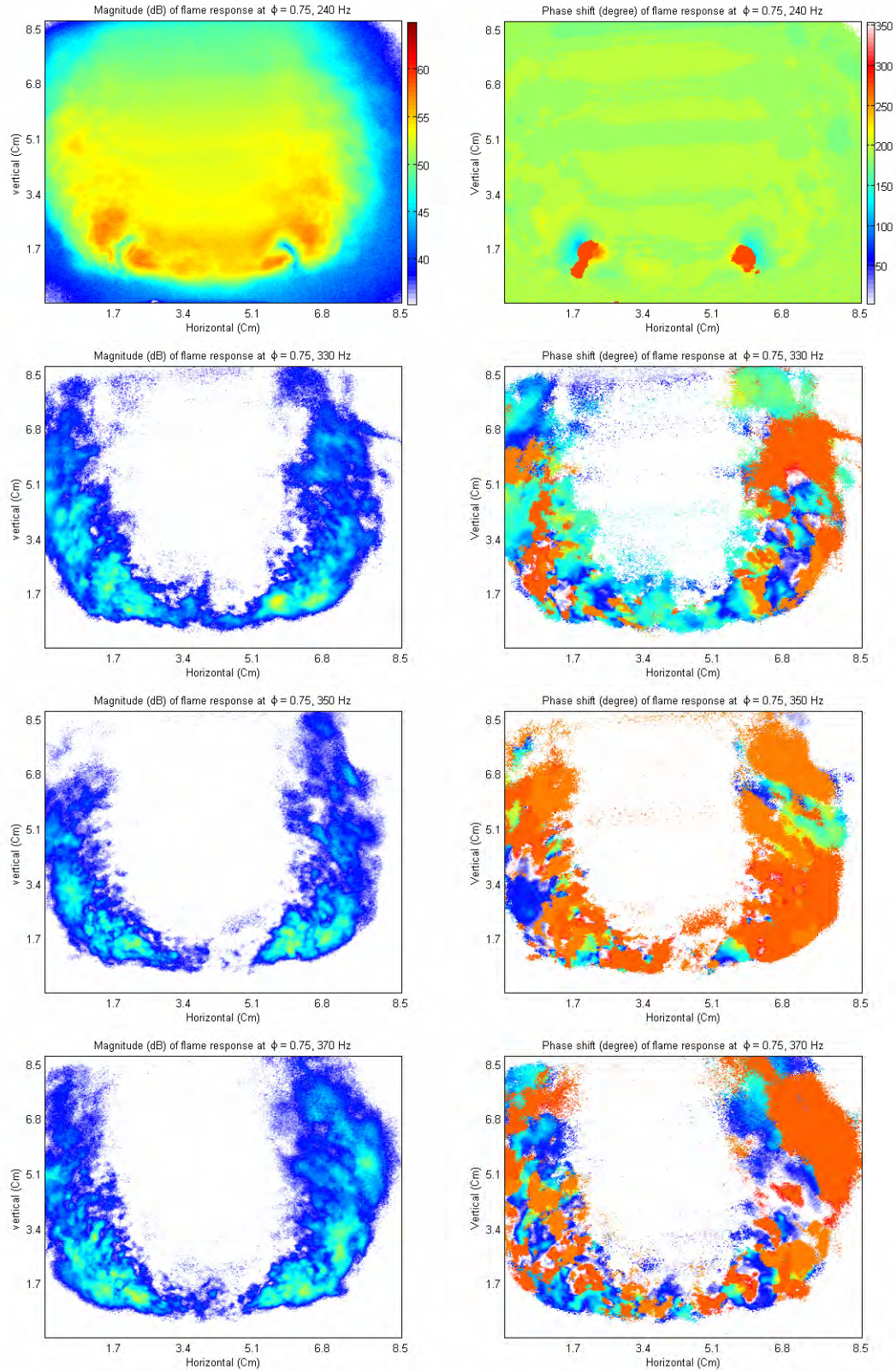


**Figure D.39. Local magnitude (left), and phase shift (right) of flame response,  $\phi = 0.75$ .**

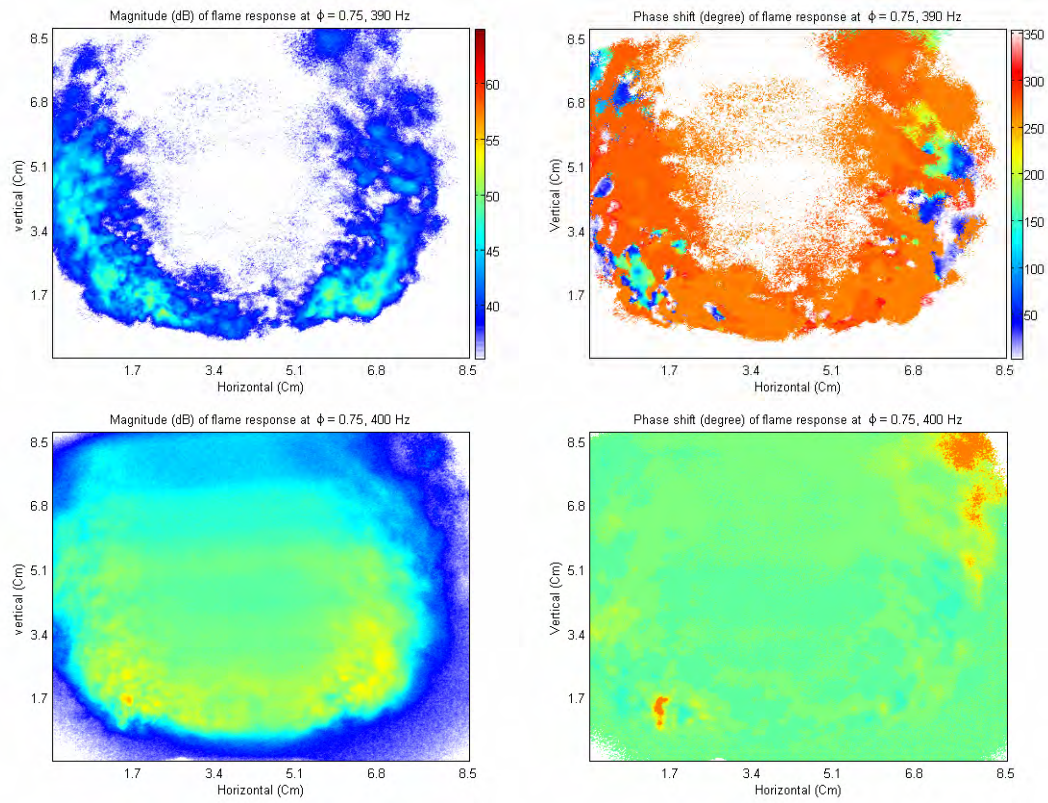


**Figure D.40. Local magnitude (left), and phase shift (right) of flame response,  $\phi = 0.75$ .**

# References

---

- Allen, M.G., McManus, K.R., Sonnenfroh, D.M., and Paul, P.H., (1995) "Planar laser-induced fluorescence imaging measurements of OH and hydrocarbon fuel fragments in high-pressure spray-flame combustion", *Applied Optics*, Vol. 34, No. 27.
- Anderson, W. E., Miller, K. L., Ryan, H. M., Pal, S., Santoro, R. J., and Dressler, J. L. (1998) "Effects of periodic atomization on combustion instability in liquid-fueled propulsion systems", *J. of Prop. Power*, Vol. 14, No. 5, pp. 818-825.
- Bernier, D., Lacas, F., and Candel, S. (2004), "Instability mechanisms in a premixed prevaporized combustor", *J. Prop. Power*, Vol. 20, No. 4, pp. 648-656.
- Bessler, W.G., Schulz, C., and Lee, T. (2002) "Strategies for laser-induced fluorescence detection of nitric oxide in high-pressure flames. I. A-X(0,0) excitation", *Applied optics*, Vol. 41, No. 18, pp. 3547-3557.
- Bessler, W.G., Schulz, C, and Lee, T. (2002) "Quantitative NO-LIF imaging in high-pressure flames", *Applied physics B*, Vol. 75, No. 1, pp. 97-102.
- Bloxside, G.J., Dowling A.P., and Langhorne, P.J. (1988) "Reheat buzz: an acoustically coupled combustion instability. Part 2. Theory", *J. Fluid Mech.*, Vol. 193, pp. 445-473.
- Broda, J. C., Seo, S., Santoro, R. J., Shirhattikar, G., and Yang, V. (1998) "An Experimental Study of Combustion Dynamics of a Premixed Swirl Injector", 27th Symposium (International) on Combustion, The combustion Institute, pp. 1849-1856.

- Cadou, C.P., Logan, P., Karagozian, A.R., and Smith, O.I. (1991) "Laser diagnostic techniques in a resonant incinerator", *Environ. Sensing Combust. Diagn.*, SPIE, Vol. 1434, pp. 67-77.
- Cadou, C. P., Smith, O. I., and Karagozian, A. R. (1998) "Transport enhancement in acoustically excited cavity flows, Part 2: Reactive flow diagnostics", *AIAA Journal*, Vol. 36, No. 9, pp. 1568-1574.
- Cattolica, R.J. (2003). Personal Communications by F. Ciucci, San Diego, CA.
- Chen, T. Y., Hegde, U. G., Daniel, B. R., and Zinn, B. T. (1993) "Flame radiation and acoustic intensity measurements in acoustically excited diffusion flames *J. of Prop. Power*, Vol. 9, No. 2, pp. 210-216.
- Chen, J. H., and Echehki, T. (1999) "The mechanism of two-dimensional pocket formation in lean premixed methane-air flames with implications to turbulent combustion", *Combustion and flame*, Vol. 116, No. 1-2, pp. 15-48.
- Chen, J. Y., and Echehki, T. (2001) "Numerical study of buoyancy effects on the structure and propagation of triple flames" *Combustion theory and modeling*, Vol. 5, No. 4, pp. 499-515.
- Cheng, R.K. (1999) "Low-emission Burners", EETD news letters, world-wide-web [http://eetd.lbl.gov/newsletter/NL2/Low-emission\\_burner.html](http://eetd.lbl.gov/newsletter/NL2/Low-emission_burner.html).
- Cheng, R.K., Yegian, D.T., Miyasato, M.M., Samuelsen, G.S., Benson, C.E., Pellizzari, R., and Loftus, P. (2000) "SCALING AND DEVELOPMENT OF LOW-SWIRL BURNERS FOR LOW-EMISSION FURNACES AND BOILERS", 27th Symposium (International) on Combustion, The combustion Institute, pp.1305-1313.

- Chu, B.-T. (1964) "On the Energy Transfer to Small Disturbances in Fluid Flow (Part I)", *Acta Mech.*, I/3, pp. 215-234.
- Cohen, J. M., Stufflebeam, J. H., and Proscia, W. (2001) "The effect of fuel/air mixing on actuation authority in an active combustion instability control system", *J. Eng. Gas Turbines and Power*, Vol. 123, No. 3, pp. 537-542.
- Cohen, J. M., and Banaszuk, A. (2003) "Factors affecting the control of unstable combustors", *J. of Prop. Power*, Vol. 19, No. 5, pp. 811-821.
- Cooper, C. (1997) "Effect of pulsed dye-laser wavelength stabilization on spectral overlap in atmospheric NO fluorescence studies", *Applied optics*, Vol. 36, No. 21, pp. 5262-5265.
- Cooper, C.S., and Laurendeau, N.M. (2000) "In-situ calibration technique for laser-induced fluorescence measurements of nitric oxide in high-pressure, direct-injection, swirling spray flames", *Combust. Sci. Tech.*, Vol. 161, pp. 165-189.
- Culick, F.E.C. (1973) "The stability of one-dimensional motions in a rocket motor", *Combust. Sci. Tech.*, Vol. 7, pp. 165-175.
- Culick, F.E.C. (1975) "Stability of three-dimensional motions in a combustion chamber", *Combust. Sci. Tech.*, Vol. 10, pp. 109-124.
- Culick, F.E.C. (1976) "Nonlinear behavior of acoustic waves in combustion chambers, Part I", *Acta Astronautica*, Vol. 47, No. 13, pp. 715-734.
- Culick, F.E.C. (1976) "Nonlinear behavior of acoustic waves in combustion chambers, Part II", *Acta Astronautica*, Vol. 47, No. 13, pp. 735-757.

- Culick, F.E.C. (1981) "Combustion instability in solid rocket motors. Volume II: A guide for motor designers", Chemical Propulsion Information Agency, CPIA publication 290, Johns Hopkins Applied Physics Laboratory.
- Culick, F.E.C. (1987) "A NOTE ON RAYLEIGH CRITERION", *Combust. Sci. and Tech.*, Vol. 56, No.4-6, pp. 159-166.
- Culick, F.E.C. (1997) "A note on ordering perturbations and the insignificance of linear coupling in combustion instabilities", *Combust. Sci. and Tech.*, Vol. 126, No. 1-6, pp. 359-379.
- Culick, F.E.C. (2004), AFSOR final report, AFSOR\_F49620-99-1-0118.
- Culick, F.E.C. (2005), AGARDOGRAPH, *In progress*.
- Daily, J. W., Bessler, W. G., Schulz, C., Sick, V., and Settersten, T. B. (2005) "Nonstationary collisional dynamics in determining nitric oxide laser-induced fluorescence spectra", *AIAA Journal*, Vol. 43, No. 3, pp. 458-464.
- Demare, D., and Baillot, F. (2004) "Acoustic enhancement of combustion in lifted nonpremixed jet flames", *Combustion and flame*, Vol. 139, No. 4, pp. 312-328.
- Demayo, T. N., Leong, M. Y., Samuelsen, G. S., and Holdeman, J. D. (2003) "Assessing jet-induced spatial mixing in a rich, reacting crossflow", *J. of Prop. Power*, Vol. 19, No. 1, pp. 14-21.
- Dieke, G.H. and Crosswhite, H.M. (1962) "The Ultraviolet Bands of OH", *J. Quant. Spectrosc. Radiat. Transfer*, Vol. 2, pp. 97-199.
- Dimotakis, P. E., and Miller, P. L. (1990) "Some consequences of the boundedness of scalar fluctuations", *Phys. Fluids A*, Vol. 2, No. 11, pp. 1919-1920.

- Dowling, A.P., and Bloxsidge, G.J. (1984), "Reheat Buzz – An Acoustically Driven Combustion Instability", AIAA/NASA 9<sup>th</sup> Aeroacoustics Conference, AIAA-84-2321.
- Dowling, A.P. (1984) "CORRECTION", J. Sound Vib., Vol. 94, No. 2, pp. 317-317.
- Dowling, A. P. (2000) "The 1999 Lanchester lecture - Vortices, sound and flames - a damaging combination", Aeronautical Journal, Vol. 104, No. 1033, 105-116.
- Durox, D., Schuller, T., and Candel, S. (2002) "Self-induced instability of a premixed jet flame impinging on a plate", 29th Symposium (International) on Combustion, The combustion Institute, pp. 69-75.
- Durox, D., Schuller, T., and Candel, S. (2005) "Combustion dynamics of inverted conical flames", 30th Symposium (International) on Combustion, The combustion Institute, pp. 1717-1724.
- Dyer, M.J., and Crosley, D.R. (1982) "Two-dimensional imaging of OH laser-induced fluorescence in a flame", Optical letters, Vol. 7, No. 8, pp. 382-384.
- Eckbreth, A.C. (1996) "Laser Diagnostics for Combustion Temperature and Species", Gordon and Breach Publishers, 2<sup>nd</sup> Ed.
- Fernandez, V., Ratner, A., and Culick, F. E. C. (2003) "Measured Influence of Oscillations in Fuel Mixture Fraction on Flame Behavior", Proceedings of the Third Joint Meeting of the U.S. Sections of The Combustion Institute, Chicago, IL, March 16-19, 2003.
- Fric, T. F. (1993) "EFFECTS OF FUEL-AIR UNMIXEDNESS ON NOX EMISSIONS", J. of Prop. Power, Vol. 9, No. 5, pp. 708-713.

- Ganapathisubramani, B., Longmire, E.K., and Maruic, I. (2002) "Investigation of three dimensionality in the near field of a roundjet using stereo PIV", *J. Turbulence*, Vol. 3, Art. No. 016.
- Gulati, A., and Warren, R. E. (1994) "NO<sub>2</sub>-BASED LASER-INDUCED FLUORESCENCE TECHNIQUE TO MEASURE COLD-FLOW MIXING", *J. of Prop. Power*, Vol. 10, No. 1, pp. 54-61.
- Hantschk, C. C., and Vortmeyer, D. (2002) "Numerical simulation of self-excited combustion oscillations in a non-premixed burner", *Combust. Sci. and Tech.*, Vol. 174, pp. 189-204.
- Hardalupas, Y., and Selbach, A. (2002) "Imposed oscillations and non-premixed flames", *Progress in energy and combustion science*, pp. 75-104.
- Harrje, D.T., and Reardon, F.H. (1972) "Liquid Propellant Rocket Combustion Instability", NASA, SP-194.
- Heneghan, S.P., and Vansness, M. (1990) "INSTRUMENT NOISE AND WEIGHTING FACTORS IN DATA-ANALYSIS ", *Experiments in fluids*, Vol. 9, No. 5, pp. 290-294.
- Johnson, R.O., Karis, S.J., and Perram, G.P. (1998) "Characterization of a Br(P-2(1/2))-CO<sub>2</sub>(10(0)1-10(0)0) transfer laser driven by photolysis of iodine monobromide", *Applied Physics B*, Vol. 66, No. 4, pp. 411-415.
- Kappei, F., Lee, J. Y., Johnson, C. E., Lubarsky, E., Neumeier, Y., and Zinn, B. T. (2000) "Investigation of Oscillatory Combustion Processes In Actively Controlled Liquid Fuel Combustor", 36th Joint Propulsion Conference, AIAA 2000-3348.

- Kendrick, D. W., Anderson, T. J., and Sowa, W. A. (1999) "Acoustic Sensitivities of Lean-Premixed Fuel Injectors in a Single Nozzle Rig", *J. Eng. Gas Turbines and Power*, Vol. 121, pp. 429-436.
- Kim, T. K., Park, J., and Shin, H. D. (1993) "MIXING MECHANISM NEAR THE NOZZLE EXIT IN A TONE EXCITED NON-PREMIXED JET FRAME", *Combust. Sci. and Tech.*, Vol. 89, No. 1-4, pp. 83-100.
- Kobayashi, H. (2002) "Experimental study of high-pressure turbulent premixed flames", *Experimental thermal and fluid science*, Vol. 26, No. 2-4, pp. 375-387.
- Langhorne, P.J. (1988) "Reheat buzz: an acoustically coupled combustion instability. Part 1. Experiment", *J. Fluid Mech.*, Vol. 193, pp. 417-443.
- Lawn, C. J. (2000) "The acoustic self-excitation of a bluff-body stabilised, premixed flame", *Combust. Sci. and Tech.*, Vol. 154, pp. 57-74.
- Lee T., Shin, D.-I, Jeffries, J.B., Hanson, R.K., Bessler, W.G., and Schultz, C. (2002) "Laser-Induced Fluorescence Detection of NO in High-Pressure Flames with A-X(0,0), (0,1), and (0,2) Excitation", AIAA 2002-0399.
- Lieuwen, T., Neumeier, Y., and Zinn, B. T. (1998) "The Role of Unmixedness and Chemical Kinetics in Driving Combustion Instabilities in Lean Premixed Combustors", *Combust. Sci. and Tech.*, Vol. 135, No. 1-6, pp. 193-211.
- Lieuwen, T., and Neumeier, Y. (2002) "Nonlinear pressure-heat release transfer function measurements in a premixed combustor", *27th Symposium (International) on Combustion*, The combustion Institute, pp. 99-105.
- Littlejohn, D., Majeski, A.J., Tonse, S., Castaldini, J., and Cheng, R.K. (2003) "Laboratory investigation of an ultralow NO<sub>x</sub> premixed combustion concept for

- Industrial boilers”, 29th Symposium (International) on Combustion, The combustion Institute, pp. 1115-1121.
- Lozano, A., Yip, B., and Hanson, R. K. (1992) "Acetone : a Tracer for Concentration Measurements in Gaseous Flows by Planar Laser-Induced Fluorescence", *Experiments in Fluids*, Vol. 13, pp. 369-376.
- Matta, L. M., Zhu, C., Jagoda, J. I., and Zinn, B. T. (1996) "Mixing by resonant acoustic driving in a closed chamber", *J. of Prop. Power*, pp. 366-370.
- Menon, S., and Soo, J.H. (2004) "Simulation of vortex dynamics in three-dimensional synthetic and free jets using the large-eddy lattice Boltzmann method", *J. Turbulence*, Vol. 5, Article No. 5.
- Meyer, T. R., King, G. F., Martin, G. C., Lucht, R. P., Schauer, F. R., and Dutton, J. C. (2002) "Accuracy and resolution issues in NO/acetone PLIF measurements of gas-phase molecular mixing" *Experiments in fluids*, Vol. 32, No. 6, pp. 603-611.
- Nguyen, Q. (1996) "Raman-LIP measurements of temperature, major species, OH, and NO in a methane-air Bunsen flame", *Combustion and flame*, Vol. 105, No. 4, pp. 499-510.
- Nguyen, Q. V., and Paul, P. H. (2001) "Photochemical effects of KrF excimer excitation in laser-induced fluorescence measurements of OH in combustion environments", *Applied Physics B*, Vol. 72, No. 4, pp. 497-505.
- Nooren, P. A., Versluis, M., van der Meer, T. H., Barlow, R. S., and Frank, J. H. (2000) "Raman-Rayleigh-LIF measurements of temperature and species concentrations in the Delft piloted turbulent jet diffusion flame", *Applied Physics B*, Vol. 71, No. 1, pp. 95-111.

- Paschereit, C.O., Gutmark, E., and Weisenstein, W. (2000) "Excitation of thermo-acoustic instabilities by interaction of acoustics and unstable swirling flow", *AIAA Journal*, Vol. 38, No. 6, pp. 1025-1034.
- Papas, P., Monkewitz, P. A., and Tomboulides, A. G. (1999) "New instability modes of a diffusion flame near extinction", *Physics of fluids*, Vol. 11, No. 10, pp. 2818-2820.
- Paul, P. (1996) "Collisional electronic quenching rates for  $\text{NO} \text{ A}(2)\Sigma^+(\text{u})\text{v}'=0$ ", *Chemical physics letters*, Vol. 259, No. 5-6, pp. 508-514.
- Paul, P. H., and Najm, H. N. (1998) "Planar laser-induced fluorescence imaging of flame heat release rate", *27th Symposium (International) on Combustion*, The combustion Institute, pp. 43-50.
- Perucho, M., Marti, J.M., and Hanasz, M. (2004) "Stability of hydrodynamical relativistic planar jets", *Astronomy & Astrophysics*, Vol. 427, No. 2, pp. 431-444.
- Pun, W., Palm, S. L., and Culick, F. E. C. (2000) "PLIF Measurements of Combustion Dynamics in a Burner under Forced Oscillatory Conditions", *36th Joint Propulsion Conference*, AIAA-2000-3123.
- Pun, W. (2001) "Measurements of thermo-acoustic coupling", Ph.D. Thesis, California Institute of Technology.
- Pun, W., Palm, S.L. and Culick, F.E.C. (2001) "PLIF Measurements of Combustion Dynamics in a Burner Under Forced Oscillatory Conditions", *36th AIAA/ASME/SAE/ASEE Joint Propulsion Conference & Exhibit (July 2000)* Huntsville, AL, Paper No. AIAA 2000-3123.

- Pun, W. Ratner, A., and Culick, F.E.C. (2002) "Phase-resolved chemiluminescence of an acoustically forced jet flame at frequencies  $< 60$  Hz. 40th", AIAA Aerospace Sciences Meeting & Exhibit AIAA-2002-0194.
- Pun, W., Palm, S. L., and Culick, F. E. C. (2003) "Combustion dynamics of an acoustically forced flame", *Combust. Sci. and Tech.*, Vol. 175, No. 3, pp. 499-521.
- Putnam, A.A. (1964) "General considerations of autonomous combustion oscillations", The MacMillan Co., New York.
- Ratner, A., Pun, W., Palm, S. L., and Culick, F. E. C. (2002) "Comparison of Chemiluminescence, OH PLIF, and NO PLIF for Determination of Flame Response to Acoustic Waves", Western States Section Meeting of the Combustion Institute.
- Ratner, A., Pun, W., Palm, S. L., and Culick, F. E. C. (2003) "Phase-resolved no planar laser-induced fluorescence of a jet flame in an acoustic chamber with excitation at frequencies  $< 60$  Hz", 29th Symposium (International) on Combustion, The combustion Institute, pp. 85-90.
- Ryleigh, J.W.S. (1945) "The Theory of Sound Vol. II", Dover Publications.
- Reisel, J. R., Carter, C. D., Laurendeau, N. M., and Drake, M. C. (1993) "LASER-SATURATED FLUORESCENCE MEASUREMENTS OF NITRIC-OXIDE IN LAMINAR, FLAT, C<sub>2</sub>H<sub>6</sub>/O<sub>2</sub>/N<sub>2</sub> FLAMES AT ATMOSPHERIC-PRESSURE", *Combust. Sci. and Tech.*, Vol. 91, No. 4-6, pp. 271-295.
- Reisel, J.R. (2000) „Effects of Mass Flow Rate and Initial Temperature on Predictions of NO and OH from Detailed Chemical Kinetics Models”, *Combust. Sci. and Tech.*, Vol. 160, pp. 47-63.

- Richards, G.A., Gemmen, R.S., and Yip, M.J. (1997) "A test device for premixed gas turbine combustion oscillations", *J. Eng. Gas Turbines and Power*, Vol. 119, No. 4, pp. 776-782.
- Rosfjord, T. (1995) "Lean-Limit Combustion Instability" United Technologies Research Center.
- Schuller, T., Durox, D., and Candel, S. (2002) "Dynamics of and noise radiated by a perturbed impinging premixed jet flame", *Combustion and flame*, Vol. 128, No.1-2, pp. 88-110.
- Schuller, T., Durox, D., and Candel, S. (2003) "Self-induced combustion oscillations of laminar premixed flames stabilized on annular burners", *Combustion and flame*, Vol. 135, No. 4, pp. 525-537.
- Schultz, C., Jeffries, J.B., Koch, D.F., Wolfrum, J., and Hanson, R.K. (2003) „Impact of UV by CO<sub>2</sub> and H<sub>2</sub>O on NO LIF in High-Pressure Combustion Applications”, 20th Symposium (International) on Combustion, The combustion Institute, pp. 2735-2742.
- Shih, W.P, Lee, J.G., and Santavicca, D.A., (1996) "Stability and Emissions Characteristics of a Lean Premixed Gas Turbine Combustor", Twenty-Sixth Symposium (International) on Combustion, The Combustion Institute.
- Sivasegaram, S., Tsai, R.F., and Whitelaw, J.H. (1995) "Control of combustion oscillations by forced oscillation of part of the fuel supply", *Combust. Sci. Tech.*, Vol. 105, No. 1-3, pp. 67-83.
- Sterling, J. D., and Zukoski, E. E. (1991) "Nonlinear Dynamics of Laboratory Combustor Pressure Oscillations", *Combust. Sci. and Tech.*, Vol. 77, pp. 225-238.

- Tamura, M., Luque, J., Harrington, J. E., Berg, P. A., Smith, G. P., Jeffries, J. B., and Crosley, D. R. (1998) "Laser-induced fluorescence of seeded nitric oxide as a flame thermometer", *Applied Physics B*, Vol. 66, No. 4, pp. 503-510.
- Thurber, M. C., Grisch, F., and Hanson, R. K. (1997) "Temperature imaging with single- and dual-wavelength acetone planar laser-induced fluorescence", *Optics letters*, Vol. 22, No. 4, pp. 251-253.
- Thurber, M. C., Grisch, F., Kirby, B. J., Votsmeier, M., and Hanson, R. K. (1998) "Measurements and modeling of acetone laser-induced fluorescence with implications for temperature-imaging diagnostics", *Applied optics*, Vol. 37, No. 21, pp. 4963-4978.
- Thurber, M. C., and Hanson, R. K. (1999) "Pressure and composition dependences of acetone laser-induced fluorescence with excitation at 248, 266, and 308 nm", *Applied Physics B*, Vol. 69, No. 3, pp. 229-240.
- Thurber, M. C., and Hanson, R. K. (2001) "Simultaneous imaging of temperature and mole fraction using acetone planar laser-induced fluorescence", *Experiments in Fluids*, Vol. 30, No. 1, pp. 93-101.
- Torger, J.A., Kendrick, D.W., and Cohen, J.M. (1998) "Measurement of Spray/Acoustic Coupling in Gas Turbine Fuel Injectors", presented at the *36<sup>th</sup> Aerospace Sciences Meeting & Exhibit*, Reno, NV, AIAA 98-0718.
- Venkataraman, K. K., Preston, L. H., Simons, D. W., Lee, B. J., Lee, J. G., and Santavicca, D. A. (1999) "Mechanism of Combustion Instability in a Lean Premixed Dump Combustor". *J. Prop. Power*, Vol. 15, No. 6, pp. 909-918.

- Warnatz, J. (2000) "Hydrocarbon oxidation high-temperature chemistry", Pure and applied chemistry, Vol. 72, No. 11, pp. 2101-2110.
- Wolfrum, J. (1998). "Lasers in Combustion: From Basic Theory to Practical Devices", 27th Symposium (International) on Combustion, The combustion Institute, pp. 1-41.
- Wu, W.-J., and Kung, L.-C. (2000) "Determination of Triggering Condition of Vortex-Driven Acoustic Combustion Instability in Rocket Motors", J. of Prop. Power, Vol. 16, No. 6, pp. 1022-1029.
- Yip, B., Miller, M. F., Lozano, A., and Hanson, R. K. (1994) "A COMBINED OH/ACETONE PLANAR LASER-INDUCED FLUORESCENCE IMAGING TECHNIQUE FOR VISUALIZING COMBUSTING FLOWS", Experiments in fluids, Vol. 17, No. 5, pp. 330-336.
- Zinn, B.T. (1986) "Advanced Combustion Methods", Academic Press, London.